

REGIONAL PROPERTIES OF ANGULAR REFLECTANCE MODELS

by J. M. Davis and S. K. Cox



Atmospheric Science
PAPER NO.
338

US ISSN 0067-0340

DEPARTMENT OF ATMOSPHERIC SCIENCE
COLORADO STATE UNIVERSITY
FORT COLLINS, COLORADO

REGIONAL PROPERTIES OF ANGULAR REFLECTANCE MODELS

By
J. M. Davis
and
S. K. Cox

Research supported by
The National Science Foundation (under
Grants ATM 78-12631 and ATM 80-10691)

Department of Atmospheric Science
Colorado State University
Fort Collins, Colorado

November, 1981

Atmospheric Science Paper Number #338

ABSTRACT

REGIONAL PROPERTIES OF ANGULAR REFLECTANCE MODELS

The inference of the reflected flux density from satellite radiance measurements requires a knowledge of the angular properties of the reflected radiance field. This study examines the angular dependence and the spatial variability of the radiance fields reflected from 30 regional atmospheric scenes. The reflected radiance data set was collected from a high altitude aircraft during the Summer Monsoon Experiment using a unique multi-detector instrument which permitted an instantaneous sampling of the radiance fields from twelve angular viewing coordinates. All of the scenes display sufficient anisotropy to conclude that neglecting the angular variation of the reflected radiances would lead to significant errors (10 - 100%) in the inferred flux density. Radiances over the relatively isotropic scenes converge to their regional mean values on a spatial scale which is small compared to that of the total region. For example, the mean behavior of the radiance field for a 1000 km segment of desert is approached usually after sampling any 25 km portion of the segment. At the other extreme, the mean behavior of the radiance pattern over the same expanse of clear ocean is approached only after a sampling distance of 250 km. The data are analyzed to search for angular coordinates which are optimal for flux density inference. For example, over the clear ocean scene the variance of the inferred flux density is significantly reduced by using radiances reflected at small or large nadir angles and at azimuth angles which are small relative to the azimuth of the sun. It is also shown that a two satellite system is adequate for inferring

ABSTRACT (Continued)

REGIONAL PROPERTIES OF ANGULAR REFLECTANCE MODELS

flux densities over the relatively isotropic scenes while anisotropic scenes benefit from using, at most, three satellites. The angular patterns are applied to TIROS-N measurements over the monsoon region to assess their impact on flux density inferences for a climatically significant region. Use of the angular models results in increases in directional reflectances of up to 2.7% compared to isotropically inferred values for individual scene types. The directional reflectance over the entire region is increased by 1.5% due to the application of the angular reflectance patterns.

ACKNOWLEDGEMENTS

Parts of this research were significantly expedited by the able computer programming assistance provided by Mr. Curtis R. Vogel and Mr. John J. Graffy and by the availability of a set of previous bi-directional reflectance models which were provided by Mr. Eric A. Smith. Appreciation is also extended to Mr. Randy Horn, Mr. Bob Jonas and Mr. Charles Wilkins for constructing a very dependable data collection instrument, and to Mr. Steven Ackerman who monitored the performance of the instrument throughout much of Summer MONEX. This manuscript was expertly typed by Ms. Sandy Wunch and technically edited by Ms. Pauline Martin.

This research was supported by the National Science Foundation under grants ATM-78-12631 and ATM-80-10691. Computer resources were provided by the National Center for Atmospheric Research which is sponsored by the National Science Foundation. The author gratefully acknowledges the contributions of resources and personnel by the NASA/Ames Research Laboratory in the flight testing and data acquisition phase of this investigation.

TABLE OF CONTENTS

	<u>PAGE</u>
ABSTRACT	iii
ACKNOWLEDGMENTS	v
TABLE OF CONTENTS	vi
LIST OF TABLES	viii
LIST OF FIGURES	x
LIST OF SYMBOLS	xxiii
1.0 INTRODUCTION	1
2.0 DESCRIPTION OF THE EXPERIMENT	9
2.1 Description of the 'bugeye instrument'	9
2.2 Calibration of the Instrument	12
2.3 Deployment of the Instrument	14
3.0 DATA ANALYSIS	27
3.1 Angular Reflectance Models	35
3.2 Comparison with Previous Results	51
4.0 IMPLICATIONS CONCERNING THE APPLICATION OF ANGULAR REFLECTANCE MODELS ON A REGIONAL BASIS	66
4.1 Spectral Considerations	66
4.2 Spatial Convergence of the Angular Reflectance Models	71
4.3 Optimal Viewing Angles for Flux Density Inference Based on Application of Angular Models in a 1, 2 or 3 Satellite System	80
4.4 Impact of the Angular Reflectance Models when Applied to a Climatically Significant Region	103
5.0 SUMMARY AND CONCLUSIONS	118
REFERENCES	124

TABLE OF CONTENTS (Continued)

	<u>PAGE</u>
APPENDIX I - Electrical and Optical Characteristics of the Bugeye Photodiode	AI-1
APPENDIX II - Description of the Upward Looking Bugeye Instrument	AII-1
APPENDIX III - The Interpolated χ^{-1} Patterns and Plots of the Flight Tracks over which the data were collected.	AIII-1
APPENDIX IV - The Spherical Harmonic Regression Coefficients of the χ^{-1} Patterns	AIV-1

LIST OF TABLES

	<u>PAGE</u>	
Table 1.	The nadir and azimuthal coordinates of the bugeye photodiodes in degrees.	11
Table 2.	The fraction of the 0.3 - 3.0 μm radiances reflected by various surface and cloud types within the spectral bandpass of the bugeye photodiode. Spectral distributions are from <u>The Infrared Handbook</u> , 1978, edited by Wolfe and Zissis.	34
Table 3.	The directional reflectance values measured by the bugeye and the Eppley 0.3 - 3.0 μm pyranometer for various scene types (top) and the linear regression relation between the directional reflectance values (bottom).	69
Table 4.	The mean and standard deviation of the fraction of the total data sample required for conver- gence to within 5% of the mean angular reflec- tance model for the various scene types.	74
Table 5.	The r.m.s. deviation between inferred and measured, scene averaged reflected flux density averaged over all observation angles and solar zenith angles.	97
Table 6.	The best observational position for a single platform inference and the resulting r.m.s. deviation between the inferred and measured reflected flux density expressed as a percent of the average 0.3 - 3.0 μm reflected flux density.	104
Table 7.	The criteria for and specification of alternate procedures in applying the angular reflectance correction functions.	108
Table 8.	Directional reflectances inferred from TIROS-N 0.55 - 0.90 μm reflectances measured over the monsoon region assuming isotropy (Column 1), the same quantity corrected with the angular reflectance models (Column 2), and the differ- ences [isotropically inferred minus corrected], (Column 2).	116
Table AI-1.	Optical and electrical characteristics of the SGD-100A photodiode.	AI-2

LIST OF TABLES (Continued)

	<u>PAGE</u>
Table AII-1. Angular positions and fields of view of the upward looking bugeye detectors.	AII-2
Table AIV-1. Modified spherical harmonic functions which form the basis of the $\hat{\chi}^{-1}$ approximations.	AIV-2

LIST OF FIGURES

	<u>PAGE</u>
Figure 1. The multidetector bugeye instrument.	10
Figure 2. The spectral response of the silicon photodiodes used in the bugeye instrument.	13
Figure 3. The mounting position of the bugeye instrument on NASA's Convair 990 in relation to the Eppley radiometers.	15
Figure 4a. Two photographs typical of the ice fields of Hudson's Bay.	17
Figure 4b. Two photographs typical of the Saudi Arabian Desert scene.	18
Figure 4c. Two photographs typical of the 'clear' ocean atmospheric scene.	19
Figure 4d. Two photographs typical of the Indian subcontinent scene.	21
Figure 4e. Two photographs typical of the Himalaya scene.	22
Figure 4f. Two photographs typical of the middle and low cloud atmospheric scene.	23
Figure 4g. Two photographs typical of the altostratus cloud scene.	25
Figure 5. Depiction of the geometry of the measurement.	28
Figure 6. A comparison of the flux density reflected from broken clouds over ocean as measured by the Eppley 0.3 - 3.0 μm radiometer to the integral of the radiance field derived from the bugeye measurements.	31 33
Figure 7. Relative spectral distributions of the satellite measured radiances reflected from various underlying surfaces.	
Figure 8. A comparison of a single scattering approximation for Rayleigh scattering to the corresponding multiple scattering calculation, for solar zenith angles of 37 and 66°.	38
Figure 9a. The spherical harmonic approximation to the angular reflectance (χ^{-1}) model for the 0-10° solar zenith angle desert case.	41

LIST OF FIGURES (Continued)

	<u>PAGE</u>
Figure 9b. The spherical harmonic approximation to the angular reflectance (χ^{-1}) model for the 30-40° solar zenith angle desert case.	41
Figure 9c. The spherical harmonic approximation to the angular reflectance (χ^{-1}) model for the 70-80° solar zenith angle desert case.	42
Figure 10. The spherical harmonic approximation to the angular reflectance (χ^{-1}) model for the 20-30° solar zenith angle Himalayas case.	44
Figure 11a. The spherical harmonic approximation to the angular reflectance (χ^{-1}) model for the 0-10° solar zenith angle Indian subcontinent case.	45
Figure 11b. The spherical harmonic approximation to the angular reflectance (χ^{-1}) model for the 30-40° solar zenith angle Indian subcontinent case.	45
Figure 12a. The spherical harmonic approximation to the angular reflectance (χ^{-1}) model for the 0-10° solar zenith angle clear ocean case.	47
Figure 12b. The spherical harmonic approximation to the angular reflectance (χ^{-1}) model for the 50-60° solar zenith angle clear ocean case.	47
Figure 13a. The spherical harmonic approximation to the angular reflectance (χ^{-1}) model for the 10-20° solar zenith angle middle and low level cloud case.	48
Figure 13b. The spherical harmonic approximation to the angular reflectance (χ^{-1}) model for the 50-60° solar zenith angle middle and low level cloud case.	48
Figure 14a. The spherical harmonic approximation to the angular reflectance (χ^{-1}) model for the 20-30° solar zenith angle altostratus cloud case.	50
Figure 14b. The spherical harmonic approximation to the angular reflectance (χ^{-1}) model for the 40-50° solar zenith angle altostratus cloud case.	50

LIST OF FIGURES (Continued)

	<u>PAGE</u>
Figure 15. A comparison of normalized reflected radiances derived from bugeye measurements over the clear Arabian Sea to the same quantity derived from TIROS measurements over the clear Pacific Ocean.	53
Figure 16a. A comparison between the angular reflectance (χ^{-1}) model for the 40-50° solar zenith angle altostratus cloud case and a cloud model derived from the data of Ruff et al.	54
Figure 16b. A comparison between the angular reflectance (χ^{-1}) model for the 40-50° solar zenith angle middle and low level cloud case and a cloud model derived from the data of Ruff et al.	54
Figure 17a. A comparison between the angular reflectance (χ^{-1}) model for the 40-50° solar zenith angle altostratus cloud case and an altostratus cloud model from measurements by Salomonson.	56
Figure 17b. A comparison between the angular reflectance (χ^{-1}) model for the 40-50° solar zenith angle middle and low level cloud case and an altostratus cloud model from measurements by Salomonson.	56
Figure 18. A comparison between the angular reflectance (χ^{-1}) 70-80° solar zenith angle model for desert and a desert model derived from measurements by Salomonson.	58
Figure 19. A comparison between normalized radiances reflected from altostratus cloud derived from bugeye measurements and the same quantity from measurements by Griggs et al.	60
Figure 20. A comparison between the angular reflectance (χ^{-1}) 40-50° solar zenith angle clear ocean case and an ocean model derived from measurements by Brennan and Bandeen.	61
Figure 21a. A comparison between normalized radiances reflected from the clear Arabian Sea measured by the bugeye for a 0-10° solar zenith angle range and a calculation of the same quantity by Plass and Kattawar.	63

LIST OF FIGURES (Continued)

	<u>PAGE</u>
Figure 21b. A comparison between normalized radiances reflected from the clear Arabian Sea measured by the bugeye for a 50-60° solar zenith angle range and a calculation of the same quantity by Plass and Kattawar.	64
Figure 22. A comparison between the spectral bandpass of the photodiode used in the bugeye with the spectral bandpasses of the TIROS-N and GOES-1 visible channels.	67
Figure 23. The fraction of the total data sample required for convergence to within 5% of the mean displayed as a function of observation nadir and relative azimuth for the 0-10° solar zenith angle desert case.	76
Figure 24. The fraction of the total data sample required for convergence to within 5% of the mean displayed as a function of observation nadir and relative azimuth for the 10-20° solar zenith angle Himalaya case.	76
Figure 25. The fraction of the total data sample required for convergence to within 5% of the mean displayed as a function of observation nadir and relative azimuth for the 40-50° solar zenith angle clear ocean case.	77
Figure 26. The fraction of the total data sample required for convergence to within 5% of the mean displayed as a function of observation nadir and relative azimuth for the 20-30° solar zenith angle Indian subcontinent case.	77
Figure 27. The fraction of the total data sample required for convergence to within 5% of the mean displayed as a function of observation nadir and relative azimuth for the 30-40° solar zenith angle middle and low level cloud case.	78
Figure 28. The fraction of the total data sample required for convergence to within 5% of the mean displayed as a function of observation nadir and relative azimuth for the 30-40° solar zenith angle altostratus cloud case.	78

LIST OF FIGURES (Continued)

	<u>PAGE</u>
Figure 29. The fraction of the total data sample required for convergence to within 5% of the mean displayed as a function of observation nadir and relative azimuth for the 50-60° solar zenith angle ice field case.	79
Figure 30. The nadir and azimuthal dependence of the r.m.s. deviations between average measured 0.3 - 3.0 μm reflected flux density and the inference of the same quantity made from 1, 2 or 3 instantaneous radiance measurements over the desert expressed as a percent of the average reflected flux density.	83
Figure 31. The nadir and azimuthal dependence of the r.m.s. deviations between average measured 0.3 - 3.0 μm reflected flux density and the inference of the same quantity made from 1, 2 or 3 instantaneous radiance measurements over the Himalayas expressed as a percent of the average reflected flux density.	85
Figure 32. The nadir and azimuthal dependence of the r.m.s. deviations between average measured 0.3 - 3.0 μm reflected flux density and the inference of the same quantity made from 1, 2 or 3 instantaneous radiance measurements over the clear ocean expressed as a percent of the average reflected flux density.	87
Figure 33. The nadir and azimuthal dependence of the r.m.s. deviations between average measured 0.3 - 3.0 μm reflected flux density and the inference of the same quantity made from 1, 2 or 3 instantaneous radiance measurements over the Indian subcontinent expressed as a percent of the average reflected flux density.	89
Figure 34. The nadir and azimuthal dependence of the r.m.s. deviations between average measured 0.3 - 3.0 μm reflected flux density and the inference of the same quantity made from 1, 2 or 3 instantaneous radiance measurements over middle and low level clouds expressed as a percent of the average reflected flux density.	91

LIST OF FIGURES (Continued)

	<u>PAGE</u>
Figure 35. The nadir and azimuthal dependence of the r.m.s. deviations between average measured 0.3 - 3.0 μm reflected flux density and the inference of the same quantity made from 1, 2 or 3 instantaneous radiance measurements over altostratus clouds expressed as a percent of the average reflected flux density.	93
Figure 36. The nadir and azimuthal dependence of the r.m.s. deviations between average measured 0.3 - 3.0 μm reflected flux density and the inference of the same quantity made from 1, 2 or 3 instantaneous radiance measurements over ice expressed as a percent of the average reflected flux density.	95
Figure 37. A depiction of the separation of the 'monsoon region' (between 45 and 85° east longitude and 0 and 35° north latitude) into various surface or target types for the application of the angular reflectance (χ^{-1}) models.	106
Figure 38. Values of reflected flux density ($\text{watts}\cdot\text{m}^{-2}$) associated with TIROS-N 0.55 - 0.90 μm reflectance measurements on 30 May 1979 using the isotropic assumption over the region between 30 - 100° east longitude and 0 - 35° north latitude.	109
Figure 39. Values of reflected flux density ($\text{watts}\cdot\text{m}^{-2}$) associated with TIROS-N 0.55 - 0.90 μm reflectance measurements on 30 May 1979 resulting from application of the angular reflectance (χ^{-1}) models over the 'monsoon region'.	110
Figure 40. Values of the differences between isotropically inferred reflected flux density ($\text{watts}\cdot\text{m}^{-2}$) and the same quantity derived from application of the angular reflectance (χ^{-1}) models to TIROS-N 0.55 - 0.90 μm reflectances on 30 May 1979 over the 'monsoon region'.	111
Figure 41. Values of the reflected flux density ($\text{watts}\cdot\text{m}^{-2}$) associated with TIROS-N 0.725 - 1.10 μm reflectance measurements on 30 May 1979 using the isotropic assumption over the region between 30 - 100° east longitude and 0 - 35° north latitude.	112

LIST OF FIGURES (Continued)

		<u>PAGE</u>
Figure 42.	Values of the reflected flux density ($\text{watts}\cdot\text{m}^{-2}$) associated with TIROS-N 0.725 - 1.10 μm reflectance measurements on 30 May 1979 resulting from application of the angular reflectance (χ^{-1}) models over the 'monsoon region'.	113
Figure 43.	Values of the differences between isotropically inferred reflected flux density ($\text{watts}\cdot\text{m}^{-2}$) and the same quantity derived from application of the angular reflectance (χ^{-1}) models to TIROS-N 0.725 - 1.10 μm reflectances on 30 May 1979 over the 'monsoon region'.	114
Figure AIII-1.	Interpolated χ^{-1} pattern (left) and associated flight track (right) for the 0-10° solar zenith angle desert case.	AIII-2
Figure AIII-2.	Interpolated χ^{-1} pattern (left) and associated flight track (right) for the 10-20° solar zenith angle desert case.	AIII-3
Figure AIII-3.	Interpolated χ^{-1} pattern (left) and associated flight track (right) for the 20-30° solar zenith angle desert case.	AIII-4
Figure AIII-4.	Interpolated χ^{-1} pattern (left) and associated flight track (right) for the 30-40° solar zenith angle desert case.	AIII-5
Figure AIII-5.	Interpolated χ^{-1} pattern (left) and associated flight track (right) for the 40-50° solar zenith angle desert case.	AIII-6
Figure AIII-6.	Interpolated χ^{-1} pattern (left) and associated flight track (right) for the 50-60° solar zenith angle desert case.	AIII-7
Figure AIII-7.	Interpolated χ^{-1} pattern (left) and associated flight track (right) for the 60-70° solar zenith angle desert case.	AIII-8
Figure AIII-8.	Interpolated χ^{-1} pattern (left) and associated flight track (right) for the 70-80° solar zenith angle desert case.	AIII-9
Figure AIII-9.	Interpolated χ^{-1} pattern (left) and associated flight track (right) for the 10-20° solar zenith angle Himalaya case.	AIII-10

LIST OF FIGURES (Continued)

	<u>PAGE</u>
Figure AIII-10. Interpolated χ^{-1} pattern (left) and associated flight track (right) for the 20-30° solar zenith angle Himalaya case.	AIII-11
Figure AIII-11. Interpolated χ^{-1} pattern (left) and associated flight track (right) for the 0-10° solar zenith angle ocean case.	AIII-12
Figure AIII-12. Interpolated χ^{-1} pattern (left) and associated flight track (right) for the 10-20° solar zenith angle ocean case.	AIII-13
Figure AIII-13. Interpolated χ^{-1} pattern (left) and associated flight track (right) for the 20-30° solar zenith angle ocean case.	AIII-14
Figure AIII-14. Interpolated χ^{-1} pattern (left) and associated flight track (right) for the 30-40° solar zenith angle ocean case.	AIII-15
Figure AIII-15. Interpolated χ^{-1} pattern (left) and associated flight track (right) for the 40-50° solar zenith angle ocean case.	AIII-16
Figure AIII-16. Interpolated χ^{-1} pattern (left) and associated flight track (right) for the 50-60° solar zenith angle ocean case.	AIII-17
Figure AIII-17. Interpolated χ^{-1} pattern (left) and associated flight track (right) for the 0-10° solar zenith angle Indian subcontinent case.	AIII-18
Figure AIII-18. Interpolated χ^{-1} pattern (left) and associated flight track (right) for the 10-20° solar zenith angle Indian subcontinent case.	AIII-19
Figure AIII-19. Interpolated χ^{-1} pattern (left) and associated flight track (right) for the 20-30° solar zenith angle Indian subcontinent case.	AIII-20
Figure AIII-20. Interpolated χ^{-1} pattern (left) and associated flight track (right) for the 30-40° solar zenith angle Indian subcontinent case.	AIII-21
Figure AIII-21. Interpolated χ^{-1} pattern (left) and associated flight track (right) for the 0-10° solar zenith angle middle and low level cloud case.	AIII-22

LIST OF FIGURES (Continued)

	<u>PAGE</u>
Figure AIII-22. Interpolated χ^{-1} pattern (left) and associated flight track (right) for the 10-20° solar zenith angle middle and low level cloud case.	AIII-23
Figure AIII-23. Interpolated χ^{-1} pattern (left) and associated flight track (right) for the 20-30° solar zenith angle middle and low level cloud case.	AIII-24
Figure AIII-24. Interpolated χ^{-1} pattern (left) and associated flight track (right) for the 30-40° solar zenith angle middle and low level cloud case.	AIII-25
Figure AIII-25. Interpolated χ^{-1} pattern (left) and associated flight track (right) for the 40-50° solar zenith angle middle and low level cloud case.	AIII-26
Figure AIII-26. Interpolated χ^{-1} pattern (left) and associated flight track (right) for the 20-30° solar zenith angle altostratus cloud case.	AIII-27
Figure AIII-27. Interpolated χ^{-1} pattern (left) and associated flight track (right) for the 30-40° solar zenith angle altostratus cloud case.	AIII-28
Figure AIII-28. Interpolated χ^{-1} pattern (left) and associated flight track (right) for the 40-50° solar zenith angle altostratus cloud case.	AIII-29
Figure AIII-29. Interpolated χ^{-1} pattern (left) and associated flight track (right) for the 40-50° solar zenith angle ice case.	AIII-30
Figure AIII-30. Interpolated χ^{-1} pattern (left) and associated flight track (right) for the 50-60° solar zenith angle ice case.	AIII-31
Figure AIV-1. Regression coefficients of the spherical harmonic approximation to the desert CHI**-1 pattern for solar zenith angles from 0 to 10 degrees and the corresponding plot of the pattern.	AIV-4
Figure AIV-2. Regression coefficients of the spherical harmonic approximation to the desert CHI**-1 pattern for solar zenith angles from 10 to 20 degrees and the corresponding plot of the pattern.	AIV-5

LIST OF FIGURES (Continued)

	<u>PAGE</u>
Figure AIV-3. Regression coefficients of the spherical harmonic approximation to the desert CHI** ⁻¹ pattern for solar zenith angles from 20 to 30 degrees and the corresponding plot of the pattern.	AIV-6
Figure AIV-4. Regression coefficients of the spherical harmonic approximation to the desert CHI** ⁻¹ pattern for solar zenith angles from 30 to 40 degrees and the corresponding plot of the pattern.	AIV-7
Figure AIV-5. Regression coefficients of the spherical harmonic approximation to the desert CHI** ⁻¹ pattern for solar zenith angles from 40 to 50 degrees and the corresponding plot fo the pattern.	AIV-8
Figure AIV-6. Regression coefficients of the spherical harmonic approximation to the desert CHI** ⁻¹ pattern for solar zenith angles from 50 to 60 degrees and the corresponding plot of the pattern.	AIV-9
Figure AIV-7. Regression coefficients of the spherical harmonic approximation to the desert CHI** ⁻¹ pattern for solar zenith angles from 60 to 70 degrees and the corresponding plot of the pattern.	AIV-10
Figure AIV-8. Regression coefficients of the spherical harmonic approximation to the desert CHI** ⁻¹ pattern for solar zenith angles from 70 to 80 degrees and the corresponding plot of the pattern.	AIV-11
Figure AIV-9. Regression coefficients of the spherical harmonic approximation to the Himalaya CHI** ⁻¹ pattern for solar zenith angles from 10 to 20 degrees and the corresponding plot of the pattern.	AIV-12
Figure AIV-10. Regression coefficients of the spherical harmonic approximation to the Himalaya CHI** ⁻¹ pattern for solar zenith angles from 20 to 30 degrees and the corresponding plot of the pattern.	AIV-13

LIST OF FIGURES (Continued)

	<u>PAGE</u>
Figure AIV-11. Regression coefficients of the spherical harmonic approximation to the ocean CHI** ⁻¹ pattern for solar zenith angles from 0 to 10 degrees and the corresponding plot of the pattern.	AIV-14
Figure AIV-12. Regression coefficients of the spherical harmonic approximation to the ocean CHI** ⁻¹ pattern for solar zenith angles from 10 to 20 degrees and the corresponding plot of the pattern.	AIV-15
Figure AIV-13. Regression coefficients of the spherical harmonic approximation to the ocean CHI** ⁻¹ pattern for solar zenith angles from 20 to 30 degrees and the corresponding plot of the pattern.	AIV-16
Figure AIV-14. Regression coefficients of the spherical harmonic approximation to the ocean CHI** ⁻¹ pattern for solar zenith angles from 30 to 40 degrees and the corresponding plot of the pattern.	AIV-17
Figure AIV-15. Regression coefficients of the spherical harmonic approximation to the ocean CHI** ⁻¹ pattern for solar zenith angles from 40 to 50 degrees and the corresponding plot of the pattern.	AIV-18
Figure AIV-16. Regression coefficients of the spherical harmonic approximation to the ocean CHI** ⁻¹ pattern for solar zenith angles from 50 to 60 degrees and the corresponding plot of the pattern.	AIV-19
Figure AIV-17. Regression coefficients of the spherical harmonic approximation to the Indian CHI** ⁻¹ pattern for solar zenith angles from 0 to 10 degrees and the corresponding plot of the pattern.	AIV-20
Figure AIV-18. Regression coefficients of the spherical harmonic approximation to the Indian CHI** ⁻¹ pattern for solar zenith angles from 10 to 20 degrees and the corresponding plot of the pattern.	AIV-21

LIST OF FIGURES (Continued)

	<u>PAGE</u>
Figure AIV-19. Regression coefficients of the spherical harmonic approximation to the Indian CHI**-1 pattern for solar zenith angles from 20 to 30 degrees and the corresponding plot of the pattern.	AIV-22
Figure AIV-20. Regression coefficients of the spherical harmonic approximation to the Indian CHI**-1 pattern for solar zenith angles from 30 to 40 degrees and the corresponding plot of the pattern.	AIV-23
Figure AIV-21. Regression coefficients of the spherical harmonic approximation to the Cloud 1 CHI**-1 pattern for solar zenith angles from 0 to 10 degrees and the corresponding plot of the pattern.	AIV-24
Figure AIV-22. Regression coefficients of the spherical harmonic approximation to the Cloud 1 CHI**-1 pattern for solar zenith angles from 10 to 20 degrees and the corresponding plot of the pattern.	AIV-25
Figure AIV-23. Regression coefficients of the spherical harmonic approximation to the Cloud 1 CHI**-1 pattern for solar zenith angles from 20 to 30 degrees and the corresponding plot of the pattern.	AIV-26
Figure AIV-24. Regression coefficients of the spherical harmonic approximation to the Cloud 1 CHI**-1 pattern for solar zenith angles from 30 to 40 degrees and the corresponding plot of the pattern.	AIV-27
Figure AIV-25. Regression coefficients of the spherical harmonic approximation to the Cloud 1 CHI**-1 pattern for solar zenith angles from 40 to 50 degrees and the corresponding plot of the pattern.	AIV-28
Figure AIV-26. Regression coefficients of the spherical harmonic approximation to the Cloud 2 CHI**-1 pattern for solar zenith angles from 20 to 30 degrees and the corresponding plot of the pattern.	AIV-29

LIST OF FIGURES (Continued)

	<u>PAGE</u>
Figure AIV-27. Regression coefficients of the spherical harmonic approximation to the Cloud 2 CHI**-1 pattern for solar zenith angles from 30 to 40 degrees and the corresponding plot of the pattern.	AIV-30
Figure AIV-28. Regression coefficients of the spherical harmonic approximation to the Cloud 2 CHI**-1 pattern for solar zenith angles from 40 to 50 degrees and the corresponding plot of the pattern.	AIV-31
Figure AIV-29. Regression coefficients of the spherical harmonic approximation to the ice CHI**-1 pattern for solar zenith angles from 40 to 50 degrees and the corresponding plot of the pattern.	AIV-32
Figure AIV-30. Regression coefficients of the spherical harmonic approximation to the ice CHI**-1 pattern for solar zenith angles from 50 to 60 degrees and the corresponding plot of the pattern.	AIV-33

LIST OF SYMBOLS

$A(\theta, \phi)$	Angular variation of the reflected radiance field
C	Sensitivity of the silicon photodiode
$C(I)$	i th coefficient in the spherical harmonic expansion of the angular reflectance pattern
X	Bi-directional reflectance normalization coefficient.
$\delta(\theta_i, \theta_j, \theta_k)$	r.m.s. deviation between the average of the measured reflected flux density and that inferred by a measurement of the radiances reflected at angles θ_1 , θ_2 and θ_3
E	Upwelling filtered reflected flux density
\hat{E}	Inferred reflected flux density
\bar{E}	Measured, scene averaged reflected flux density
$E_o(\lambda)$	Spectral solar constant
E_S	Upwelling solar reflected flux density
E_v'	Upwelling 'voltage irradiance'
$F(\lambda)$ or $f(\lambda)$	Filter function
k_i	Relative response of the i th diode amplifier combination.
κ	Proportionality constant between the Eppley measured and bugeye deduced reflected flux densities
λ	Wavelength
$N(\theta, \phi, \lambda)$	Spectral radiance
\hat{N}	Spectral radiance averaged over the detectors field of view
Ω_i	Solid angle of the field of view of the i th detector
ϕ	Relative azimuth angle
ϕ_S	Solar azimuth angle
R	Reflectance
τ	Optical depth for Rayleigh scattering

LIST OF SYMBOLS (Continued)

ϵ	Observation nadir angle
V_i	Voltage output of the i th detector
v'	Voltage output adjusted for relative sensitivity
$W(\lambda)$	Spectral variation of the radiance field
$Y_n^m(\theta, \phi)$	Spherical harmonic basis function
z	Solar zenith angle

1.0 INTRODUCTION

The feasibility of monitoring the earth's radiation budget was greatly enhanced with the advent of the earth orbiting satellite platform. Because of its altitude, high above the radiatively active atmosphere, a satellite-borne radiometer is ideally located for measurements of the earth's longwave emitted flux as well as the shortwave reflected flux. From the first proposal for taking such measurements, (Suomi, 1958) a steadily increasing effort has been put forth to adequately monitor the exchange of radiative energy at the outer limits of our atmosphere.

Initial efforts addressed the problem of the determination of the long term, planetary scale, bulk radiative properties such as equator to pole gradients of longwave radiation loss and shortwave radiation gain. The difference between these quantities is the gradient of the net radiation which is the ultimate energy source for the oceanic and atmospheric circulation systems. The earliest studies were based on data collected by wide field of view radiometers (flat plate or hemispheric) which measured the total upwelling radiant exitance at the point of the satellite sensor. Weinstein and Suomi (1961) used measurements of terrestrial radiation at night from Explorer VII and showed that a definite relationship exists between the radiation centers and low and high pressure centers. Bandeen et al. (1964) analyzed data from TIROS II, III, IV and VII and inferred a slightly larger longwave radiative loss and a significantly smaller albedo than previously calculated; for example, London (1957). In addition to the types of instruments borne by Explorer VII, the TIROS series included a medium

resolution scanning radiometer with a 5° field of view and the capability of measuring absolute intensities in five spectral intervals. Rasool and Prabhakara (1966) also reported on the data collected by the TIROS meteorological satellites during 1962 and 1963. They calculated albedo values over the deserts of North Africa and Arabia between 40 and 45 percent, contradicting earlier results which had estimated these albedos to be between 20 and 25 percent. The higher values were large enough to imply a net radiative deficit for these regions as compared to the earlier results (20-25%) which indicated a positive radiation balance. House (1965) examined data collected by the hemispherical sensor aboard TIROS IV and found that the measurements of the planetary albedo confirmed earlier estimates, however, the equator to pole gradient of albedo was found to be somewhat larger than previously thought. Winston and Taylor (1967), and Winston (1967) compiled global maps of longwave radiation and albedo from TIROS IV and TIROS VII measurements. Their results indicated an inverse correlation between albedo and longwave radiation on a broad scale and that both quantities were generally related to the strength and location of features of the westerlies over the Northern Hemisphere.

All of the efforts reported above utilized data collected with hemispheric sensors for the analysis of the reflected shortwave component, or, when medium scanning radiometer data were used, assumed that the reflecting surface was isotropic. Arking (1965), pointed out that the measured reflected intensity depended on the solar zenith angle, the satellite viewing angle and the relative azimuth between the sun and the satellite. Arking and Levine (1964) used correction

factors, averaged over the 'quasi-globe',¹ in an analysis of TIROS VII data and arrived at a value of albedo of 20.6% averaged over an annual period and the 'quasi-globe'.

Raschke and Pasternak (1967) included correction factors for non-Lambertian surfaces which were derived from 'many measurements of the angular dependence of reflected solar radiation' in an analysis of the radiation data from Nimbus 2. For the approximately 2.5 month period included in the study, the value of planetary albedo was significantly smaller than the annual global values previously calculated, (28.1 - 30.6% compared to 35%), but apparently larger than earlier satellite measurements (Vonder Haar, 1968), which yielded a reflected component too small ($\sim 25\%$) to be in balance with the corresponding incoming solar and emitted longwave fluxes. The intermediate value of albedo apparently resulted from the application of the anisotropic reflectance models. Raschke and Bandeen (1970) extended the analysis of Nimbus 2 data to include a total of five successive semimonthly periods and arrived at a value of the planetary albedo of 29-31%.

Vonder Haar and Suomi (1971) summarized the series of radiation budget studies resulting from measurements by the first and second generation United States Meteorological satellites. For the 39 months of available data, 80% of which was acquired from sensors of low spatial resolution, a value of 30% was deduced for the mean planetary albedo. It was also determined that the earth was in radiative balance to within the accuracy of the measurements. Raschke et al. (1973)

¹The 'quasi-globe' is a region encompassing 85% of the earth's surface. Excluded are the polar regions beyond 60° latitude and small areas of southern South America and Siberia.

reported on the earth's radiation budget monitored from Nimbus 3. This study provided for the first time estimates of the 'annual' (10 month) budget with a high spatial resolution ($10^2 - 10^3$ km) over the entire globe. The improvement of the spatial resolution was accomplished by using nine empirically derived models of the angular variation of the upwelling radiance fields, which were derived from airplane, balloon and satellite measurements of reflected solar radiation. Smith et al. (1977), described the Nimbus 6 earth radiation budget experiment, which has, as one of its primary objectives, the collection of an adequate data base to be used for modelling the angular variation of reflected radiance fields. The instrument package includes a four channel scanning radiometer which is capable of sampling the angular radiance field once as the satellite travels 700 km along the subpoint track. Preliminary results show the relatively isotropic nature of the radiance field measured over the Sahara compared to the anisotropic nature of field measured over the ice surface of Greenland. Gruber and Winston (1978) provide a brief description of an earth radiation budget data set collected from NOAA operational satellites. These data were compiled assuming isotropy of the reflected radiation field. Jacobowitz et al. (1979) discuss the planetary radiation budget measured by the low spatial resolution sensors on Nimbus 6, from July 1975 to December 1976. The importance of high resolution features in the radiation budget shown by the scanning radiometer data from Nimbus 6 are yet to be published.

As time has passed there has been a tendency toward increased spatial resolution in the measurements of the earth's radiation budget components. In order to obtain higher spatial resolution from a

limited number of satellite platforms, scanning radiometers with narrow fields of view are required. Since radiation reflected from natural surfaces is in general anisotropic, adequate angular models of the reflected component are necessary to interpret such measurements. As these models were developed they were incorporated into most of the more recent radiation budget studies. Summarized below are the major efforts in developing such angular reflectance models.

As noted previously Arking (1965) developed angular patterns of upwelling radiance averaged over the quasi-globe. The patterns were compiled from TIROS IV observations over a large time and space scale. Ruff et al. (1968) used data from the 0.55 - 0.75 μm TIROS IV channel to develop angular reflection patterns for clouds. The data were collected over three approximately 30 day periods during the spring of 1962. The measurements were limited to clouds by selecting only those targets which had an effective black body equivalent temperature less than 252°K as monitored by the 8 - 12 μm TIROS IV channel. Their results clearly indicate the anisotropic nature of the radiation field. Salomonson and Marlatt (1968) used data collected by the Nimbus 3 medium resolution radiometer, flown on a low altitude aircraft (\sim 3 km) to measure the angular patterns of reflected radiation over stratus clouds near the California coast and in the mountain valleys of Utah. In addition measurements were made over white sand, snow, a dry desert lake bed, a grassland sod surface, a swampy-dense vegetation surface and water. Anisotropy in the reflected solar radiation was observed in varying degrees for all the surfaces studied. Salomonson (1968) has shown that the measured stratus cloud patterns compare well to published results derived from Monte Carlo simulations by Kattawar and

Platt (1968a,b). Griggs and Marggraf (1967) used a photometric polarimeter to measure the reflectance characteristics of stratus clouds, of snow surfaces and of the ocean in the 0.4 to 0.96 μm portion of the spectrum. The instrument was capable of completing a full scan (42 different angular measurements) in about four minutes. The instrument was mounted on a DC-3 aircraft and flown at a height of about 1000 feet above the various targets. The basic anisotropic nature of the various reflected fields is obvious in their results. Bartman (1968) measured the angular pattern of reflected radiation in the 0.55 - 0.75 μm and the 0.20 - 5.0 μm spectral regions with TIROS and Nimbus type radiometers carried aloft on a balloon gondola at an altitude of 32 to 34 km. Angular reflectance patterns were presented for stratocumulus clouds, cirrus above stratocumulus clouds, broken cumulus and cirrus above scattered cumulus. A high degree of anisotropy was found in all cases. Brennan and Bandeen (1970) presented patterns of reflected solar radiation from cloud, water and land surfaces with an aircraft borne medium resolution radiometer. Reflectances in the 0.2 - 4.0 μm and 0.55 - 0.85 μm portions of the spectrum were measured from an altitude of about 12 km. Angular patterns were measured for stratocumulus clouds, forest, ocean and farmland. As previously mentioned, one of the major objectives of the Nimbus series earth radiation budget program is to compile a data base which could be used to produce adequate angular reflectance models. This effort continues, and some preliminary results are found in Stowe et al. (1980). These measurements ultimately will be paired with a description of the state of the underlying atmosphere and the nature of the surface. Stowe et al. reported angular patterns for high ice clouds for which it was found that

errors of up to 800% may be made if the isotropic assumption is applied.

The research which will be presented here is similar in many respects to the studies of the angular characteristics of reflected solar radiation cited above. Our goal is to assess the applicability of angular patterns of reflected radiation on a regional scale. There are, however, significant and important differences between the present effort and previous studies. First, the data presented here have been collected with a new type of instrument, which allows instantaneous angular sampling of the upwelling radiation field, whereas all previous efforts have utilized scanning radiometers which require an extended time and space scale to complete a sampling process. The instrument will be described in the next section. Secondly, previous studies have analyzed reflection patterns over extremely large geographical areas such as the 'quasi-globe', or, for quite specific targets such as a stratocumulus cloud deck, a forest, a swamp etc., which required data collection over a very small geographical area. This study focuses on radiance patterns which may be applicable over space scales of from 250 km to 1000 km which is the scale of interest for regional climate modeling. Because of the ability to sample the radiance field on an almost instantaneous basis it was possible to examine the spatial convergence properties of the various angular patterns. None of the previous efforts have specified a spatial scale over which their results may be valid. Thirdly, results are presented in the literature for discrete values of, or limited ranges of solar zenith angle. Measurements over a variety of zenith angle ranges by a single instrument are lacking. These data are indispensable for the determination of an

adequate stratification of reflectance models with respect to zenith angle, or for attempting to specify a model which might be used over the total daytime period to interpret geostationary satellite readings. Finally, although this document is far from an exhaustive study, it is believed to be the most comprehensive study in terms of surface type and solar zenith angle range to date.

With these goals in mind the next section will describe the method of data collection, including a detailed description of the measuring instrument. This will be followed by a section describing the method of data reduction and a presentation of the results. Comparison with previous results follows and the final section discusses the implications of the present findings regarding the use of angular reflectance models for inferring the total reflected solar flux.

2.0 DESCRIPTION OF THE EXPERIMENT

The data used in this report were collected during the summer MONsoon EXperiment (MONEX). The measuring instrument was flown on NASA's Convair 990 aircraft at an altitude of 10-12 km. By including data taken on the ferry flights it was possible to sample a wide variety of reflecting surfaces from the ice fields of Hudson Bay to the sands of the Saudi Arabian empty quarters, for a variety of solar zenith angles. All of the data used in the present study were collected with a single instrument which is described below.

2.1 Description of the 'bugeye instrument'

The instrument used to collect the data presented in this report consists of a hemispherical array of thirteen high quality silicon photodiodes and associated electrical circuitry mounted in an aluminum housing; see Figure 1. The instrument is hereafter referred to as the bugeye instrument. The angular positions of the photodiodes are given in Table 1 and the field of view of each detector was limited to $10^\circ \pm 1^\circ$ full angle by inserting each diode in a collimator tube. The 10° field of view combined with the flight altitude of 10-12 km produces a sub-measurement spot size of 1.75 km which compares with sub-satellite resolutions of 0.9 km, 1.0 km for the visible GOES and TIROS channels. The Nimbus scanning radiometers have a field of view of $5.12^\circ \times .25^\circ$ which translates into a much coarser resolution of approximately 40×2 km. The 10° full angle field of view on each of the thirteen sensors permits instantaneous sampling of 5% of the total downward facing hemisphere. A complete tabulation of the electrical and optical properties of the silicon photodiode is given in Appendix I. For the

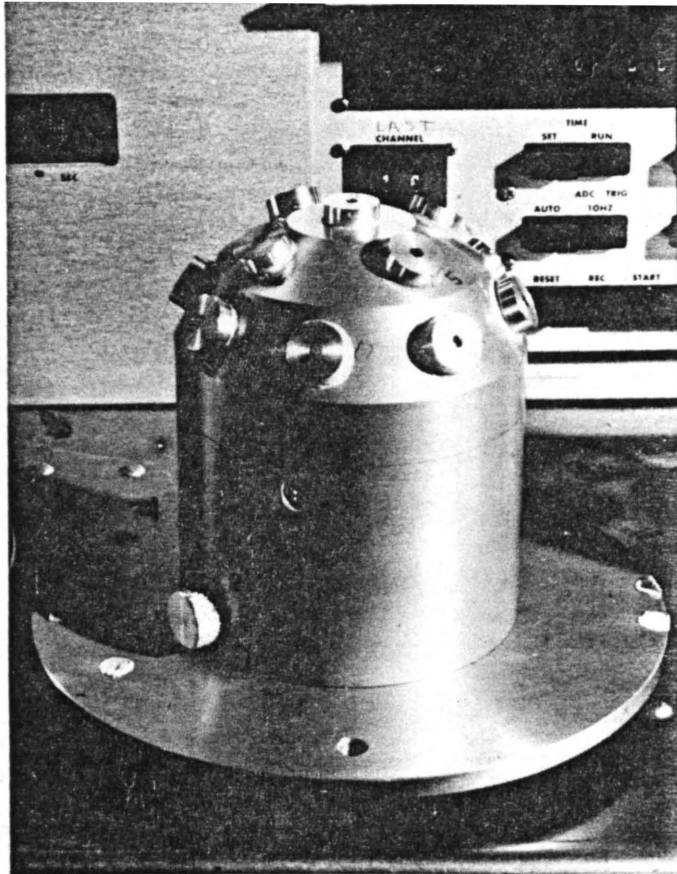


Figure 1. The multidetector bug-eye instrument.

Detector Number	Angle from Nadir	Azimuth Angle *	Field of View Steradian
1	0°	—	.0239
2	30°		"
3	30°	90°	"
4	30°	180°	"
5	30°	270°	"
6	60°	0°	"
7	60°	45°	"
8	60°	90°	"
9	60°	135°	"
10	60°	180°	"
11	60°	225°	"
12	60°	270°	"
13	60°	315°	"

*The azimuth angle is measured relative to the forward direction of the aircraft increasing toward the direction of the right wing

Table 1. The nadir and azimuthal coordinates of the bug-eye photodiodes in degrees.

purpose of the following presentation it is important to note the spectral response of the photodiode depicted in Figure 2. The diode and amplification circuit have a response time on the order of a few milliseconds, and the response of the diode is linear with incident irradiance over seven decades. In addition, the upper limit of the aircraft data system input (10 volts) was exceeded by the bugeye channels only when the aircraft entered the upper regions of thick cirrus outflow; none of these data are used in this report.

2.2 Calibration of the Instrument

The sampling advantages of a multidetector instrument are obvious. However, the advantage of a simplified flight pattern required to sample the angular pattern of reflected radiation must be weighed in relation to the disadvantage of a more complicated calibration procedure. Since the goal of the experiment is to examine the properties of reflected solar radiation, and in view of the limited spectral response of the photodiodes, no attempt was made to obtain the absolute sensitivities of the individual diodes. Rather, it is assumed that the angular properties of the total reflected solar component in the 0.3 to 3.0 μm spectral range behave in the same manner as the measured 0.4 to 1.1 μm portion of the spectrum. The extent to which this assumption may be valid is treated in the next section. Thus, it is necessary only to specify the relative sensitivities of the bugeye channels which were determined from measurements on ten occasions prior to, during and after the experiment. Prior to the experiment the individual detectors were illuminated with an incandescent lamp through a diffusing surface. The lamp was supplied with an adjustable but regulated voltage and

Spectral Response of the Bugeye Photodiode

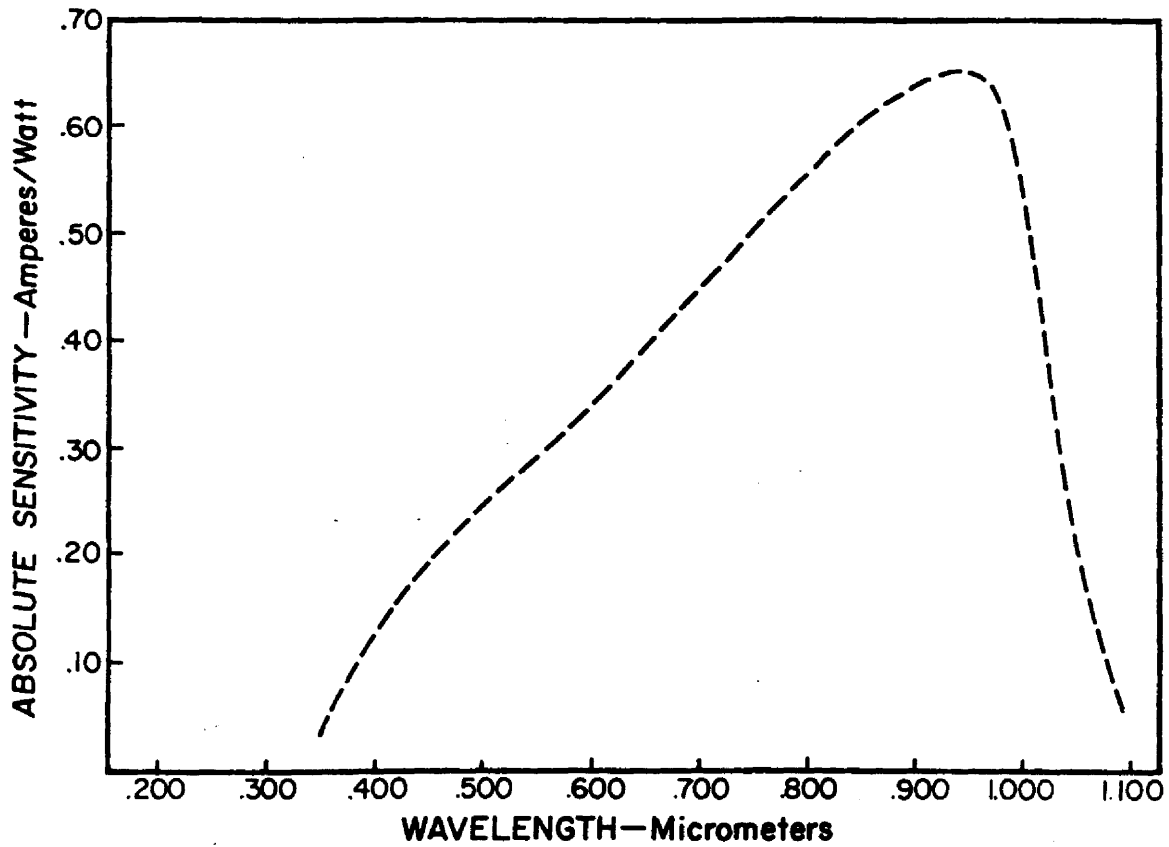


Figure 2. The spectral response of the silicon photodiodes used in the bugeye instrument.

relative sensitivities were obtained for a range of detector output voltages. During the experiment calibrations were performed using a portable unit consisting of a battery powered lamp which illuminated a small diffusing sphere. Because the supply voltage could not be held constant in this case, the output of the lamp was monitored by a separate diode of the identical type used in the bug-eye, so that as the calibrator was moved from one diode to the next any changes in light output could be accounted for. After the experiment the relative sensitivities were again measured using the portable unit. When all of the calibrations are considered the relative sensitivities displayed a standard deviation of less than 5% of their respective mean values. This figure is used as an estimate of the experimental error in the measurements used in this report.

2.3 Deployment of the Instrument

The bug-eye instrument was mounted within a cowling, on the underside, near the front of NASA's Convair 990 high altitude research aircraft. Three other instruments were mounted within the same cowling: an Eppley 0.3 - 3.0 μm pyranometer, an Eppley 0.7 - 3.0 μm pyranometer and an Eppley pyrgeometer, see Figure 3. The instruments were arranged so that none of the Eppley instruments obstructed the field of view of any of the bug-eye channels. After some initial adjustments the instrument was never removed from the aircraft until the termination of summer MONEX. All field calibrations were taken with the instrument in place.

In total, data were collected on 30 flights of the Convair 990 aircraft during April through July of 1979. However, since the data



Figure 3. The mounting position of the bugeye instrument on NASA's Convair 990 in relation to the Eppley radiometers.

are analyzed with satellite applications in mind, and because only certain flights were flown over surfaces which are easily categorized, this report focuses on data collected during 13 of the missions. The first of these took place on April 30 originating at Malmstrom Air Force Base near Great Falls, Montana and terminating at Sondre Stromfjord, Greenland. During a portion of this flight data were taken over the broken ice of Hudson Bay for solar zenith angle ranges of 40° - 50° and 50° - 60° , see Figure 4a.

The second target was the desert sands of the Empty Quarters in Saudi Arabia. Data were taken for increments of solar zenith angle of 10° between the limits of 0° and 80° . Care was taken to eliminate any measurements near or beyond the coast line which may have been contaminated with reflection from stratus cloud or water. This was accomplished by setting upper and lower bounds for the 0.3 to 3.0 μm upwelling irradiance and for the individual bugeye readings. When any of the bugeye channels failed a test criterion all of the readings taken at that instant were discarded. These flights took place on May 9, 10, 12 and 14. Figure 4b shows two photographs typical of the desert scenes.

The third target was that of a reasonably unobscured ocean surface. These data were taken before the onset of the monsoon on the 29th and 31st of May and on June 3. The ocean surface was reasonably calm (no whitecaps were seen) and convection was suppressed. Fair weather cumulus clouds were almost always present but were of small horizontal extent and estimated to be below satellite resolution, see Figure 4c. Some altocumulus clouds were observed and the minimum-maximum criterion was applied to the upwelling irradiance and bugeye readings to eliminate

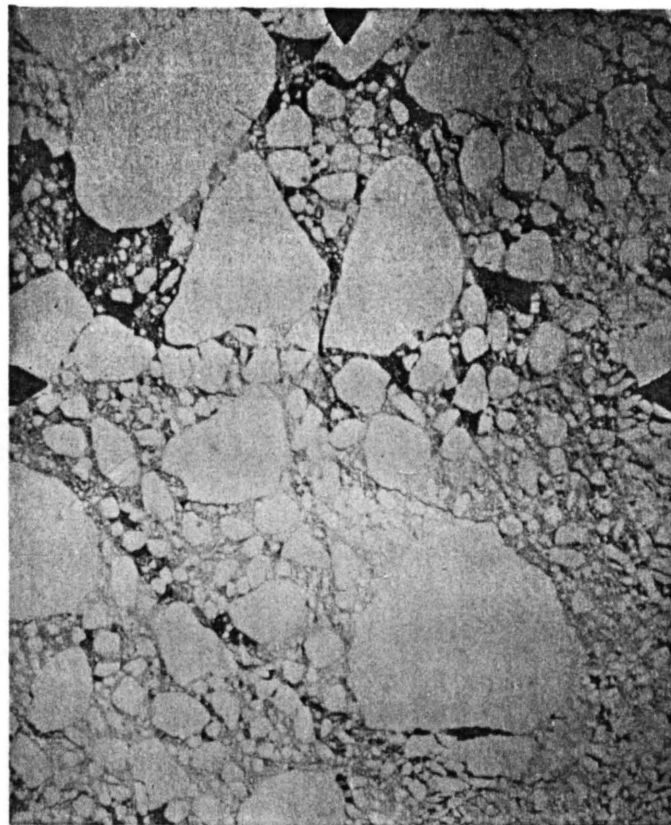
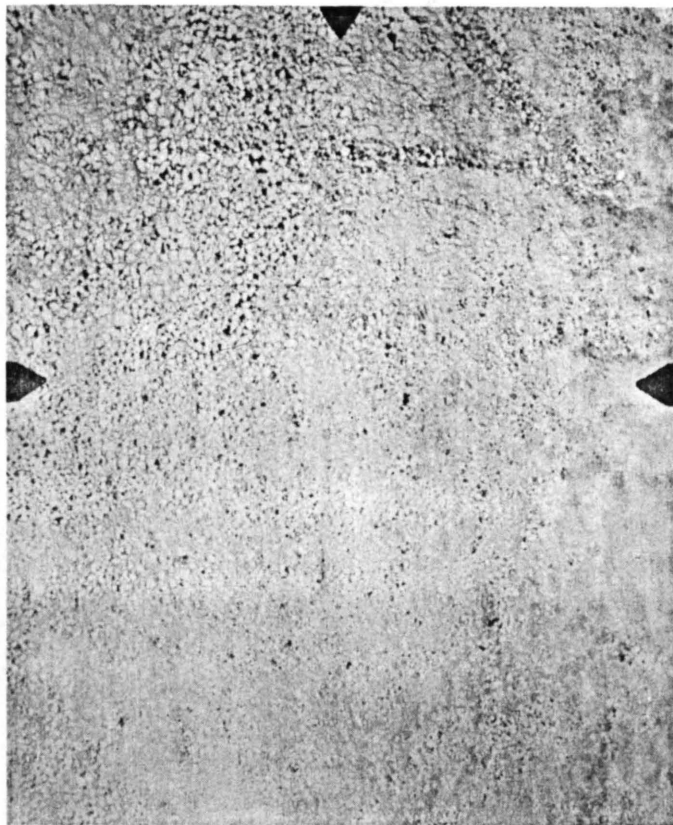


Figure 4a. Two photographs typical of the ice fields of Hudson's Bay.

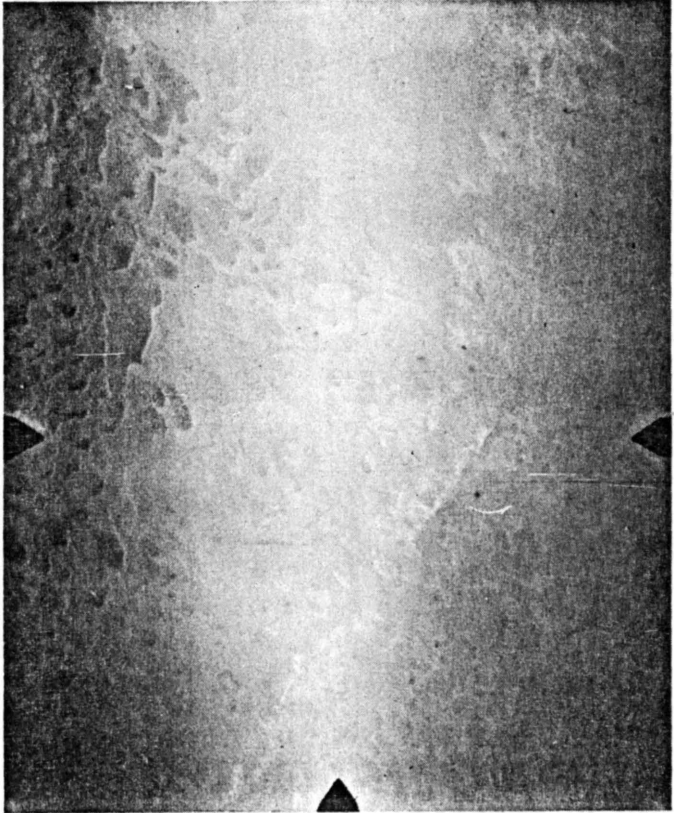


Figure 4b. Two photographs typical of the Saudi Arabian Desert scene.

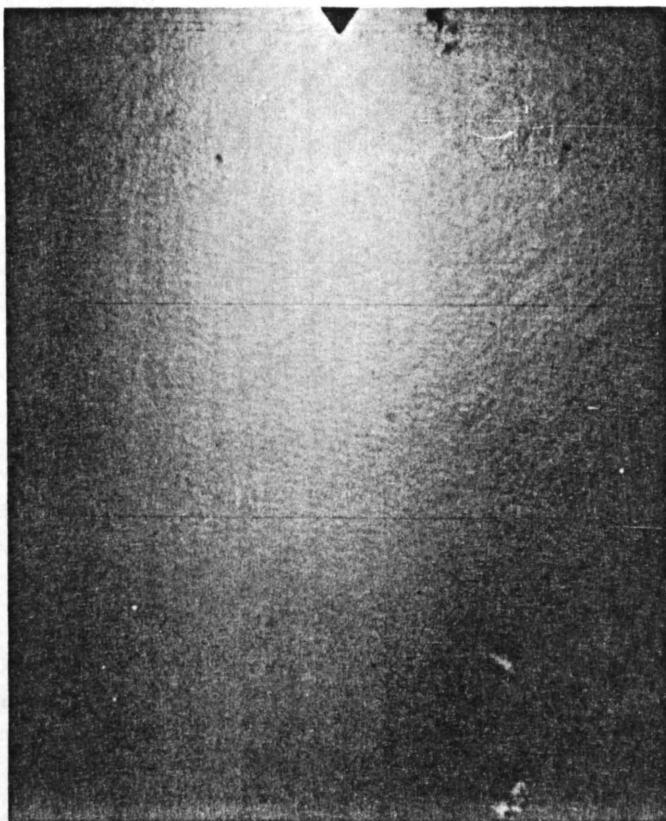


Figure 4c. Two photographs typical of the 'clear' ocean atmospheric scene.

the small fraction of the data which may have been collected in close proximity to such anomalously bright features. Data were collected for six solar zenith angle increments of 10° each from 0° to 60° .

Data collected over the Indian subcontinent comprises the fourth category. These data were collected on the flights of the 5th and 11th of June. Analysis was limited to data collected south of 30°N latitude and inland of coastal stratus and altocumulus cloud features. Sufficient data were obtained for four 10° zenith angle increments from 0° to 40° . The data analyzed are characterized by an almost complete absence of cloud although a heavy haze and dust loading was observed throughout these missions, see Figure 4d.

The data taken north of 30°N latitude on June 11 provided sufficient information to compile two zenith angle stratifications from 10° to 20° and 20° to 30° of radiance reflected from the Himalayan mountains and plateau region. These scenes were characterized by steeply sloping barren surfaces partially covered with old snow and partially obscured by broken altocumulus cloudiness, as shown in Figure 4e.

Five 10° zenith angle regimes for mixed middle and low clouds over ocean were obtained on two flights into the northern edge of highly convective regions. Cloud conditions on these missions are difficult to categorize but varied from fairly thick cirrus to clear sky at and above flight level accompanied by altocumulus and fair weather cumulus below with the ocean surface often visible, see Figure 4f. Data collected under moderate to thick cirrus were excluded from the analysis by a check on the total downward irradiance as measured by an Eppley pyranometer mounted on top of the aircraft. A 90% transmittance threshold on a horizontal surface was used for this purpose. Since the



Figure 4d. Two photographs typical of the Indian Subcontinent scene.



Figure 4e. Two photographs typical of the Himalaya scene.

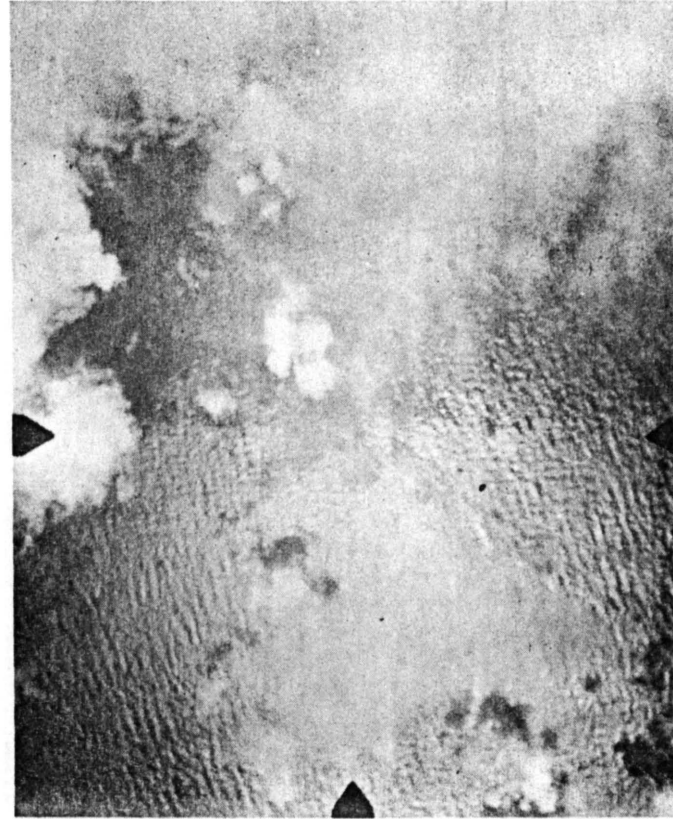
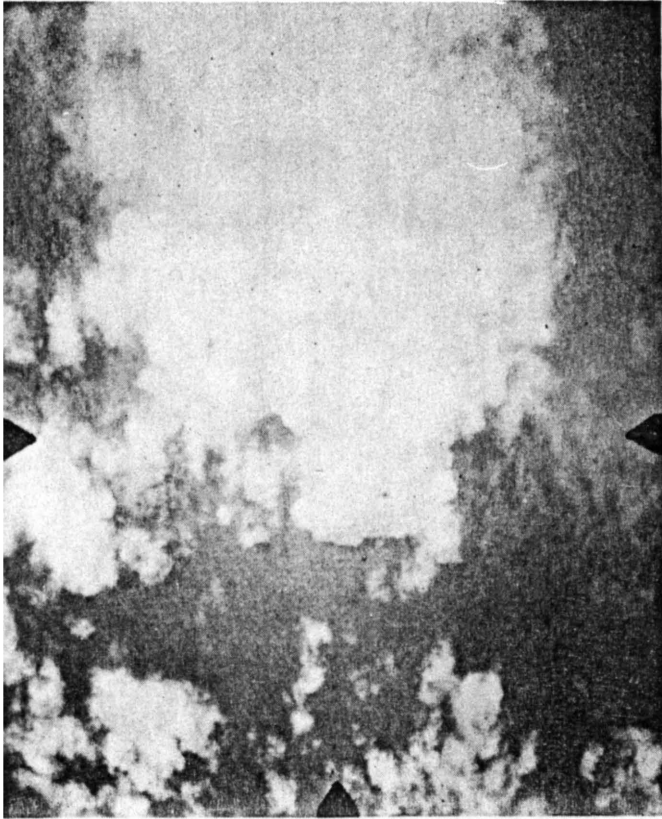


Figure 4f. Two photographs typical of the middle and low cloud atmospheric scene.

goal of this study is to provide reflectance patterns for atmospheric scenes and not to limit the analysis of radiances exiting solely from clouds, no lower limit was applied to the individual bugeye channels. However, in order to ensure that the scene was characterized by a significant amount of underlying clouds only data which resulted in an upwelling (0.3 to 3.0 μm) irradiance of $150 \text{ watts}\cdot\text{m}^{-2}$ or greater were included in this analysis.

The final category presented in this report is for altostratus clouds over the Pacific. These data were collected on the ferry flight of July 7 from Anchorage, Alaska to Moffet Field at Ames, California. Conditions of total undercast prevailed while the sun was between $20^\circ - 30^\circ$, $30^\circ - 40^\circ$ and $40^\circ - 50^\circ$ from the zenith. Figure 4g shows representative photographs.

The descriptions presented above define some of the specific features of the regions of data collection for the models which will be presented in the next section. In addition the following comments apply in general to all of the above categories. First, all of the analyses are limited to data collected above an altitude of 20,000 feet (6.3 km), which was the altitude commonly observed as the top of the dust - haze layer typical of the pre-monsoon atmosphere. Second, except as noted in the description of the low and middle cloud scene, the amount of cirrus cloudiness above the aircraft was observed to be negligible. This condition was confirmed quantitatively by measurement from a second bugeye type instrument mounted atop the aircraft, which was designed to measure the relative magnitudes of the direct and diffuse components of the downwelling solar irradiance. A description of this instrument is given in Appendix II. Although the performance

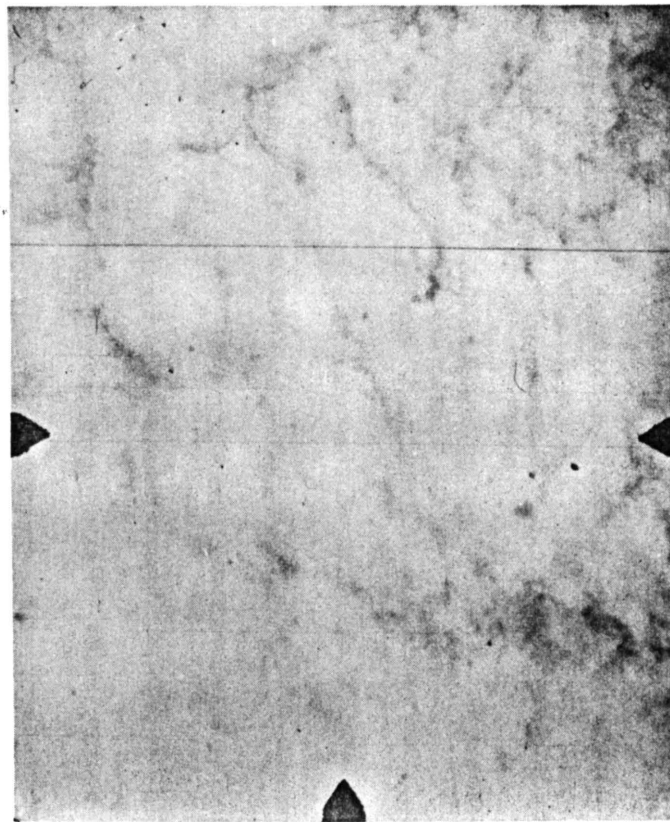
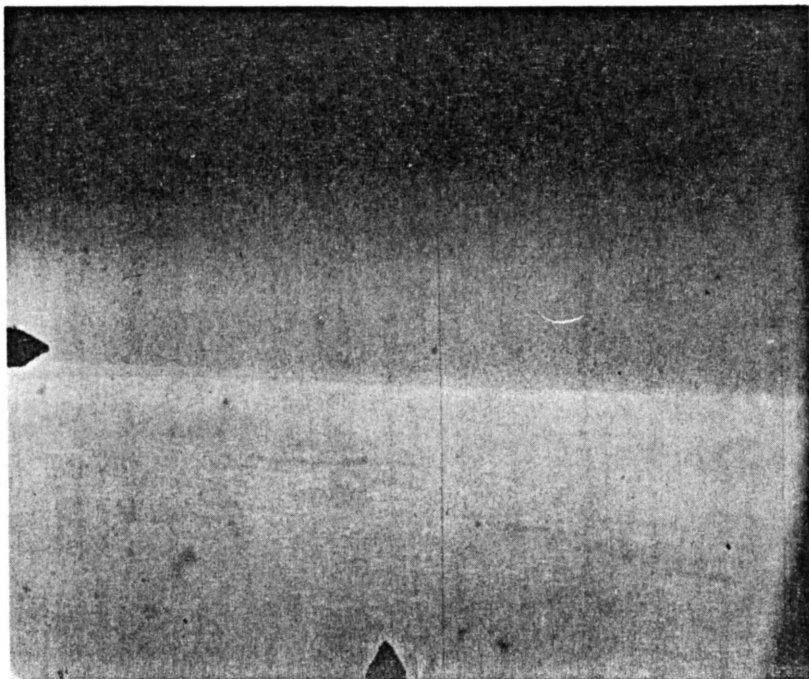


Figure 4g. Two photographs typical of the altostratus cloud scene.

of this instrument is still being evaluated the preliminary data analysis indicates a ratio of diffuse to total downward irradiance of from 2% to 5% for all data used in the present analysis with the exception of the mixed low and middle cloud cases. When the data from the top bugeye were analyzed for the low and middle cloud cases more than 90% of the points failed a diffuse to total irradiance test of 10%, while observations indicated much more of the data should have been acceptable. Because the top bugeye's performance is still under evaluation the alternate test criterion was applied as described above.

Finally, since most of the missions were not dedicated solely to the collection of angular reflectance data, the actual flight patterns varied considerably among the categorizations listed above. Thus, the actual number of data points differed considerably from scene to scene. Nevertheless, for all but a few of the cases, the space scale of data collection is greater than 250 km. The actual flight tracks which correspond to the categories given above are shown in Appendix III along with the corresponding average reflectance model.

3.0 DATA ANALYSIS

In the two previous sections the term "angular reflectance" has been used in a general way. Below, its definition is given, along with the method of assembling the data into angular reflectance models.

Figure 5 shows the geometry of an idealized measurement. Solar energy is incident on the target at a zenith angle z and azimuth angle ϕ_s . The target is considered to be the atmosphere beneath the aircraft and the underlying surface as previously categorized. The energy is scattered and absorbed by the atmosphere and the surface, and arrives at the level of measurement traveling in an upward direction at an angle θ from the zenith and a relative azimuth angle ϕ . ϕ is 0 when looking into the direction of the sun and is taken as positive for clockwise rotation about this reference. The bugeye instrument instantaneously measures the normal component of the radiant power incident on the active element of an individual photodiode within its spectral bandpass. Or if V_i is the voltage output of the i th diode amplifier system;

$$V_i = C \cdot k_i \int_{\lambda} \int_{\Omega_i} N(\theta, \phi, \lambda) F(\lambda) \cos(\theta - \theta_{N_i}) d\Omega d\lambda \quad (1)$$

where

k_i is the relative sensitivity of the i th diode amplifier combination

N is the spectral radiance arriving at the detector

λ is the wavelength of the energy

Ω_i is the amount of solid angle subtended by the aperture of the collimator tube on the i th diode

$F(\lambda)$ is the spectral response function of the diode (see Figure 2)

Geometry of the measurement

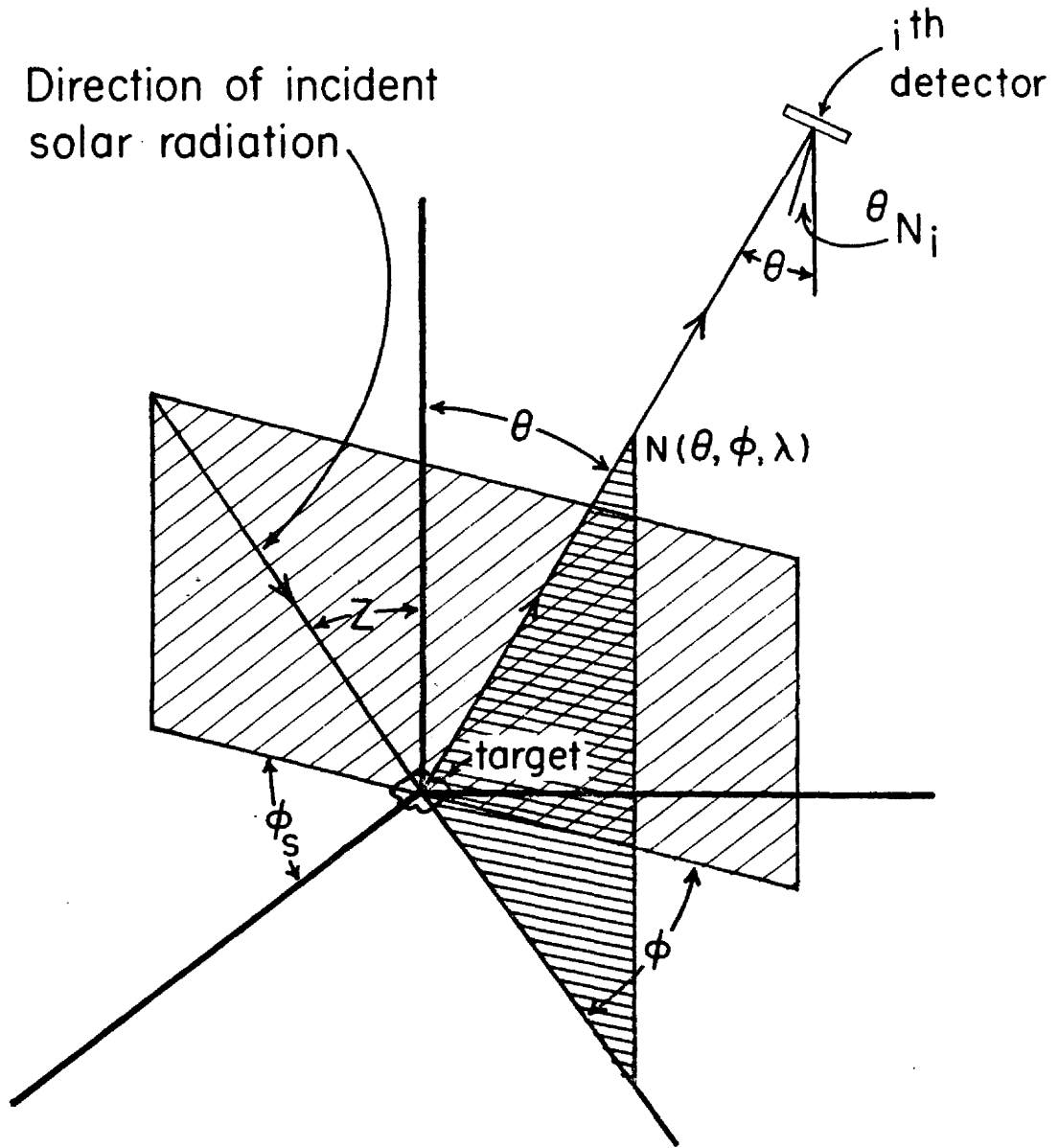


Figure 5. Depiction of the geometry of the measurement.

θ_{N_i} is the nadir angle of the normal to the active area of the i th photodiode

and C is the absolute sensitivity of the photodiode.

Since the collimator tubes have a narrow field of view $10^\circ \pm 1^\circ$ full angle and considering the angular resolution of interest, it is sufficient to invoke the mean value theorem with respect to the angular integration so that;

$$\begin{aligned}
 V_i &= C \cdot k_i \int_{\lambda} \int_{\Omega_i} N(\theta, \phi, \lambda) F(\lambda) \cos(\theta - \theta_{N_i}) d\Omega d\lambda \\
 &= C \cdot k_i \cdot \Omega_i \int_{\lambda} \hat{N}(\lambda, \theta_i, \phi_i) F(\lambda) d\lambda \quad (2)
 \end{aligned}$$

where $\hat{N}(\lambda, \theta_i, \phi_i)$ is the average radiance in the solid angle Ω_i centered at (θ_i, ϕ_i) . The integral on the right of Eq. (2) is the filtered radiance and after division by the appropriate relative amplifier sensitivities (k_i) and the detector field of view (Ω_i), the adjusted voltage $V'(\theta, \phi)$ is proportional to the filtered radiance. The constant of proportionality is the absolute sensitivity of the photodiode C . The bug-eye measured twelve² filtered radiances at every data scan (taken at one second intervals) at the angular positions of the diodes (given in Table 1). At each data scan the appropriate navigational parameters of the aircraft were used to form a rotation matrix which transformed

²Due to a wiring error on the Convair 990 only the first twelve diode outputs were recorded.

the angular coordinates from the aircraft frame to a fixed north-south horizontal reference frame. The solar azimuth measured in the same reference frame was used to obtain the position of each measurement in a "horizontal-solar" reference frame.

In the above manner a large number of measurements were compiled for a particular scene. The measurements were stratified in nadir and relative azimuth in 10° increments from $0^\circ - 90^\circ$ and $0^\circ - 360^\circ$ respectively and averages at each angular position were taken. The array of averaged, adjusted voltages was integrated over the downward facing hemisphere to obtain a number proportional to the filtered irradiance (E) on a downward facing horizontal plane according to;

$$E_V' = \int_{\theta=0}^{\pi/2} \int_{\phi=0}^{2\pi} V'(\theta, \phi) \cos\theta \sin\theta \, d\theta \, d\phi, \quad (3)$$

where filtered irradiance is given by $E = E_V'/C$. If the filtered irradiance were proportional to the upwelling $0.3 - 3.0 \mu\text{m}$ reflected flux density E_S , the constant of proportionality would be given by the ratio $\kappa = E_S/E$. Figure 6 shows a plot of $\kappa \cdot E$ vs E_S for data collected over and within clouds of variable horizontal and vertical extent over the Arabian Sea. Here κ has the average value of E_S/E over the data record. Although some relatively large discrepancies are evident, the agreement is generally good and is an indication that the spectral deficiencies of the measurements are not serious.

Since this research deals with the angular properties of reflected solar radiation in the 0.3 to $3.0 \mu\text{m}$ portion of the spectrum, it would be ideal if $F(\lambda) \equiv 1.0$ throughout that spectral region. However, since

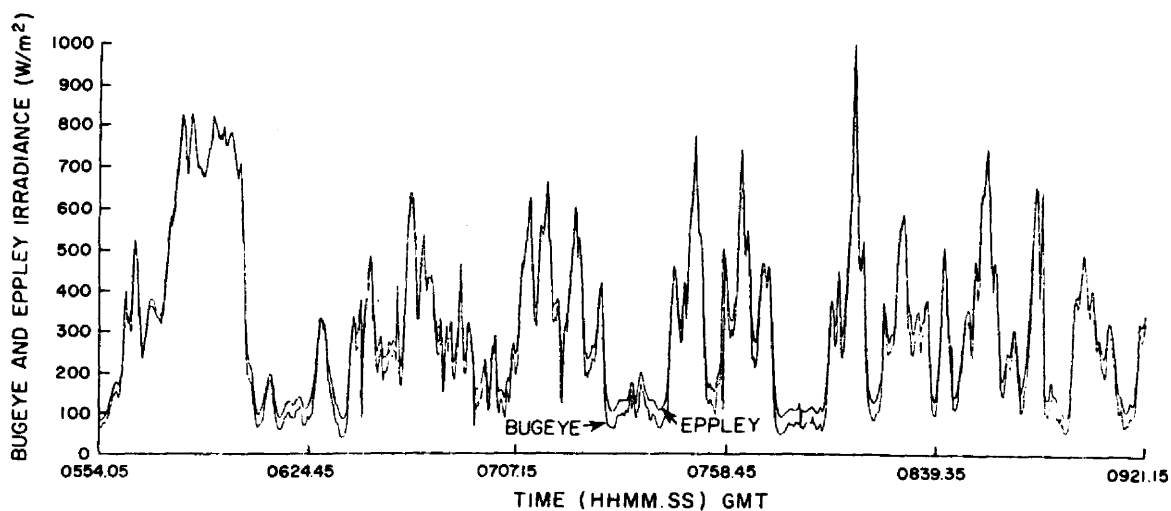


Figure 6. A comparison of the flux density reflected from broken clouds over ocean as measured by the Eppley 0.3 - 3.0 μm radiometer to the integral of the radiance field derived from the bugeye measurements.

this is not the case the following remarks should be considered. First, a significant fraction of the radiant energy reflected from various atmosphere-surface combinations lies within the spectral bandpass of the bugeye. A probable exception occurs in the case of high clouds. For example, Figure 7 shows a plot of relative spectral distribution of various targets and the photodiode spectral response. Table 2 gives the fractions of the total reflected energy which would be measured by the bugeye given the spectral response of the photodiode. Note the relatively constant ratio of filtered radiance to total radiance displayed by the entires. Similar ratios calculated for the 0.5 - 0.9 μm TIROS and the 0.5 - 0.9 μm GOES channels show much greater variability.

Measurements by Griggs et al. (1967) indicate even greater fractions of reflected energy are contained in the bugeye spectral bandpass for snow, ocean and various cloud targets. Salomonson (1968) presents results which indicate that a normalized radiance pattern for the 0.55 - 0.85 μm region is nearly identical to the same parameter taken over the 0.2 - 4.0 μm region for stratus cloud, dry lake bed and white sand surfaces. This similarity is probably even more pronounced for the present study which utilizes data collected at an altitude (~ 10 km) compared to Salomonson's data collected at altitudes from 1 to 3 km, due to the enhanced Rayleigh contribution for $\lambda < 1.1 \mu\text{m}$ and the added gaseous absorption for $\lambda > 1.1 \mu\text{m}$. For these reasons the angular properties which are analyzed in this report are assumed to be representative of the same properties of reflected solar radiation in the 0.3 - 3.0 μm portion of the spectrum. However, it is not necessary to assume that the radiances in the two spectral regions are related by a proportionality constant in all the analyses which follow.

Relative spectral response of the Bugeye Photodiode
and various relative spectral radiances

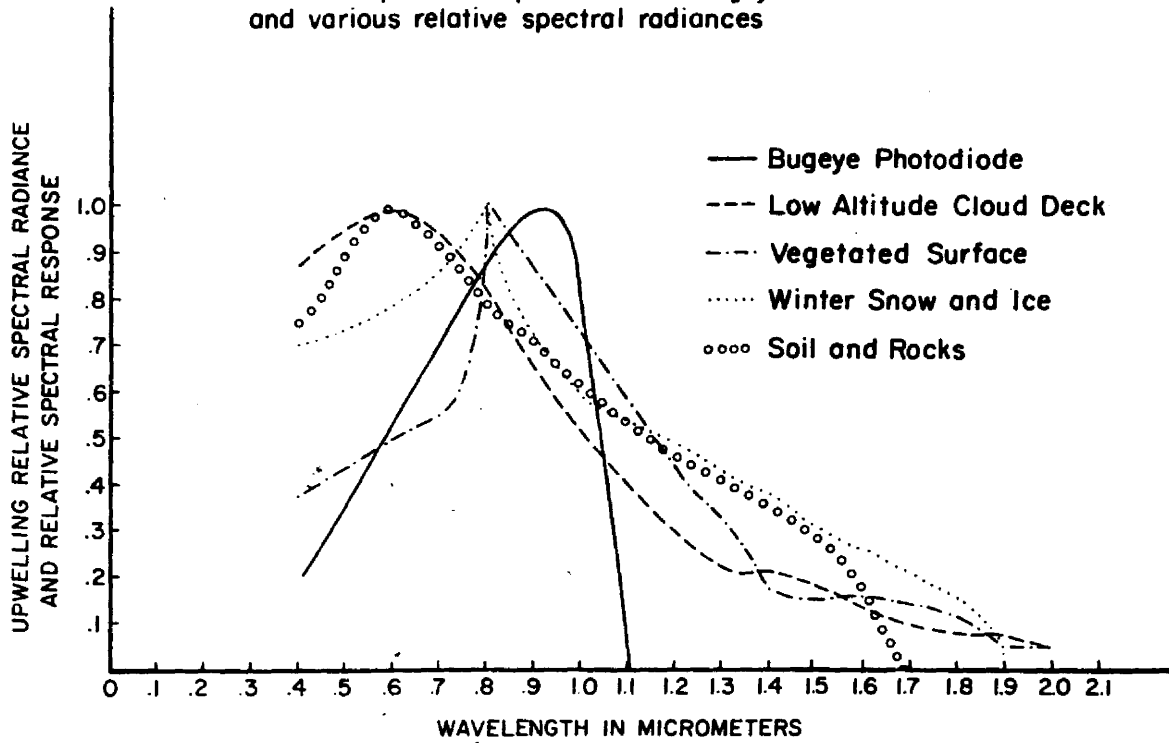


Figure 7. Relative spectral distributions of the satellite measured radiances reflected from various underlying surfaces.

Type of Surface	Fraction of 0.3 - 3.0 μm energy within bugeye spectral bandpass
Earth's surface obscured by a low altitude cloud deck for solar zenith of 30°	.46
Vegetated surface for a solar zenith of 30°	.42
Winter snow and ice for a solar zenith of 30°	.41
Earth's surface composed of soil and rocks for solar zenith angle of 30°	.44

Table 2. The fraction of the 0.3 - 3.0 μm radiances reflected by various surface and cloud types within the spectral bandpass of the bugeye photodiode. Spectral distributions are from The Infrared Handbook, 1978, edited by Wolfe & Zissis.

3.1 Angular Reflectance Models

The development of typical angular reflectance models follows the procedure set forth in several of the studies mentioned in the introduction. The goal is to provide an angular model which may be used to infer the upward flux density of reflected solar radiation from a region, by measuring the radiance exiting the region in one or at most a few angular directions. This is normally accomplished by specifying a bi-directional normalization coefficient χ defined by:

$$\chi(\theta, \phi, z) = \frac{\int_{\Omega} N(\theta, \phi, z) \cos\theta \, d\Omega}{\pi \cdot N(\theta, \phi, z)}, \quad (4)$$

where N , θ , ϕ , z and Ω have the definitions given in the preceding section. The analogous expression in terms of filtered radiances and irradiances is given by:

$$\chi(\theta, \phi, z) = \frac{C \cdot E_V'}{C \cdot \pi \cdot V'(\theta, \phi, z)} = \frac{E_V'}{\pi \cdot V'(\theta, \phi, z)} \quad (5)$$

Note that using χ obtained by the latter expression for its 0.3 - 3.0 μm equivalent requires the assumption of proportionality between the 0.4 - 1.1 μm and 0.3 - 3.0 μm radiances.

For the purposes of specifying a typical angular model the values of $V'(\theta, \phi, z)$ are azimuthally averaged about the principal plane [$\bar{V}'(\theta, \phi, z) = \bar{V}'(\theta, 2\pi - \phi, z)$]. Although the symmetrical model is not as representative as the asymmetric version for the particular surface over which the data were collected, it is considered optimal for application to all similar scene types. For example, if a particular pattern obtained from measurements over the Saudi Arabian Desert was to be used to interpret data collected over the Saharan Desert, non-symmetrical features caused by sand dune orientation in the Empty Quarters would almost certainly lead to larger errors than would result from use of a symmetric model.

The parameter χ is useful since its multiplication by a measured radiance and π results in a value of reflected flux density. This is the procedure envisioned as the solution to the problem of monitoring the reflected component of the radiation budget of a region from satellite-borne scanning radiometers. Questions concerning the applicability of these average models to regional scales will be considered in the next sections. In this study the average angular reflectance models are presented in terms of χ^{-1} , which corresponds to a normalized brightness. More significantly the deviation of $\chi^{-1}(\theta, \phi, z)$ from unity represents the fractional error between the true reflected flux density and a flux density inferred from application of the isotropic assumption to a radiance measured at the angular position (θ, ϕ) . Thus, for a scene which is isotropic $\chi^{-1} \cong 1.0$.

Since the bidirectional reflectance normalization coefficient is usually applied to satellite radiance data it is important to consider the effect on the angular variation of χ^{-1} of the atmosphere above

the level of data collection (~ 200 mb). The most important and most consistently applicable adjustment to angular patterns measured by high altitude aircraft is due to Rayleigh scattering. In order to account for the Rayleigh contribution above the level of data acquisition a single scattering approximation given in Paltridge and Platt (1976) is used. Figure 8 shows the single scattering approximation compared to the exact calculation (taken from Coulson, 1959) for solar radiation reflected by an atmosphere of optical depth $\tau = .05$ for solar zenith angles of 66° and 37° . The spectrally averaged Rayleigh optical depth of the 200 mb layer above the level of data collection was calculated to be .035 so that the single scattering approximation applied to the angular models will result in smaller errors than indicated in Figure 8. Errors of similar magnitude result when the approximation is applied to the forward scattered component. In order to apply the Rayleigh correction the measured filtered radiances are scaled to 0.3 - 3.0 μm values using the assumption of proportionality and the scaling factor κ . The single scattering approximation is applied to each angular component to obtain the forward scattered component at the top of the 200 mb layer above the aircraft. These values are added to the transmitted upwelling component and the solar reflected component calculated with the single scattering approximation (using a value of 1375 watts $\cdot \text{m}^{-2}$ for the solar constant) to obtain the distribution of the 0.3 - 3.0 μm radiance field. Equation 4 is reapplied to find χ^{-1} at the top of the 200 mb layer. The magnitude of the Rayleigh adjustment expressed as a percentage of the upwelling radiance incident on the 200 mb layer is about 1.5% for the forward scattered component, and 6% due to the

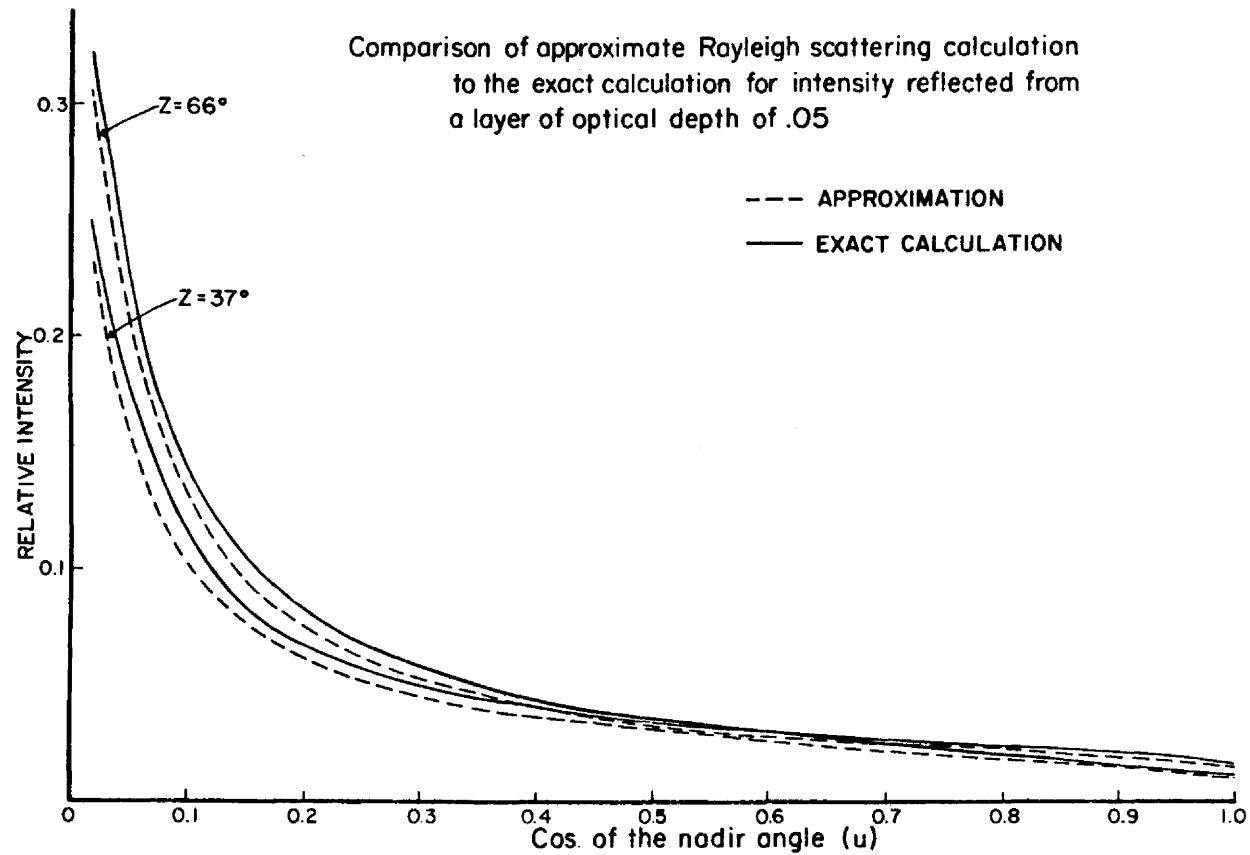


Figure 8. A comparison of a single scattering approximation for Rayleigh scattering to the corresponding multiple scattering calculation, for solar zenith angles of 37° and 66° .

solar reflected component with essentially 97% of the upwelling radiance being transmitted through the layer.

A simple interpolation scheme is used to fill in the missing values in the χ^{-1} array. The scheme uses the inverse of the angular distance between the interpolated point and all points within an angular neighborhood as a weighting function in such a way so that local characteristics are not influenced by values of χ^{-1} located more than 30° away. The complete set of χ^{-1} patterns are shown in Appendix III along with pertinent information regarding the locale of data collection.

Because the interpolation scheme was used to supply only angular positions which were missing, several points are included which were derived from only a few measurements. This results in an unsmoothed or fairly noisy pattern. The general characteristics of the χ^{-1} field are more discernable in a smoothed version of the pattern. Also it is convenient to have some means of accessing a particular value of χ^{-1} other than graphical interpolation or tabular look-up. For these reasons the data were fitted using as a basis the set of spherical harmonic functions in a slightly modified form with a simple least squares technique. In this case the entries are number weighted so that points resulting from only a few measurements have little effect on the fit. For the spherical harmonic function $Y_n^m(\theta, \phi)$, there are $2n + 1$ values of m for each value of n . The maximum value of n used in any of the fits to the data was 6 which allowed for a maximum of 49 basis functions to be included. The amount of the variance attributed to each term of the fit was calculated and terms which accounted for less than 0.25% of the norm of χ^{-1} were discarded. The number weighted r.m.s. error, calculated after the least significant terms were deleted ranged from 4%

to 28% depending upon the variability of the data field. The complete set of fitted χ^{-1} patterns, spherical harmonic coefficients and resulting r.m.s. error are given in Appendix IV. A few of the smoothed patterns are shown below and some of the more interesting features are discussed.

Figures 9a,b,c show the smooth χ^{-1} reflectance models resulting from measurements over the Saudi Arabian Desert for zenith angle ranges of $0^\circ - 10^\circ$, $30^\circ - 40^\circ$ and $70^\circ - 80^\circ$. Figure 9a shows a nearly isotropic pattern with values of χ^{-1} ranging from 0.90 to 1.1. The pattern shows a bright region near the center of the figure (small values of the nadir angle) with a slight tendency toward backscatter at intermediate nadir angle values. In this and all similar figures the nadir angle varies from 0° at the center to 70° at the outer rim of the figure while values of relative azimuth vary from 0° (facing the direction of the sun) to 180° in the anti-solar direction. Figure 9b indicates a higher degree of anisotropy with values ranging from 0.80 to 1.20 and shows a more pronounced backscatter. For the largest zenith angle range, Figure 9c shows a transition to a forward scattering maximum probably due to scattering from the atmosphere. The backscatter feature is still evident with the darkest features indicated near the nadir. The fitted χ^{-1} values range from 0.50 to 1.70 for the last case while the corresponding interpolated pattern shown in Appendix III indicates a slightly smaller range, $0.6 \leq \chi^{-1} \leq 1.70$. In either case an overestimate of 70% in the reflected flux density would result if the isotropic assumption were applied to radiances measured near the $\theta = 70^\circ$, $\phi = 0^\circ$ direction.

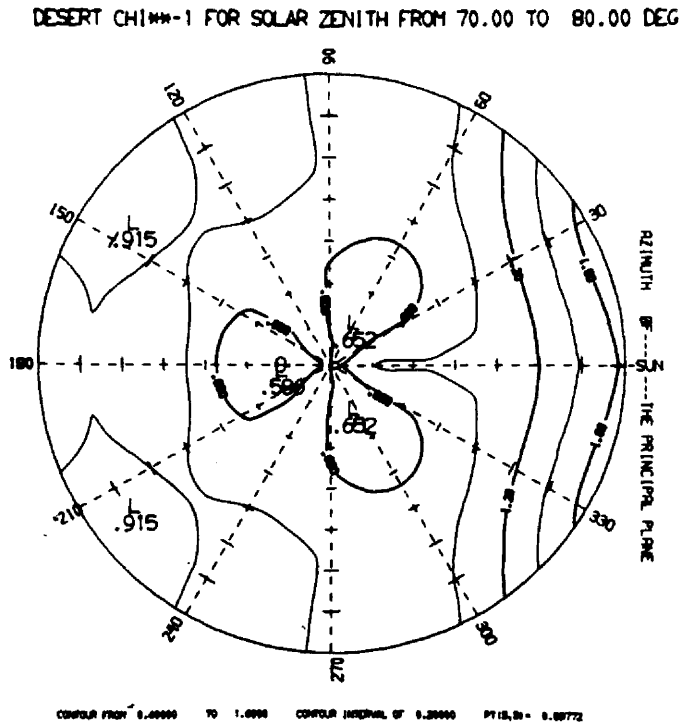


Figure 9c. The spherical harmonic approximation to the angular reflectance (χ^{-1}) model for the 70-80° solar zenith angle desert case.

Figure 10 shows the smoothest version of χ^{-1} for data collected over the Himalayas. This figure should be used to denote only the coarsest features of the scene since the r.m.s. error of the data fit is nearly 20%. A broad brighter region is evident extending from the nadir out to 50° and 60° in the solar and anti-solar directions respectively. The χ^{-1} coefficient ranges from 0.9 to 1.1 in the fitted pattern but ranges from 0.8 to 1.1 in the interpolated version. In either case photographs suggest that the general feature of a darker region toward the horizon may be the result of bare rock features which protrude above and obscure the intervening valleys where brighter snow and ice have accumulated.

Figures 11a and b show the fitted χ^{-1} patterns for the Indian sub-continent in the solar zenith angle regimes of $0^\circ - 10^\circ$ and $30^\circ - 40^\circ$. Figure 11a shows a slightly more specular nature of the Indian sub-continent compared to the corresponding pattern measured in Saudi Arabia. The relatively greater specular component is probably the result of reflection off the surface of various rivers which typify the central western portion of that country. A detailed examination of the photographic record indicates the specular reflectance. Inspection of the interpolated results for the same scene indicates values of χ^{-1} as high as 1.35 for a nadir angle of 5° while at 15° nadir the highest reading is 1.13 which is another indication of specular reflection from the water surfaces. It should also be noted, however, that much of the data collected over the Ganges River portion of the flight was collected at low altitude and thus excluded from the sample. In Figure 11b

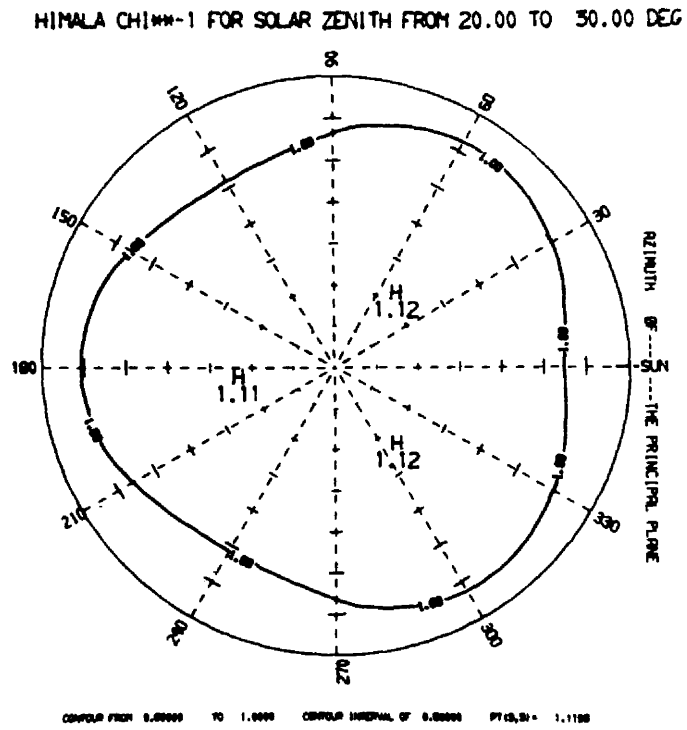


Figure 10. The spherical harmonic approximation to the angular reflectance (χ^{-1}) model for the 20-30° solar zenith angle Himalayan case.

INDIAN CHIM-1 FOR SOLAR ZENITH FROM 0.00 TO 10.00 DEG

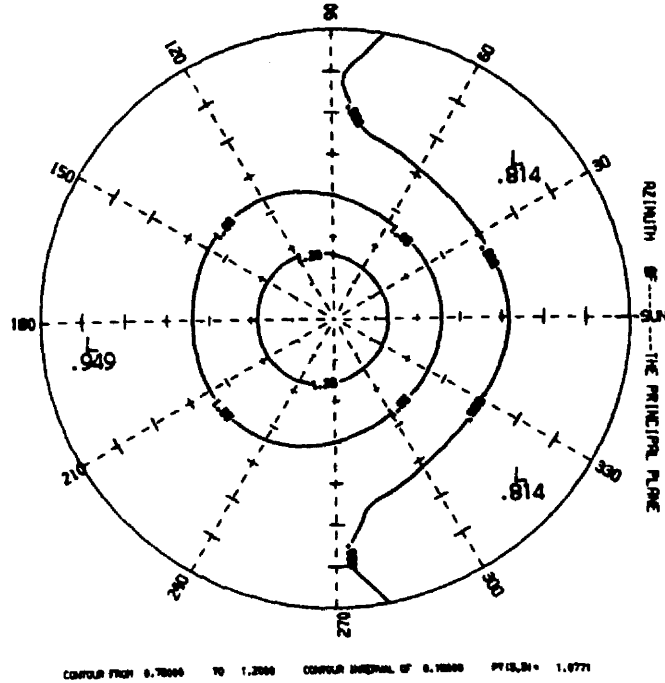


Figure 11a. The spherical harmonic approximation to the angular reflectance (χ^{-1}) model for the 0-10° solar zenith angle Indian subcontinent case.

INDIAN CHIM-1 FOR SOLAR ZENITH FROM 30.00 TO 40.00 DEG

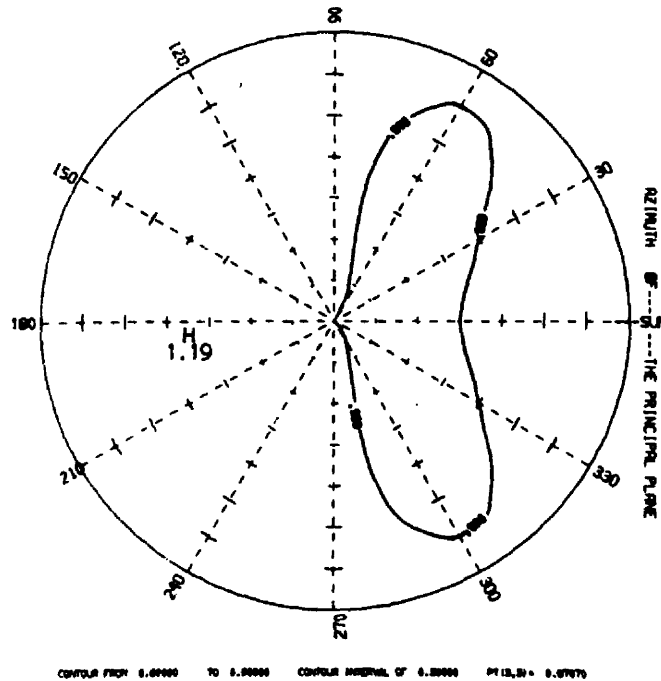


Figure 11b. The spherical harmonic approximation to the angular reflectance (χ^{-1}) model for the 30-40° solar zenith angle Indian subcontinent case.

the χ^{-1} values range from 0.75 to 1.20 and a prominent backscatter feature is evident. This figure should be compared with Figure 9b, the 30° - 40° desert case.

Zenith angle ranges of 0° - 10° and 50° - 60° are shown in Figures 12a,b for the clear ocean cases. χ^{-1} ranges from 0.25 to 2.00 and from 0.18 to 2.75 respectively. (The interpolated pattern for the latter case shows a χ^{-1} range of $0.25 \leq \chi^{-1} \leq 2.75$.) Obvious in these plots is the sunglint feature which may be seen to progress outward to the horizon upon inspection of the complete set of χ^{-1} plots in Appendix III.

Figures 13a,b represent the data fits to the middle and low level cloud cases (hereafter referred to as CLOUD1) for zenith angle ranges of 10° - 20° and 30° - 40° respectively. A slight tendency toward backscattering is observed in the smaller zenith angle cases with χ^{-1} ranging from 0.75 to 1.05. The situation is reversed in the latter case which displays a strong and broad region of scattering in the forward direction and a larger range in normalized brightness from $\chi^{-1} = 0.50$ to 1.75. It is noted here that it is difficult to be certain that the scene type is not significantly different between these cases because of changing cloud type. Even though the data were collected in the same geographical locations and cloud conditions were observed to be similar, the different features of the patterns may have resulted to a large extent from undetected differences in the type or amount of cloud cover. Nevertheless the patterns are representative of the regions of broken, variable, middle and low level cloudiness encountered during the experiment. The slight backscatter feature at the smaller zenith angle ranges may be attributable to reflection off the

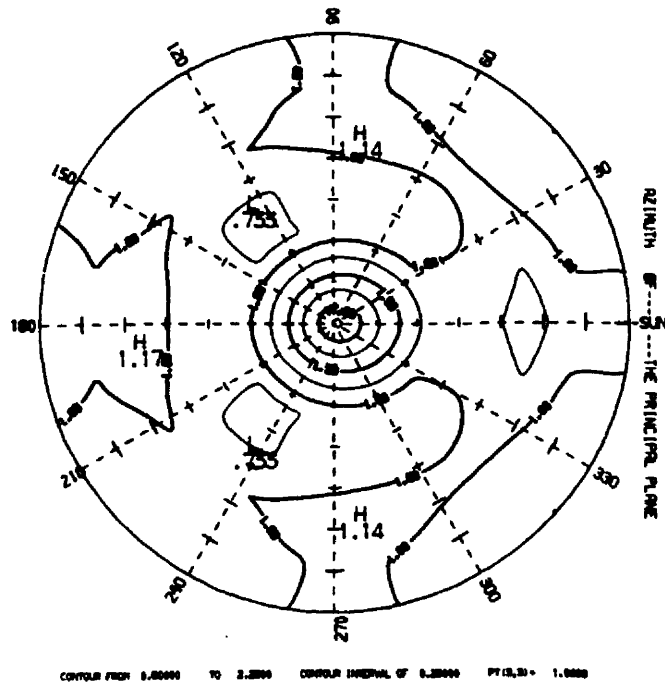
OCEAN χ^{-1} FOR SOLAR ZENITH FROM 0.00 TO 10.00 DEG

Figure 12a. The spherical harmonic approximation to the angular reflectance (χ^{-1}) model for the 0-10° solar zenith angle clear ocean case.

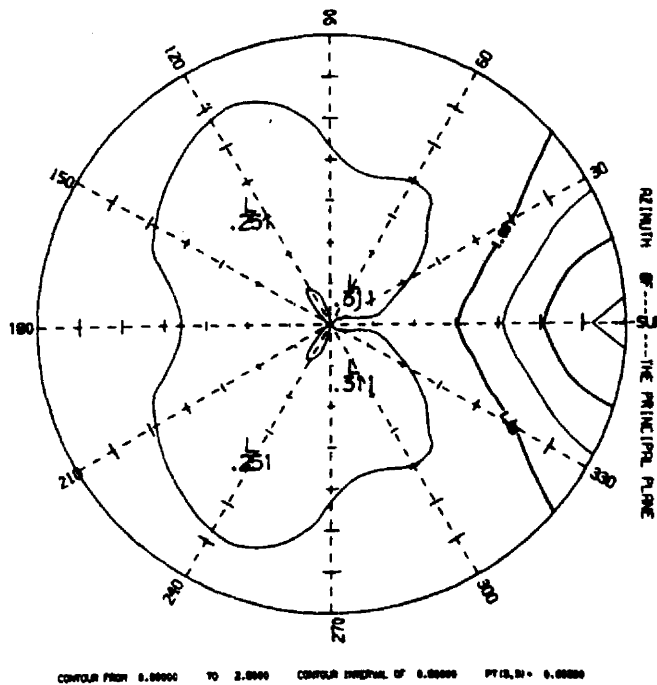
OCEAN χ^{-1} FOR SOLAR ZENITH FROM 50.00 TO 60.00 DEG

Figure 12b. The spherical harmonic approximation to the angular reflectance (χ^{-1}) model for the 50-60° solar zenith angle clear ocean case.

CLOUD1 CHI**H-1 FOR SOLAR ZENITH FROM 10.00 TO 20.00 DEG

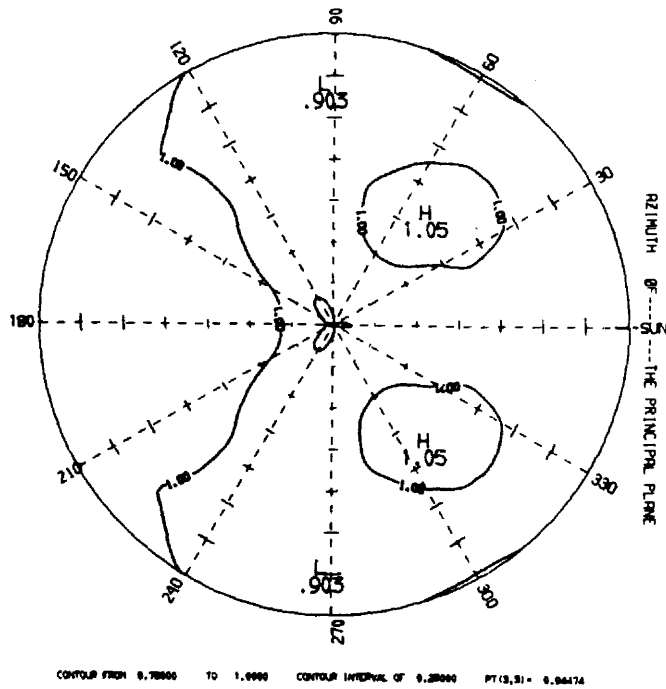


Figure 13a. The spherical harmonic approximation to the angular reflectance (χ^{-1}) model for the 10-20° solar zenith angle middle and low level cloud case.

CLOUD1 CHI**H-1 FOR SOLAR ZENITH FROM 30.00 TO 40.00 DEG

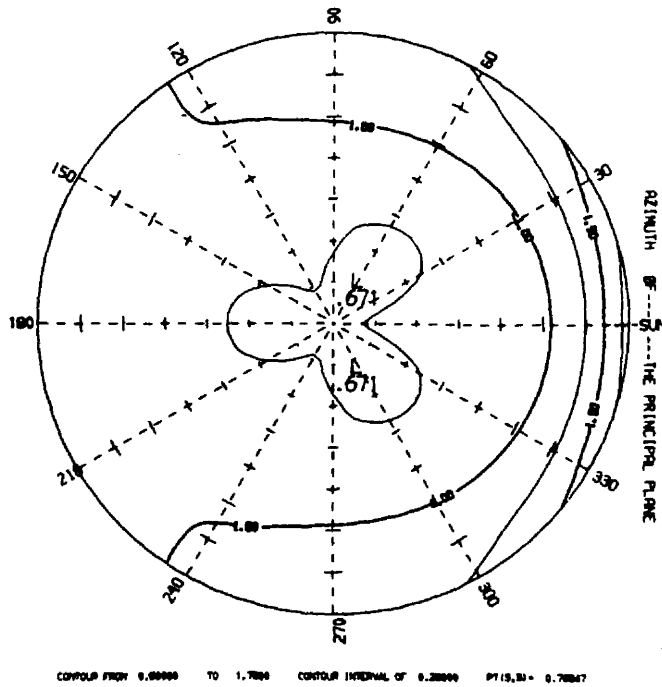


Figure 13b. The spherical harmonic approximation to the angular reflectance (χ^{-1}) model for the 50-60° solar zenith angle middle and low level cloud case.

vertical walls of individual clouds into the upward direction. As the zenith angle increases reflection from the cloud tops in the forward direction becomes important as well as an increased contribution due to sunglint measured between the clouds.

Figures 14a,b show the patterns for data collected over a reasonably homogeneous altostratus deck (hereafter referred to as CLOUD2). For a solar zenith of from 20° to 30° there is both forward and backward scattering evident at the larger nadir angles with a rather broad region of smaller normalized radiances in the anti-solar direction at small and intermediate nadir angles. For the larger solar zenith angle case $40^\circ \leq z \leq 50^\circ$ a more pronounced forward scatter feature is evident. Also the region of lower χ^{-1} values has shifted to the solar side of the scene. The backscatter in this case may be attributable to one or both of two processes. First, although the clouds are stratiform in this case Figure 4g shows the cellular nature of the layer. Thus the possibility for backscatter from the individual vertical protrusions exists. Second the presence of ice crystals in the layer may add to the backscatter feature because of the secondary maximum displayed by the scattering phase functions of ice crystals for scattering angles near 180° .

The brief descriptions and explanations given above are not meant to completely account for all of the features in the patterns. Some of the properties such as those found in the clear ocean cases are easily accounted for. Others, such as the prominent backscatter in the small zenith angle cloud cases may be explained with much less confidence and are subject to further verification. The most general conclusion which may be drawn from the ensemble of the angular reflectance models,

CLOUD2 CHI**1 FOR SOLAR ZENITH FROM 20.00 TO 30.00 DEG

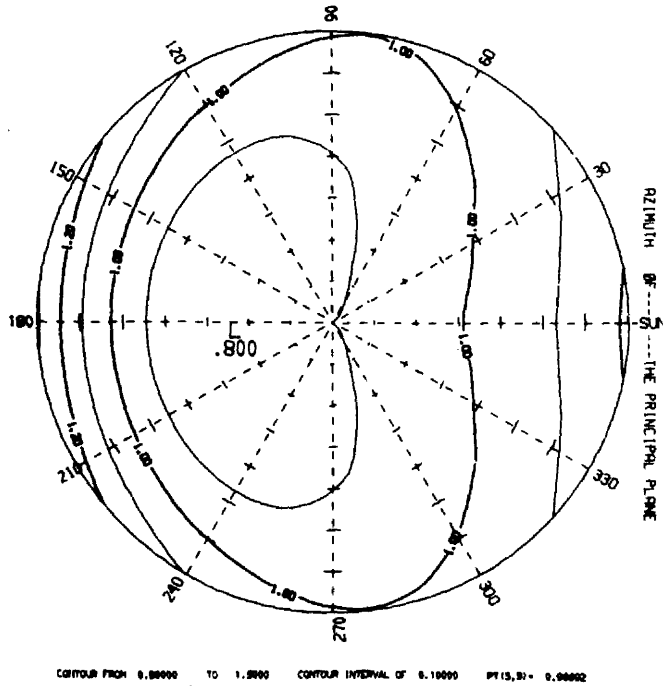


Figure 14a. The spherical harmonic approximation to the angular reflectance (χ^{-1}) model for the 20-30° solar zenith angle altostratus cloud case.

CLOUD2 CHI**1 FOR SOLAR ZENITH FROM 40.00 TO 50.00 DEG

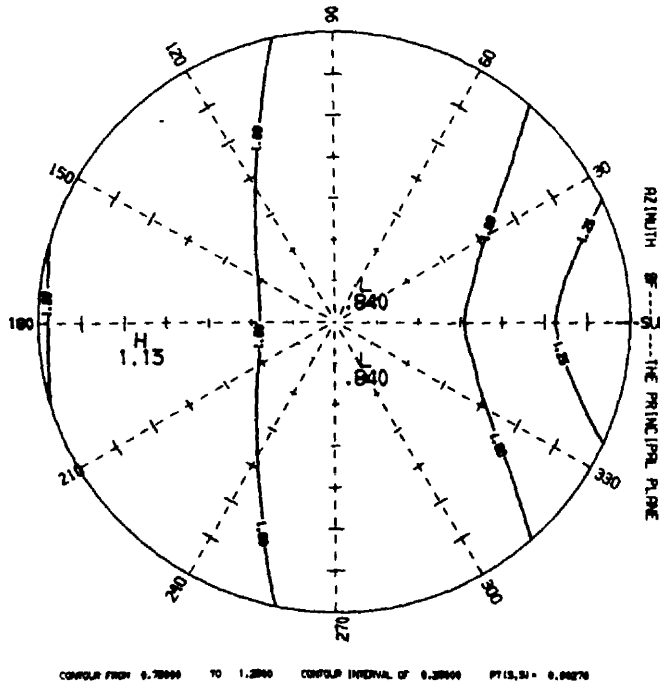


Figure 14b. The spherical harmonic approximation to the angular reflectance (χ^{-1}) model for the 40-50° solar zenith angle altostratus cloud case.

and the most important, is that the anisotropy displayed by all scene types is of sufficient magnitude to have a significant impact on reflected flux densities inferred from scanning radiometer measurements.

3.2 Comparison with Previous Results

Because there have been only a few experimental programs dedicated to the measurement of angular reflectance patterns it is important to compare the data presented here to previous studies whose results have been incorporated into various radiative energy budget estimates (see Introduction). Also, some theoretical efforts have been published which are sufficiently rigorous to offer a good basis for comparison. The comparisons below will be made following the historical perspective given in the Introduction. Many of the angular reflectance models used in the comparisons which follow were compiled by Mr. Eric A. Smith and were supplied to the author by personal communication. These models are indicated below by an asterisk.

The first comparison was made between the clear Arabian Sea data collected with the bugeye and clear Pacific Ocean data from (0.2 - 6.0 μm) TIROS IV measurements compiled by Arking (1965). Arking's data were presented in terms of an apparent reflectance $R = (\pi \cdot N) / (F_0 \cdot \cos z)$, where F_0 is the solar constant (the symbols N and z have been changed from the original document to comply with present notation). In order to affect the comparison a value for F_0 of $1375 \text{ watts} \cdot \text{m}^{-2}$ was used to recover N , the (0.2 - 6.0 μm) radiance, from the original apparent reflectance values. The average of the adjusted voltages measured by the bugeye in the principal plane was used to obtain a factor to scale the bugeye readings to the average radiance value from

the previous study. Figure 15 shows a plot of the comparison in the principal plane for a solar zenith angle of 53° . In view of the differences between the data collection techniques the agreement is good. The figure also indicates the general validity of scaling (0.4 to 1.1 μm) data to represent the behavior in the broader spectral region.

Figures 16a and b show comparisons between an angular model* compiled from the data of Ruff et al. (1968) for clouds and the χ^{-1} patterns compiled from the bugeye measurements of altostratus and middle and low level broken clouds respectively. The plots show contours of the difference between the χ^{-1} values with positive numbers indicating that relatively brighter regions were measured by the bugeye while negative numbers indicate regions of greater brightness resulting from the previous study. Also shown near the bottom left of the figure is the average difference in the χ^{-1} values taken over the $0^\circ - 70^\circ$ nadir angle and the $0^\circ - 360^\circ$ relative azimuth range. The average of the differences would be zero for the entire $0^\circ - 90^\circ$ nadir angle range, however the bugeye measurements for nadir angles beyond 70° are considered to be extrapolations supported by sparse data only. A positive value of the average error indicates that an overall brighter field was measured by the bugeye for the $0^\circ - 70^\circ$ nadir angle range. The corresponding r.m.s. error is given at the bottom right of the figure indicating the average magnitude of the difference in the χ^{-1} values over the field displayed in the figure. In Figure 16a which represents measurements taken over altostratus clouds for a solar zenith angle range of $40^\circ - 50^\circ$, the average error of $-.02$ indicates that the bugeye measured values are relatively smaller over the $0^\circ - 70^\circ$ range. The primary contributions to the negative overall error are found in a

Comparison of clear Arabian Sea data with clear Pacific Ocean data
 from Tiros IV for a solar zenith angle of 53° and $\phi = 0^\circ, 180^\circ$

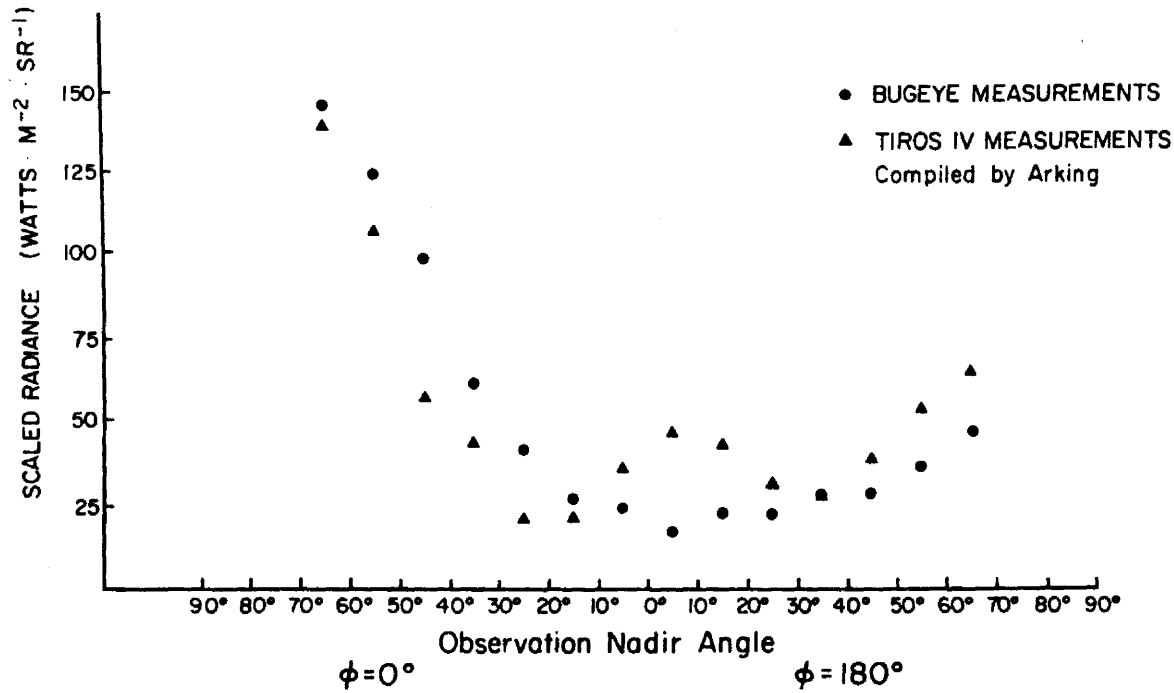


Figure 15. A comparison of normalized reflected radiances derived from bugeye measurements over the clear Arabian Sea to the same quantity derived from TIROS measurements over the clear Pacific Ocean.

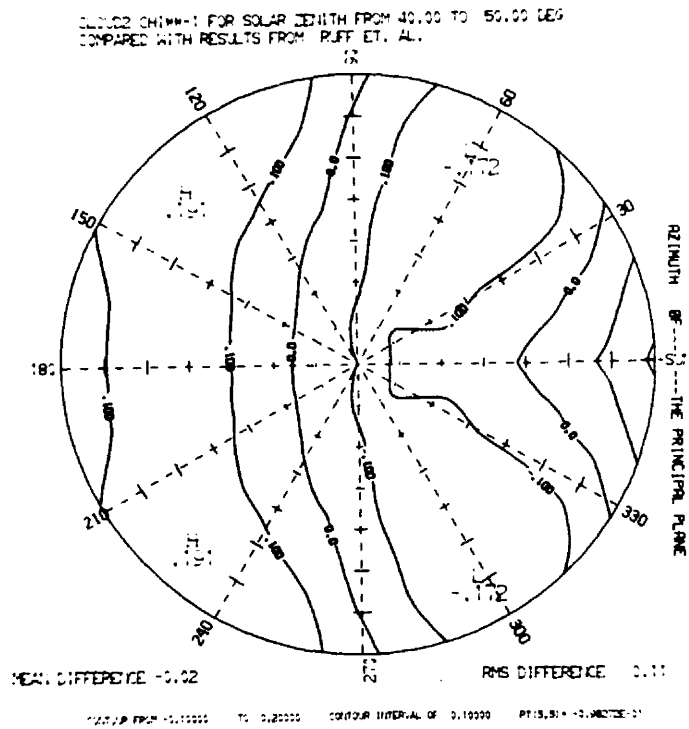


Figure 16a. A comparison between the angular reflectance (χ^{-1}) model for the 40-50° solar zenith angle altostratus cloud case and a cloud model derived from the data of Ruff et al.

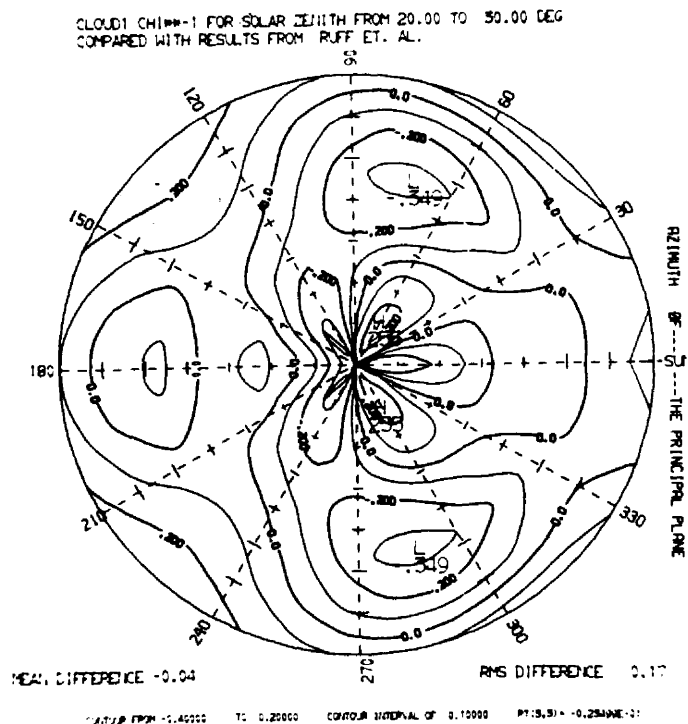


Figure 16b. A comparison between the angular reflectance (χ^{-1}) model for the 20-30° solar zenith angle middle and low level cloud case and a cloud model derived from the data of Ruff et al.

broad region in the forward scattering direction. Also indicated is the greater backscatter measured by the bugeye instrument with a 0.19 maximum difference indicated at the 60° nadir position at relative azimuths of 135° and 225°. The r.m.s. error of 0.11 indicates fair agreement on a point by point basis. In Figure 16b the χ^{-1} pattern* from Ruff et al. (1968) is compared to the bugeye measured middle and low level cloud case for a solar zenith angle range of 20° - 30°. In this case slightly poorer agreement is found for the average and r.m.s. differences stemming from disagreement throughout the nadir-azimuth array. Since the data used by Ruff et al. were obtained from 0.55 - 0.75 μm TIROS IV measurements and included only those cases which filled the field of view of an 8 - 12 μm channel, one might expect poorer agreement with measurements over broken clouds as indicated by these comparisons.

Figure 17a shows a similar comparison between the bugeye 40° - 50° solar zenith angle altostratus cloud case and a χ^{-1} model* generated from the measurements by Salomonson (1968) over stratus clouds off of the California coast. In this case the bugeye measures a relatively brighter field over the 0° - 70° nadir angle range with the greatest differences indicated in the backscatter regime. The r.m.s. difference of 0.09 shows moderately good agreement considering the spectral differences between the measurements (0.4 - 1.1 μm vs 0.2 - 4.0 μm) and the differences between the altitudes of the measurements (10 km vs \sim 1.0 km). In Figure 17b the same results* from Salomonson are compared to the 40° - 50° middle and low level cloud case. The average agreement is somewhat better for the 0° - 70° nadir angle range than with the bugeye stratus case and the average magnitude or r.m.s. difference

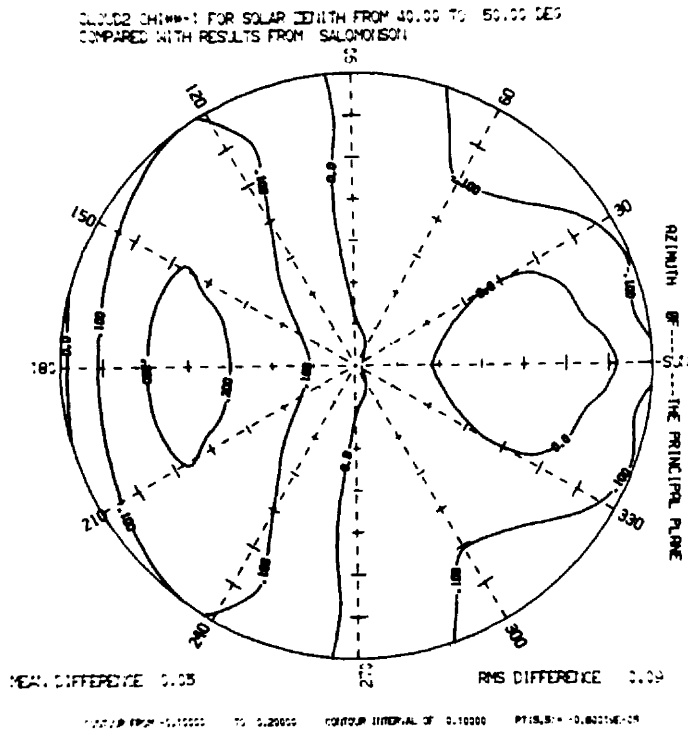


Figure 17a. A comparison between the angular reflectance (χ^{-1}) model for the 40-50° solar zenith angle altostratus cloud case and an altostratus cloud model from measurements by Salomonson.

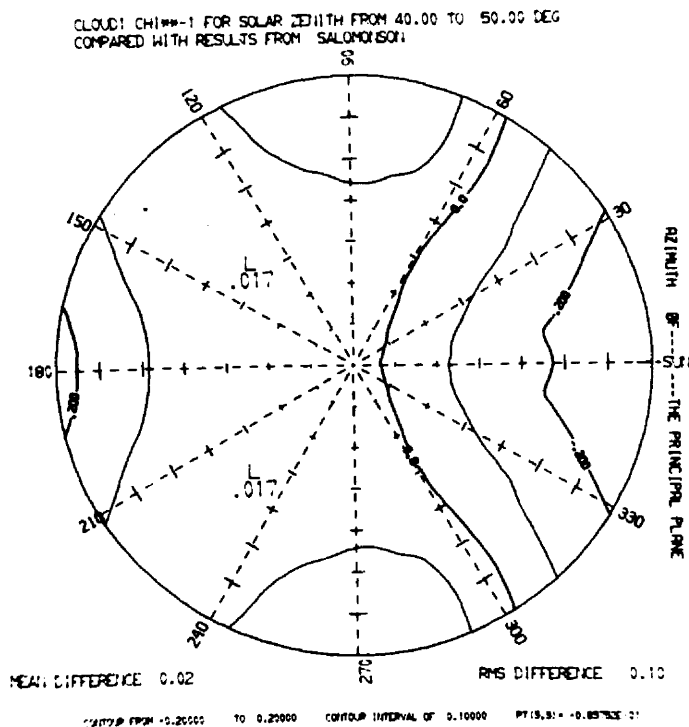


Figure 17b. A comparison between the angular reflectance (χ^{-1}) model for the 40-50° solar zenith angle middle and low level cloud case and an altostratus cloud model from measurements by Salomonson.

is only slightly worse. The figure clearly indicates the relatively stronger forward scatter and weaker backscatter measured over the low stratus deck, a feature which is most probably due to the differences between scattering properties of horizontally continuous and broken cloud fields.

Figure 18 is a comparison between bugeye measurements taken over the desert for a $70^\circ - 80^\circ$ solar zenith angle range and a χ^{-1} model* compiled from the data which Salomonson (1968) collected over a dry desert lake bed. The small average error indicates nearly equal apportionment by the two data sets into the less than 70° and greater than 70° nadir angle regimes. However, the figure shows great disagreement between the data sets resulting from the strong forward scatter measured by the bugeye and the relatively strong backscatter in the results of Salomonson. In this case the r.m.s. difference is over 0.43 and a disagreement of 1.11 occurs at the maximum nadir in the solar direction. It is remarkable that the disagreement is so great between patterns generated from data collected over a desert scene which is normally accepted as isotropic and envisioned as the case for which angular reflectance modelling is least required. The differences exhibited in this case are almost certainly due to the forward scattering off the relatively thicker and dust laden intervening atmosphere between the bugeye and the desert sands although spectral differences may not be ruled out as a contributing factor. Also Salomonson's data were collected over a dry desert lake bed and exhibited strong backscatter even in visual observations. Salomonson remarks that "the degree of reflection back toward the sun in this case is more than that to be expected over desert sand".

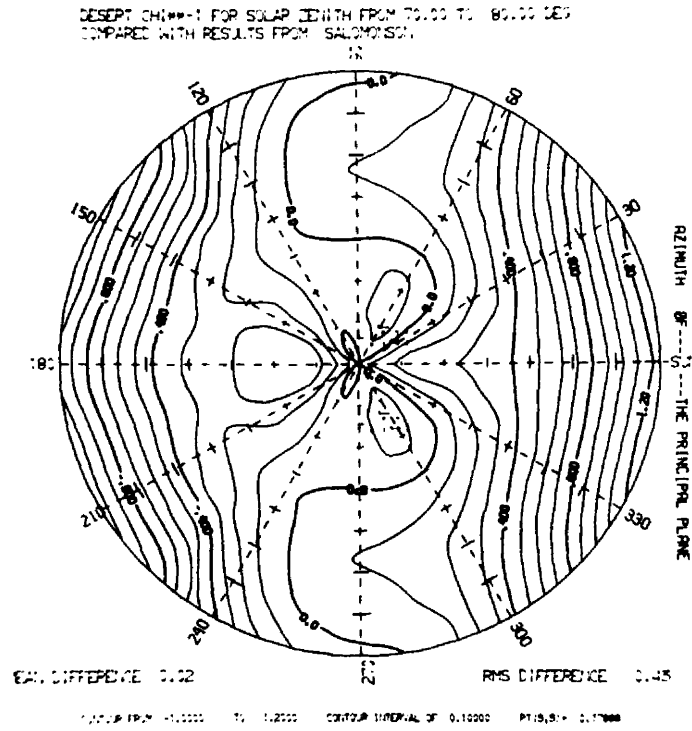


Figure 19 shows a comparison between measurements by Griggs et al. (1967) over a 3 km thick stratus cloud deck for a solar zenith angle of 50.1° and the $40^\circ - 50^\circ$ measurements of an altostratus deck by the bug-eye. In this case an average scaling factor has been applied to the adjusted bug-eye voltages to scale them to radiance values and the plot is shown as a function of the angle of scatter from the incident solar direction. The values from Griggs et al. are unsmoothed measurements and display a wide variance. The curve through the points is an estimate of the best fit. The bug-eye values show the same trends toward forward and backward scatter over the range of angles measured and the scaled voltages generally lie within the scatter of the previous measurements.

Figure 20 compares the $40^\circ - 50^\circ$ Arabian Sea bug-eye measurements with a χ^{-1} pattern* generated from the results of Brennan and Bandeen (1970) whose data were obtained over the Pacific Ocean from aircraft at an altitude of about 12 km. Overall the bug-eye measurements are 0.025 lower in the $0^\circ - 70^\circ$ nadir angle range and an r.m.s. difference of 0.20 was calculated. Much of the disagreement is found in the forward and backward scattering directions which in this case may be caused by significant differences in sea surface conditions. In fact a positive difference of 1.07 is found in the region of the sun's glint indicating that the feature is much less prominent in the Pacific Ocean data. In addition, spectral differences must again be mentioned and the presence of the dust-haze layer which was typical of the Arabian Sea area during the pre-monsoon period. However, it is unlikely that either of the last two features could account for the large discrepancies between the angular patterns.

Comparison of Bugeye measurements over alto stratus with
 measurements by Griggs et al. for a solar zenith of 50.1°

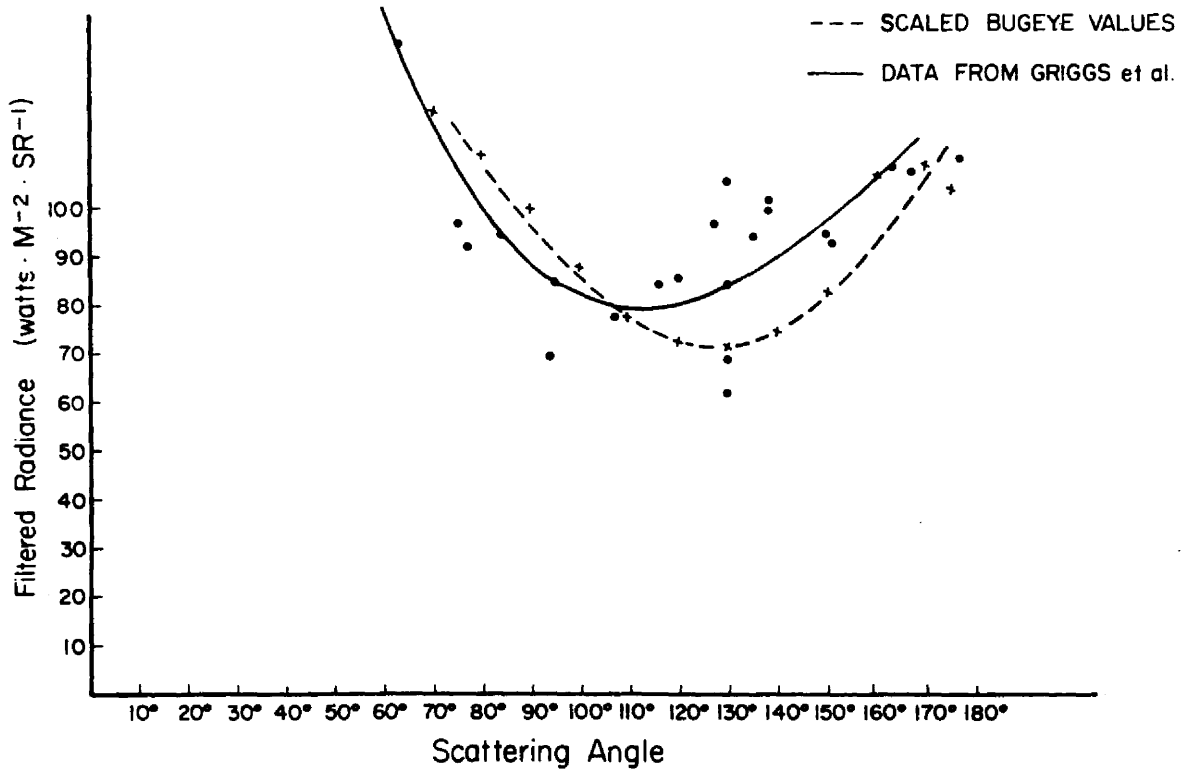


Figure 19. A comparison between normalized radiances reflected from altostratus cloud derived from bugeye measurements and the same quantity from measurements by Griggs et al.

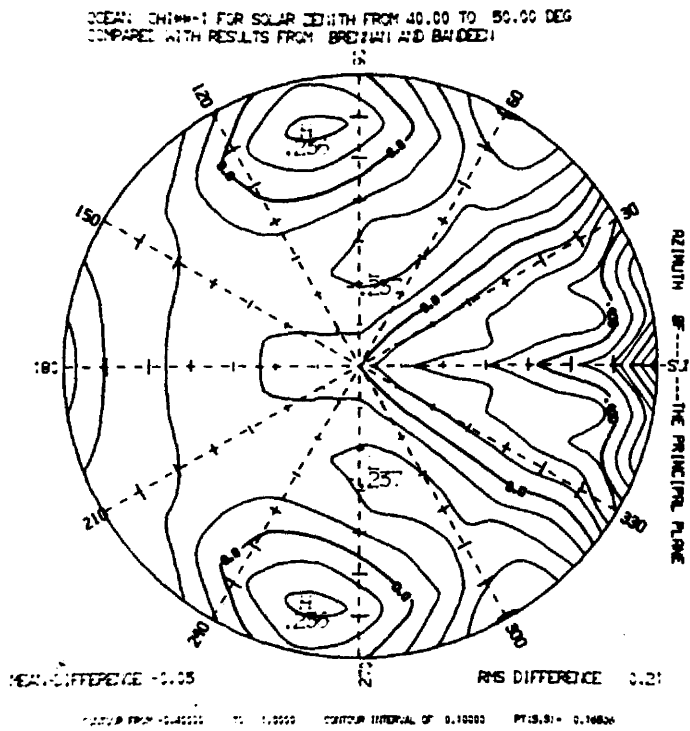


Figure 20. A comparison between the angular reflectance (X^{-1}) 40-50° solar zenith angle clear ocean case and an ocean model derived from measurements by Brennan and Bandeen.

The final comparisons are presented in Figures 21a and b again for clear ocean scenes. In this case, however, the results from calculations by Plass et al. (1975) are used. Their Monte Carlo calculation takes into account the effects of Rayleigh scattering and Mie scattering by aerosols as well as molecular and aerosol absorption in the atmosphere. At the air-ocean interface the Cox-Munk wave slope distributions were used to determine reflection characteristics. In the ocean Rayleigh scattering by the water molecules and Mie scattering by the hydrosols as well as absorption by both were accounted for. The calculation was carried out for a wavelength of 0.46 μm . Figure 21a compares the scaled bugeye radiance to the radiance calculated as emerging from the top of the atmosphere for a solar zenith angle of 0° and a wind speed of 10 knots. Figure 21b shows a similar comparison for a zenith angle of 57° . The agreement between the trends in the two cases is reasonably good in view of the probable differences in aerosol distribution, the spectral discrepancies and the fact that the computation is cloud free.

The comparisons given above are intended only as a sampling of many more which could be made. The specific cases were selected with no a priori information regarding the extent of the agreement with the various χ^{-1} models obtained from the bugeye. It is highly unlikely that the cases selected offer the worst possible agreement with the present data. Thus there is a high probability that many of the angular reflectance models examined may not be generally representative of their respective, similarly described target types. Differences in the spectral bandpass of the measurement and the altitude at which the data were taken have been invoked as possible explanations for lack of

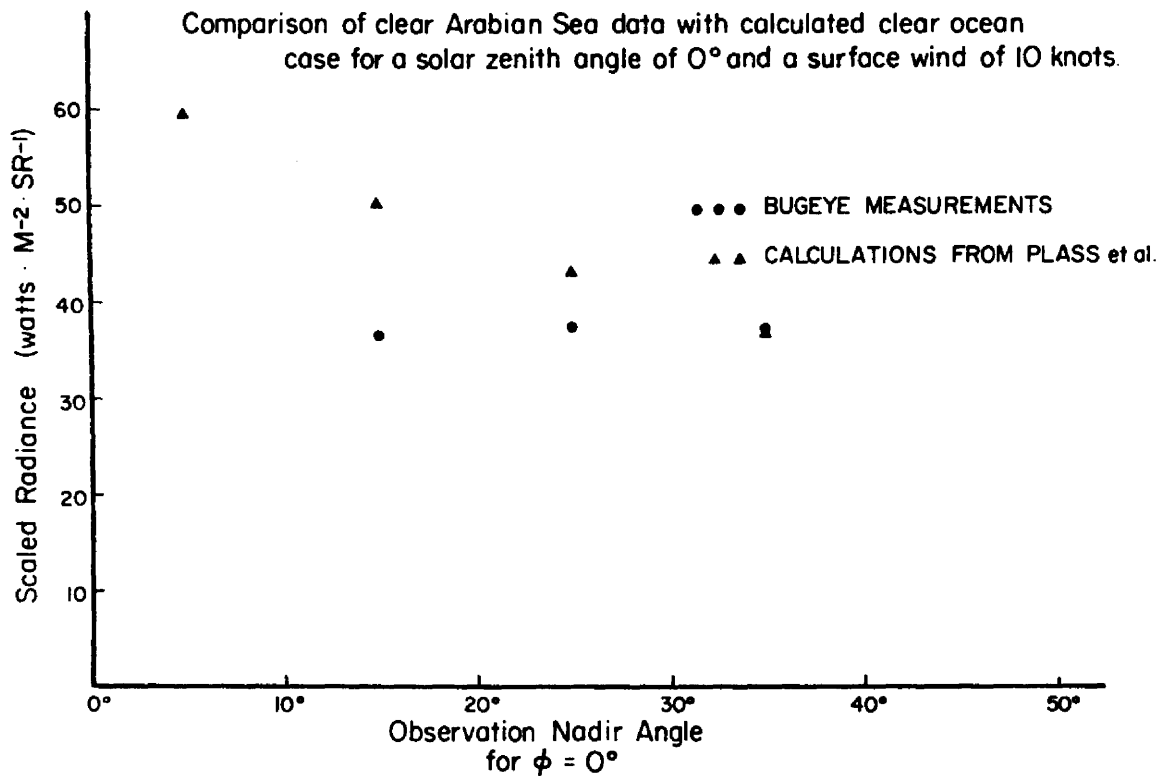


Figure 21a. A comparison between normalized radiances reflected from the clear Arabian Sea measured by the bugeye for a $0-10^\circ$ solar zenith angle range and a calculation of the same quantity by Plass and Kattawar.

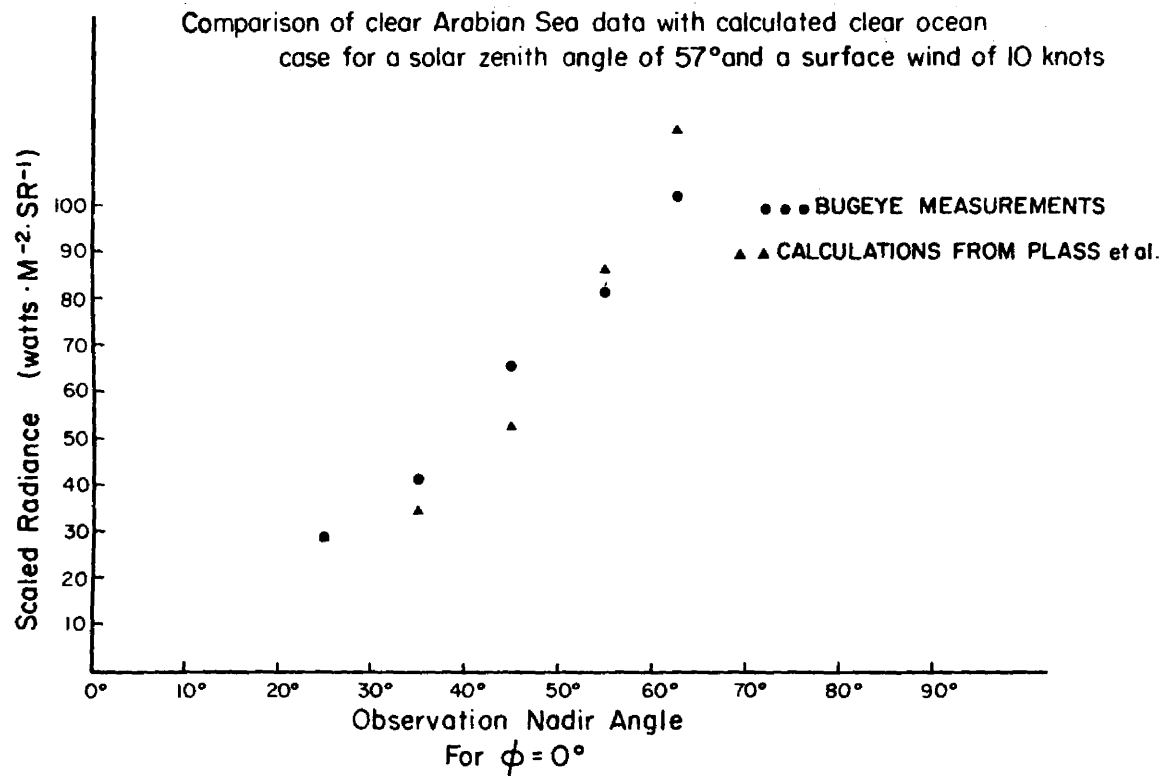


Figure 21b. A comparison between normalized radiances reflected from the clear Arabian Sea measured by the bugeye for a 50-60° solar zenith angle range and a calculation of the same quantity by Plass and Kattawar.

agreement between the measured patterns. Most of the disagreement, however, almost certainly results from the natural variability in the radiances reflected from the earth-atmosphere scenes. Because of the bugeye instrument's multi-sensor configuration it is possible to examine the nature of this variability for the atmospheric scenes studied during the experiment. This discussion is included in Section 4.2.

4.0 IMPLICATIONS CONCERNING THE APPLICATION OF ANGULAR REFLECTANCE MODELS ON A REGIONAL BASIS

Having obtained the average angular reflectance models over various atmospheric scene types one could proceed to apply the various models to satellite radiance measurements and compile reflected flux densities. Before making such casual use of the models some note should be made concerning the limitations of the models. Considerations relating to the spectral characteristics and spatial convergence behavior are given below.

4.1 Spectral Considerations

It has been pointed out in several instances that the spectral response of the bugeye photodiode may have resulted in angular reflectance characteristics unique to some extent to the bugeye instrument. Ideally measurements would have been made over the 0.2 - 4.0 μm spectral region and the resulting χ^{-1} models would be most properly applied to radiance measurements in the same spectral interval. Because of the limited spectral response of these measurements and the temptation to apply the models to operational satellite data which are even more spectrally constrained (see Figure 22) some method of conversion is dictated. Smith et al. (1981) indicate that GOES-1 0.5 - 0.9 μm radiance measurements may be converted to GOES-1 0.3 - 4.0 μm broadband measurements by using simple linear regression coefficients which are target specific. They indicate r.m.s. errors in inferred reflectance of less than 1% using the simple model. A similar attempt was made to convert bugeye directional reflectance to the 0.3 - 3.0 μm directional reflectance measured by the Eppley instruments on the

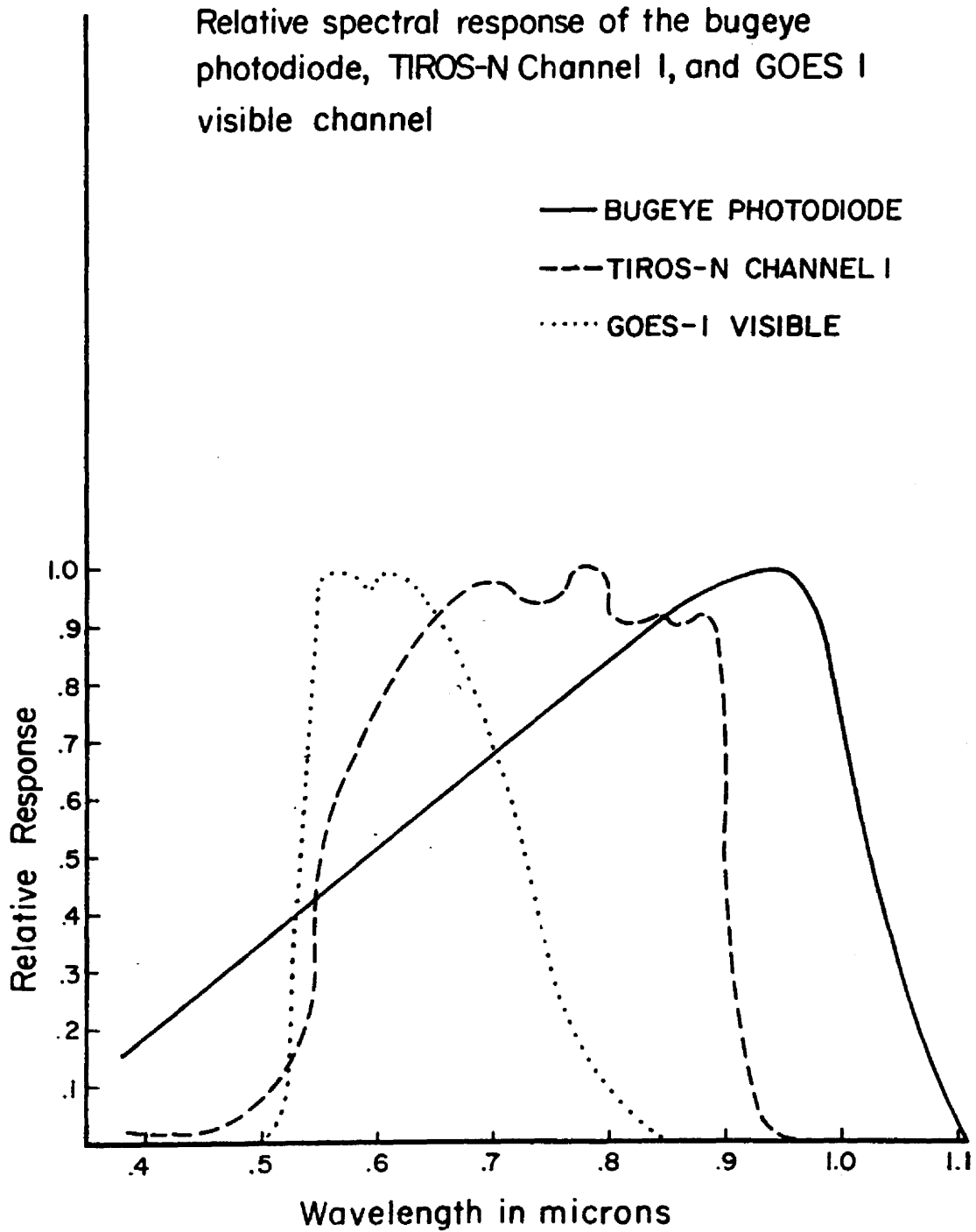


Figure 22. A comparison between the spectral bandpass of the photodiode used in the bug-eye with the spectral bandpasses of the TIROS-N and GOES-1 visible channels.

CV 990. In this case averages of the directional reflectance measured by both instruments were taken over a given scene type based on the total data set for the scene. Usually this resulted in computing a bug-eye directional reflectance from the set of average bug-eye radiances compiled at over 100 angular positions.

Table 3 lists the bug-eye and Eppley measured directional reflectance values for various scene types. Although there are not enough data to regress the directional reflectances one on the other for each scene type it is possible to construct a single linear regression model using all pairs regardless of scene type. The result of this regression is shown at the bottom of Table 3. The r.m.s. error figure is quite large and when computed separately by scene type indicates that errors of 10% in the inferred 0.3 - 3.0 μm reflectance are common using this scheme and that a 30% error may be incurred in a few cases. It must be reiterated that these comparisons are being made between average directional reflectance values collected over a region and that several target types for various solar zenith angles have been included. Thus, although Figure 6 indicates that a simple regression may be valid over a particular scene type a universal application is not advisable.

Given a conversion relation between 0.4 - 1.0 μm and 0.2 - 4.0 μm directional reflectance values one could conceivably construct similar relationships between the bug-eye reflectance measurements and those of the TIROS-N or GOES-1 channels. A two step transfer from operational reflectance values first to bug-eye directional reflectances and then to broadband directional reflectances might then be affected. Such a procedure, however, does not appear feasible at this stage. Thus,

Solar Zenith Angle Range	Desert		Ocean		Himalaya		Indian		Middle & Low Cloud		Altostratus	
	DR _B	DR _E	DR _B	DR _E	DR _B	DR _E						
0° - 10°	.26	.24	.04	.07			.15	.14	.25	.31		
10° - 20°	.26	.30	.04	.09	.22	.26	.13	.13	.23	.30	.19	.23
20° - 30°	.24	.28	.06	.09	.28	.32	.13	.19	.33	.41	.22	.38
30° - 40°	.26	.31	.05	.10			.12	.14	.19	.23	.26	.30
40° - 50°	.27	.32	.06	.09					.33	.41		
50° - 60°	.30	.35	.10	.11								
60° - 70°	.30	.38										
70° - 80°	.34	.48										

$$DR_E = 1.17 * DR_B + .015, \text{ Correlation coefficient} = .96, \text{ r.m.s. error} = .034$$

Table 3. The directional reflectance values measured by the bugeye and the Eppley 0.3 - 3.0 μm pyranometer for various scene types (top) and the linear regression relation between the directional reflectance values (bottom).

application of the present results to operational satellite data must rely upon the approximate similitude of the χ^{-1} patterns among the various filter functions involved and an independent satellite calibration. The assumption that the similitude among χ^{-1} functions is more reliable than correlation among the filtered reflectances may be examined if only approximately. First, a filtered bidirectional reflectance (BDR) is defined as

$$\text{BDR}_i(\theta, \phi) = \frac{\int_{\lambda} N(\theta, \phi, \lambda) f_i(\lambda) d\lambda}{\cos z \cdot \int_{\lambda} E_o(\lambda) f_i(\lambda) d\lambda},$$

where $f_i(\lambda)$ represents the i th filter function, $E_o(\lambda)$ the incident solar radiation and the remaining symbols retain their previous meanings. The corresponding directional reflectance is given by,

$$\begin{aligned} \text{DR}_i &= \int_{\Omega} \text{BDR}_i(\theta, \phi) \cos\theta d\Omega \\ &= \frac{\int_{\Omega} \left(\int_{\lambda} N(\theta, \phi, \lambda) f_i(\lambda) d\lambda \right) \cos\theta d\Omega}{\cos z \int_{\lambda} E_o(\lambda) f_i(\lambda) d\lambda}. \end{aligned}$$

The corresponding angular reflectance model $\chi_i^{-1}(\theta, \phi)$ is given by

$$\chi_i^{-1}(\theta, \phi) = \frac{\pi \cdot \int_{\lambda} N(\theta, \phi, \lambda) f_i(\lambda) d\lambda}{\int_{\Omega} \left(\int_{\lambda} N(\theta, \phi, \lambda) f_i(\lambda) d\lambda \right) \cos\theta d\Omega}.$$

If it is assumed that the radiance $N(\theta, \phi, \lambda)$ may be approximated as the product of a function of angle $A(\theta, \phi)$ and a function of wavelength $W(\lambda)$, then the expressions above reduce to:

$$\text{BDR}_i(\theta, \phi) = \frac{A(\theta, \phi) \bar{W}_i \Delta\lambda_i}{\cos z \cdot \int_{\lambda} E_o(\lambda) f_i(\lambda) d\lambda}$$

$$\text{DR}_i = \frac{\bar{W}_i \Delta\lambda_i \int_{\Omega} A(\theta, \phi) \cos\theta d\Omega}{\cos z \cdot \int_{\lambda} E_o(\lambda) f_i(\lambda) d\lambda},$$

and

$$\chi_i^{-1}(\theta, \phi) = \frac{\pi \cdot \bar{W}_i \Delta\lambda_i A_i(\theta, \phi)}{\bar{W}_i \Delta\lambda_i \int_{\Omega} A(\theta, \phi) \cos\theta d\Omega}$$

$$= \frac{\pi \cdot A(\theta, \phi)}{\int_{\Omega} A(\theta, \phi) \cos\theta d\Omega},$$

where \bar{W}_i represents the filtered mean of $W_i(\lambda)$. Under these assumptions χ_i^{-1} is no longer dependent on the type of filter function used in the measurements. However correlations among BDR values or DR values still depend on the extent to which a relationship exists among the \bar{W}_i weighted means.

4.2 Spatial convergence of the angular reflectance models

If angular reflectance models are to be used to infer flux densities on a regional basis (250 - 1000 km) it is important to assess how

rapidly the models converge to the respective mean patterns. An examination of the rate of the convergence is made possible because of the multi-sensor design of the bugeye instruments. The convergence characteristics of the various models were examined by performing the following numerical experiment. For a particular target scene type an angular array of average normalized radiances was compiled subject to the same maximum-minimum criteria described in Section 2.3. The instantaneous radiance measurements were normalized by the upwelling (0.3 - 3.0 μm) irradiance which was simultaneously measured by the Eppley pyranometer. The resulting angular array is thus proportional to the average of a large number of instantaneous samples of the χ^{-1} pattern. The result is an unsmoothed, partially filled, non-symmetric field which is the most representative version of an angular model for the specific target which can be obtained from the present data. Having established the mean pattern, the sequence of measurements is then entered at a randomly selected point and a running mean computation is begun at each of the angular positions for which at least 30 data points exist for examination. The computation continues and establishes the number of points required at each angular position such that the fractional difference between the running mean and the true mean is less than 5%. The number of data points needed to achieve this error threshold is recorded for each angular point. This process was repeated for 100 different random entries into the data set and the average and standard deviation of the number of points needed for convergence computed at each angular position. Finally a number weighted mean of the latter two quantities was taken over all angular positions as an indication of the convergence properties of the data set as a whole. These

results are shown in Table 4 for each scene type. Also shown in the last column is an equivalent distance corresponding to the length of the total data sample.

In general the results of Table 4 support the premise that angular reflectance models are a useful tool for diagnosing the reflected flux density over a fairly large region. The indications are that on the average a maximum from 5-28% of the total region must be sampled in order to insure that the normalized radiance measured at a particular angular position is representative of the average of the same quantity taken over the region as a whole. The standard deviation of this number taken over the 100 trials does indicate however that in most cases (except for the desert and ice) the convergence fraction is quite variable, and assuming a normal distribution of the convergence figures, high confidence of convergence requires over half of the data set to be sampled.

It must be pointed out here that it is difficult to avoid biases in the results of Table 4 due to samples collected over small spatial scales, since the comparison was made for every angular position at which at least 30 measurements had been made. No attempt was made to differentiate between cases in which the measurements were taken consecutively over a small space scale and those cases in which the measurements were taken non-consecutively over a much larger space scale. The number weighting of the various fractional convergence values certainly diminishes the possible effect of such a bias but in order to insure that this influence is minimized, the mean fractional values should certainly not be used to infer convergence over space scales larger than the equivalent distance given in the table.

Scene Type	Solar Zenith Angle Range	Mean Fraction of data needed for convergence	Standard Deviation of the fraction needed for convergence	Equivalent Length in km of the entire data set
Desert	0° - 10°	0.03	0.04	400
"	10° - 20°	0.04	0.06	1100
"	20° - 30°	0.03	0.04	700
"	30° - 40°	0.09	0.11	1000
"	40° - 50°	0.01	0.02	1200
"	50° - 60°	0.02	0.03	1000
"	60° - 70°	0.04	0.07	675
"	70° - 80°	0.04	0.05	500
Himalaya	10° - 20°	0.18	0.20	220
"	20° - 30°	0.22	0.21	100
Clear Ocean	0° - 10°	0.14	0.14	800
" "	10° - 20°	0.17	0.19	1200
" "	20° - 30°	0.21	0.21	1100
" "	30° - 40°	0.23	0.22	900
" "	40° - 50°	0.13	0.16	1200
" "	50° - 60°	0.20	0.18	600
Indian Subcontinent	0° - 10°	0.09	0.09	250
" "	10° - 20°	0.13	0.13	275
" "	20° - 30°	0.05	0.07	450
" "	30° - 40°	0.04	0.06	400
Altostratus	20° - 30°	0.28	0.23	175
"	30° - 40°	0.12	0.14	275
"	40° - 50°	0.19	0.20	150
Broken Cloud	0° - 10°	-	-	-
" "	10° - 20°	0.14	0.17	175
" "	20° - 30°	0.19	0.20	150
" "	30° - 40°	0.16	0.19	100
" "	40° - 50°	0.28	0.23	25
Ice	50° - 60°	0.03	0.04	500

Table 4. The mean and standard deviation of the fraction of the total data sample required for convergence to within 5% of the mean angular reflectance model for the various scene types.

These results may be taken one step further, to search for angular viewing coordinates which display minimum convergence fractions. This exercise was carried out for all of the angular models presented in this study. The results may be briefly summarized by stating that no angular regions were found which displayed the preferred convergence statistics. Figures 23-29 are presented which show the fractions of the data samples required for convergence as a function of observation nadir and relative solar azimuth. These plots are typical of those which pertain to the remainder of the angular models. It should be noted that there is no reason to expect continuity in the convergence arrays as evidenced by the contour behavior across the principal plane. The convergence arrays were finally averaged with respect to the relative azimuth angle to examine their variation with nadir angle. Only in a few instances did a particular nadir angle exhibit convergence fractions which deviated by more than a few hundredths from the fractions listed in Table 4. Thus, there appears to be little reason to anticipate the existence of angular positions at which the angular reflectance models show preferred spatial convergence behavior.

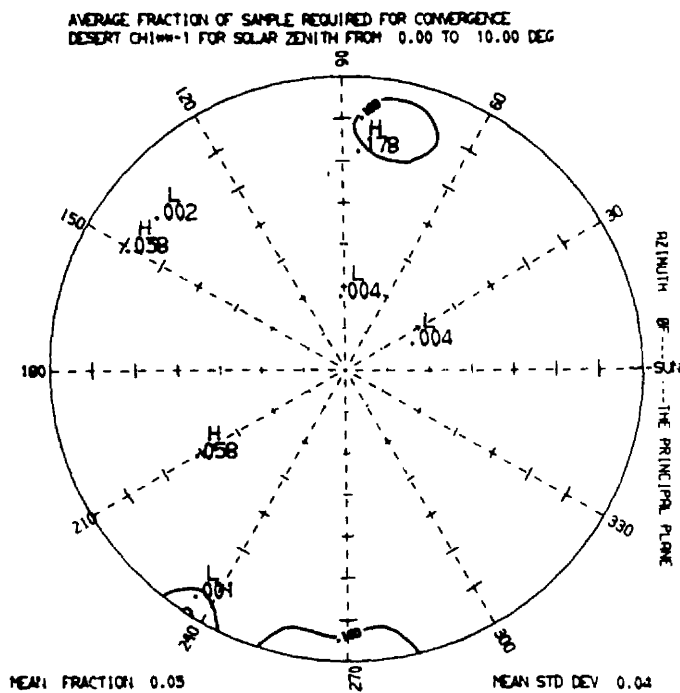


Figure 23. The fraction of the total data sample required for convergence to within 5% of the mean displayed as a function of observation nadir and relative azimuth for the 0-10° solar zenith angle desert case.

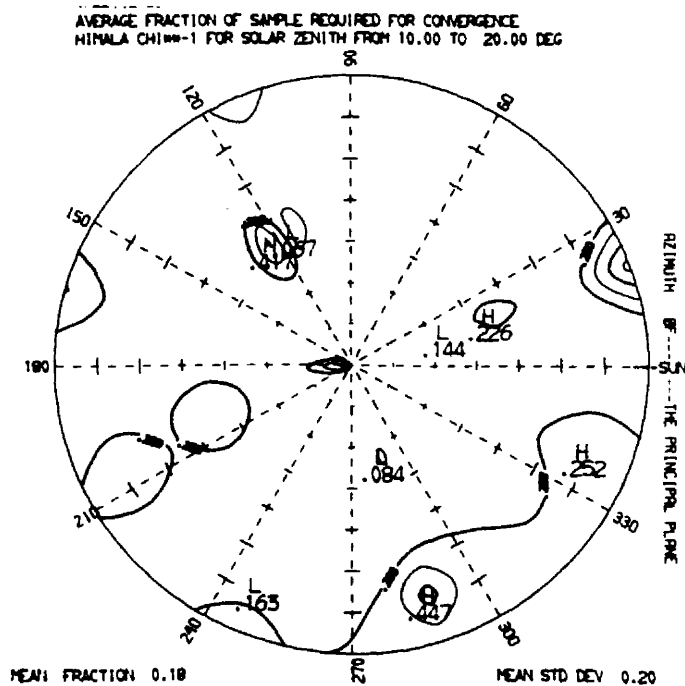


Figure 24. The fraction of the total data sample required for convergence to within 5% of the mean displayed as a function of observation nadir and relative azimuth for the 10-20° solar zenith angle Himalaya case.

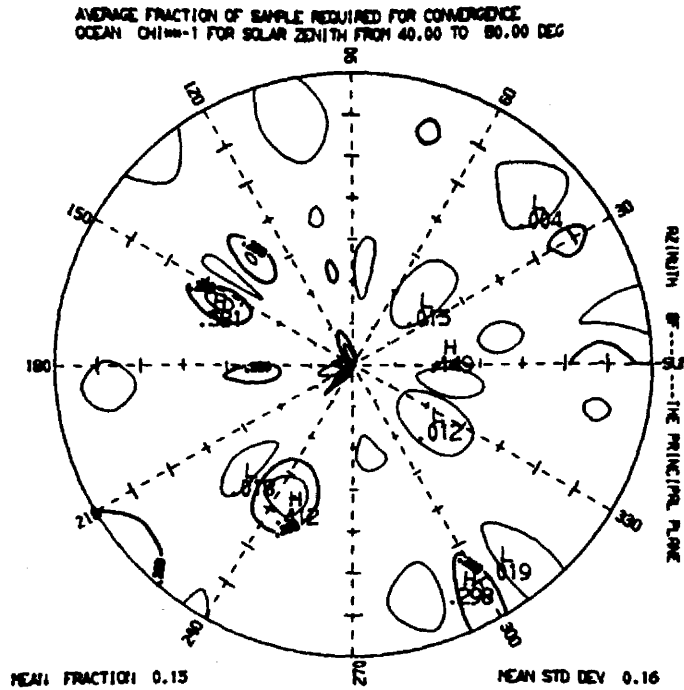


Figure 25. The fraction of the total data sample required for convergence to within 5% of the mean displayed as a function of observation nadir and relative azimuth for the 40-50° solar zenith angle clear ocean case.

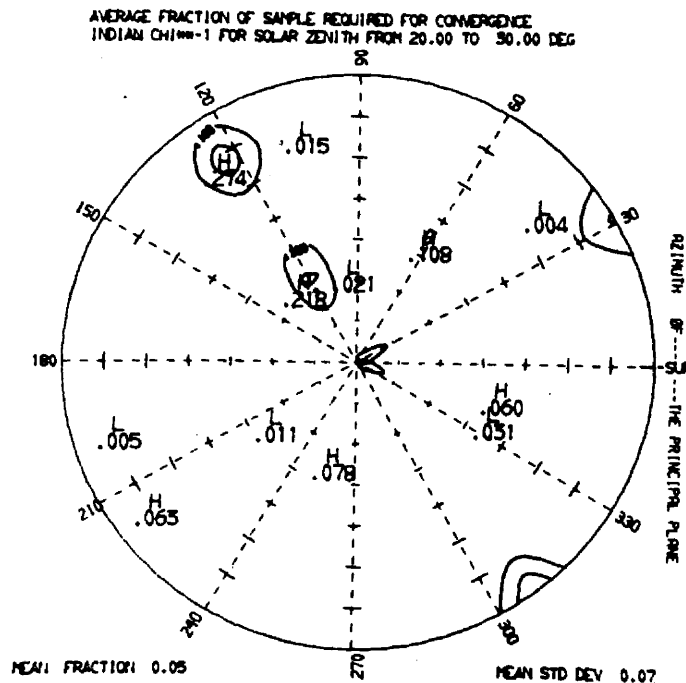


Figure 26. The fraction of the total data sample required for convergence to within 5% of the mean displayed as a function of observation nadir and relative azimuth for the 20-30° solar zenith angle Indian subcontinent case.

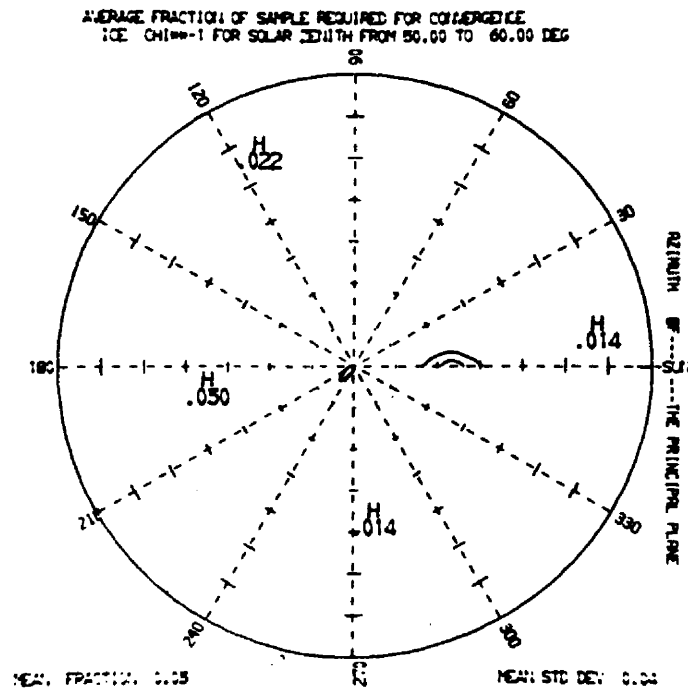


Figure 29. The fraction of the total data sample required for convergence to within 5% of the mean displayed as a function of observation nadir and relative azimuth for the 50-60° solar zenith angle ice field case.

4.3 Optimal Viewing Angles for Flux Density Inference Based on Application of Angular Models in a 1, 2 or 3 Satellite System

The previous section concluded that the rate of spatial convergence displayed by the measured radiances was essentially independent of angular coordinates. This conclusion was based on an examination of the behavior of the cumulative or running mean of the normalized radiances as a function of angle. There is yet another criterion which may be invoked to categorize a particular observation coordinate as optimal, namely the absolute magnitude of the error between the instantaneously inferred reflected flux density and the scene average of the same quantity. This absolute difference is related to the variance of the radiances evaluated over the scene and the variation of the absolute error as a function of observation angle is useful under the following circumstances. First, if inferences of reflected flux densities must be made over a space scale smaller than those established in the previous section it would be preferable to utilize radiances for which the magnitude of the absolute error is minimized. Second, if more than one observation platform is available, negative correlations may exist between or among the errors in the inferences made at two or three angular coordinates which may dictate preferences in pairs or triplets of nadir or relative azimuth positions.

In order to examine the possibility that optimum angular coordinates exist under these circumstances the following numerical experiment was performed. The mean χ^{-1} pattern was obtained for a particular reflecting target in a specified zenith angle range. The data were left in an asymmetric form so that taken over the entire scene, $\bar{E} = \bar{N}(\theta, \phi, z) \cdot \bar{\chi}(\theta, \phi, z) \cdot \pi$, where the overbar indicates taking the

scene average. The r.m.s. deviation $\delta(\theta, \phi, z)$ between \bar{E} and $\hat{E}(\theta, \phi, z)$ was evaluated using all measurements acquired over the scene, where $\hat{E}(\theta, \phi, z)$ is the reflected flux density inferred from the instantaneous radiance measurement $N(\theta, \phi, z)$ through the mean $\bar{\chi}(\theta, \phi, z)$ model. The deviations were analyzed in the following manner primarily with geostationary satellite applications in mind. For a particular type of surface the deviations were averaged over all relative azimuth and solar zenith angles to produce nadir dependent deviations δ_θ . Likewise an average over all nadir and solar zenith angles was taken to form deviations δ_ϕ which depend only on the relative azimuth angle. For the case of an inference made from a pair of satellites the pertinent statistic is the deviation between the actual scene averaged reflected flux density and the average of the inferences made by the two observations $[\hat{E}(\theta_1, \phi_1, z) + \hat{E}(\theta_2, \phi_2, z)]/2$. This r.m.s. deviation is denoted by $\delta(\theta_1, \theta_2, \phi_1, \phi_2, z)$; its value when averaged over all pairs of relative azimuths $\{\phi_i, \phi_j\}$ and over all solar zenith angles is denoted by $\delta_{\theta_i, \theta_j}$, and when averaged over all pairs of nadir angles $\{\theta_1, \theta_2\}$ and all solar zenith angles by δ_{ϕ_1, ϕ_2} . In a similar way it is possible to construct the statistics $\delta_{\theta_i, \theta_j, \theta_k}$ and $\delta_{\phi_i, \phi_j, \phi_k}$ for the case of an inference made from three satellites.

Although the data were originally stratified into 10° nadir and relative azimuth resolutions, for practical reasons three nadir stratifications were considered, $0^\circ \leq \theta < 20^\circ$, $20^\circ \leq \theta < 50^\circ$ and $50^\circ \leq \theta < 70^\circ$ hereafter referred to as low (L), medium (M) and high (H) regimes. The original 36 relative azimuth stratifications were degraded to six 60° sectors; the first sector was centered on the solar azimuth so that it extends from -30° to $+30^\circ$ in relative azimuth and

the second through sixth sectors were numbered in a clockwise sense looking down on the scene. When calculating the values which apply to the multiple satellite system, combinations of inferences which involve identical pairs or triplets of a particular observation angle (nadir or azimuth) on the 10° resolution scale were not allowed. Thus, it is possible to calculate a value for δ_{LL} comprised of data taken at $0 - 10^\circ$ and $10 - 20^\circ$ nadir angles but δ_{LLL} is excluded since this would require a pairing of one of the nadir ranges $0 - 10^\circ$ or $10 - 20^\circ$. Note that δ_{MMM} is allowed which would be comprised of the average of the inferences made at $20 - 30^\circ$, $30 - 40^\circ$ and $40 - 50^\circ$.

The results of the analysis are shown in Figures 30 through 36 for the various types of reflecting surfaces. Table 5 presents the average values of the deviations made with a one, two or three satellite system. The left half of each of the figures depicts the behavior of the deviations with nadir and the right side shows the azimuthal dependencies. All values are presented as percentages of the $0.3 - 3.0 \mu\text{m}$ reflected flux density. The order of the inference, i.e. the number of different angles involved in the inference increases from the top to the bottom of each figure. Single position deviations are represented as a row vector, double angle deviations by a symmetric array and triple position deviations by the 'upper' ($i \geq j, k$) portion of a symmetric three dimensional array. Values which are not allowed because of duplication of the indices at the 10° resolution scale are indicated with a dash (-), and in cases for which insufficient data exists to perform the calculation the letter M is used to indicate the missing entry.

Deviations between measured and inferred reflected flux density for the desert

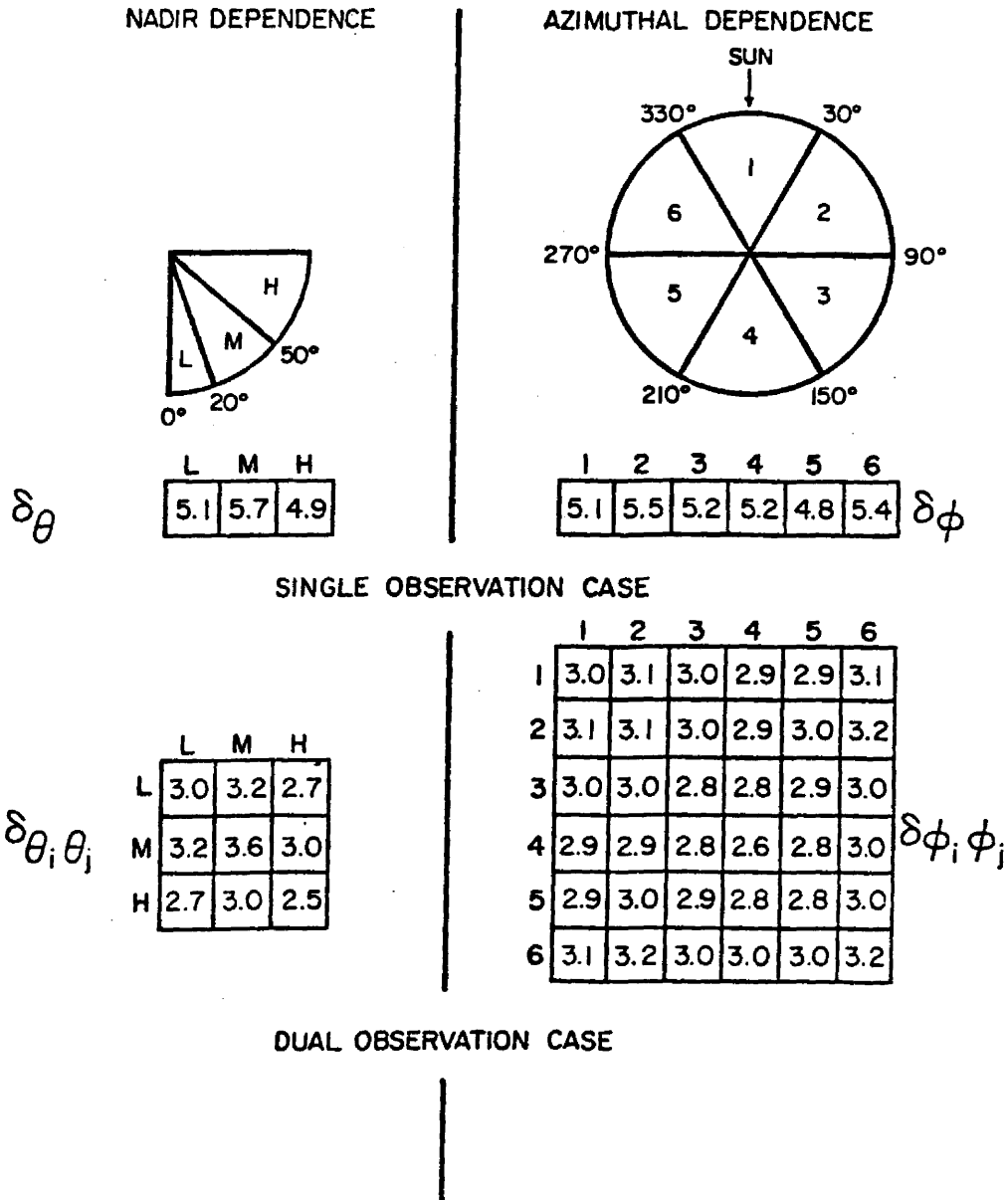
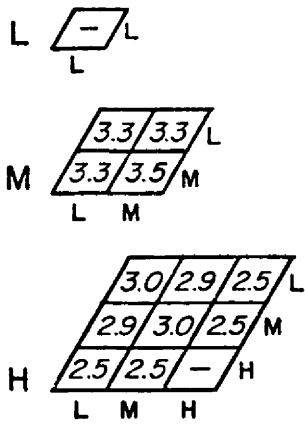


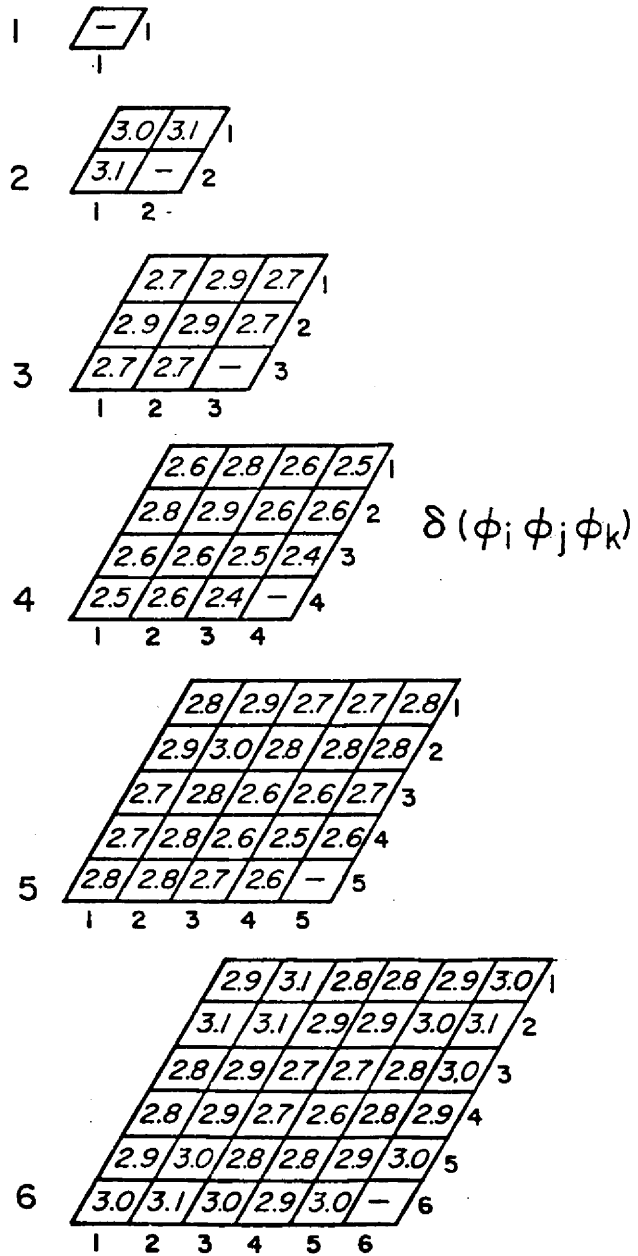
Figure 30. The nadir and azimuthal dependence of the r.m.s. deviations between average measured 0.3 - 3.0 μm reflected flux density and the inference of the same quantity made from 1, 2 or 3 instantaneous radiance measurements over the desert expressed as a percent of the average reflected flux density.

NADIR DEPENDENCE



$$\delta(\theta_i \theta_j \theta_k)$$

AZIMUTHAL DEPENDENCE



TRIPLE OBSERVATION CASE

Figure 30. (Continued).

Deviations between measured and inferred reflected flux density for the Himalayas

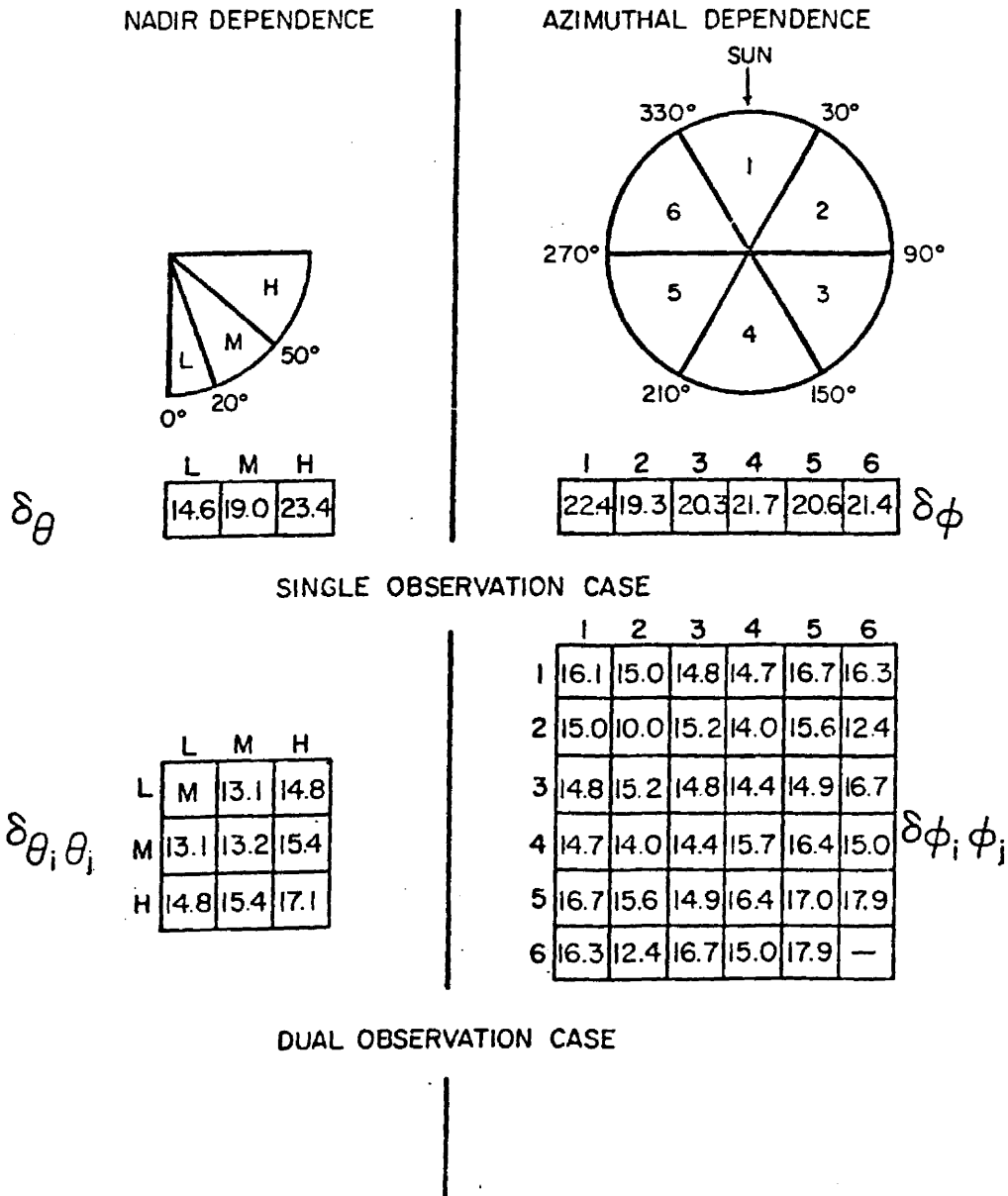
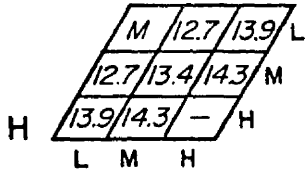
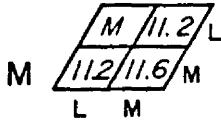


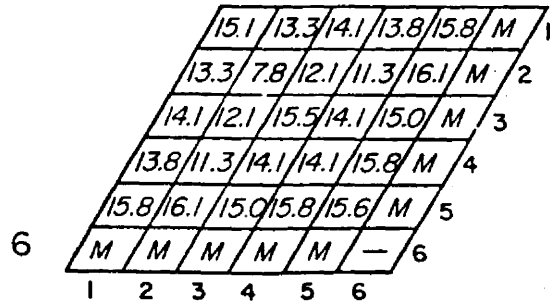
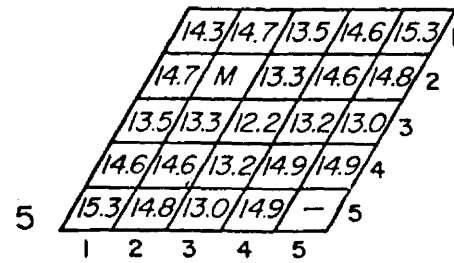
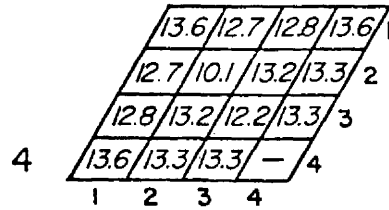
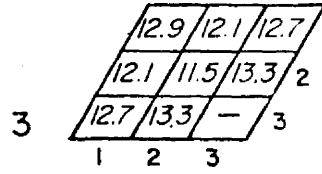
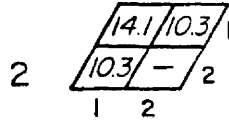
Figure 31. The nadir and azimuthal dependence of the r.m.s. deviations between average measured 0.3 - 3.0 μm reflected flux density and the inference of the same quantity made from 1, 2 or 3 instantaneous radiance measurements over the Himalayas expressed as a percent of the averaged reflected flux density.

NADIR DEPENDENCE



$$\delta(\theta_i, \theta_j, \theta_k)$$

AZIMUTHAL DEPENDENCE



$$\delta(\phi_i, \phi_j, \phi_k)$$

TRIPLE OBSERVATION CASE

Figure 31. (Continued).

Deviations between measured and inferred reflected flux density for the ocean

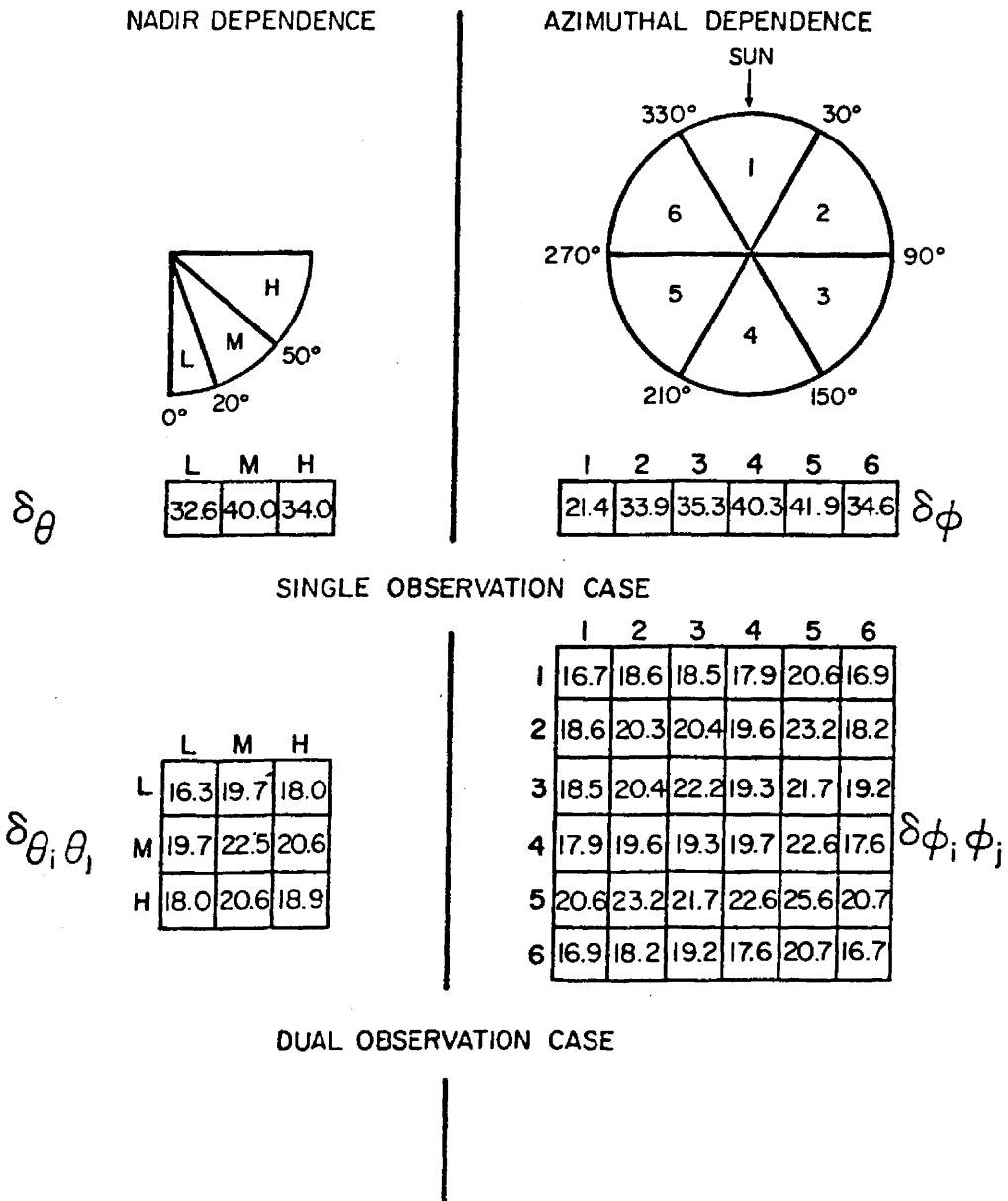
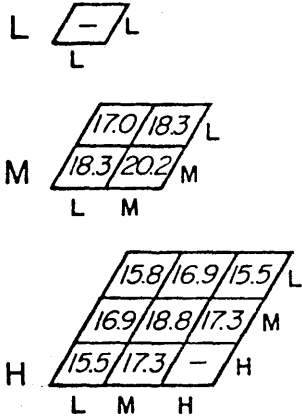


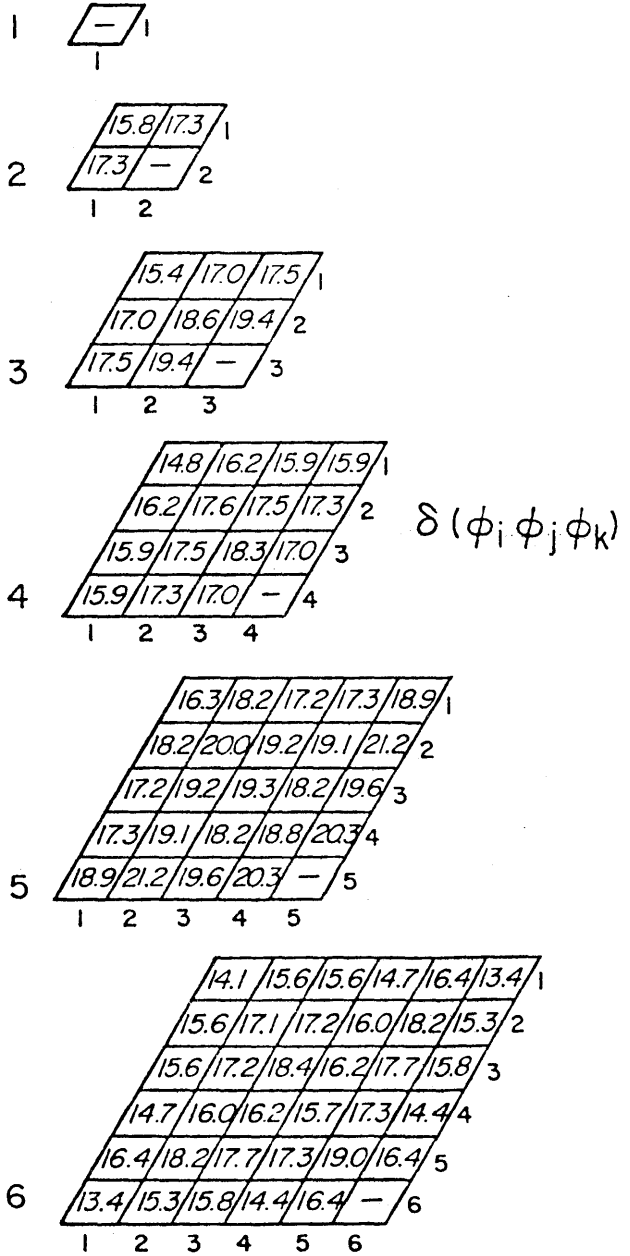
Figure 32. The nadir and azimuthal dependence of the r.m.s. deviations between average measured 0.3 - 3.0 μm reflected flux density and the inference of the same quantity made from 1, 2 or 3 instantaneous radiance measurements over the clear ocean expressed as a percent of the average reflected flux density.

NADIR DEPENDENCE



$$\delta(\theta_i, \theta_j, \theta_k)$$

AZIMUTHAL DEPENDENCE



$$\delta(\phi_i, \phi_j, \phi_k)$$

TRIPLE OBSERVATION CASE

Figure 32. (Continued).

Deviations between measured and inferred reflected flux density for the Indian subcontinent

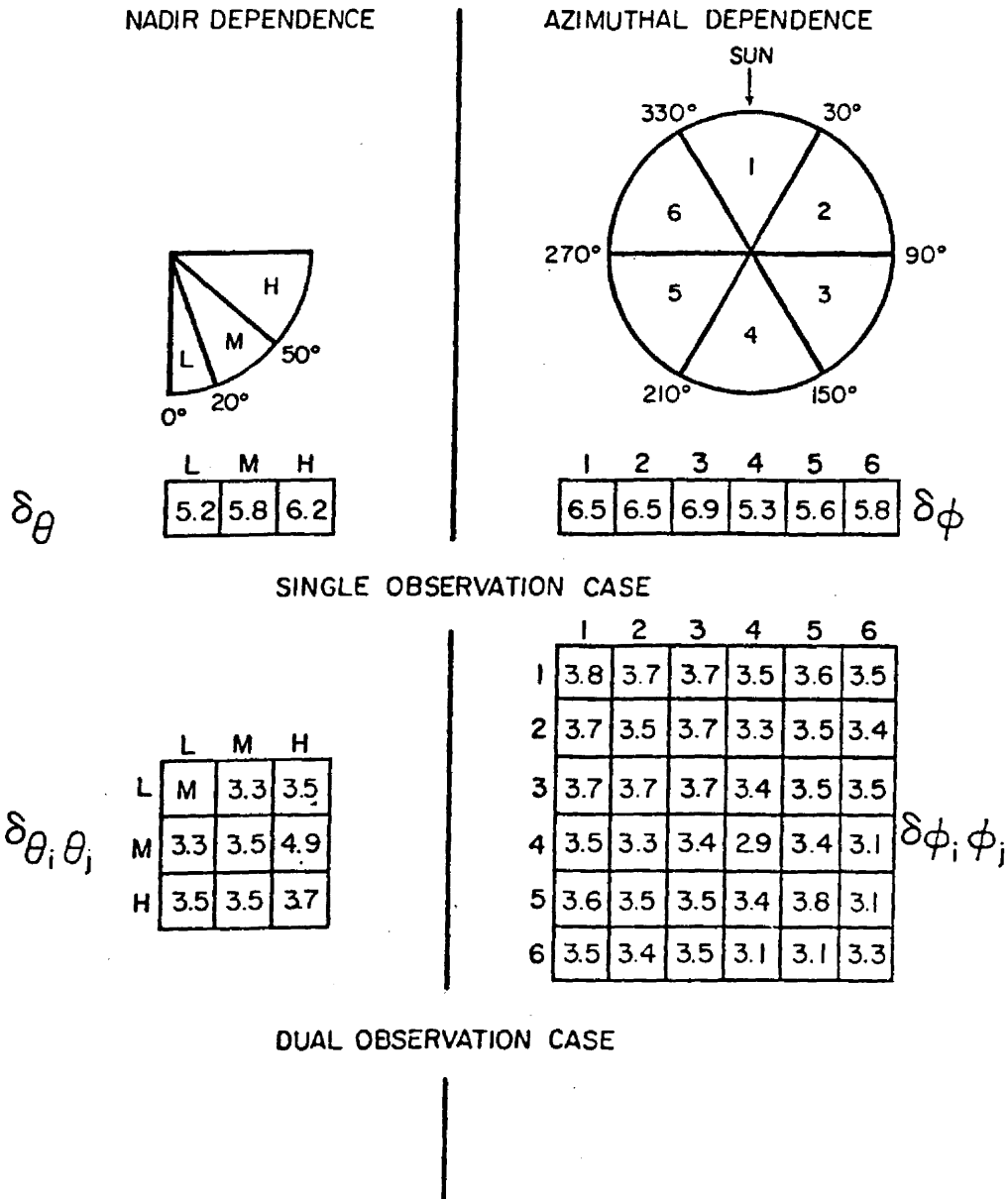
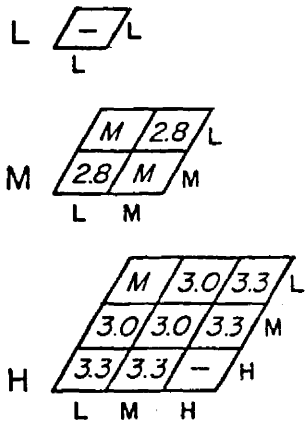


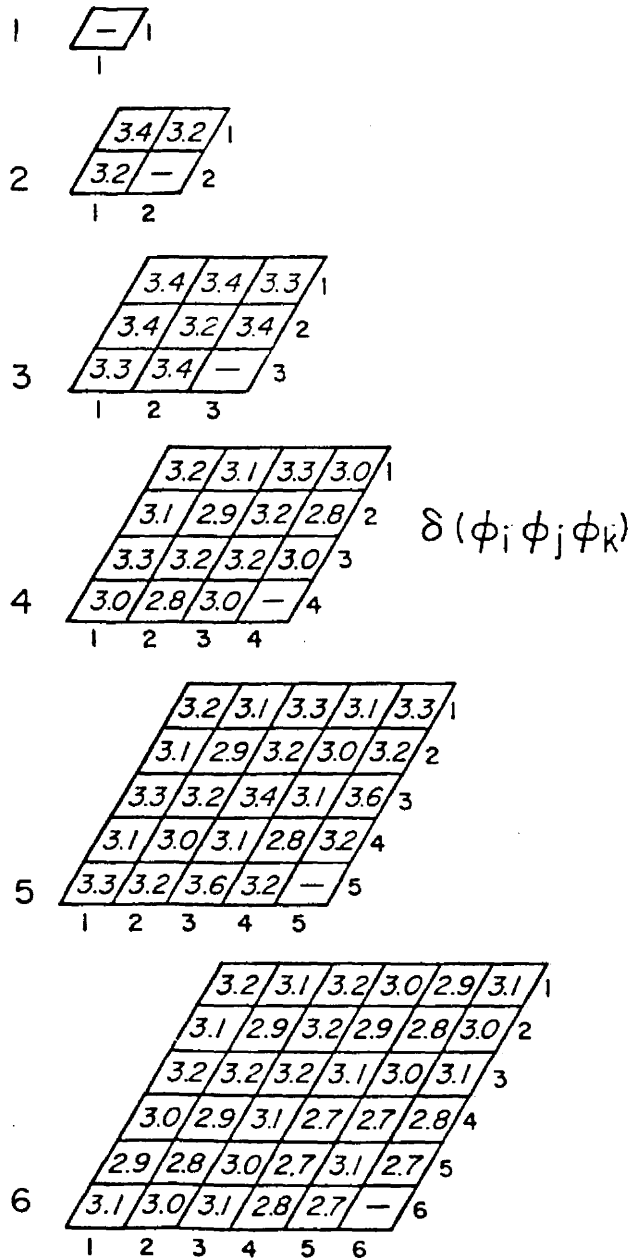
Figure 33. The nadir and azimuthal dependence of the r.m.s. deviations between average measured 0.3 - 3.0 μm reflected flux density and the inference of the same quantity made from 1, 2 or 3 instantaneous radiance measurements over the Indian Subcontinent expressed as a percent of the average reflected flux density.

NADIR DEPENDENCE



$$\delta(\theta_i \theta_j \theta_k)$$

AZIMUTHAL DEPENDENCE



$$\delta(\phi_i \phi_j \phi_k)$$

TRIPLE OBSERVATION CASE

Figure 33. (Continued).

Deviations between measured and inferred reflected flux density for the cloud I case

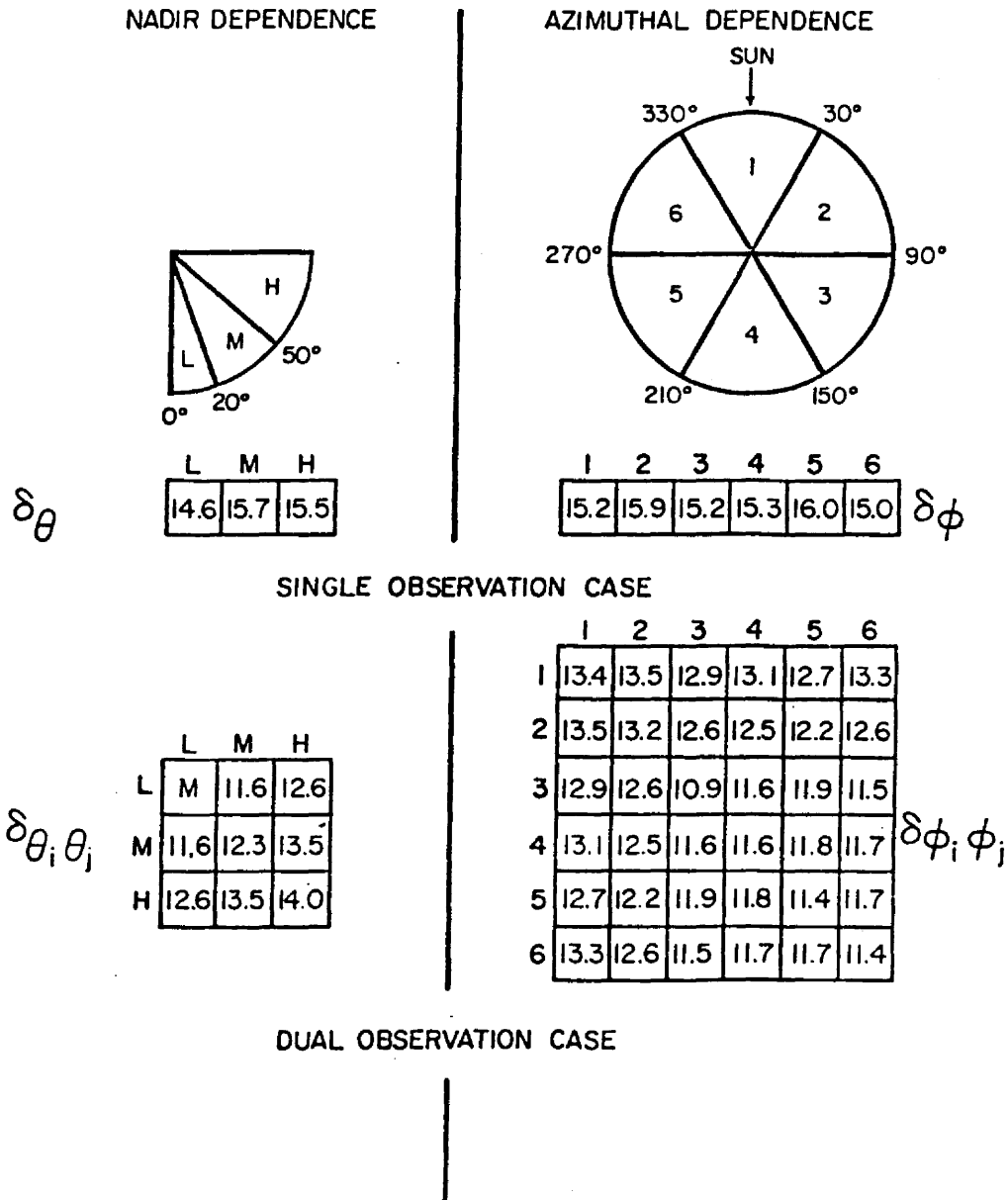
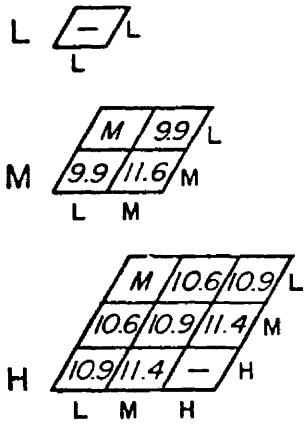


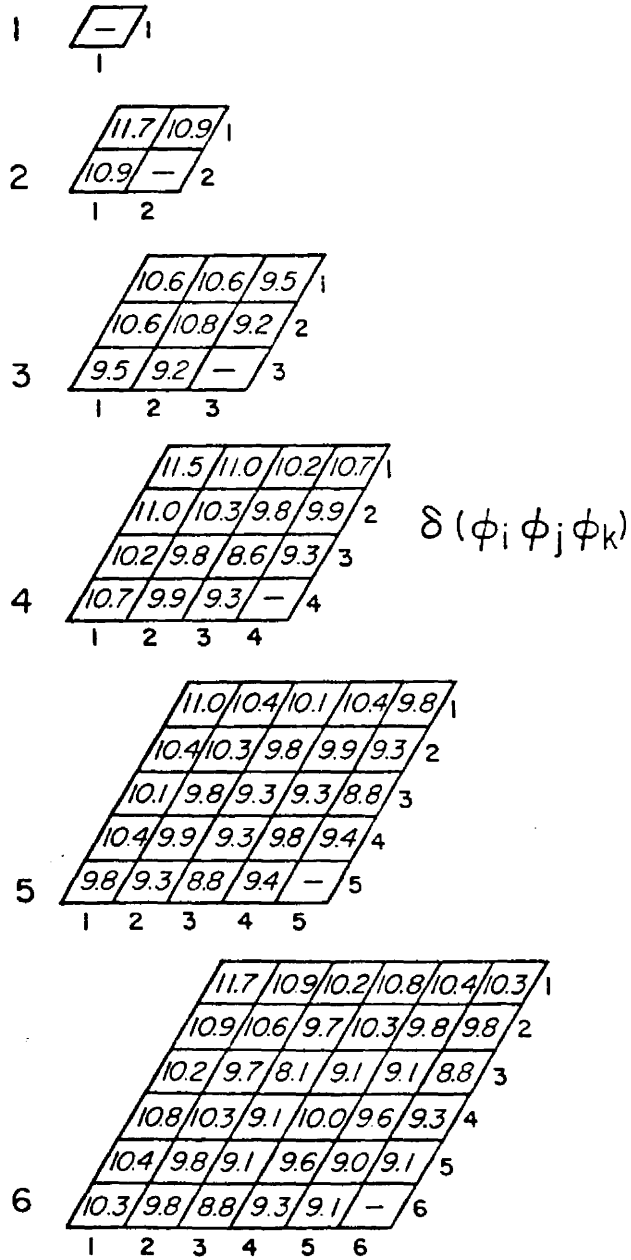
Figure 34. The nadir and azimuthal dependence of the r.m.s. deviations between average measured 0.3 - 3.0 μm reflected flux density and the inference of the same quantity made from 1, 2 or 3 instantaneous radiance measurements over middle and low level clouds expressed as a percent of the average reflected flux density.

NADIR DEPENDENCE



$$\delta(\theta_i, \theta_j, \theta_k)$$

AZIMUTHAL DEPENDENCE



$$\delta(\phi_i, \phi_j, \phi_k)$$

TRIPLE OBSERVATION CASE

Figure 34. (Continued).

Deviations between measured and inferred reflected flux density for the cloud 2 case

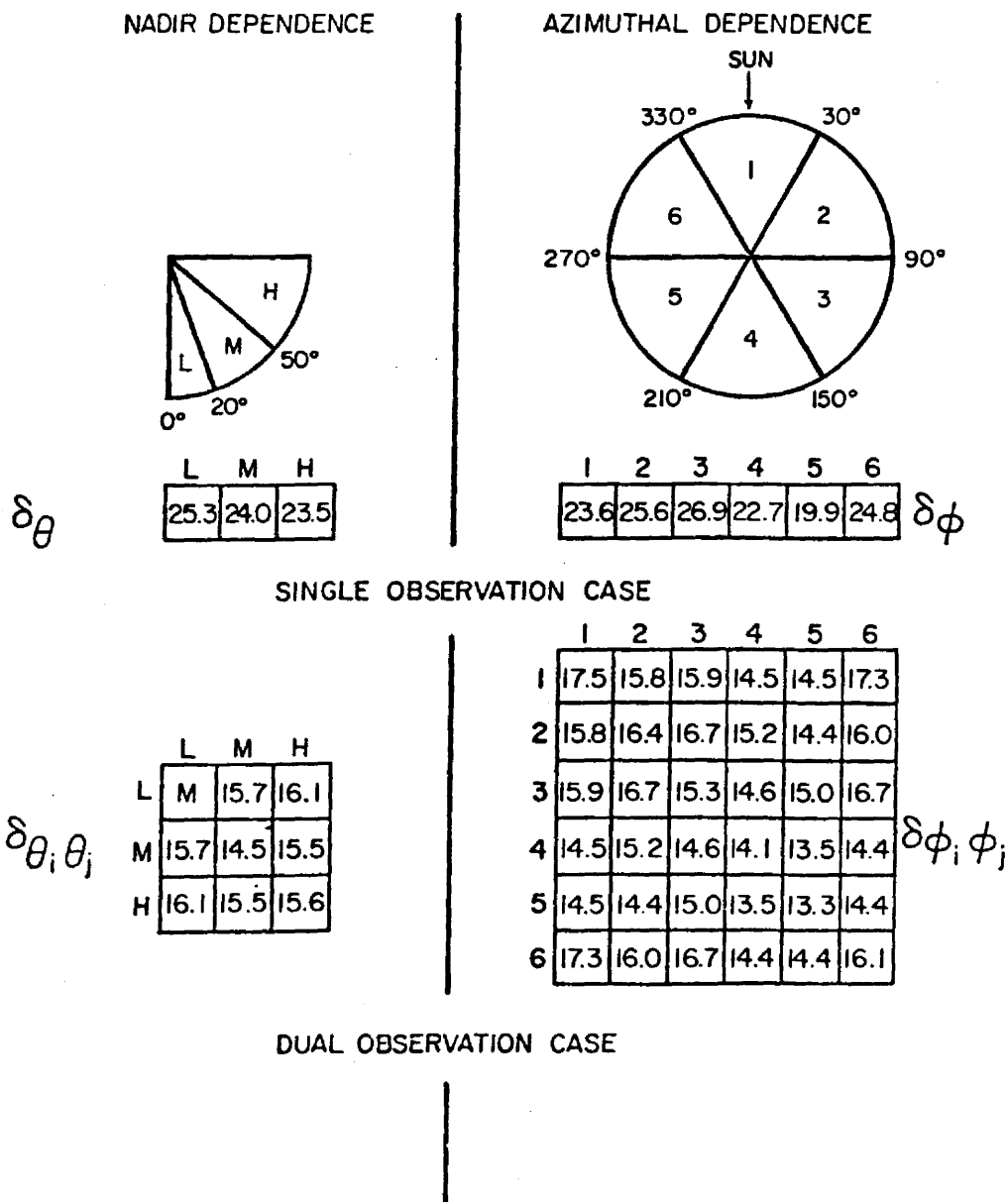
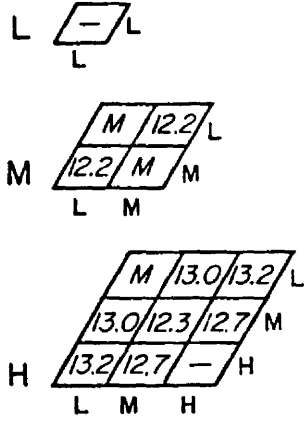


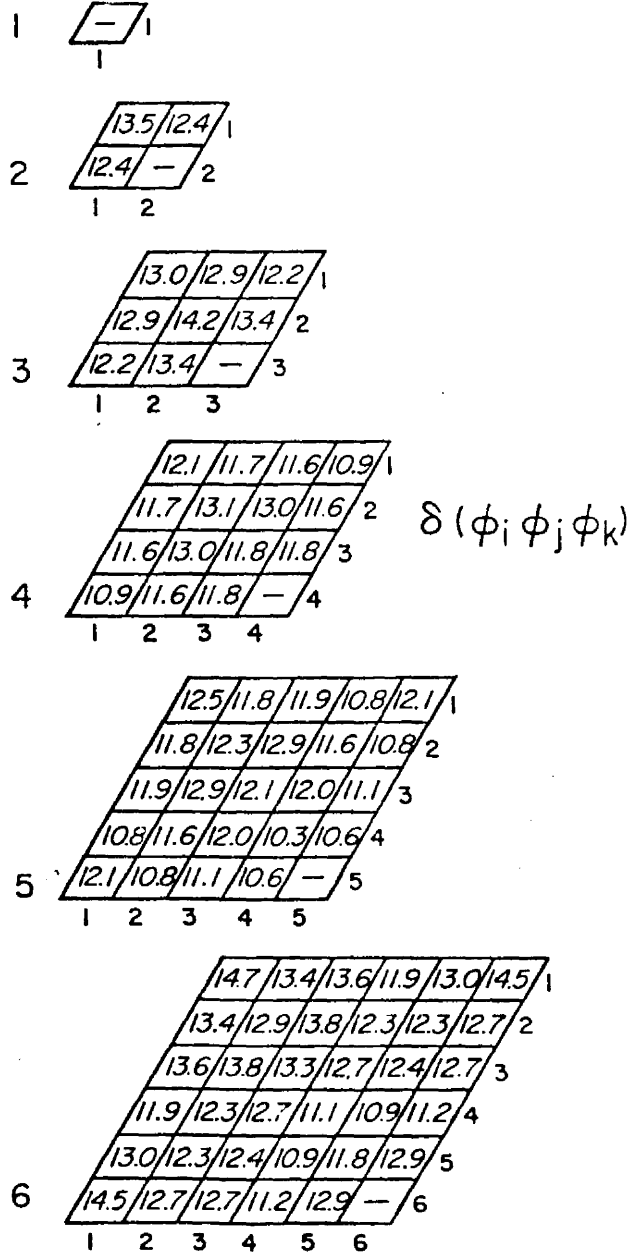
Figure 35. The nadir and azimuthal dependence of the r.m.s. deviations between averaged measured 0.3 - 3.0 μm reflected flux density and the inference of the same quantity made from 1, 2 or 3 instantaneous radiance measurements over altostratus clouds expressed as a percent of the average reflected flux density.

NADIR DEPENDENCE



$$\delta(\theta_i \theta_j \theta_k)$$

AZIMUTHAL DEPENDENCE



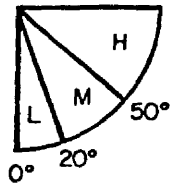
$$\delta(\phi_i \phi_j \phi_k)$$

TRIPLE OBSERVATION CASE

Figure 35. (Continued).

Deviations between measured and inferred reflected flux density for ice

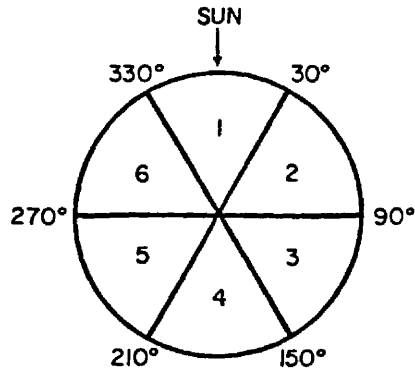
NADIR DEPENDENCE



L	M	H
6.3	8.0	6.1

δ_θ

AZIMUTHAL DEPENDENCE



1	2	3	4	5	6
9.2	6.0	5.7	6.8	6.3	6.7

δ_ϕ

SINGLE OBSERVATION CASE

	L	M	H
L	M	3.5	3.1
M	3.5	4.2	3.4
H	3.1	3.4	3.0

$\delta_{\theta_i, \theta_j}$

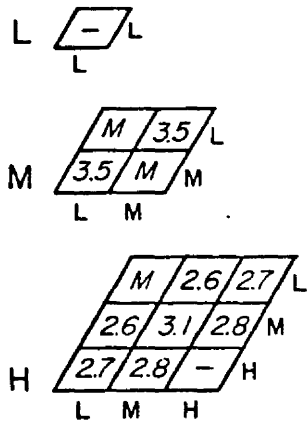
	1	2	3	4	5	6
1	M	4.0	3.2	4.1	4.0	3.9
2	4.0	3.9	2.3	3.2	3.5	2.8
3	3.2	2.3	2.7	3.5	3.5	3.0
4	4.1	3.2	3.5	M	3.7	4.0
5	4.0	3.5	3.5	3.7	3.7	3.7
6	3.9	2.8	3.0	4.0	3.7	M

δ_{ϕ_i, ϕ_j}

DUAL OBSERVATION CASE

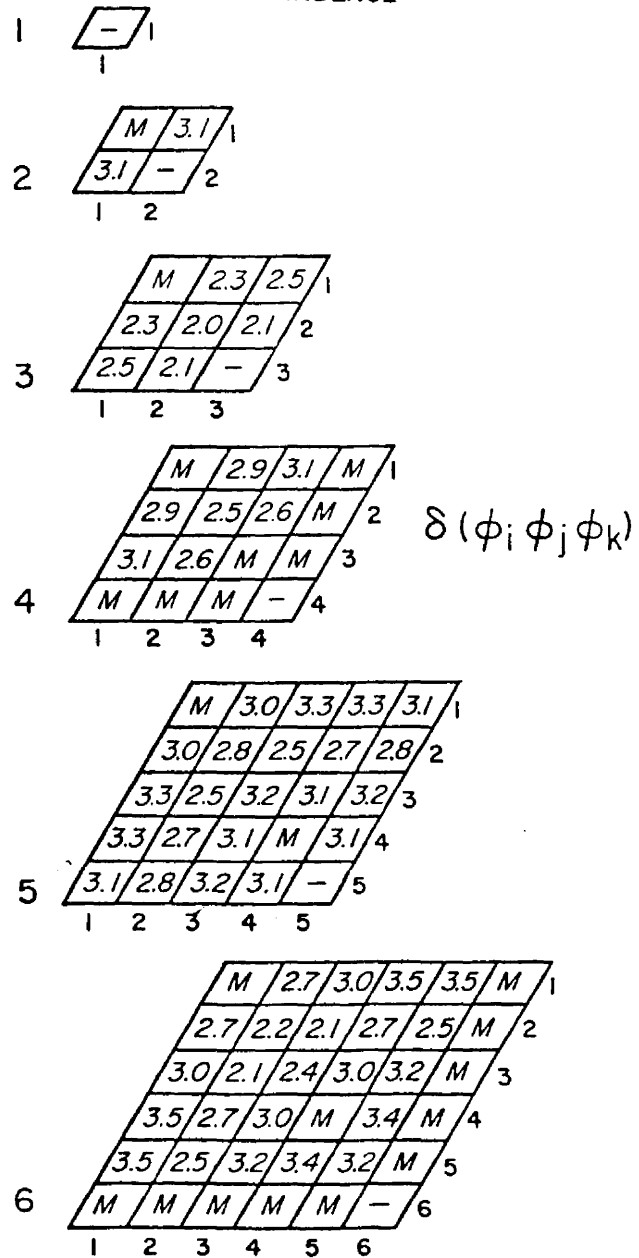
Figure 36. The nadir and azimuthal dependence of the r.m.s. deviations between average measured 0.3 - 3.0 μm reflected flux density and the inference of the same quantity made from 1, 2 or 3 instantaneous radiance measurements over ice expressed as a percent of the average reflected flux density.

NADIR DEPENDENCE



$$\delta(\theta_i, \theta_j, \theta_k)$$

AZIMUTHAL DEPENDENCE



$$\delta(\phi_i, \phi_j, \phi_k)$$

TRIPLE OBSERVATION CASE

Figure 36. (Continued).

Surface Type	Number of solar zenith angles	Average deviation inferred vs measured flux density		
		One Satellite	Two Satellites	Three Satellites
Desert	8	5.2%	3.0%	3.0%
Himalaya	2	19.0%	14.7%	13.2%
Ocean	6	35.5%	19.3%	17.5%
Indian Sub. Con.	4	5.7%	3.5%	3.1%
Cloud 1	6	15.3%	12.1%	10.9%
Cloud 2	3	24.3%	15.5%	12.7%
Ice	1	6.8%	3.7%	2.9%

Table 5. The r.m.s. deviation between inferred and measured, scene averaged reflected flux density averaged over all observation angles and solar zenith angles.

The results of this analysis reinforce the assumption that certain reflecting surfaces are spatially homogeneous with respect to reflected flux density. The smaller values of the deviations evident in the desert, Indian subcontinent and ice scenes indicate that inferences made from one or two instantaneous radiance measurements would result in an error of only a few percent in the average scene reflected flux densities. Little additional reduction in the error results if a third platform is used. For these spatially homogeneous surfaces the ice case indicates the greatest dependence on observation geometry, where in the single observation geometry intermediate nadir angles and small relative azimuth angles are indicated as the poorest observation positions based on the minimum variance criterion. It should be pointed out however that the data collected over ice were limited to a single solar zenith angle range ($50 - 60^\circ$) while an average over four and seven zenith angle ranges has been included in the respective Indian subcontinent and desert cases. It is certainly possible that inclusion of several zenith angle cases especially obscures nadir angle preferences. Nevertheless, because observations taken from geostationary satellites over a diurnal period will include a range of solar zenith angles, the averaging process over that variable seems justified.

The most spatially inhomogeneous surface type based on the present results with respect to reflected flux density is that of relatively unobscured ocean. The maximum deviation is nearly 42% of the total average reflected flux density; a result which seems initially to cast doubt on the feasibility of flux density inference. However, two

aspects of this analysis may act to restore confidence in the procedure. First, the reader is reminded that the value is an r.m.s. calculated deviation and does not benefit from fluctuations about the mean with inclusion of more than a single measurement in time, and while a deviation of 40% seems high, 84% of the variance is explained in this worst case example. Second, the magnitude of the deviation includes all of the variance due to spatial differences in the reflected flux density, i.e. even if instantaneously measured flux densities were used to infer the scene average an r.m.s. deviation of 12% would result from spatial fluctuations over the distance pertaining to the data set (~ 1000 km). The results of the clear ocean case indicate a much stronger dependence on observation geometry. In the single observation platform case the deviation is reduced from 40% to 32.6% when the nadir regime is changed from the middle to lower ranges. The best relative azimuth position was found to be in the solar direction where the deviation was equal to half of the worst case value. The clear ocean case benefits greatly from an additional observation platform, the average of the deviations falling from 35.5% to 19.3% of the average total reflected flux density. With the addition of the third observation this figure is reduced further to 17.5%. When a pair of observations are available both should be made at small nadir angles while using two observations at intermediate nadir angles should be avoided. The two satellite azimuthal dependence shows the persistence of small deviations when one or both observations are made toward the sun, however relative azimuths between 270° and 330° also result in deviations of equal magnitude. Azimuthal observations between 210° and 270° increase the best case deviation by a factor of 1.5. If three nadir observations

are available the smallest deviation values result when inferences from intermediate nadir angles are avoided and in the azimuthal sense, optimum results are indicated in general for all measurements between 270° and 30°.

The lack of symmetry displayed in the azimuthal deviations is somewhat unexpected and may have resulted from two factors. First, an asymmetric distribution about the principal plane of low level, fair weather cumulus cloudiness could have introduced this behavior. Examination of the photographic record indicates that the low level clouds are randomly distributed about the principal plane. However, the photographs were limited by a 41° full angle field of view lens. Thus, it was not possible to examine the entire scene measured by the bugeye detectors from the photographic data. Second, since the measurements taken at a particular relative azimuth angle were not necessarily taken consecutively due to changes in aircraft heading, variations due to changes in sea state may have been introduced into the data set in an asymmetric manner. As was done in the presentation of the average χ^{-1} models, the most generally applicable set of deviations may result from a simple average of the values with respect to the principal plane.

The results given in Table 5 for the Himalayas indicate a substantial improvement (19% to 13.2%) in the average deviation figures as the number of observation platforms is increased from one to three. In the single observation case small values of the nadir are indicated while no clear azimuthal preference emerges. When two measurements are available for the inference the preference for small nadir angles persists and a slight tendency toward intermediate relative azimuth

measurements is evident. An increase to three measurement platforms shows a persistence of increased deviation values at large nadir angles and an increased trend toward preferred low and intermediate relative azimuth angles.

The average deviation decreases from 15.3% to 10.9% if the number of observation positions is increased from one to three in the middle and low level cloud case. A slight improvement is indicated for single measurements made at intermediate nadir angles but the deviations are almost invariant with relative azimuth. The smallest deviations in the multiple observation case as a function of nadir occur when low and intermediate nadir measurements are combined. The results also indicate multiple observations should exclude measurements in the solar direction.

The altostratus cloud case also demonstrates the general improvement in the inference process with an increase in the number of observational positions, the average deviation decreasing from 24.3% to 12.7%. A slight improvement is seen at large nadir angles in the single observation case and intermediate nadir angles are indicated if more than one observation position is available but only by about a one percent reduction in the deviation values. The azimuthal dependence shows a 7% reduction in the deviation if the altostratus deck is observed between 210° and 270° rather than between the 90° to 150° relative azimuth sector. This asymmetric behavior is difficult to explain but may be the result of the alignment of the small convective cells with respect to the solar geometry, or asymmetric distributions of small breaks in the cloud structure. The azimuthal dependence for the case of two observation positions indicates that combining

—

inferences made from relative azimuths between -90° and $+30^\circ$ lead to the largest deviations. This tendency is also evident for the case when three observations are used in the inference.

In summary the results of Table 5 indicate that for relatively homogeneous surfaces, little improvement is gained with the addition of a third observation platform and for the most inhomogeneous cases the trend in the reduction of the average deviations indicates that addition of a fourth observation position may not be warranted. The breakdown of the deviations as a function of observation geometry indicates that appreciable reduction in the deviation value is possible in some instances by choosing the appropriate observation angle(s), however, in many cases a clear indication of the optimal position(s) was not revealed by examining the r.m.s. deviations. Also, it must be noted that the choice of the deviation between measured and inferred flux densities as the basis of the analysis is somewhat arbitrary. It is not to be implied that the values presented in Figures 30 through 36 are typical of the errors which would be made in an operational sense. Rather, this statistic was chosen as representative of a worst case inference process for it represents the magnitude of the error which would be made if the reflected flux density of a large region were inferred from an instantaneous sampling of the radiance field. Also, the slight trends indicated by Figures 30-36 may be even less significant in the operational mode when an average of many data points is available to affect the inference.

Finally, it is noted that the best single observation coordinate for a specific surface in terms of a observation nadir, relative azimuth and solar zenith angle has been obscured in the averaging

processes which led to the results in Figures 30-36. Table 6 presents the best case inference for each of the surface types. The angular resolutions are those of the original analysis i.e., 10° in the solar zenith, 10° in observation nadir and 30° in relative azimuth. The results of Table 6 indicate substantial improvements in the inference are possible if specific observation positions could be achieved.

4.4 Impact of the Angular Reflectance Models when Applied to a Climatically Significant Region

We stress during this report that the angular reflectance patterns are characteristic of regional scale atmospheric scenes. The convergence properties and optimum angular viewing coordinates have been examined in relation to an extended space scale. In this section the models are applied to a climatically significant region in order to assess their impact on the reflected flux density. Green (1980) has shown that improper modeling of the directional features of reflected radiation may lead to errors of up to $5 \text{ watts} \cdot \text{m}^{-2}$ in the average reflected flux density over a 10° zone of latitude. This error resulted when measurements of the reflected radiance fields were simulated assuming isotropy and compared to a simulation which accounted for the angular anisotropy. The simulated field of view associated with the $5 \text{ watts} \cdot \text{m}^{-2}$ error was over 40° half angle and the angular anisotropy was introduced using a bidirectional reflectance function³ which was independent of latitude, longitude and surface type. Greater corrections may result if target specific reflectance functions are applied

³The bidirectional reflectance function is equivalent to χ^{-1}/π .

Target Type	Solar Zenith Angle in Degrees	Observation Nadir Angle in Degrees	Relative Azimuth Angle in Degrees	R.M.S. deviation expressed as a percent of the mean reflected flux density
Desert	40 - 50	20 - 30	60 - 90	1.0
Himalayas	20 - 30	0 - 10	330 - 360	15.7
Ocean	50 - 60	20 - 30	300 - 330	1.6
Indian Subcontinent	10 - 20	60 - 70	180 - 210	2.0
Cloud1	30 - 40	0 - 10	120 - 150	7.3
Cloud2	30 - 40	20 - 30	180 - 210	7.0
Ice	50 - 60	60 - 70	90 - 120	1.1

Table 6. The best observational position for a single platform inference and the resulting r.m.s. deviation between the inferred and measured reflected flux density expressed as a percent of the average 0.3 - 3.0 μm reflected flux density.

to measurements of a zonally inhomogeneous region by a scanning radiometer with a much smaller field of view.

The data used to compile most of the χ^{-1} patterns in this study were collected over the region between 45 and 80° east longitude and 0 to 35° north latitude, hereafter referred to as the monsoon region. The χ^{-1} patterns should be representative of this region which will now be used to examine the sensitivity of reflected flux density to application of the angular reflectance models. In fact, the comparison will be made using TIROS-N data collected on May 30, 1979, a date almost halfway through the duration of Summer MONEX. Data from the TIROS-N 0.55 - 0.90 μm and 0.725 - 1.10 μm channels were obtained from four ascending orbits over the region between 9:30 and 12:00 z. The sub-satellite resolution of a TIROS-N measurement in these spectral bandpasses is about 1 km.

In order to apply the χ^{-1} correction to the TIROS-N data the monsoon region was divided into 1400 area elements, their boundaries formed by the whole number degrees of latitude and longitude. Each of these elements was assigned one of five surface or target identifications as shown in Figure 37 which delineates desert, ocean, the Indian subcontinent, the northern latitudes of the Himalayas and the coastal regions. Each value of reflectance R measured by the satellite was identified with a particular target type according to the latitude and longitude of reflecting surface. The solar zenith angle z , nadir angle of the reflected radiation θ , and relative azimuth angle ϕ , were computed, and for the ocean target, the angle β between the direction of the measurement and the direction of the specular reflection from a flat water surface were calculated. The angular patterns were then

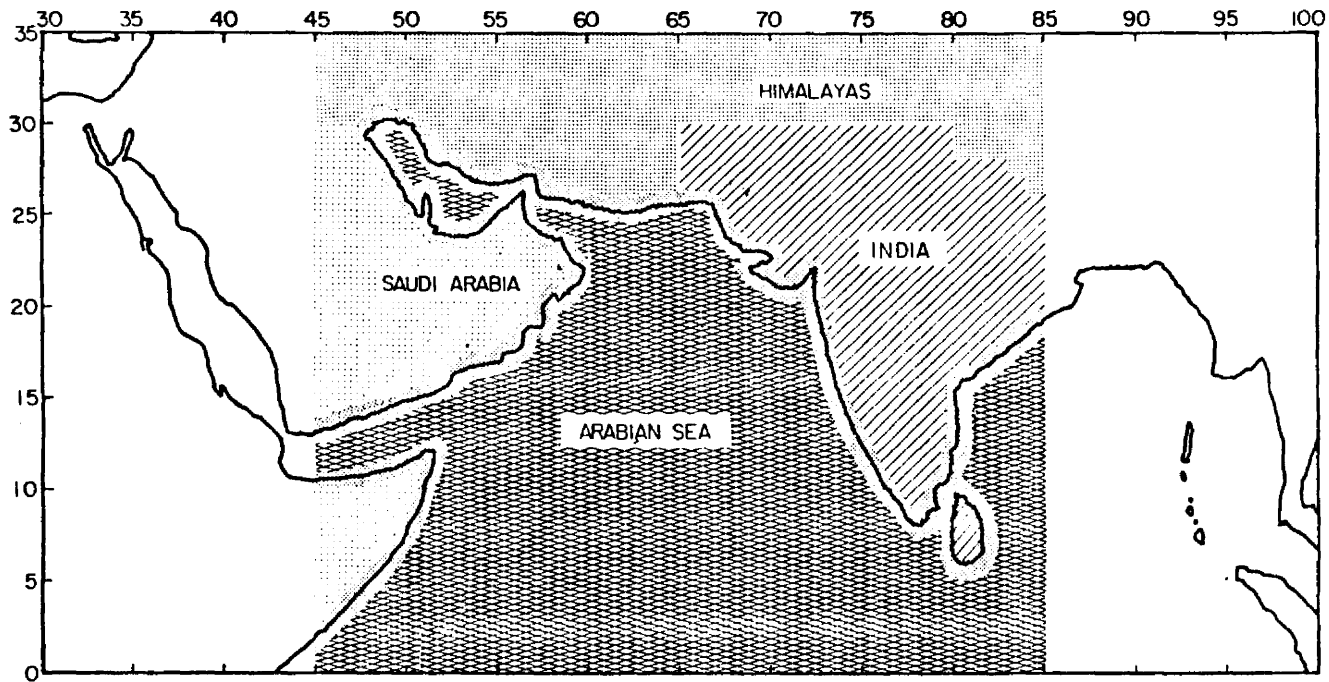


Figure 37. A depiction of the separation of the 'monsoon region' (between 45 and 85° east longitude and 0 and 35° north latitude) into various surface or target types for the application of the angular reflectance (χ^{-1}) models.

applied wherever appropriate to obtain corrected reflectance values $R' = R/\chi^{-1}$ for each TIROS-N channel. In a few instances the angular patterns were extrapolated and applied to solar zenith angle ranges outside of the angular range over which they were measured, (primarily for the Himalaya target). Also, whenever high reflectances indicated obvious regions of cloudiness the Cloud1 (middle and low level) model was applied. A complete list of the exceptions and extrapolations to the normal application of the angular models is given in Table 7.

The reflectance values were converted to their approximate flux density equivalents through multiplication by the extraterrestrial incident solar flux density in each spectral bandpass; 467 and 339 watts·m⁻² respectively. Average values of measured (isotropic) and corrected reflected flux density were calculated for each 1° x 1° element comprising the region from 45 to 85° east longitude and 0 to 35° north latitude. The averages were computed from about 500 measurements in each area element. The difference between the reflected flux densities (measured minus corrected), was also calculated and is meaningful only in what has been defined as the monsoon region since the corrections were not applied outside that area.

The average measured, corrected and differenced flux density values are shown in Figures 38, 39 and 40 for TIROS-N channel 1 and in Figures 41, 42 and 43 for TIROS-N channel 2. Note that negative flux density corrections imply that the application of the χ^{-1} models has resulted in relatively greater values of reflected flux density and positive values indicate that the original measurements were larger. The signs of the differences are appropriate for the additional flux density absorbed in the earth-atmosphere system for each area element

Surface Type(s)	Criterion for Alternate Procedure	Alternate Procedure
All	$z > 80^\circ$	$R' = R$
All	$\theta > 70^\circ$	$R' = R$
Coastal	$R < 0.20$	$R' = R$
	$R \geq 0.20$ and $z \leq 50^\circ$	Cloud1 χ^{-1} pattern used
	$R \geq 0.20$ and $z > 50^\circ$	$R' = R$
Himalayas	$R < 0.40$	$R' = R$
	$R \geq 0.40$ and $z \leq 10^\circ$	Himalaya χ^{-1} pattern for $10 \leq z \leq 20^\circ$ used
	$R \geq 0.40$ and $30^\circ \leq z \leq 40^\circ$	Himalaya χ^{-1} pattern for $20 \leq z \leq 30^\circ$ used
	$R \geq 0.40$ and $z \geq 40^\circ$	$R' = R$
Ocean	$R \geq 0.15$ and $\beta > 30^\circ$	Cloud1 χ^{-1} pattern used
	$R < 0.15$ and $60^\circ \leq z \leq 70^\circ$	Ocean χ^{-1} pattern for $50^\circ \leq z \leq 60^\circ$ used
Indian Subcontinent	$R \geq 0.25$ and $0^\circ \leq z < 60^\circ$	Cloud1 χ^{-1} pattern used
	$R \geq 0.25$ and $60^\circ < z$	$R' = R$

Table 7. The criteria for and specification of alternate procedures in applying the angular reflectance correction functions.

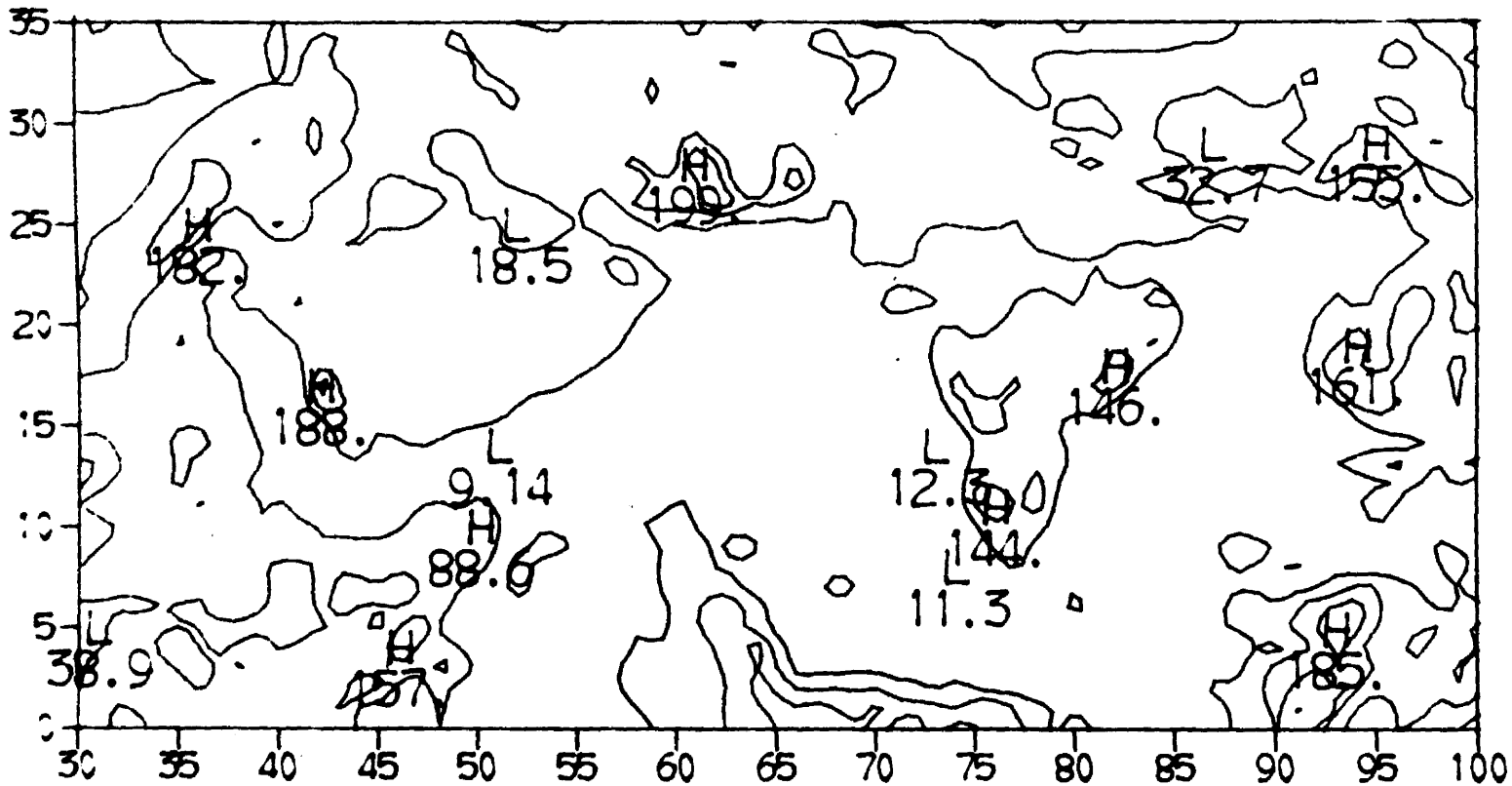


Figure 38. Values of reflected flux density ($\text{watts}\cdot\text{m}^{-2}$) associated with TIROS-N 0.55 - 0.90 μm reflectance measurements on 30 May 1979 using the isotropic assumption over the region between 30 - 100° east longitude and 0 - 35° north latitude.

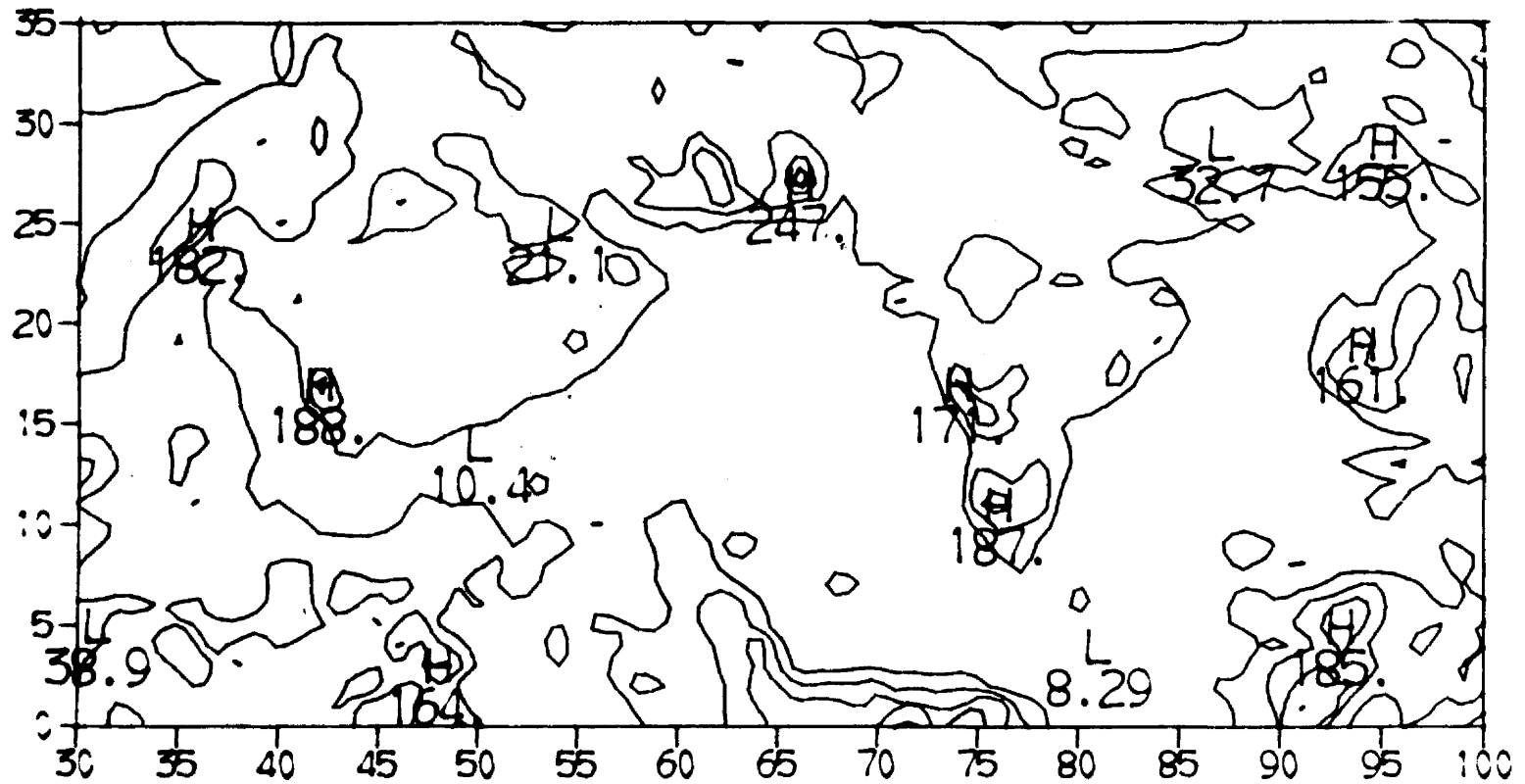


Figure 39. Values of reflected flux density (watts·m⁻²) associated with TIROS-N 0.55 - 0.90 μ m reflectance measurements on 30 May 1979 resulting from application of the angular reflectance (χ^{-1}) models over the 'monsoon region'.

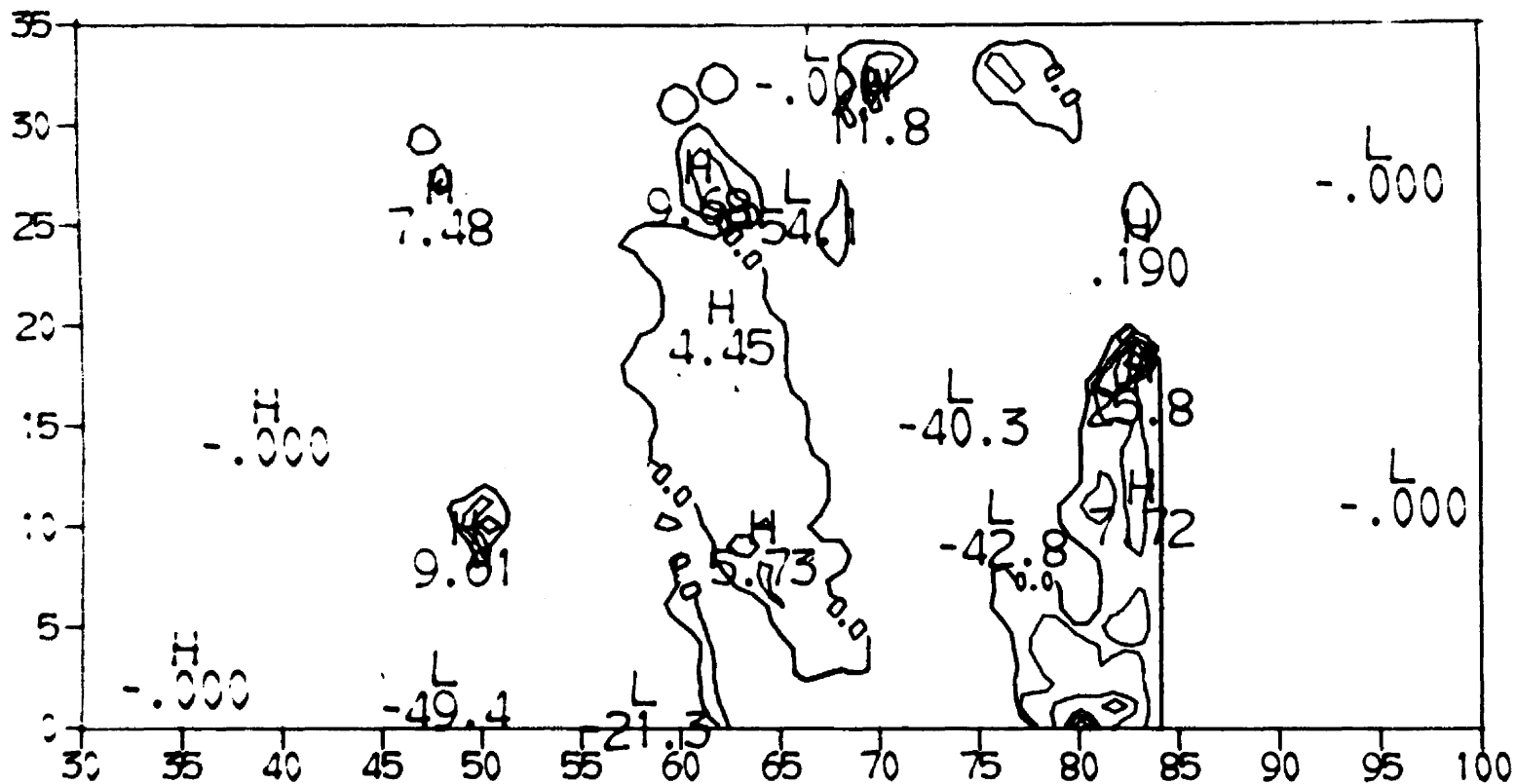


Figure 40. Values of the differences between isotropically inferred reflected flux density (watts·m⁻²) and the same quantity derived from application of the angular reflectance (χ^{-1}) models to TIROS-N 0.55 - 0.90 μm reflectances on 30 May 1979 over the 'monsoon region'.

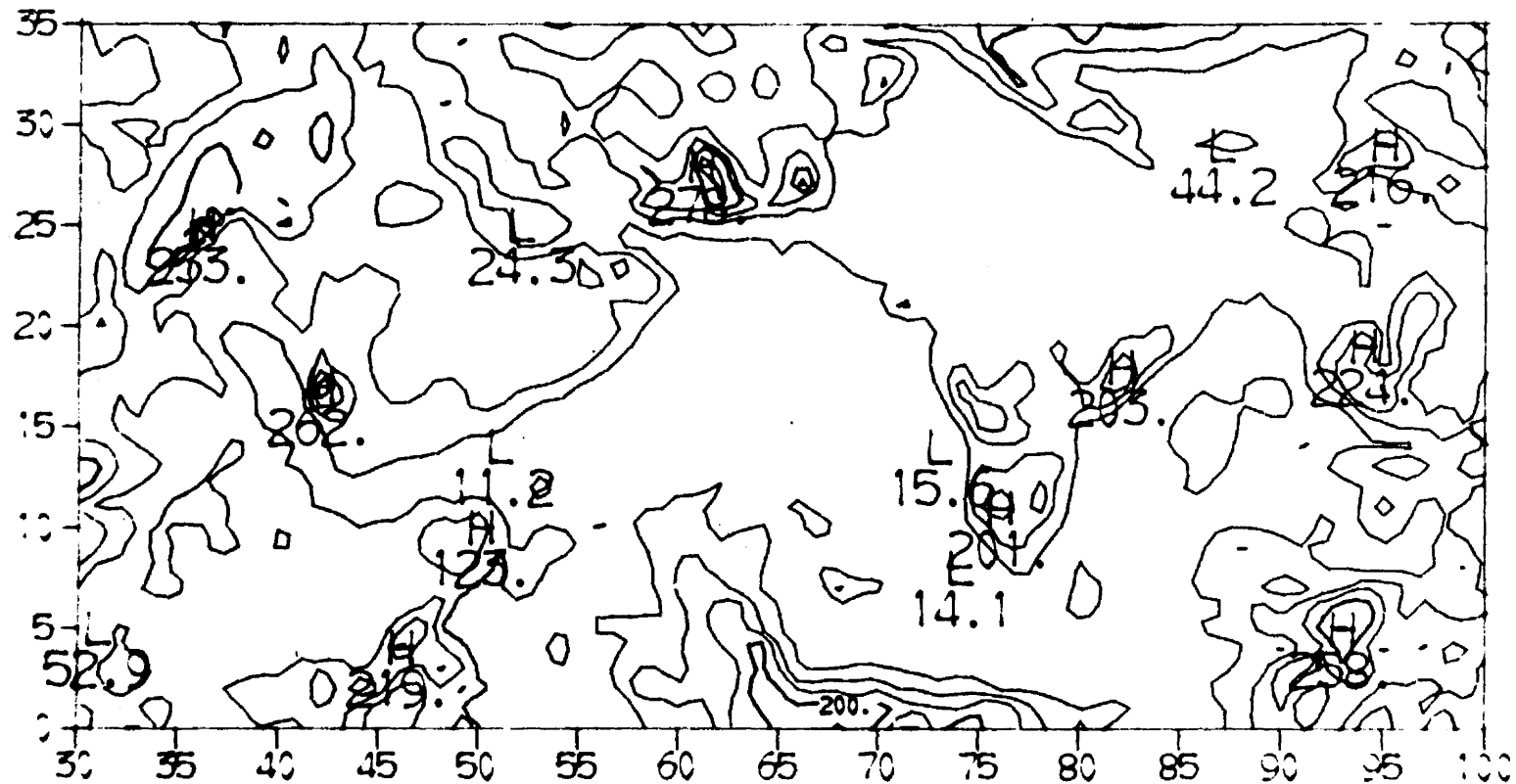


Figure 41. Values of the reflected flux density (watts·m⁻²) associated with TIROS-N 0.725 - 1.10 μ m reflectance measurements on 30 May 1979 using the isotropic assumption over the region between 30 - 100° east longitude and 0 - 35° north latitude.

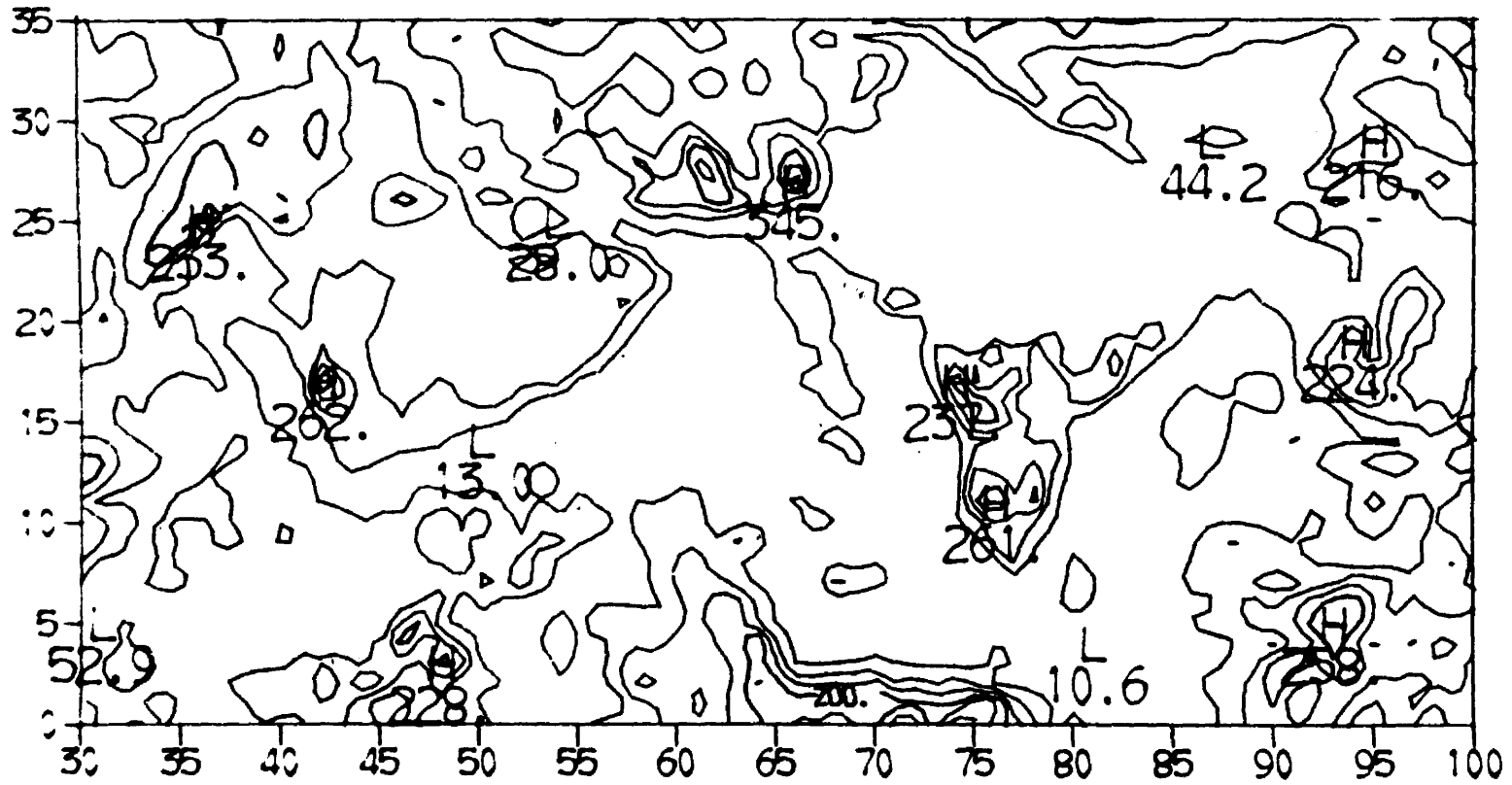


Figure 42. Values of the reflected flux density (watts·m⁻²) associated with TIROS-N 0.725 - 1.10 μm reflectance measurements on 30 May 1979 resulting from application of the angular reflectance (χ⁻¹) models over the 'monsoon region'.

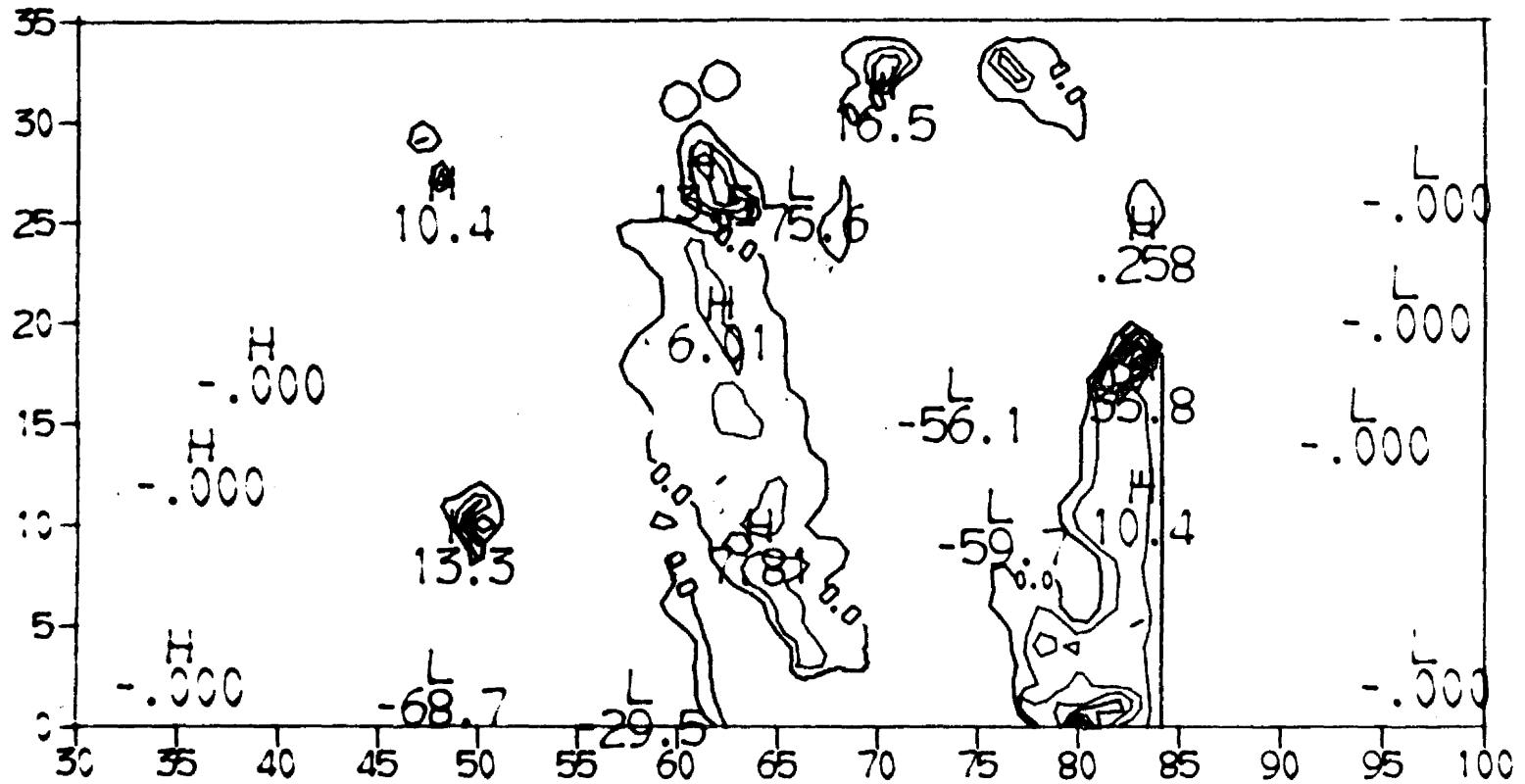


Figure 43. Values of the differences between isotropically inferred reflected flux density (watts·m⁻²) and the same quantity derived from application of the angular reflectance (χ^{-1}) models to TIROS-N 0.725 - 1.10 μm reflectances on 30 May 1979 over the 'monsoon region'.

of latitude and longitude which results from application of the angular models. Note also that if it is assumed that the values of reflectance in these spectral regions are representative of the entire solar spectrum, and if the same assumption is applied to the χ^{-1} models the magnitudes of the flux density corrections would be 3 or 4 times larger than the values calculated for the respective TIROS-N channels 1 and 2.

Figures 38 through 43 indicate that the largest flux density corrections result for the convective regions of the equator, the two convective centers in southern India and one convective region in southern Pakistan. Since the Cloud1 χ^{-1} pattern was used to interpret the radiances reflected from these convective elements it is certainly possible that the inferred flux densities are in error. (It was not possible to measure reflectances from the highest clouds from NASA's CV 990 aircraft.) What is not obvious in Figures 38-43 are the corrections of smaller magnitude but which are nevertheless just as or more important because they apply to a much larger area. In order to assess the impact of these less obvious corrections to the reflected flux density, an area weighted average correction was calculated for the different target types comprising the monsoon region. The highly convective regimes were excluded from the weighted average in order to maximize the impact of the corrections of smaller magnitude which result from application of the angular models that are most representative of the regions. Using the average zenith angle for the region to determine the incident flux density, an approximate directional reflectance, corrected directional reflectance and change in directional reflectance were calculated and the results are shown in Table 8 for

Target Type	Isotropically Inferred Directional Reflectance	Corrected Directional Reflectance	Magnitude of Directional Reflectance Correction
Desert	31.3	33.5	-2.2
Himalayas	31.4	31.3	0.1
Ocean	12.9	14.4	-1.5
Coastal Regions	19.5	20.7	-1.2
Indian Subcontinent	24.5	27.2	-2.7
Entire Monsoon region	20.2	21.7	-1.5

Table 8. Directional reflectances inferred from TIROS-N 0.55 - 0.90 μm reflectances measured over the monsoon region assuming isotropy (Column 1), the same quantity corrected with the angular reflectance models (Column 2), and the differences [isotropically inferred minus corrected], (Column 3).

the 0.55 - 0.90 μm channel. The results for the 0.725 - 1.10 μm channel are almost identical.

The results of Table 8 indicate that the overall effect of using the angular reflectance models is to increase the directional reflectance of the region over that inferred by the isotropic assumption. Only in the northern latitudes of the Himalayas is the directional reflectance decreased. The magnitude of this decrease is small because χ^{-1} correction has been applied only to reflectances greater than 0.40, which occurs only over a small fraction of the latitudes north of 30°N latitude. The majority of the reflectances measured in these latitudes are not corrected; thus the area averaging results in a small difference for the entire northern region. For the entire monsoon region, application of the angular reflectance models increases the area averaged directional reflectance from 20.2 to 21.7, an increase of 1.5, which is significant for an area as large as the monsoon region. On the space scale of the individual target types ($1 \sim 7 \times 10^6 \text{ km}^2$) the differences between corrected and isotropically inferred reflected flux densities are considerable, especially if it is assumed that similar corrections would apply over the entire solar spectrum. With this assumption, the application of the angular models results in from 15 to 27 $\text{watts} \cdot \text{m}^{-2}$ of additional reflected flux density, depending on surface type, which is typically over 10% of the total 0.3 - 3.0 μm reflected flux density.

5.0 SUMMARY AND CONCLUSIONS

The earth-atmosphere system gains or loses energy almost entirely through radiative processes. Thus, predictions of climate trends will almost certainly require an accurate accounting of the earth's radiation budget. Earth orbiting satellites provide an ideal platform from which radiative fluxes may be monitored due to their location above the earth's radiatively active atmosphere. By using wide field of view instruments, the net flux density may be measured at the satellite position, and long term (monthly), zonal averages of the radiation budget may be obtained. However, the problem is not as straightforward if the net radiative input is required on a smaller time or space scale. Sampling limitations imposed by the use of a small number of satellites require that the budget be inferred from radiance measurements made by scanning, narrow field of view instruments. This method requires some type of angular reflectance model which allows target-specific radiance measurements to be converted to emitted or reflected flux density values.

Using data acquired on high altitude (~ 10 km) flights by NASA's CV 990 aircraft during summer MONEX, thirty angular reflectance models were compiled. Each model consists of the normalized, scene-averaged, reflected radiance displayed as a function of observation nadir and the azimuth angle taken relative to the direction of the incoming solar radiation. The normalization factor is the quotient of π divided by the scene-averaged reflected flux density. The models were stratified according to the underlying reflecting surface and the value of the zenith angle of the incident solar radiation. Eight models were

compiled for the Empty Quarters of the Saudi Arabian peninsula, six for the reasonably unobscured Arabian Sea, two for the Himalaya mountains, four over the Indian Subcontinent and five over low and middle level broken clouds. By including data from two ferry flights two models were formed over the ice fields of Hudson Bay and three models were compiled for the radiance reflected from altostratus clouds in the Gulf of Alaska and near the California coast. The space scale of data collection for each model was generally between 150 and 1000 km.

The resulting angular reflectance models display many expected characteristics such as the relatively isotropic nature of the field of the radiance reflected from the Empty Quarters of the Saudi Arabian Desert for small solar zenith angles. However, one of the most anisotropic reflectance patterns was found for the 70 - 80° solar zenith angle desert case which displayed a pronounced forward peak almost certainly due to atmospheric scattering of solar radiation incident at grazing angles. Also observed was the persistent sunglint feature of a relatively unobscured, calm oceanic scene. However, patterns of radiances reflected from fields of middle and low level broken clouds indicate a significant amount of radiation backscattered toward the direction of the incident solar energy for small solar zenith angles; this may have resulted from reflection from the vertical boundaries of the finite cloud elements. The angular reflectance patterns of altostratus clouds also displayed a strong backscatter feature. In addition to reflectance from the small vertical protuberances of the cloud deck, backscatter may have resulted from the presence of ice crystals in the cloud. The scattering phase functions of ice crystals commonly display enhanced scattering at large scattering angles.

The most important conclusion to be drawn from inspection of the angular patterns is that, in nearly every case, reflected radiance fields display a sufficient degree of anisotropy to conclude that neglecting their angular variations would lead to significant errors (10 - 100%) in the inferred flux density, and that the anisotropy persists even when the data are averaged over large geographic regions.

The resulting angular characteristics of the reflected radiance fields were applied to three distinct problems related to the inference of flux density. First, the spatial convergence properties of the radiance fields were examined in order to establish minimum sampling criteria which should be observed when using the angular models. Second, the radiances from the various scenes were analyzed in a search for optimum angular sampling coordinates in a hypothetical situation in which one, two or three satellites were available to make flux density inferences. Third, the importance of applying appropriate angular models for the inference of flux density was examined for the region extending from the Saudi Arabian peninsula to the Indian subcontinent and from the equator to the Himalayan mountain range.

The spatial convergence study consisted of a repeated application of a simple running mean technique to establish the fraction of a scene-specific data set which was required for the radiance in a particular direction to converge to within 5% of the scene-averaged mean radiance in the same direction. The results indicated that for some scenes such as ice, desert or a sparsely vegetated surface, convergence was achieved after sampling a small fraction of the entire data set ($\leq 10\%$). However, for other scenes, such as clear ocean, clouds or the Himalayas, a significant fraction of the entire data set ($\approx 30\%$) was required for convergence. The conclusion of this analysis is that,

scenes which tend to be isotropic also tend to be spatially homogeneous while scenes which are anisotropic require substantial spatial sampling in order to insure convergence to the mean pattern. For example, the flux density reflected from a 1200 km segment of desert may be accurately inferred by application of the mean angular model to radiance data gathered along 25 km of the segment. At the other extreme, scanning radiometer data along a 250 km track would be required to adequately infer reflected flux density over the same amount of clear ocean.

In order to search for optimum angular viewing coordinates, the r.m.s. deviation between measured reflected flux density and the instantaneously inferred value of the same quantity was used as a worst case test statistic. Some scenes such as desert, sparsely vegetated surfaces, broken cloud and altostratus cloud showed only a slight preference for any viewing coordinate. For other scenes such as ocean, ice and the Himalayas proper choice of the nadir or relative azimuth viewing coordinate significantly reduced the value of the test statistic. For example, viewing the Himalaya scene at small rather than large nadir angles reduced the deviation (expressed as a percentage of the mean flux density) between measured and inferred flux densities from 23 to 15%. No significant dependence on the azimuthal viewing coordinate was found in the Himalayan scene. Over the ocean it was found that inferences made from intermediate nadir angles gave the poorest results and a definite preference was found for inferences made looking toward the sun. The ice scene data also indicated that intermediate nadir angles should be avoided. However, the largest deviation as a function of relative azimuth occurred when inferences were made looking into the solar direction, exactly opposite the results for clear ocean. The above analyses were carried out for hypothetical, one

two or three satellite system and when averaged over all viewing coordinates the test statistics reveal the most important finding of this analysis;

a two satellite radiation budget monitoring system is sufficient for inferring shortwave reflected flux densities over desert, ice or sparsely vegetated surfaces. Mountainous or oceanic regions or cloudy scenes benefit from a three satellite system. However, the results of this study indicated that in no case would the addition of a fourth satellite be warranted.

Finally, the sensitivity of the reflected flux density of a region to application of appropriate angular reflectance models was addressed. Using TIROS-N data for the region extending from the Saudi Arabian peninsula to the Indian subcontinent and from the equator to the Himalayas, appropriate angular reflectance models were applied to obtain corrected reflected flux densities. Even after deletion of the effects of high clouds regional directional reflectances were increased by as much as 2.7% compared to values inferred using an isotropic assumption. For the region as a whole, the area averaged directional reflectance was increased by 1.5% due to application of the models. The conclusion of this analysis is that,

application of appropriate angular reflectance models to operational satellite data resulted in corrections to the isotropically inferred flux values of from 1.5 to 2.7%. Changes of this magnitude constitute a significant fractional change (10%) in the reflected component of the radiation budget.

In summary, this study began with the goal of specifying the nature of the angular variability of various upwelling radiance fields so that satellite radiance measurements could be used to infer reflected flux densities on a regional basis. We proceeded to specify bidirectional reflectance models which could be used to interpret the satellite

results. In the process of compositing the models, the variable nature of the reflected radiance fields became evident. The angular models required to deduce the flux show significant variation even when the underlying scene does not change in a way which would cause its re-categorization. As a result the spatial convergence properties of the models were investigated and it was found that for highly anisotropic scenes, significant sampling distances were required. The search for optimum viewing co-ordinates confirmed the variability of the radiance fields; even when the flux density of a region was inferred from three different viewing co-ordinates, unacceptably large errors resulted for anisotropic scenes. Thus it is the author's suggestion that angular reflectance models should only be used if the radiance fields are averaged over an appropriate distance, so that their natural variability becomes insignificant. The scene averaged angular models presented here are certainly valid for the specific condition of the earth atmosphere system which prevailed at the time and location of the data collection. The models presented in this study are better supported statistically than those used in previous radiation budget studies. Even so, because of subtle unperceived differences in the scenes and the associated variation in the upwelling radiance fields application of these models may still lead to inferred flux densities which are in error by several percent. Thus, accurate inferences of the reflected component of the earth's radiation budget from scanning radiometer data may not be feasible unless the natural variability of the reflected radiance fields has been properly taken into account.

REFERENCES

- Arking, A., 1965: The angular distribution of scattered solar radiation and the earth albedo as observed from TIROS. Goddard Institute for Space Studies, Annual Research Report, 1 July 1964 - 30 June 1965, 47-67.
- _____, and J. S. Levine, 1967: Earth albedo measurements: July 1963 to June 1964. J. Atmos. Sci., 24, 721-724.
- Bartman, F. L., 1968: Earth reflectance patterns measured by radiometer on high altitude balloon flights. Tech. Rept. 05863-13-T, NASA Contract No. NASr-54(03), 15 pp.
- Brennan, B., and W. R. Bandeen, 1970: Anisotropic reflectance characteristics of natural earth surfaces. Appl. Opt., 9, 405-412.
- Coulson, K. L., 1959: Characteristics of the radiation emerging from the top of a Rayleigh atmosphere, 1 and 2. Planet. Space Sci., 1, 256-284.
- Green, Richard N., 1980: The effects of directional radiation models on the interpretation of earth radiation budget measurements. J. Atmos. Sci., 37, 2298-2313.
- Griggs, M., and W. A. Marggraf, 1967: Measurement of cloud reflectance properties and the atmosphere attenuation of solar and infrared energy. Final Report on Contract AF 19(628)-5517, AFCRL, 156 pp.
- Gruber, A., and J. S. Winston, 1978: Earth-atmosphere radiative heating based on NOAA scanning radiometer measurements. Bull. Amer. Meteor. Soc., 59, 1570-1573.
- House, F. B., 1965: The radiation balance of the earth from a satellite. Ph.D. Thesis, Dept. of Meteorology, Univ. of Wisconsin.
- Jacobowitz, H., W. L. Smith, H. B. Howell and F. W. Nagle, 1979: The first 18 months of planetary radiation budget measurements from the Nimbus 6 ERB experiment. J. Atmos. Sci., 36, 501-507.
- Kattawar, G. W., and G. N. Plass, 1968a: Radiant intensity of light scattered from clouds. Appl. Opt., 7, 699-704.
- _____, and _____, 1968b: Influence of particle size distributions on reflected and transmitted light from clouds. Appl. Opt., 7, 869-878.
- London, J., 1957: A study of the atmospheric heat balance. Final Report Contract AF 19(122)-165, Res. Div., College of Engineering, New York University, 99 pp.

REFERENCES (Continued)

- Paltridge, G. W., and C. M. R. Platt, 1976: Radiative Processes in Meteorology and Climatology. Elsevier Press, 318 pp.
- Plass, G. N., G. W. Kattawar and J. A. Guinn Jr., 1975: Radiative transfer in the earth's atmosphere and ocean: influence of ocean waves. Appl. Opt., 14, 1924-1936.
- Raschke, E., and M. Pasternak, 1968: The global radiation balance of the earth-atmosphere system obtained from radiation data of the meteorological satellite Nimbus 3. Proc. Symp. Physical and Dynamical Climatology, Leningrad.
- _____, and W. R. Bandeen, 1970: The radiation balance of the planet earth from radiation measurements of the satellite Nimbus 2. J. Appl. Meteor., 9, 215-238.
- _____, I. H. Vonder Haar, M. Pasternak, and W. R. Bandeen, 1973: The radiation balance of the earth-atmosphere system from Nimbus 3 radiation measurements (16 April 1969 - 3 February 1970). NASA Tech. Note G-1086, Goddard Space Flight Center, Greenbelt, MD., 73 pp.
- Rasool, S. I., and C. Prabhakara, 1966: Heat budget of the southern hemisphere. Problems of Atmospheric Circulation. Washington, D.C., Spartan Books, 76-92.
- Ruff, L., R. Koffler, S. Fritz, J. S. Winston and P. K. Rao, 1968: Angular distribution of solar radiation reflected from clouds as determined from TIROS IV radiometer measurements. J. Atmos. Sci., 25, 323-332.
- Salomonson, V. V., 1968: Anisotropy in reflected solar radiation. Atmos. Sci. Paper #128, Colo. State Univ., Ft. Collins, CO., 143 pp.
- _____, and W. E. Marlatt, 1968: Anisotropic solar reflectance over white sand, snow, and stratus clouds. Atmos. Sci. Paper #170, Colo. State Univ., Ft. Collins, CO., 41 pp.
- Smith, W. I., J. Hickey, H. B. Howell, H. Jacobowitz, D. T. Hilleary, and A. T. Drummond, 1977: Nimbus-6 earth radiation budget experiment. Appl. Opt., 16, 306-318.
- _____, E. D. Herman, T. Schreiner, H. B. Howell, and P. Menzel, 1981: Radiation budget characteristics of the onset of the summer Monsoon. Paper presented at the International Conference on the Early Results of FGGE and Large Scale Aspects of Its Monsoon experiment, Tallahassee, FL., 11 pp.

REFERENCES (Continued)

- Stowe, L. L., H. Jacobowitz, and V. R. Taylor, 1980: Reflectance characteristics of earth and cloud surfaces as measured by the ERB scanning channels on the Nimbus 7 satellite. Proc. International Radiation Symposium, Aug 11-16, Ft. Collins, CO., 430-432.
- Suomi, V. E., 1958: The radiation balance of the earth from a satellite. Ann. Intern. Geophys. Y., 1, 331-340.
- Vonder Haar, T. H., 1968: Variations of the earth's radiation budget. Ph.D. Thesis, Univ. of Wisconsin.
- _____, and V. E. Suomi, 1971: Measurements of the earth's radiation budget from satellites during a five year period. Part I: Extended time and space means. J. Atmos. Sci., 28, 305-314.
- Weinstein, M., and V. Suomi, 1961: Analysis of satellite infrared radiation measurements on a synoptic scale. Mon. Wea. Rev., 89, 419-428.
- Winston, J. S., 1967: Planetary-scale characteristics of monthly mean long-wave radiation and albedo and some year to year variations. Mon. Wea. Rev., 95, 235-256.
- _____, and V. R. Taylor, 1967: Atlas of world maps of long-wave radiation and albedo. ESSA Tech. Rept. NESC-43, Washington, D.C., 32 pp.
- Wolfe, W. L., and G. J. Zissis (editors) 1978: The Infrared Handbook. Published by the Office of Naval Research, Department of the Navy, Arlington, VA., 1720 pp.

APPENDIX I

Electrical and Optical Characteristics of the Bugeye Photodiode

The complete electrical and optical properties of the EG&G SGD-100A silicon photodiode as specified by the manufacturer are listed below in Table AI-1. Besides the spectral response which is shown in Figure 2 of the text, the most pertinent characteristics are the response time and the linearity range of the diode.

CHARACTERISTIC	MINIMUM	TYPICAL	MAXIMUM	UNITS AND CONDITIONS
Spectral Range	0.35		1.13	Micrometers
Spectral Sensitivity	0.45	0.5	0.65	Amps/Watt at 0.9 μm
Integrated Sensitivity				
2870°K Blackbody		0.12		Amps/Watt
6000°K Blackbody		0.20		Amps/Watt
Luminous Sensitivity				
2870°K Blackbody		5000		$\mu\text{A}/\text{Lumen}$
6000°K Blackbody		1500		$\mu\text{A}/\text{Lumen}$
Operating Voltage	0	100	180	Volts
Breakdown Voltage	200	600		Volts at 100 μA
Linearity of Response		5		% over 7 decades
Operating Temperature	-65	25	+150	°C
Rise Time		4×10^{-9}		Seconds at 100V
Dark Current		3×10^{-9}	20×10^{-9}	Amps at 10V at 25°C
Dark Current		10×10^{-9}	100×10^{-9}	Amps at 100V at 25°C
Capacitance		4.0	7.0	Picofarads at 100V
NEP (0.9 μm , 10^3 , 1)		1×10^{-13}		Watts at 25°C
D * (0.9 μm , 10^3 , 1)		2.3×10^{-12}		Watts ⁻¹ cm Hz ^{1/2} at 25°C
Channel Impedance		3×10^6		Ohms at 100V at 25°C
Field of View		160		Degrees-Full Angle
D.C. Photocurrent			1.0	mA at 150V
Pulsed Photocurrent			120	mA at 150V
Power Dissipation				
D.C.			0.2	Watts
Pulsed			25	Watts (1 μ sec Max.)

AI-7

Table AI-1. Optical and electrical characteristics of the SGD-100A photodiode.

APPENDIX II

Description of the Upward Looking Bugeye Instrument

The upward looking bugeye instrument was designed to measure the angular distribution of the downwelling radiation field. In this study it was used as a check on the relative magnitudes of the downwelling direct and diffuse irradiances. If the diffuse component exceeded 10% of the total downward irradiance, the bottom bugeye data were rejected on the basis that the presence of high cloud would invalidate the results. The physical characteristics of the top bugeye differed from those of the bottom bugeye by an alternate arrangement of the diodes. Table AII-1 gives the angular position of the top bugeye diodes with respect to the aircraft frame. Also, the fields of view of the diodes in the top bugeye were not constrained by collimator tubes. Rather, a small teflon disk was placed atop each diode to attenuate the signal and to extend the field of view from the 160° full angle figure quoted in the diode characteristics (Table AI-1) to 180° full angle.

The voltage output (V_i) of the i th diode is proportional to the sum of the downward direct solar irradiance E_o and the downward diffuse irradiance E_i incident on the i th diode or;

$$\begin{aligned} V_i &= k_i E_o \cos \beta_i + k_i \int_{\Omega_i} N_i(\theta, \phi) C_i(\theta, \phi) d\Omega_i \\ &= k_i E_o \cos \beta_i + k_i E_i \end{aligned}$$

UPWARD LOOKING BUGEYE			
Detector Number	Angle from Zenith	Azimuth Angle *	Field of View Steradian
1	0°	—	2π
2	30°	315°	"
3	30°	45°	"
4	30°	135°	"
5	30°	225°	"
6	45°	0°	"
7	45°	90°	"
8	45°	180°	"
9	45°	270°	"
10	60°	315°	"
11	60°	45°	"
12	60°	135°	"
13	60°	225°	"

*The azimuth angle as measured in the aircraft reference frame with the forward direction at 0° and positive taken in the clockwise sense.

Table AII-1. Angular positions and fields of view of the upward looking bug-eye detectors.

where k_i is the relative sensitivity of the i th diode and amplifier, β_i is the angle between the direction of incident direct solar radiation and the normal to the active area of the i th diode, $C_i(\theta, \phi)$ is the dot product between the normal to the i th diode and the direction of the diffuse contribution from the (θ, ϕ) direction, and Ω_i is the solid angle viewed by the i th diode. For this application $N_i(\theta, \phi)$ is assumed to be isotropic. Thus, the evaluation of the integral on the right hand side of the above equation would be trivial were it not for the truncation of the integration at the horizon (the diffuse component is assumed to be identically zero below the horizontal plane). Although the top of the NASA CV 990 aircraft was coated with a black paint, some input to the off zenith diodes is inevitable due to reflection from the aircraft. Also, the same diodes receive an unknown irradiance due to the upwelling radiation reflected from the surface and atmosphere which is subtended by the wide fields of view. These contributions are certainly small compared to the contribution from the direct solar beam but it is not clear that these contributions are negligible compared to the small Rayleigh contribution typical at the high altitudes of the measurement. Nevertheless, a solution is sought for the over-determined system consisting of thirteen equations or measurements in the two unknowns: E_o and E_i . A linear programming algorithm was used to solve the constrained system ($E_o, N_i > 0$) and the ratio $E_i / (E_i + E_o) < .10$ was used as the data filter criterion.

The results of this analysis resulted in a flight averaged diffuse to total ratio which was typically less than 0.05. However, when this criterion was applied to the flights over broken low and middle clouds a very high fraction of the data failed the test and the

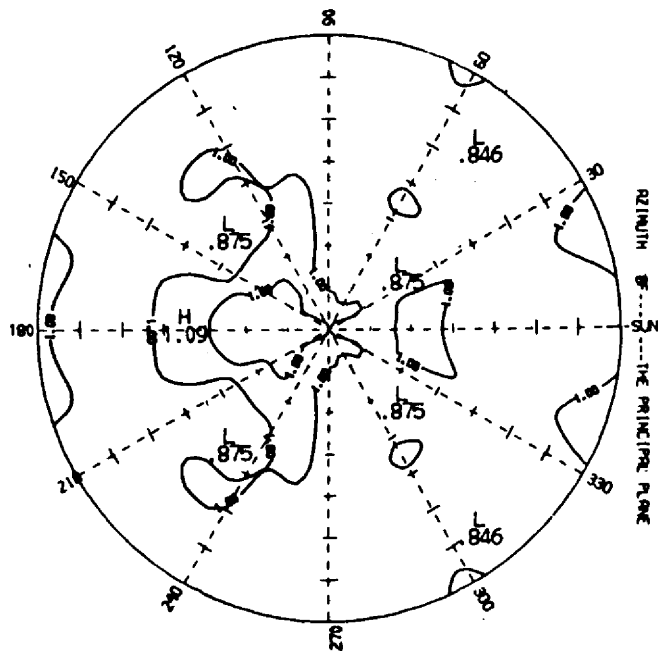
~~SECRET~~

average diffuse to total fraction was approximately 0.40 which was much greater than expected from visual flight observations. . . Because of the uncertainty of the magnitude of the contribution of the upwelling radiances (discussed above), especially in the case of the relatively bright underlying clouds, it was decided to use the alternate test for clouds above the measurement altitude described in Chapter II.

APPENDIX III

Appendix III is a compilation of the complete set of interpolated χ^{-1} patterns and plots of the flight tracks of the Convair 990 associated with each χ^{-1} pattern. The flight tracks were not subjected to the same filtering techniques which were applied to the bug-eye and irradiance data. Thus, some of the points shown in the plots of the flight tracks were not allowed into the χ^{-1} compilation. However, differences between the points of actual data collection and the flight tracks shown below are small.

DESERT χ^{-1} FOR SOLAR ZENITH FROM 0.00 TO 10.00 DEG



DESERT SPATIAL SAMPLE FOR SOLAR ZENITH ANGLES FROM 0° TO 10°

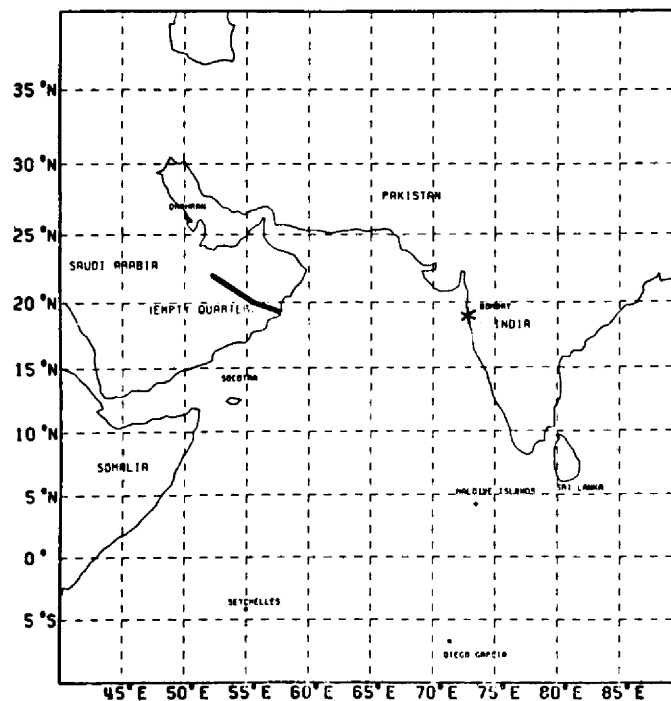
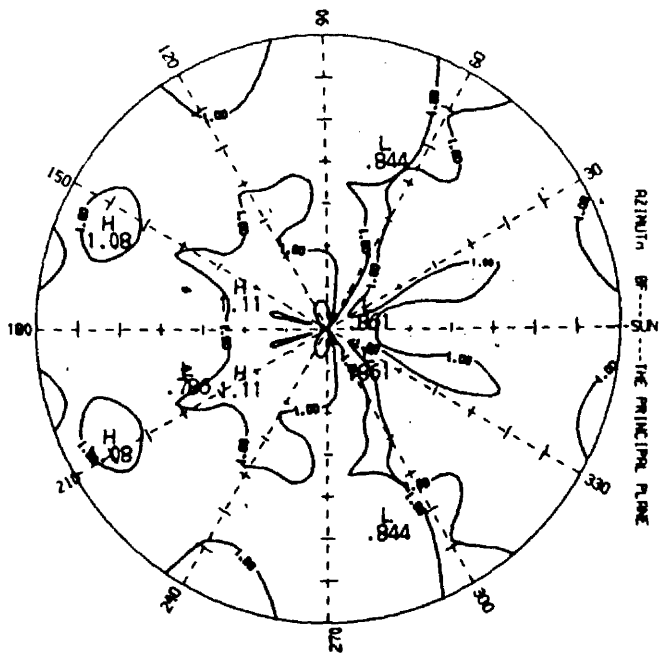


Figure AIII-1. Interpolated χ^{-1} pattern (left) and associated flight track (right) for the 0-10° solar zenith angle desert case. These data were collected during the MONEX flight(s) of the 9th and 14th of May, 1979.

DESERT CHIMM-1 FOR SOLAR ZENITH FROM 10.00 TO 20.00 DEG



DESERT SPATIAL SAMPLE FOR SOLAR ZENITH ANGLES FROM 10° TO 20°

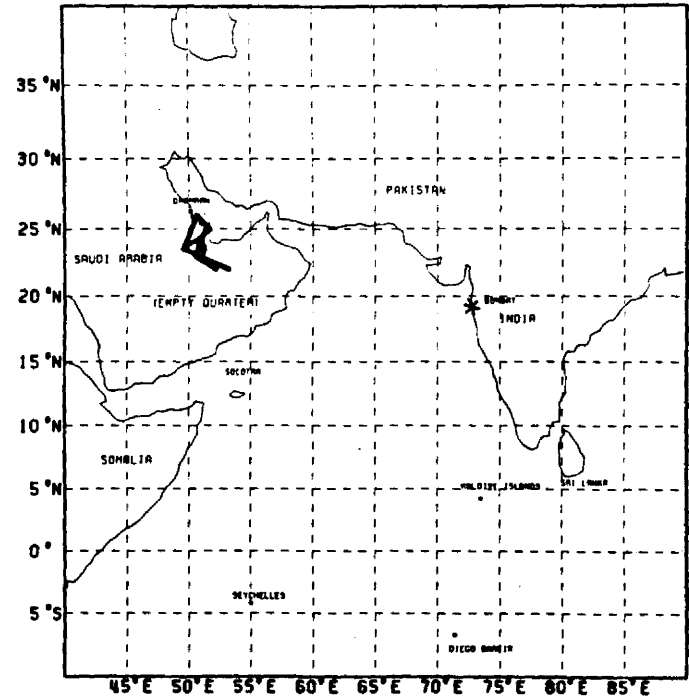
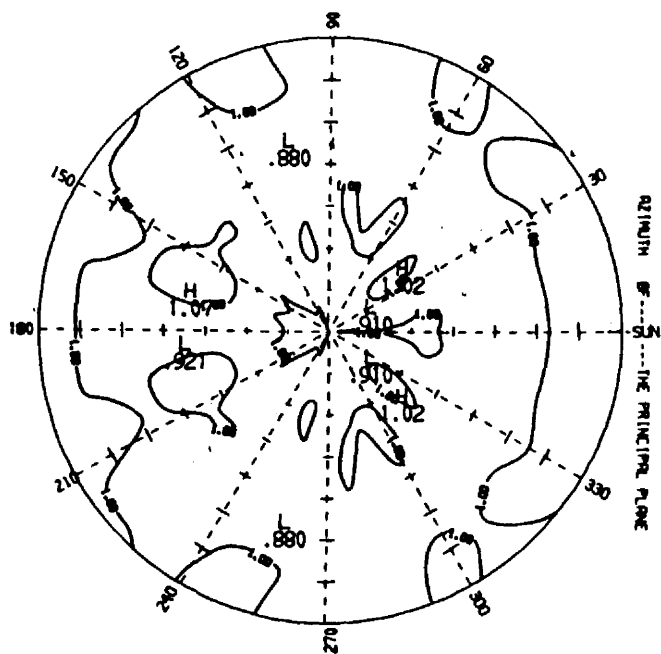


Figure AIII-2. Interpolated χ^{-1} pattern (left and associated flight track (right) for the 10-20° solar zenith angle desert case. These data were collected during the MONEX flight(s) of the 9th, 10th and 14th of May, 1979.

DESERT CHIM-1 FOR SOLAR ZENITH FROM 20.00 TO 30.00 DEG



DESERT SPATIAL SAMPLE FOR SOLAR ZENITH ANGLES FROM 20° TO 30°

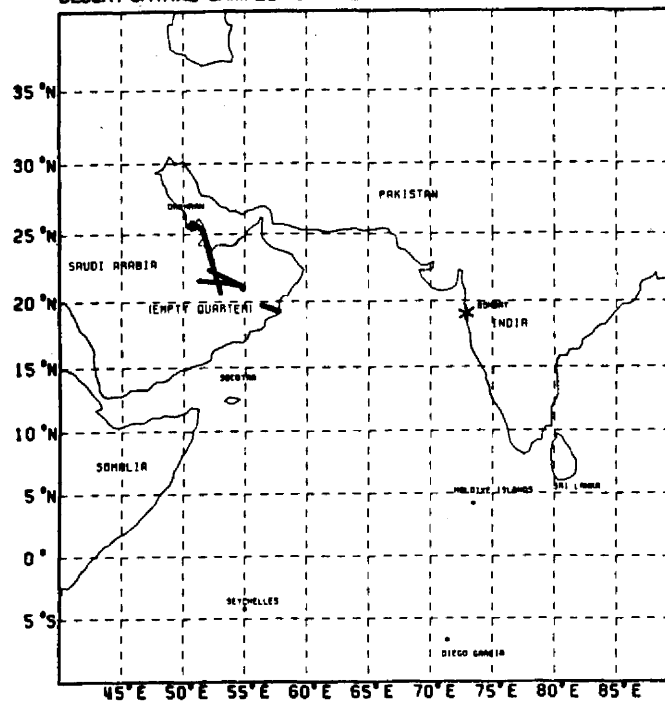
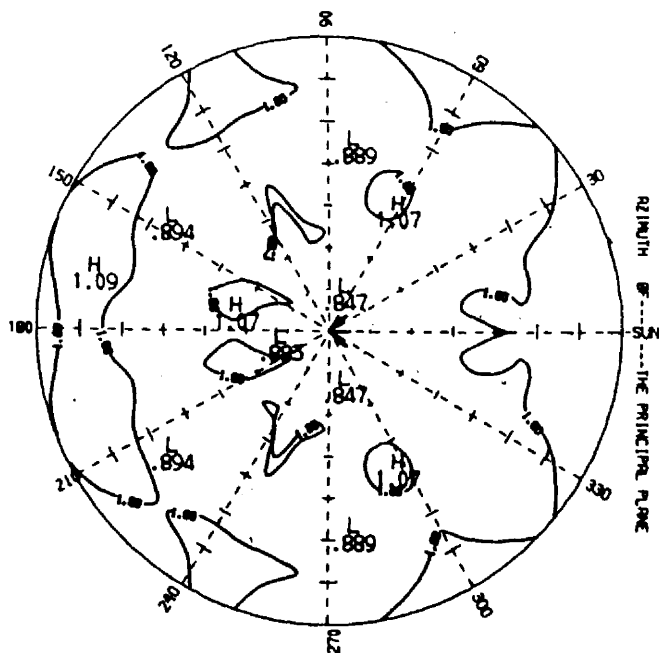


Figure AIII-3. Interpolated χ^{-1} pattern (left) and associated flight track (right) for the 20-30° solar zenith angle desert case. These data were collected during the MONEX flight(s) of the 9th, 10th, 12th and 14th of May, 1979.

DESERT χ^{-1} FOR SOLAR ZENITH FROM 30.00 TO 40.00 DEG



DESERT SPATIAL SAMPLE FOR SOLAR ZENITH ANGLES FROM 30° TO 40°

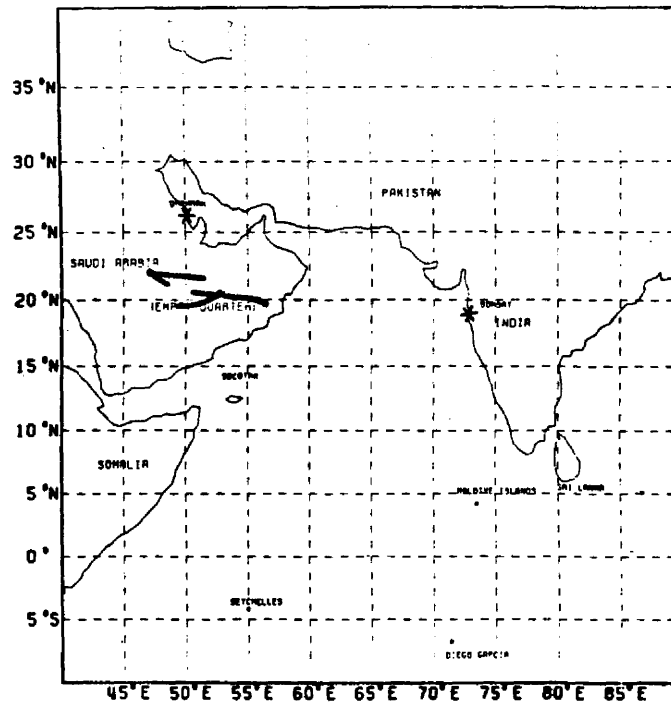
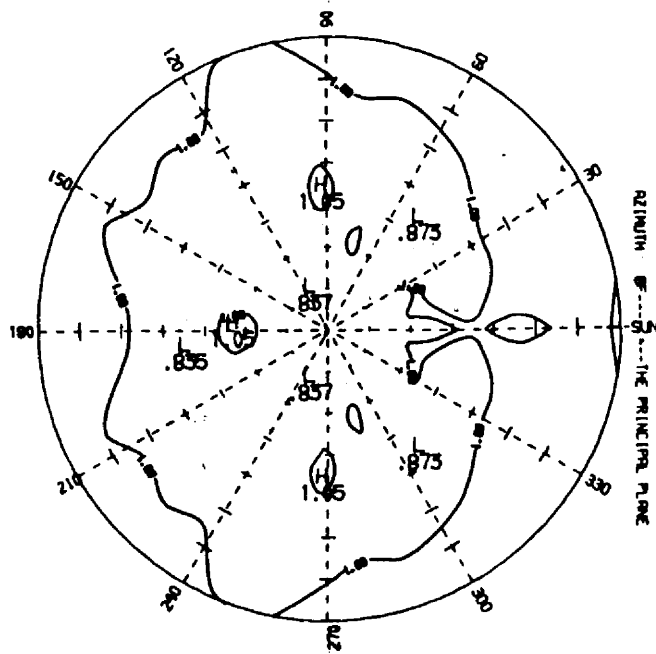


Figure AIII-4. Interpolated χ^{-1} pattern (left) and associated flight track (right) for the 30-40° solar zenith angle desert case. These data were collected during the MONEX flight(s) of the 9th, 10th, 12th and 14th of May, 1979.

DESERT χ_{**}^{-1} FOR SOLAR ZENITH FROM 40.00 TO 50.00 DEG



DESERT SPATIAL SAMPLE FOR SOLAR ZENITH ANGLES FROM 40° TO 50°

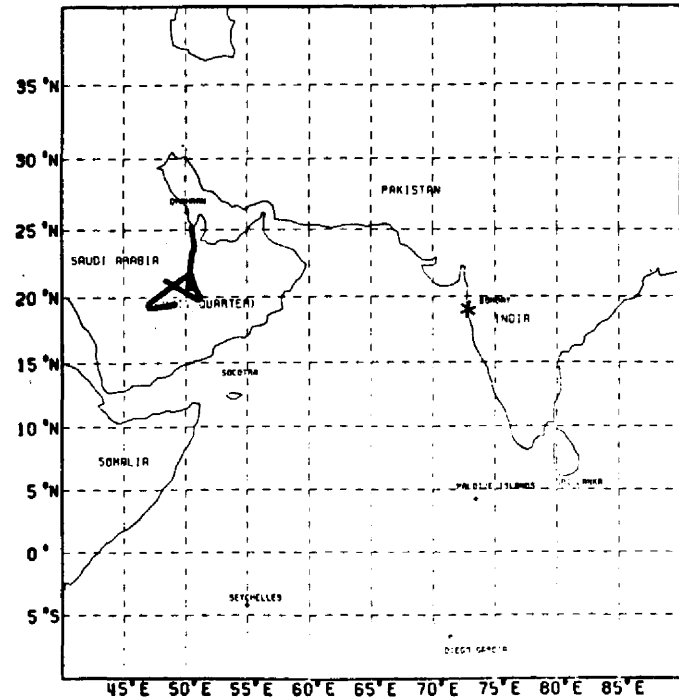
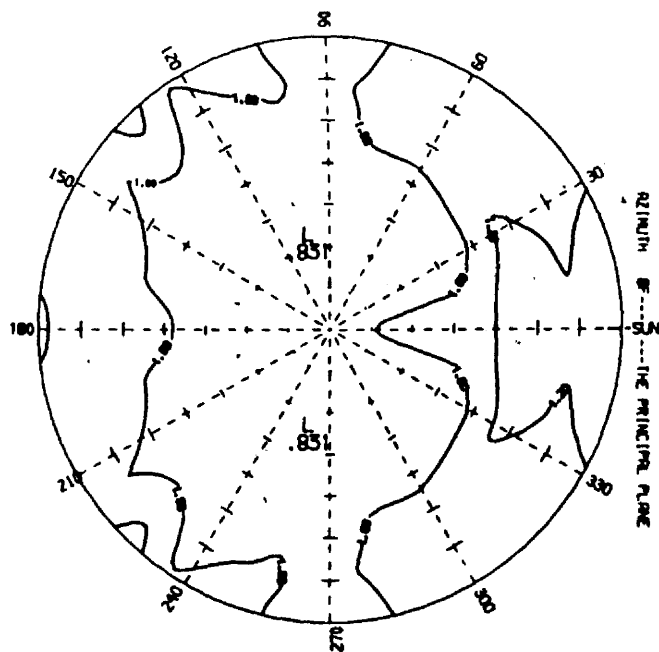


Figure AIII-5. Interpolated χ^{-1} pattern (left) and associated flight track (right) for the 40-50° solar zenith angle desert case. These data were collected during the MONEX flight(s) of the 9th, 10th, 12th and 14th of May, 1979.

DESERT CHIM-1 FOR SOLAR ZENITH FROM 50.00 TO 60.00 DEG



DESERT SPATIAL SAMPLE FOR SOLAR ZENITH ANGLES FROM 50° TO 60°

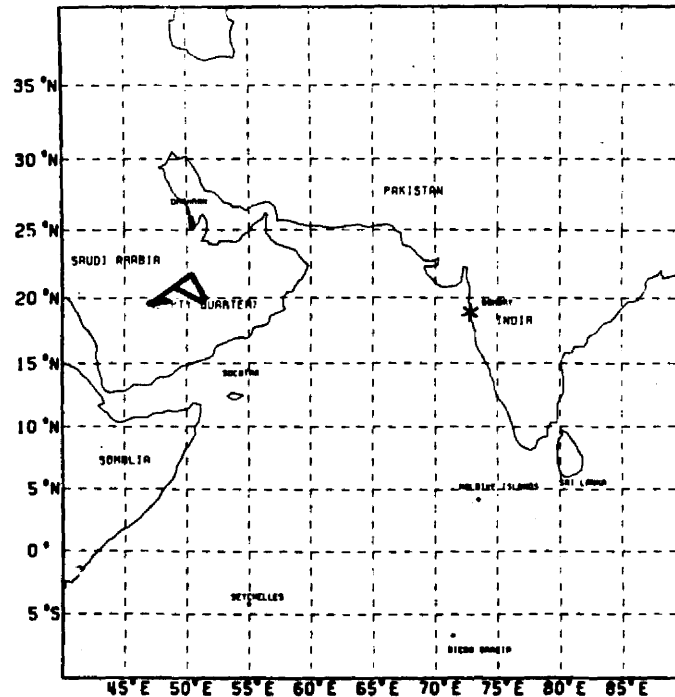
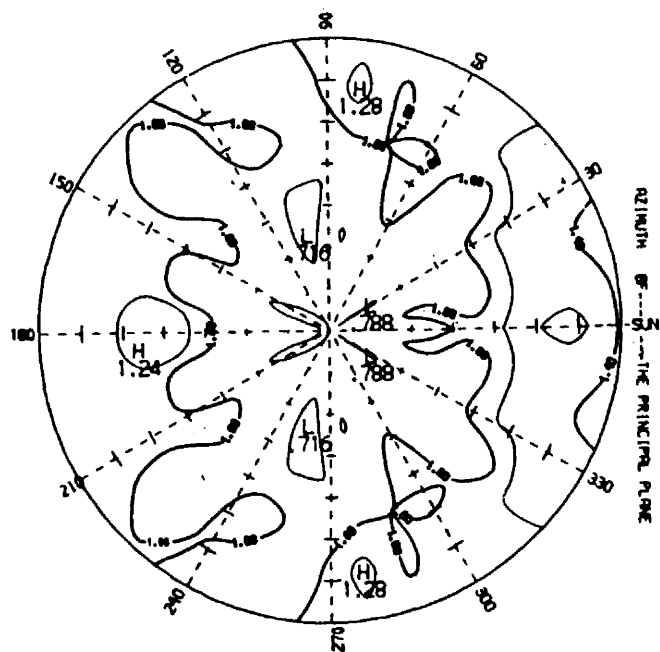
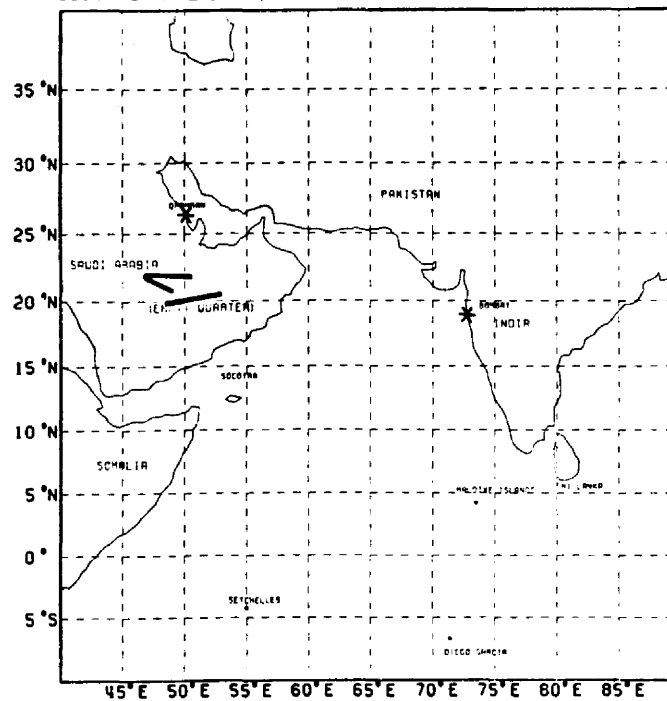


Figure AIII-6. Interpolated χ^2 pattern (left) and associated flight track (right) for the 50-60° solar zenith angle desert case. These data were collected during the MONEX flight(s) of the 9th, 10th and 12th of May, 1979.

DESERT CHIM-1 FOR SOLAR ZENITH FROM 60.00 TO 70.00 DEG



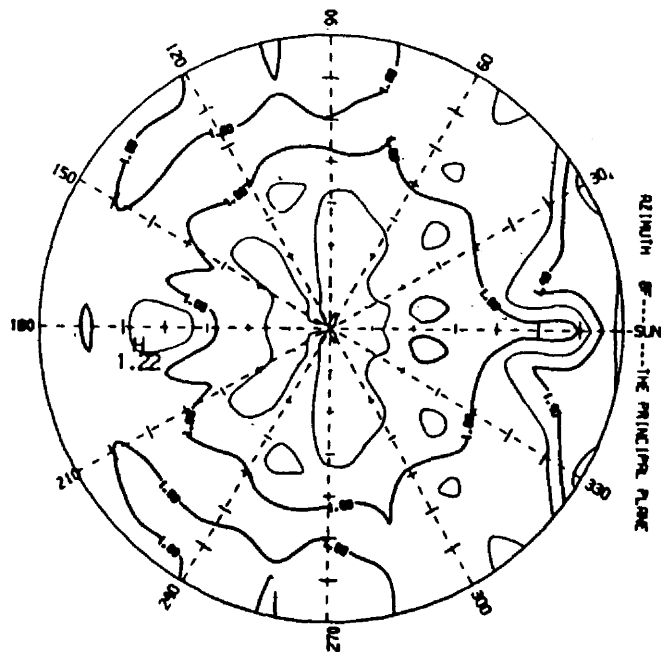
DESERT SPATIAL SAMPLE FOR SOLAR ZENITH ANGLES FROM 60° TO 70°



AIII-6

Figure AIII-7. Interpolated χ^{-1} pattern (left) and associated flight track (right) for the 60-70° solar zenith angle case. These data were collected during the MONEX flight(s) of the 9th, 10th and 12th of May, 1979.

DESERT CHIM-1 FOR SOLAR ZENITH FROM 70.00 TO 80.00 DEG



DESERT SPATIAL SAMPLE FOR SOLAR ZENITH ANGLES FROM 70° TO 80°

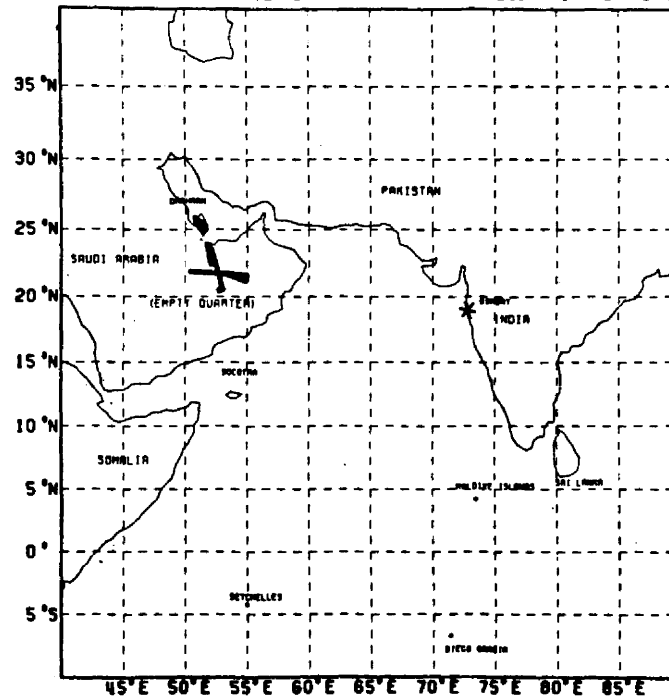
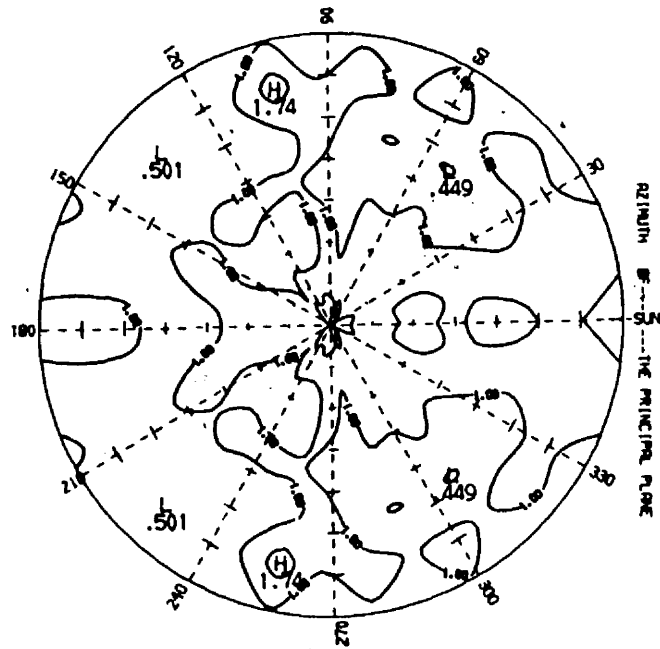


Figure AIII-8. Interpolated χ^{-1} pattern (left) and associated flight track (right) for the 70-80° solar zenith angle desert case. These data were collected during the MONEX flight(s) of the 9th, 10th and 12th of May, 1979.

HIMALA CHIM-1 FOR SOLAR ZENITH FROM 10.00 TO 20.00 DEG



HIMALAYAN SPATIAL SAMPLE FOR SOLAR ZENITH ANGLES FROM 10° TO 20°

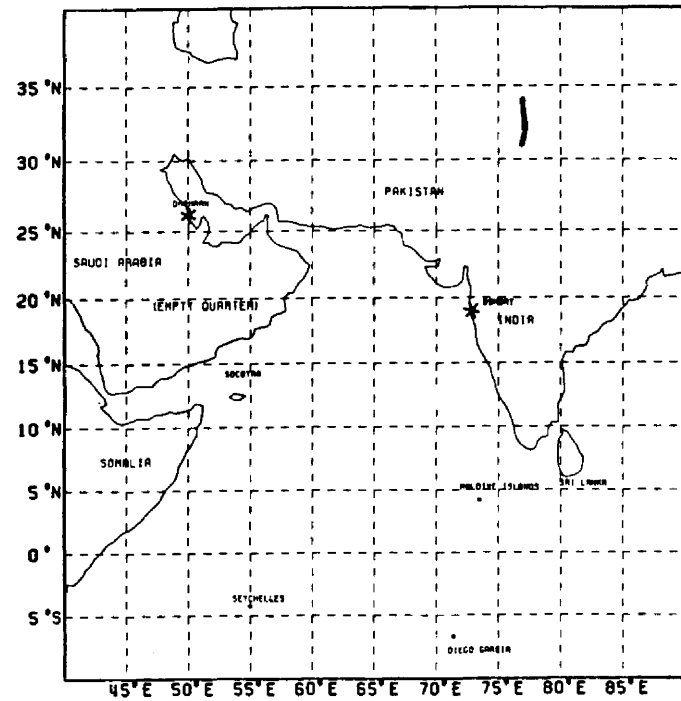
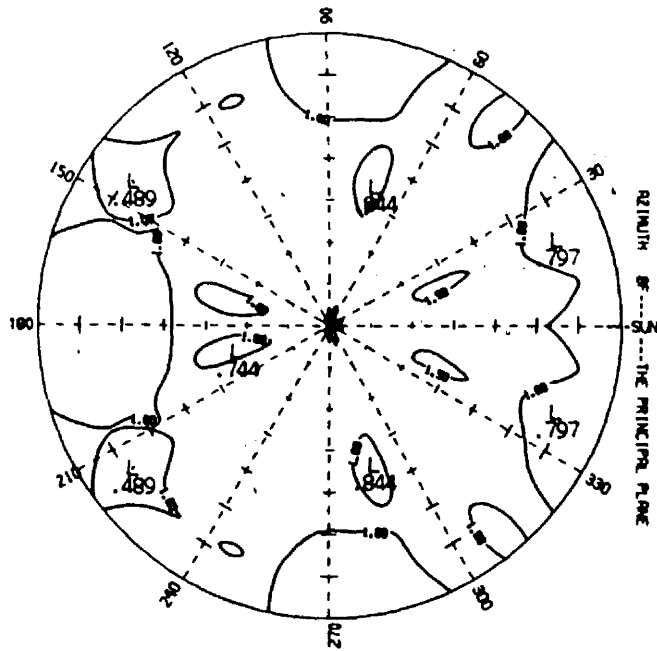


Figure AIII-9. Interpolated χ^{-1} pattern (left) and associated flight track (right) for the 10-20° solar zenith angle Himalaya case. These data were collected during the MONEX flight(s) of the 11th of June, 1979.

HIMALA CHIM-1 FOR SOLAR ZENITH FROM 20.00 TO 30.00 DEG



HIMALAYAN SPATIAL SAMPLE FOR SOLAR ZENITH ANGLES FROM 20° TO 30°

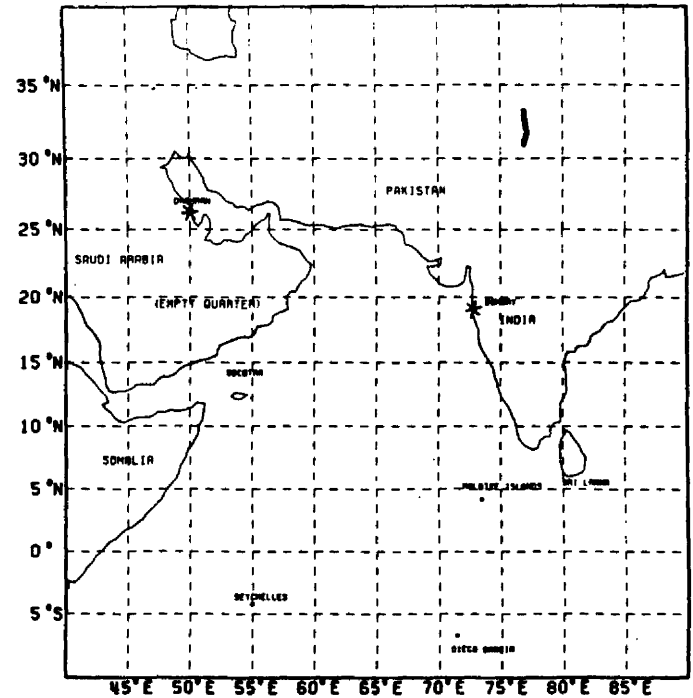
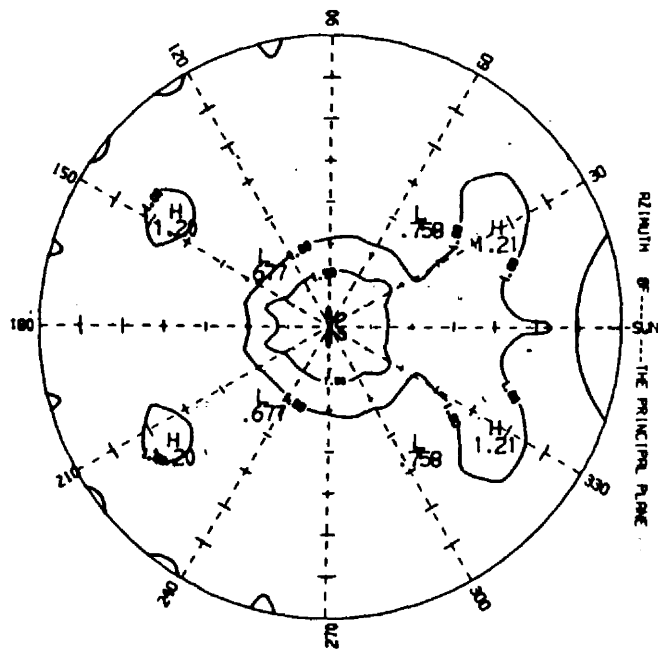


Figure AIII-10. Interpolated χ^2 pattern (left) and associated flight track (right) for the 20-30° solar zenith angle Himalaya case. These data were collected during the MONEX flight(s) of the 11th of June, 1979.

OCEAN χ^{-1} FOR SOLAR ZENITH FROM 0.00 TO 10.00 DEG



OCEAN SPATIAL SAMPLE FOR SOLAR ZENITH ANGLES FROM 0° TO 10°

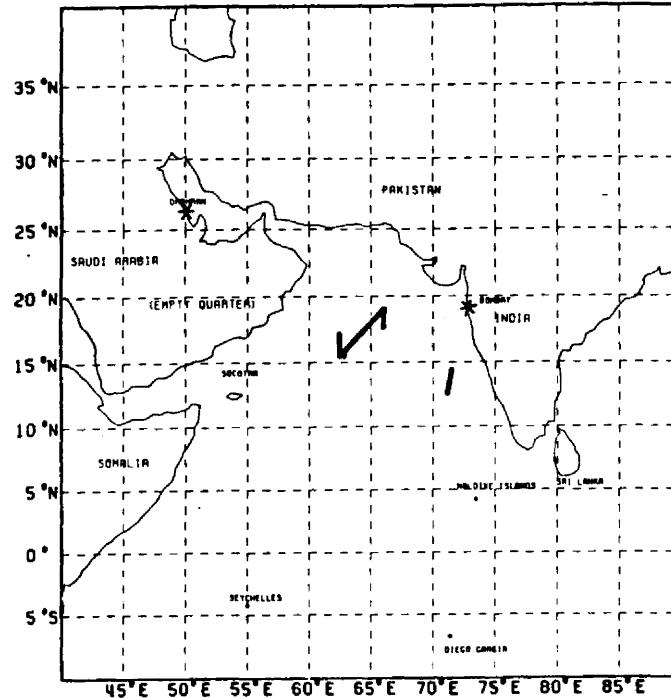
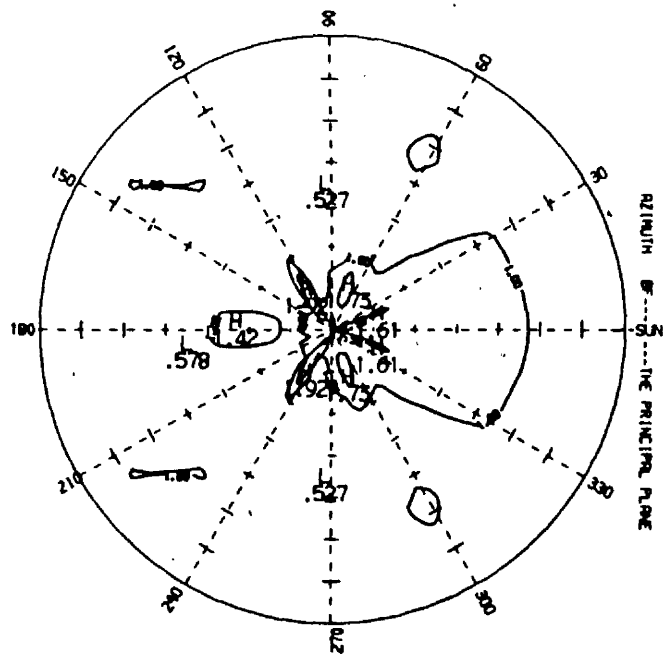


Figure AIII-11. Interpolated χ^{-1} pattern (left) and associated flight track (right) for the 0-10° solar zenith angle ocean case. These data were collected during the MONEX flight(s) of the 31st of May and 3rd of June, 1979.

OCEAN CHIM-1 FOR SOLAR ZENITH FROM 10.00 TO 20.00 DEG



OCEAN SPATIAL SAMPLE FOR SOLAR ZENITH ANGLES FROM 10° TO 20°

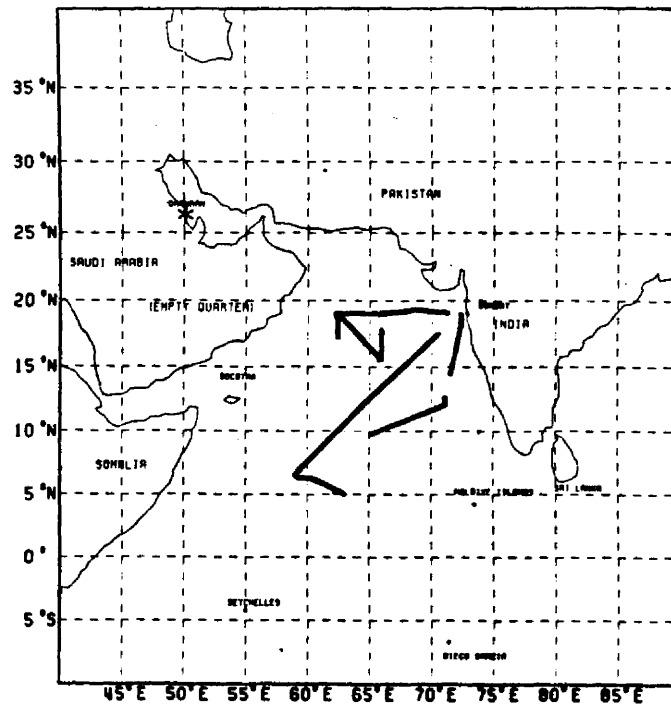
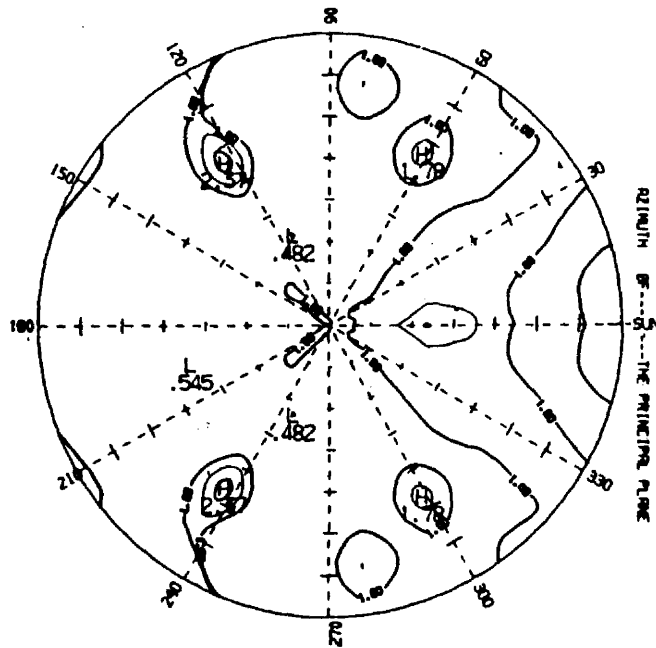


Figure AIII-12. Interpolated χ^{-1} pattern (left) and associated flight track (right) for the 10-20° solar zenith angle ocean case. These data were collected during the MONEX flight(s) of the 29th and 31st of May and the 3rd of June, 1979.

OCEAN CHIM-1 FOR SOLAR ZENITH FROM 20.00 TO 30.00 DEG



OCEAN SPATIAL SAMPLE FOR SOLAR ZENITH ANGLES FROM 20° TO 30°

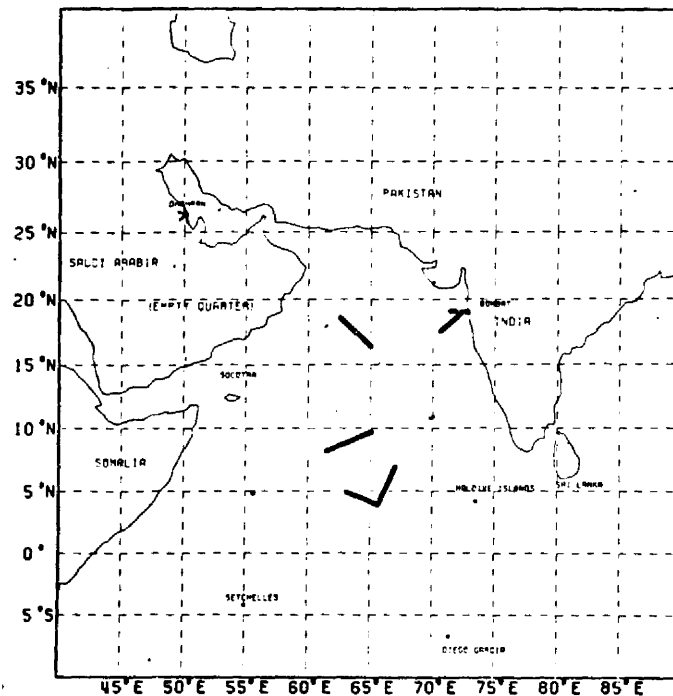
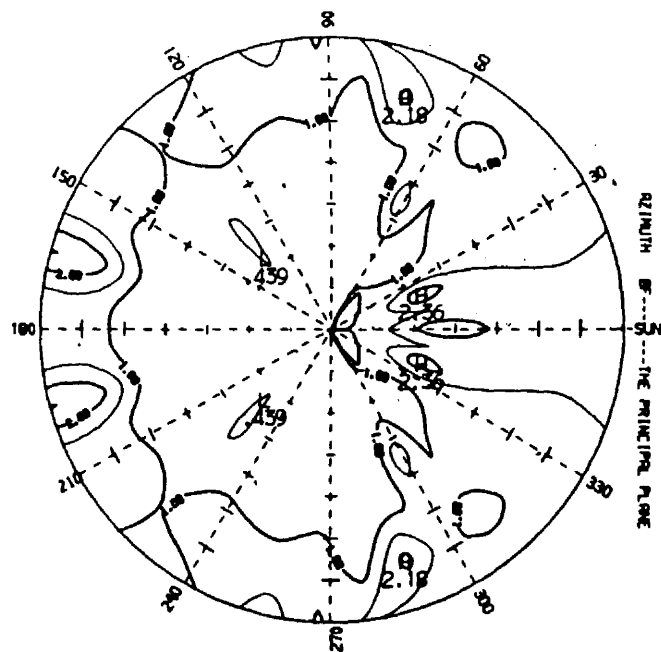


Figure AIII-13. Interpolated χ^{-1} pattern (left) and associated flight track (right) for the 20-30° solar zenith angle ocean case. These data were collected during the MONEX flight(s) of the 29th and 31st of May and the 3rd of June, 1979.

OCEAN CHIM-1 FOR SOLAR ZENITH FROM 30.00 TO 40.00 DEG



OCEAN SPATIAL SAMPLE FOR SOLAR ZENITH ANGLES FROM 30° TO 40°

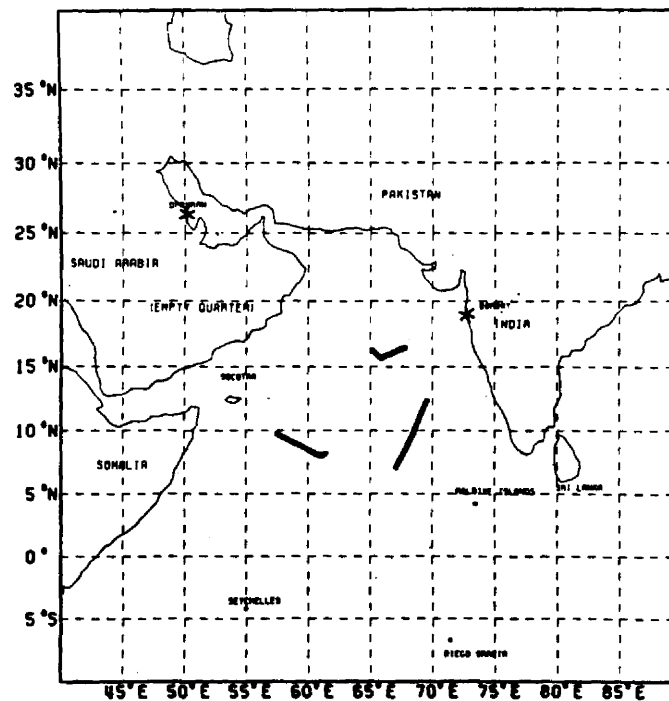
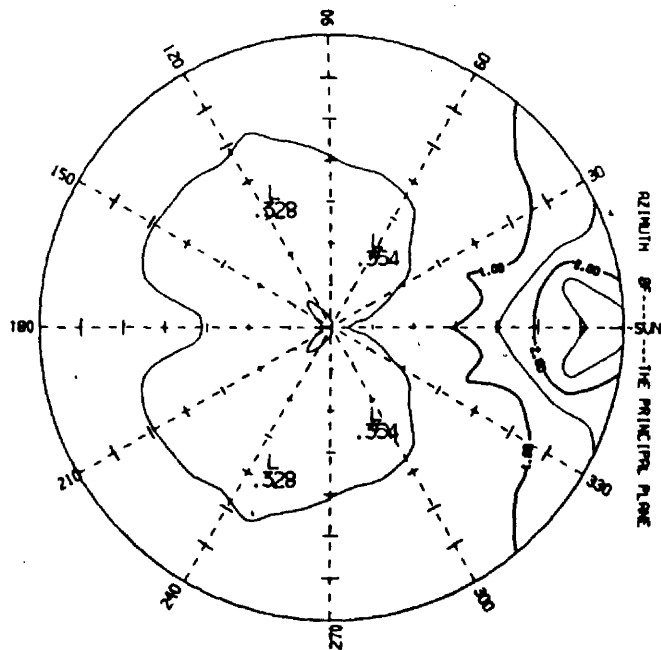


Figure AIII-14. Interpolated χ^{-1} pattern (left) and associated flight track (right) for the 30-40° solar zenith angle ocean case. These data were collected during the MONEX flight(s) of the 29th and 31st of May and the 3rd of June, 1979.

OCEAN CHIM-1 FOR SOLAR ZENITH FROM 50.00 TO 60.00 DEG



OCEAN SPATIAL SAMPLE FOR SOLAR ZENITH ANGLES FROM 50° TO 60°

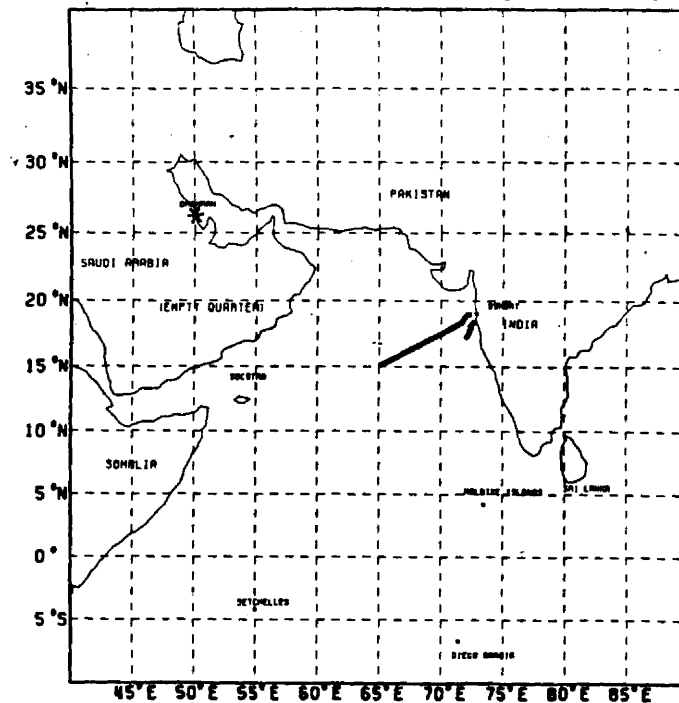


Figure AIII-16. Interpolated χ^{-1} pattern (left) and associated flight track (right) for the 50-60° solar zenith angle ocean case. These data were collected during the MONEX flight(s) of the 29th and 31st of May and the 3rd of June, 1979.

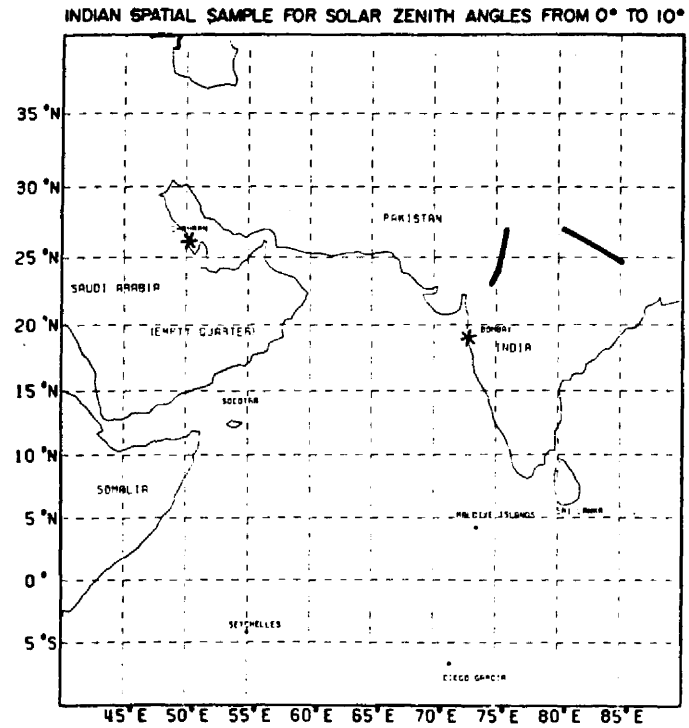
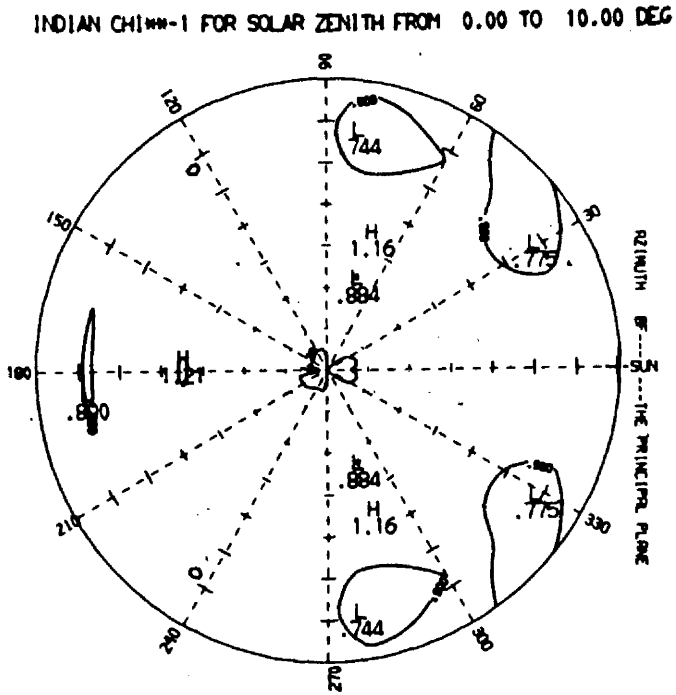
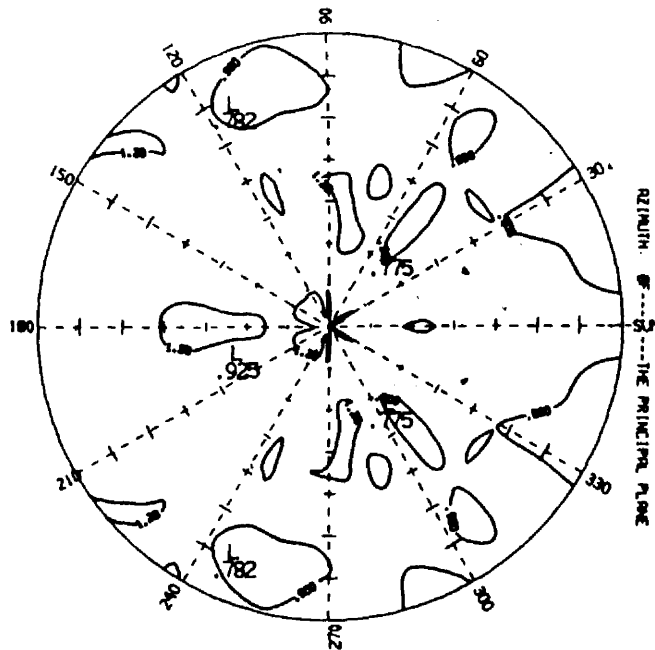


Figure AIII-17. Interpolated χ^{-1} pattern (left) and associated flight track (right) for the 0-10° solar zenith angle Indian subcontinent case. These data were collected during the MONEX flight(s) of the 5th and 11th of June, 1979.

INDIAN CHIM-1 FOR SOLAR ZENITH FROM 10.00 TO 20.00 DEG



INDIAN SPATIAL SAMPLE FOR SOLAR ZENITH ANGLES FROM 10° TO 20°

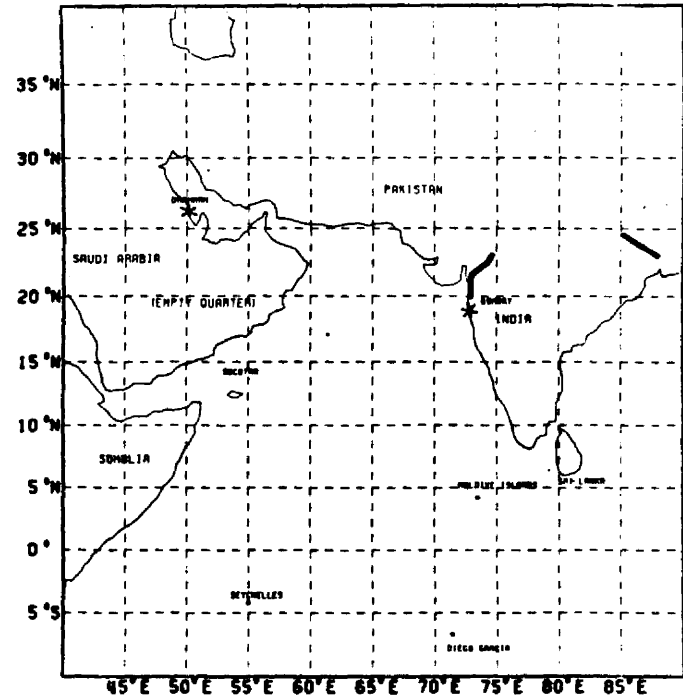
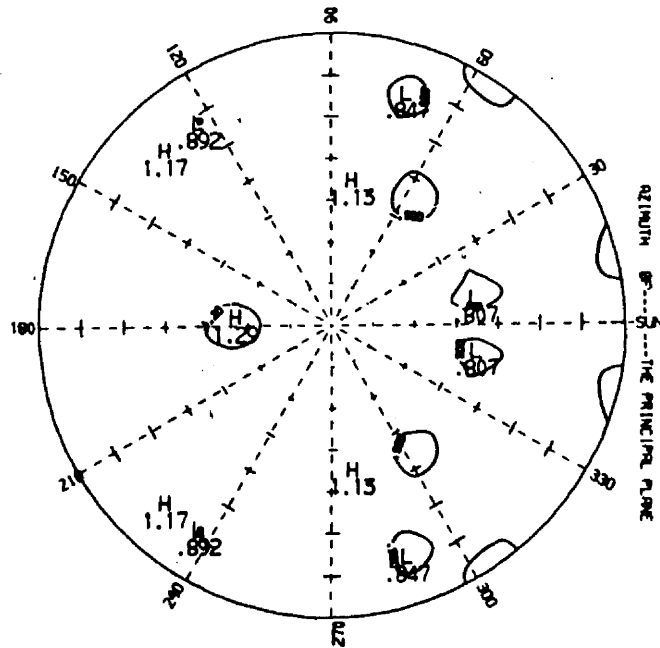


Figure AIII-18. Interpolated χ^{-1} pattern (left) and associated flight track (right) for the 10-20° solar zenith angle Indian Subcontinent case. These data were collected during the MONEX flight(s) of the 5th and 11th of June, 1979.

INDIAN CHIM-1 FOR SOLAR ZENITH FROM 20.00 TO 30.00 DEG



INDIAN SPATIAL SAMPLE FOR SOLAR ZENITH ANGLES FROM 20° TO 30°

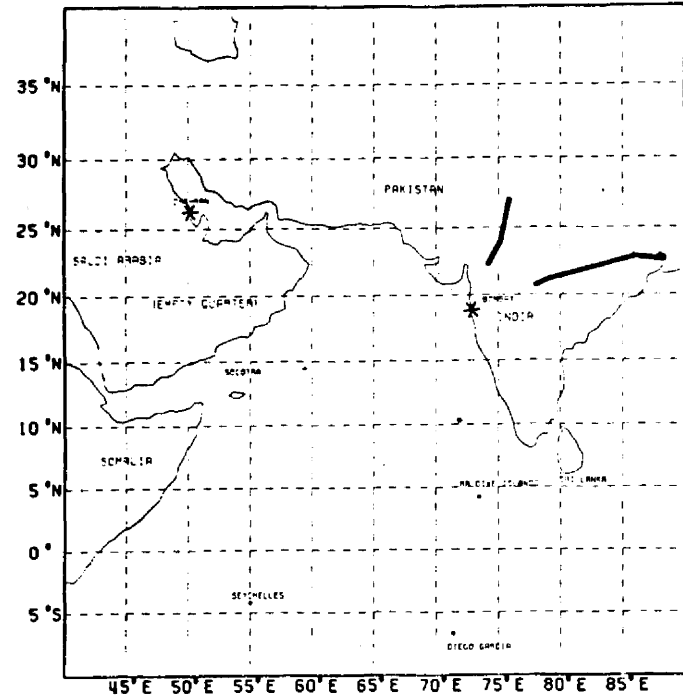
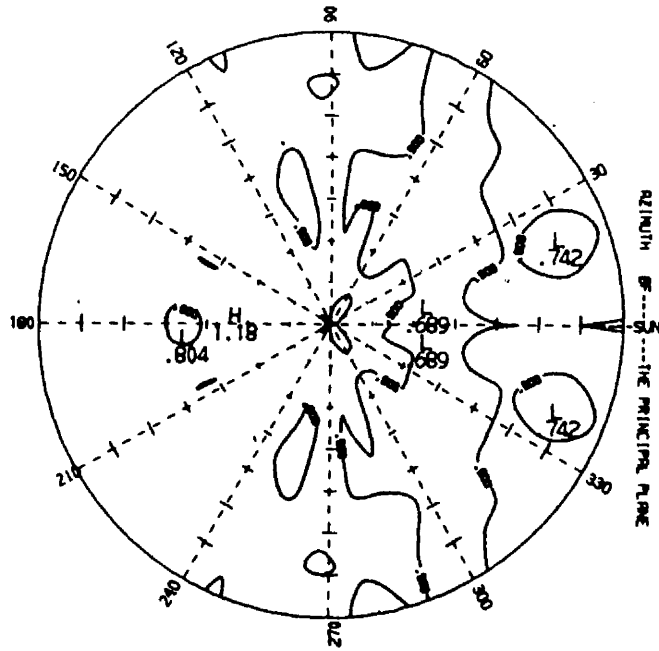


Figure AIII-19. Interpolated χ^{-1} pattern (left) and associated flight track (right) for the 20-30° solar zenith angle Indian Subcontinent case. These data were collected during the MONEX flight(s) of the 5th and 11th of June, 1979.

INDIAN CHIM-1 FOR SOLAR ZENITH FROM 30.00 TO 40.00 DEG



INDIAN SPATIAL SAMPLE FOR SOLAR ZENITH ANGLES FROM 30° TO 40°

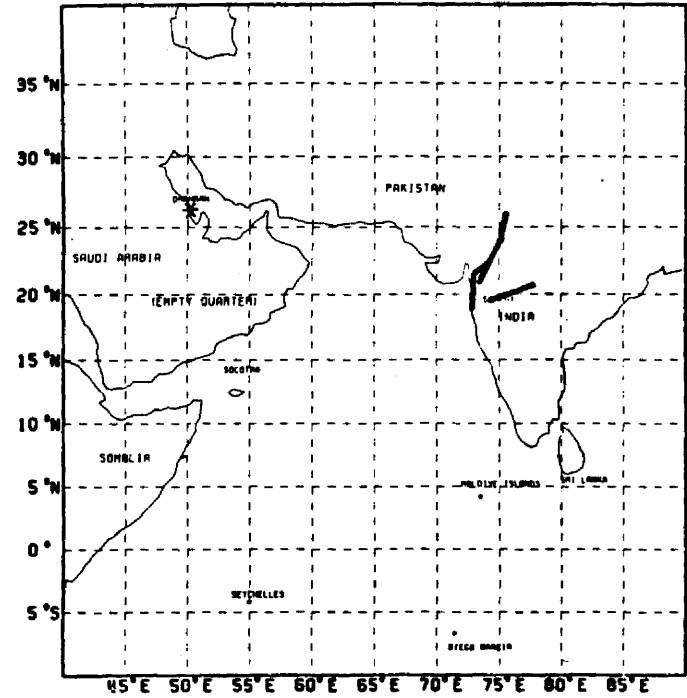
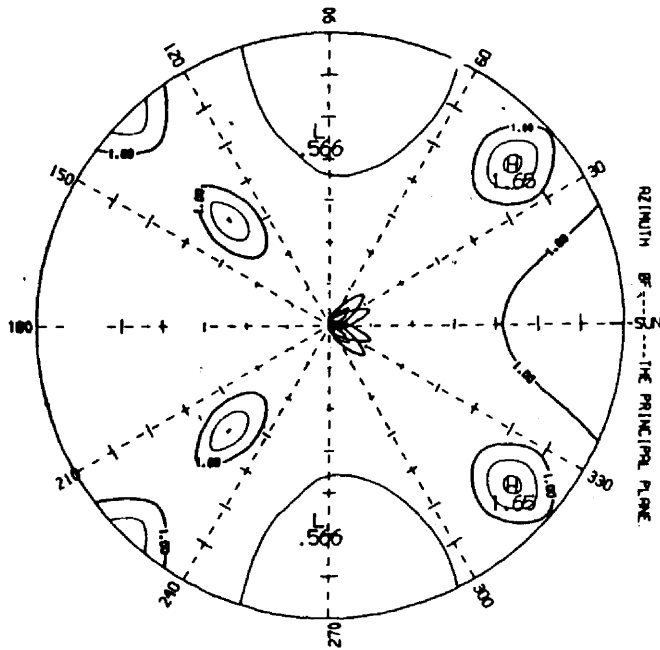


Figure AIII-20. Interpolated χ^{-1} pattern (left) and associated flight track (right) for the 30-40° solar zenith angle Indian Subcontinent case. These data were collected during the MONEX flight(s) of the 5th and 11th of June, 1979.

CLOUD1 CHI⁻¹ FOR SOLAR ZENITH FROM 0.00 TO 10.00 DEG



CLOUD1 SPATIAL SAMPLE FOR SOLAR ZENITH ANGLES FROM 0° TO 10°

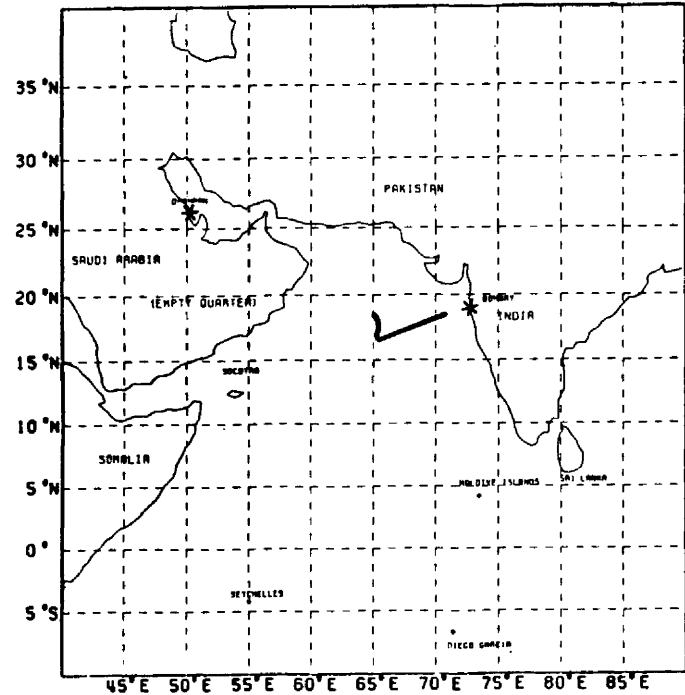
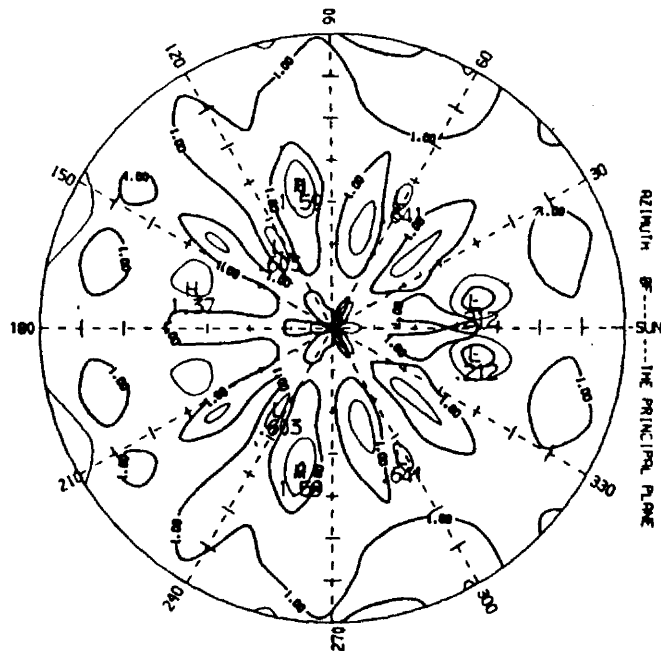


Figure AIII-21. Interpolated χ^{-1} pattern (left) and associated flight track (right) for the 0-10° solar zenith angle middle and low level cloud case. These data were collected during the MONEX flight(s) of the 23rd of June, 1979.

CLOUD1 CHI**2-1 FOR SOLAR ZENITH FROM 10.00 TO 20.00 DEG



CLOUD1 SPATIAL SAMPLE FOR SOLAR ZENITH ANGLES FROM 10° TO 20°

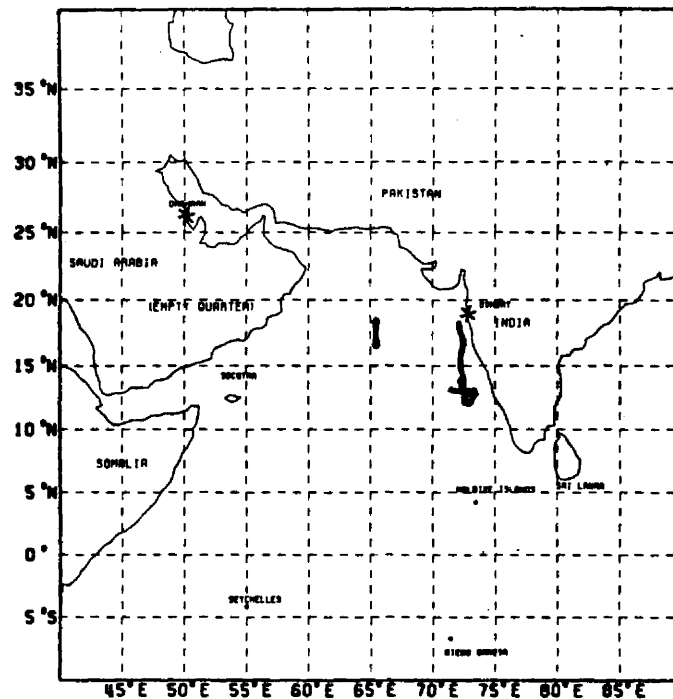
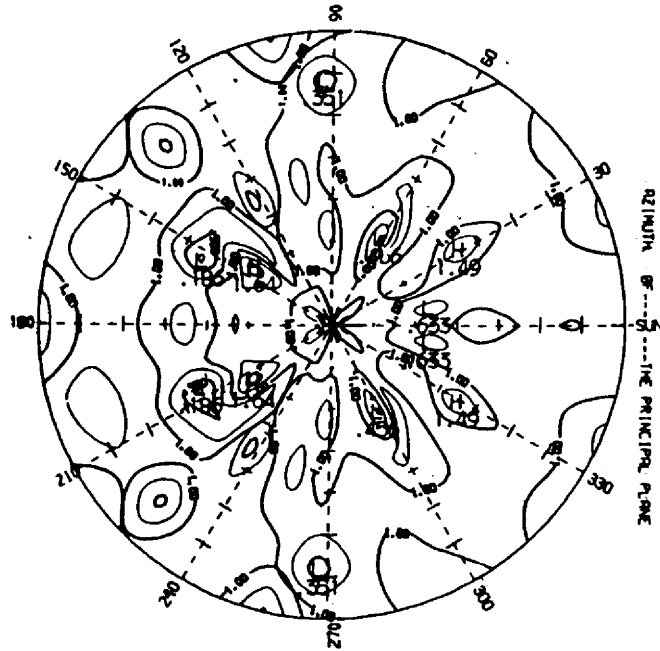


Figure AIII-22. Interpolated χ^{-1} pattern (left) and associated flight track (right) for the 10-20° solar zenith angle middle and low level cloud case. These data were collected during the MONEX flight(s) of the 19th and 23rd of June, 1979.

CLOUD1 CHI**2-1 FOR SOLAR ZENITH FROM 20.00 TO 30.00 DEG



CLOUD1 SPATIAL SAMPLE FOR SOLAR ZENITH ANGLES FROM 20° TO 30°

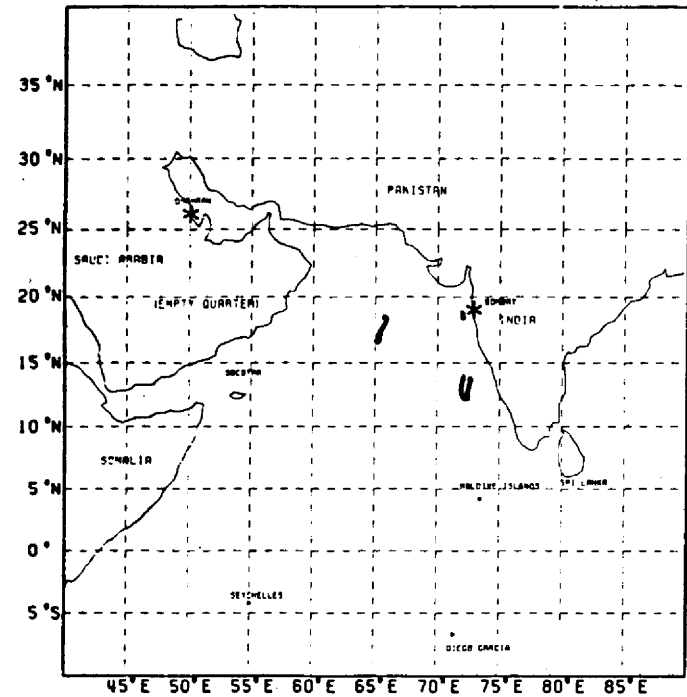
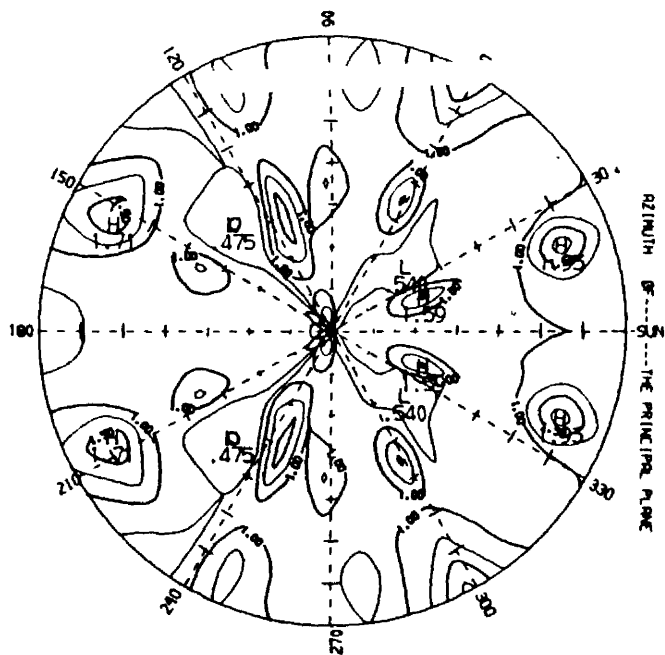


Figure AIII-23. Interpolated χ^2 pattern (left) and associated flight track (right) for the 20-30° solar zenith angle middle and low level cloud case. These data were collected during the MONEX flight(s) of the 19th and 23rd of June, 1979.

CLOUD1 CHI²-1 FOR SOLAR ZENITH FROM 30.00 TO 40.00 DEG



CLOUD1 SPATIAL SAMPLE FOR SOLAR ZENITH ANGLES FROM 30° TO 40°

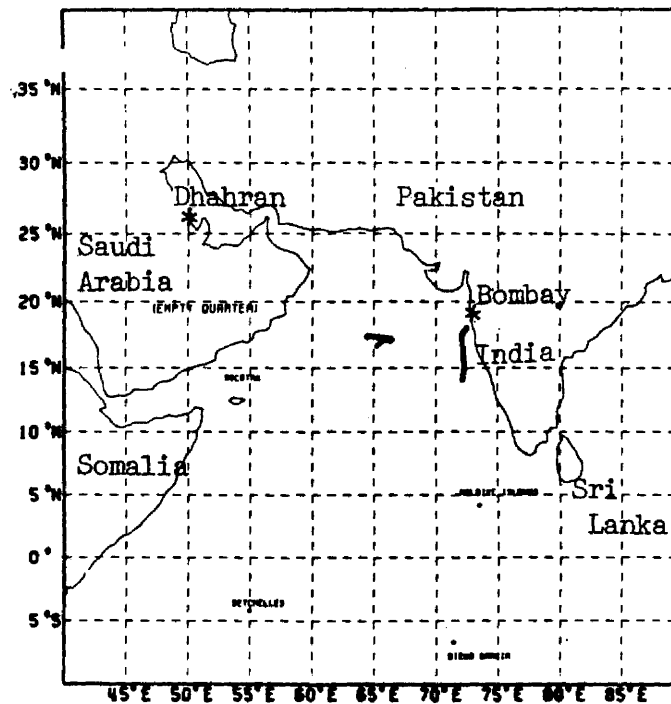
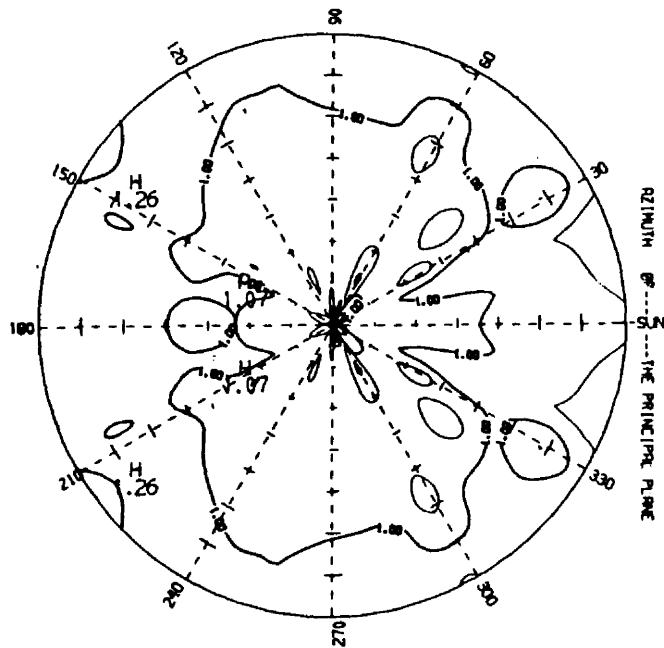
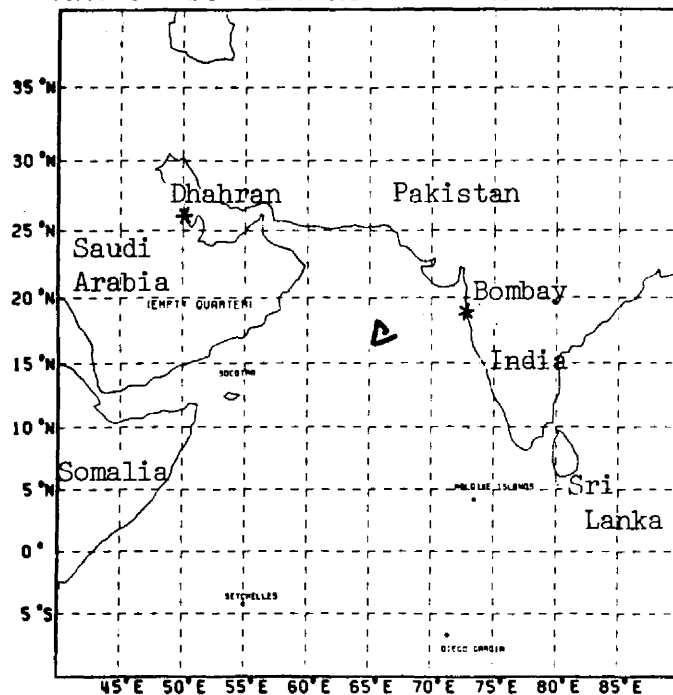


Figure AIII-24. Interpolated χ^2 pattern (left) and associated flight track (right) for the 30-40° solar zenith angle middle and low level cloud case. These data were collected during the MONEX flight(s) of the 19th and 23rd of June, 1979.

CLOUD1 CHI**2 FOR SOLAR ZENITH FROM 40.00 TO 50.00 DEG



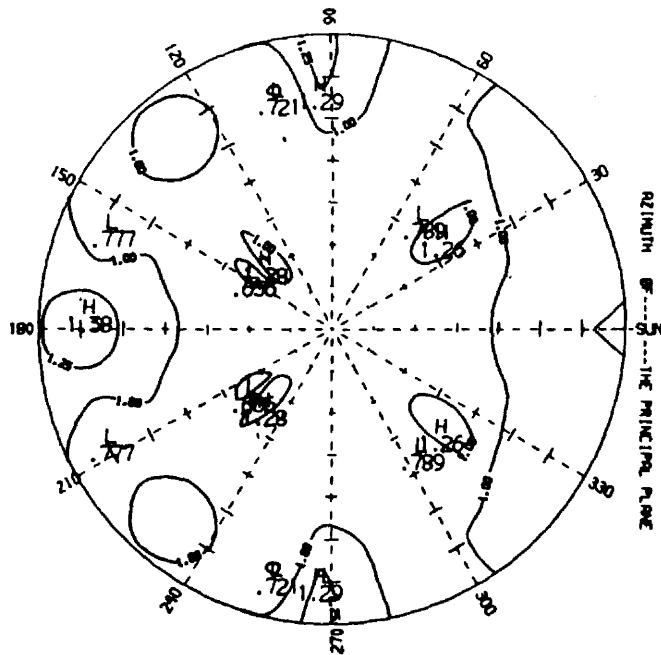
CLOUD1 SPATIAL SAMPLE FOR SOLAR ZENITH ANGLES FROM 40° TO 50°



AIII-26

Figure AIII-25. Interpolated χ^{-1} pattern (left) and associated flight track (right) for the 40-50° solar zenith angle middle and low level cloud case. These data were collected during the MONEX flight(s) of the 23rd of June, 1979.

CLOUD2 CHI⁻¹ FOR SOLAR ZENITH FROM 20.00 TO 30.00 DEG



CLOUD2 SPATIAL SAMPLE FOR SOLAR ZENITH ANGLES FROM 20° TO 30°

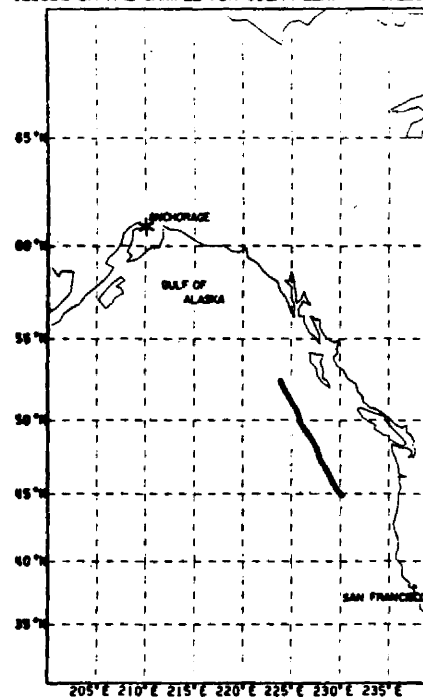
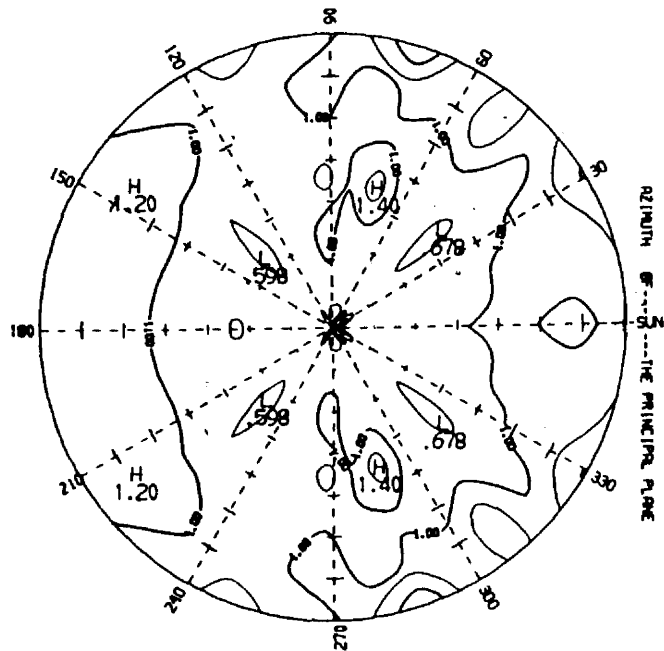


Figure AIII-26. Interpolated χ^{-1} pattern (left) and associated flight track (right) for the 20-30° solar zenith angle altostratus cloud case. These data were collected during the MONEX flight(s) of the 7th of July, 1979.

CLOUD2 CHIM-1 FOR SOLAR ZENITH FROM 30.00 TO 40.00 DEG



CLOUD2 SPATIAL SAMPLE FOR SOLAR ZENITH ANGLES FROM 30° TO 40°

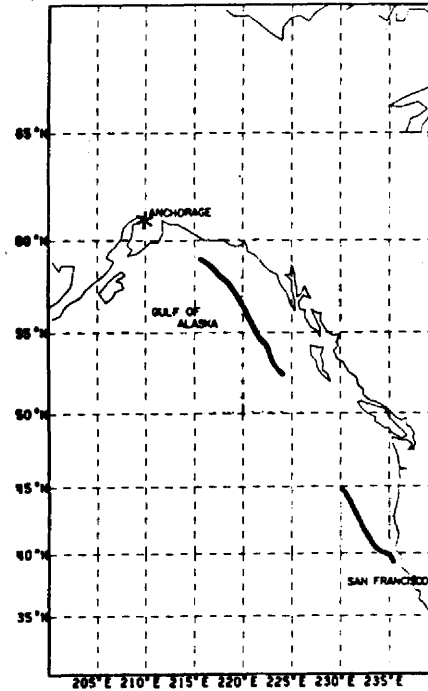


Figure AIII-27. Interpolated χ^2 pattern (left) and associated flight track (right) for the 30-40° solar zenith angle altostratus cloud case. These data were collected during the MONEX flight(s) of the 7th of July, 1979.

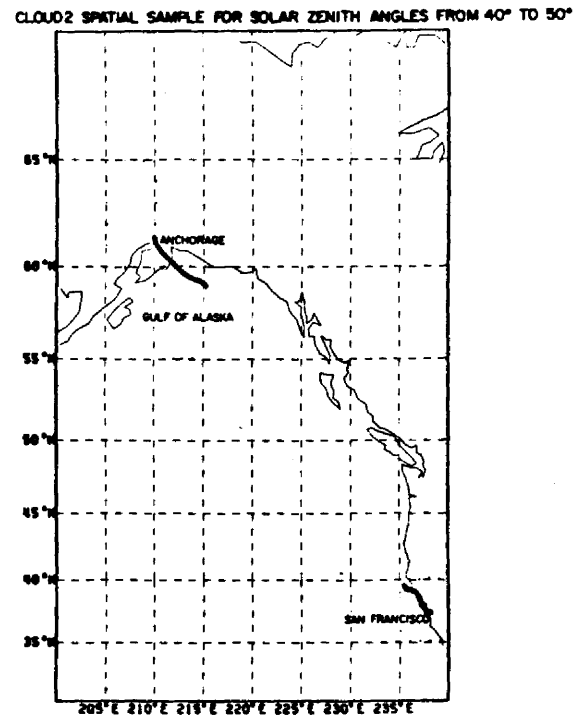
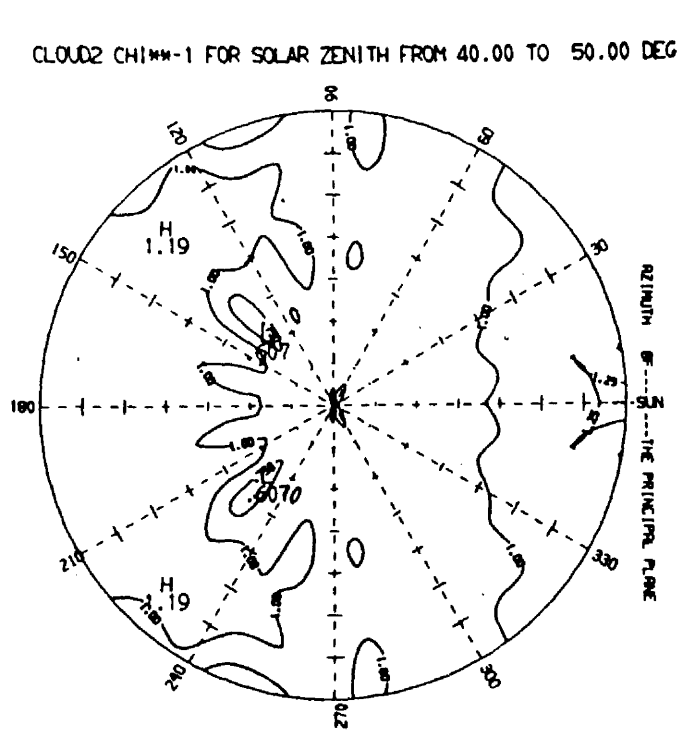


Figure AIII-28. Interpolated χ^{-1} pattern (left) and associated flight track (right) for the 40-50° solar zenith angle altostratus cloud case. These data were collected during the MONEX flight(s) of the 7th of July, 1979.

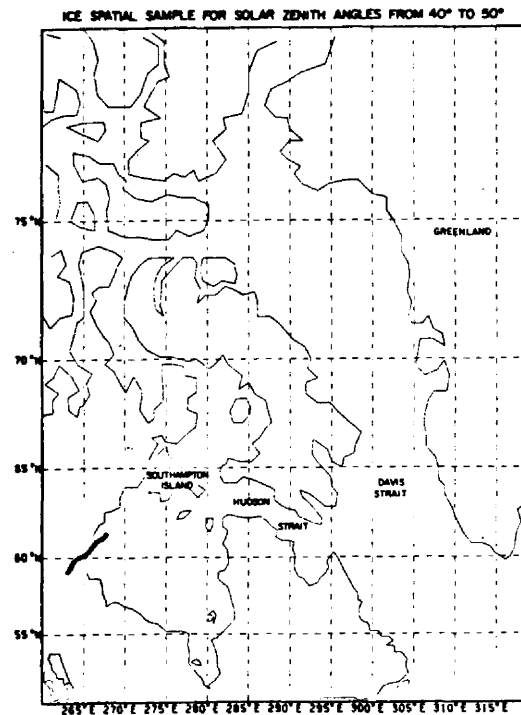
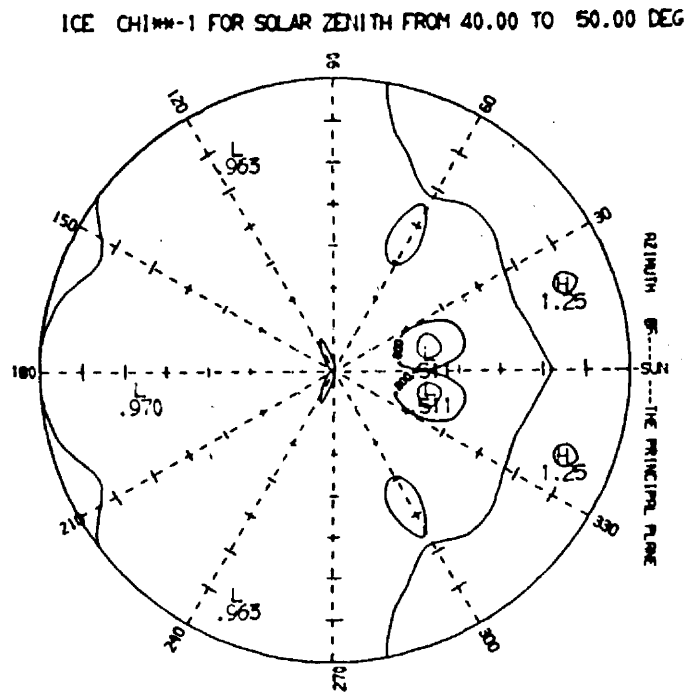


Figure AIII-29. Interpolated χ^{-1} pattern (left) and associated flight track (right) for the 40-50° solar zenith angle ice case. These data were collected during the MONEX flight(s) of the 30th of April, 1979.

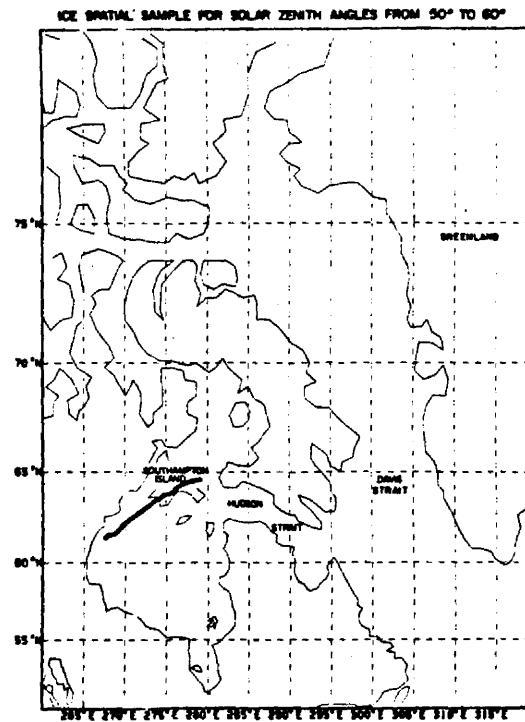
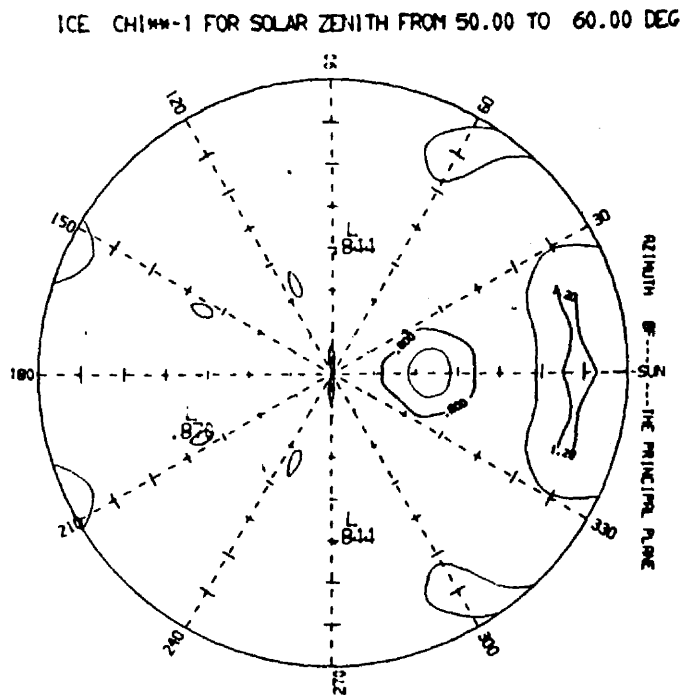


Figure AIII-30. Interpolated χ^{-1} pattern (left) and associated flight track (right) for the 50-60° solar zenith angle ice case. These data were collected during the MONEX flight(s) of the 30th of April, 1979.

APPENDIX IV

Appendix IV presents the coefficients of the least squares fit of all of the χ^{-1} patterns discussed in this study. The basis functions used in the regression are the spherical harmonic functions in a slightly modified form. Thus, each of the χ^{-1} patterns has been approximated as

$$\hat{\chi}^{-1}(\theta, \phi) = \sum_{i=1}^N c_i Y_i(\theta, \phi),$$

where θ is the nadir angle and ϕ the relative azimuth angle. $Y_i(\theta, \phi)$ is one of the spherical harmonics $Y_n^m(\theta, \phi)$, where for each value of n there are $2n+1$ possible values of m . In the approximations which follow n was allowed to range from 0 to 6 which allows i to range from 1 to 49. The terms in the fit which contribute less than 0.25% to the norm of $\hat{\chi}^{-1}$ have been discarded and a number weighted r.m.s. error has been calculated after deletion of these terms. Table AIV-1 lists the set of $Y_i(\theta, \phi)$ functions used in the fit. Figures AIV-1 through AIV-30 list the coefficients c_i , and the associated r.m.s. error of the fit. The user of these approximations is reminded that the approximations are considered valid for nadir angles of 70° or less and are considered to be extrapolations for nadir angles greater than 70° . A plot of the approximate $\hat{\chi}^{-1}$ field is also given for each scene type studied.

i	The ith basis function $Y_i(\theta, \phi)$
1	$Y_1 = 0.282094792$
2	$Y_2 = 0.488602512 \cdot \cos(\theta)$
3	$Y_3 = -0.345494149 \cdot \sin(\theta) \cdot \cos(\phi)$
4	$Y_4 = 0.345494149 \cdot \sin(\theta) \cdot \sin(\phi)$
5	$Y_5 = 0.630783130 \cdot (1.5 \cdot \cos^2(\theta) - 0.5)$
6	$Y_6 = -0.772548404 \cdot \sin(\theta) \cdot \cos(\theta) \cdot \cos(\phi)$
7	$Y_7 = 0.772548404 \cdot \sin(\theta) \cdot \cos(\theta) \cdot \sin(\phi)$
8	$Y_8 = 0.386274202 \cdot \sin^2(\theta) \cdot \cos(2\phi)$
9	$Y_9 = -0.386274202 \cdot \sin^2(\theta) \cdot \sin(2\phi)$
10	$Y_{10} = -0.417224000 \cdot \sin^3(\theta) \cdot \cos(3\phi)$
11	$Y_{11} = 0.417224000 \cdot \sin^3(\theta) \cdot \sin(3\phi)$
12	$Y_{12} = 1.021985000 \cdot \cos(\theta) \cdot \sin^2(\theta) \cdot \cos(2\phi)$
13	$Y_{13} = -1.021985000 \cdot \cos(\theta) \cdot \sin^2(\theta) \cdot \sin(2\phi)$
14	$Y_{14} = 0.323180140 \cdot (5 \cdot \cos^2(\theta) - 1) \cdot \sin(\theta) \cdot \cos(3\phi)$
15	$Y_{15} = -0.323180140 \cdot (5 \cdot \cos^2(\theta) - 1) \cdot \sin(\theta) \cdot \sin(3\phi)$
16	$Y_{16} = 0.373176300 \cdot (5 \cdot \cos^3(\theta) - 3 \cdot \cos(\theta))$
17	$Y_{17} = 0.442530000 \cdot \sin^4(\theta) \cdot \cos(4\phi)$
18	$Y_{18} = 0.442530000 \cdot \sin^4(\theta) \cdot \sin(4\phi)$
19	$Y_{19} = -1.251670000 \cdot \cos(\theta) \cdot \sin^3(\theta) \cdot \cos(3\phi)$
20	$Y_{20} = 1.251670000 \cdot \cos(\theta) \cdot \sin^3(\theta) \cdot \sin(3\phi)$
21	$Y_{21} = 0.334520000 \cdot (7 \cdot \cos^2(\theta) - 1) \cdot \sin^2(\theta) \cdot \cos(2\phi)$
22	$Y_{22} = 0.334520000 \cdot (7 \cdot \cos^2(\theta) - 1) \cdot \sin^2(\theta) \cdot \sin(2\phi)$
23	$Y_{23} = -0.283850000 \cdot (5 \cdot \cos^2(\theta) - 1) \cdot \sin(\theta) \cdot \cos(\phi)$
24	$Y_{24} = 0.283850000 \cdot (5 \cdot \cos^2(\theta) - 1) \cdot \sin(\theta) \cdot \sin(\phi)$
25	$Y_{25} = 0.105790000 \cdot (35 \cdot \cos^4(\theta) - 30 \cdot \cos^2(\theta) + 3)$
26	$Y_{26} = -0.464130000 \cdot \sin^5(\theta) \cdot \cos(5\phi)$
27	$Y_{27} = 0.464130000 \cdot \sin^5(\theta) \cdot \sin(5\phi)$
28	$Y_{28} = 1.467700000 \cdot \sin^4(\theta) \cdot \cos(\theta) \cdot \cos(4\phi)$
29	$Y_{29} = -1.467700000 \cdot \sin^4(\theta) \cdot \cos(\theta) \cdot \sin(4\phi)$
30	$Y_{30} = -0.345940000 \cdot (9 \cdot \cos^2(\theta) - 1) \cdot \cos(3\phi)$
31	$Y_{31} = 0.345940000 \cdot (9 \cdot \cos^2(\theta) - 1) \cdot \sin(3\phi)$
32	$Y_{32} = 1.694770000 \cdot (3 \cdot \cos^3(\theta) - \cos(\theta)) \cdot \cos(2\phi)$

Table AIV-1. (Page 1)

i	The ith basis function $Y_i(\theta, \phi)$
33	$Y_{33} = -1.694770000 \cdot (3 \cdot \cos^3(\theta) - \cos(\theta)) \cdot \sin(2\phi)$
34	$Y_{34} = -0.320280000 \cdot (21 \cdot \cos^4(\theta) - 14 \cdot \cos^2(\theta) + 1) \cdot \cos(\phi)$
35	$Y_{35} = 0.320280000 \cdot (21 \cdot \cos^4(\theta) - 14 \cdot \cos^2(\theta) + 1) \cdot \sin(\phi)$
36	$Y_{36} = 0.116950000 \cdot (63 \cdot \cos^5(\theta) - 70 \cdot \cos^3(\theta) + 15 \cdot \cos(\theta))$
37	$Y_{37} = 0.483080000 \cdot \sin^6(\theta) \cdot \cos(6\phi)$
38	$Y_{38} = -0.483080000 \cdot \sin^6(\theta) \cdot \sin(6\phi)$
39	$Y_{39} = 1.673450000 \cdot \sin^5(\theta) \cdot \cos(\theta) \cdot \cos(5\phi)$
40	$Y_{40} = -1.673450000 \cdot \sin^5(\theta) \cdot \cos(\theta) \cdot \sin(5\phi)$
41	$Y_{41} = 0.356780000 \cdot \sin^4(\theta) \cdot (11 \cdot \cos^2(\theta) - 1) \cdot \cos(4\phi)$
42	$Y_{42} = -0.356780000 \cdot \sin^4(\theta) \cdot (11 \cdot \cos^2(\theta) - 1) \cdot \sin(4\phi)$
43	$Y_{43} = 0.651390000 \cdot \sin^3(\theta) \cdot (11 \cdot \cos^3(\theta) - 3 \cdot \cos(\theta)) \cdot \cos(3\phi)$
44	$Y_{44} = -0.651390000 \cdot \sin^3(\theta) \cdot (11 \cdot \cos^3(\theta) - 3 \cdot \cos(\theta)) \cdot \sin(3\phi)$
45	$Y_{45} = 0.325690000 \cdot \sin^2(\theta) \cdot (33 \cdot \cos^4(\theta) - 18 \cdot \cos^2(\theta) + 1) \cdot \sin(2\phi)$
46	$Y_{46} = -0.325690000 \cdot \sin^2(\theta) \cdot (33 \cdot \cos^4(\theta) - 18 \cdot \cos^2(\theta) + 1) \cdot \cos(2\phi)$
47	$Y_{47} = 0.411980000 \cdot \sin(\theta) \cdot (77 \cdot \cos^5(\theta) - 70 \cdot \cos^3(\theta) + 5 \cdot \cos(\theta)) \cdot \cos(\phi)$
48	$Y_{48} = -0.411980000 \cdot \sin(\theta) \cdot (77 \cdot \cos^5(\theta) - 70 \cdot \cos^3(\theta) + 5 \cdot \cos(\theta)) \cdot \sin(\phi)$
49	$Y_{49} = 0.063570000 \cdot (231 \cdot \cos^6(\theta) - 315 \cdot \cos^4(\theta) + 105 \cdot \cos^2(\theta) + 5)$

Table AIV-1. Modified spherical harmonic functions which form the basis of the $\hat{\chi}^{-1}$ approximations.

I	C(I)	I	C(I)
1	-0.89984908E+02	25	-0.25278422E+02
2	0.13297564E+03	26	0.00000000E+00
3	-0.10878301E+01	27	0.00000000E+00
4	0.00000000E+00	28	0.00000000E+00
5	-0.11301137E+03	29	0.00000000E+00
6	0.10713094E+01	30	0.00000000E+00
7	0.00000000E+00	31	0.00000000E+00
8	0.30427038E+01	32	-0.28637111E-01
9	0.00000000E+00	33	0.00000000E+00
10	0.96395391E+00	34	0.00000000E+00
11	0.00000000E+00	35	0.00000000E+00
12	-0.28137626E+01	36	0.48379464E+01
13	0.00000000E+00	37	0.00000000E+00
14	-0.21033496E+00	38	0.00000000E+00
15	0.00000000E+00	39	0.00000000E+00
16	0.66471030E+02	40	0.00000000E+00
17	0.00000000E+00	41	0.00000000E+00
18	0.00000000E+00	42	0.00000000E+00
19	-0.62670764E+00	43	0.00000000E+00
20	0.00000000E+00	44	0.00000000E+00
21	0.10645928E+01	45	0.00000000E+00
22	0.00000000E+00	46	0.00000000E+00
23	-0.36653294E+00	47	0.00000000E+00
24	0.00000000E+00	48	0.00000000E+00
25	-0.25278422E+02	49	0.00000000E+00

NUMBER WEIGHTED RMS ERROR OF THE FIT EQUALS 5.3 PERCENT

DESERT CHIM-1 FOR SOLAR ZENITH FROM 0.00 TO 10.00 DEG

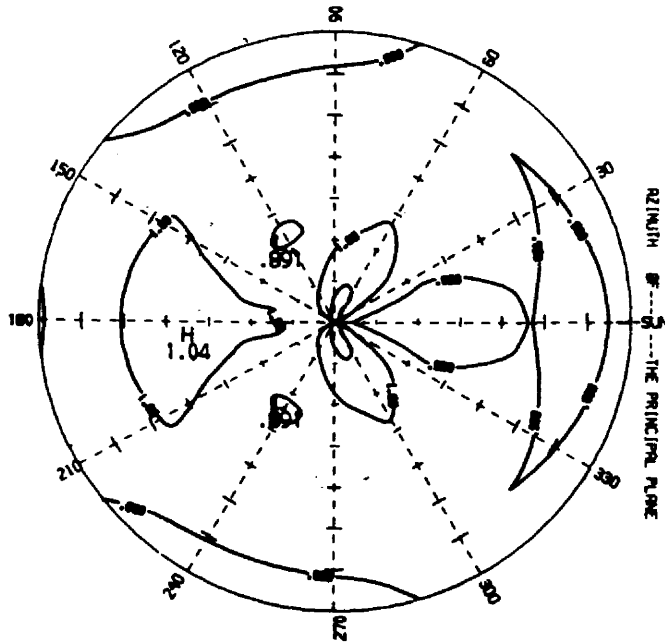


FIGURE AIV- 1. REGRESSION COEFFICIENTS OF THE SPHERICAL HARMONIC APPROXIMATION TO THE DESERT CHIM-1 PATTERN FOR SOLAR ZENITH ANGLES FROM 0. TO 10. DEGREES AND THE CORRESPONDING PLOT OF THE PATTERN

I	C(I)	I	C(I)
1	-0.22244757E+02	25	-0.51467080E+01
2	0.36070982E+02	26	0.00000000E+00
3	0.00000000E+00	27	0.00000000E+00
4	0.00000000E+00	28	0.00000000E+00
5	-0.29747529E+02	29	0.00000000E+00
6	0.00000000E+00	30	0.00000000E+00
7	0.00000000E+00	31	0.00000000E+00
8	0.00000000E+00	32	0.00000000E+00
9	0.00000000E+00	33	0.00000000E+00
10	-0.33212242E+00	34	0.00000000E+00
11	0.00000000E+00	35	0.00000000E+00
12	0.22765003E+00	36	0.11559307E+01
13	0.00000000E+00	37	0.00000000E+00
14	0.00000000E+00	38	0.00000000E+00
15	0.00000000E+00	39	0.00000000E+00
16	0.16870359E+02	40	0.00000000E+00
17	0.00000000E+00	41	0.00000000E+00
18	0.00000000E+00	42	0.00000000E+00
19	0.19910783E+00	43	0.00000000E+00
20	0.00000000E+00	44	0.00000000E+00
21	0.00000000E+00	45	0.00000000E+00
22	0.00000000E+00	46	0.00000000E+00
23	0.00000000E+00	47	0.00000000E+00
24	0.00000000E+00	48	0.00000000E+00
25	-0.51467080E+01	49	0.00000000E+00

NUMBER WEIGHTED RMS ERROR OF THE FIT EQUALS 6.5 PERCENT

DESERT CHIM--1 FOR SOLAR ZENITH FROM 10.00 TO 20.00 DEG

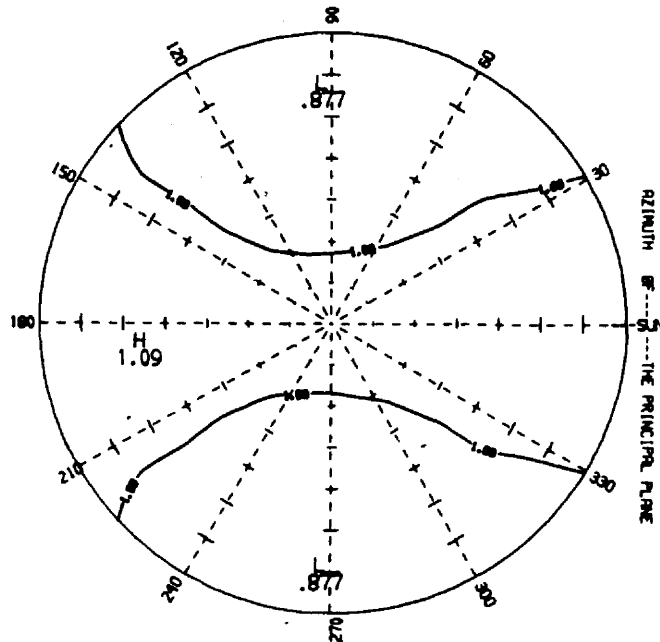


FIGURE AIV- 2. REGRESSION COEFFICIENTS OF THE SPHERICAL HARMONIC APPROXIMATION TO THE DESERT CHIM--1 PATTERN FOR SOLAR ZENITH ANGLES FROM 10. TO 20. DEGREES AND THE CORRESPONDING POLE OF THE PATTERN

I	C(I)	I	C(I)
1	-0.16611212E+02	25	-0.39576036E+01
2	0.27551747E+02	26	0.00000000E+00
3	0.32078137E+00	27	0.00000000E+00
4	0.00000000E+00	28	-0.15971842E+00
5	-0.21738561E+02	29	0.00000000E+00
6	0.00000000E+00	30	0.00000000E+00
7	0.00000000E+00	31	0.00000000E+00
8	0.00000000E+00	32	0.00000000E+00
9	0.00000000E+00	33	0.00000000E+00
10	0.00000000E+00	34	0.00000000E+00
11	0.00000000E+00	35	0.00000000E+00
12	0.27943926E+00	36	0.54317549E+00
13	0.00000000E+00	37	0.00000000E+00
14	0.00000000E+00	38	0.00000000E+00
15	0.00000000E+00	39	0.00000000E+00
16	0.11576223E+02	40	0.00000000E+00
17	0.24834504E+00	41	0.00000000E+00
18	0.00000000E+00	42	0.00000000E+00
19	0.00000000E+00	43	0.00000000E+00
20	0.00000000E+00	44	0.00000000E+00
21	0.00000000E+00	45	0.00000000E+00
22	0.00000000E+00	46	0.00000000E+00
23	0.00000000E+00	47	0.00000000E+00
24	0.00000000E+00	48	0.00000000E+00
25	-0.39576036E+01	49	0.00000000E+00

NUMBER WEIGHTED RMS ERROR OF THE FIT EQUALS 8.7 PERCENT

DESERT CHIM-1 FOR SOLAR ZENITH FROM 20.00 TO 30.00 DEG

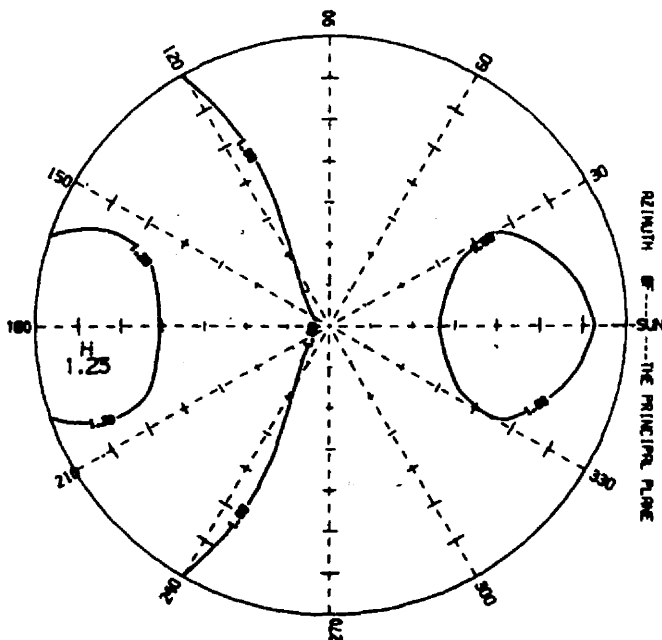


FIGURE AIV-3. REGRESSION COEFFICIENTS OF THE SPHERICAL HARMONIC APPROXIMATION TO THE DESERT CHIM-1 PATTERN FOR SOLAR ZENITH ANGLES FROM 20. DEGREES TO 30. DEGREES AND THE CORRESPONDING PLOT OF THE PATTERN

I	C(I)	I	C(I)
1	0.30507808E+02	25	0.31110688E+01
2	-0.35332370E+02	26	0.00000000E+00
3	-0.14279303E+01	27	0.00000000E+00
4	0.00000000E+00	28	0.00000000E+00
5	0.25444322E+02	29	0.00000000E+00
6	0.13454101E+01	30	0.00000000E+00
7	0.00000000E+00	31	0.00000000E+00
8	0.17380848E+01	32	0.00000000E+00
9	0.00000000E+00	33	0.00000000E+00
10	0.00000000E+00	34	0.00000000E+00
11	0.00000000E+00	35	0.00000000E+00
12	-0.15776045E+01	36	-0.25455964E+00
13	0.00000000E+00	37	0.00000000E+00
14	0.00000000E+00	38	0.00000000E+00
15	0.00000000E+00	39	0.00000000E+00
16	-0.11729097E+02	40	0.00000000E+00
17	0.00000000E+00	41	0.00000000E+00
18	0.00000000E+00	42	0.00000000E+00
19	0.00000000E+00	43	0.00000000E+00
20	0.00000000E+00	44	0.00000000E+00
21	0.57699983E+00	45	0.00000000E+00
22	0.00000000E+00	46	0.00000000E+00
23	0.00000000E+00	47	0.00000000E+00
24	0.00000000E+00	48	0.00000000E+00
25	0.31110688E+01	49	0.00000000E+00

NUMBER WEIGHTED RMS ERROR OF THE FIT EQUALS 9.0 PERCENT

DESERT CHIM-1 FOR SOLAR ZENITH FROM 30.00 TO 40.00 DEG

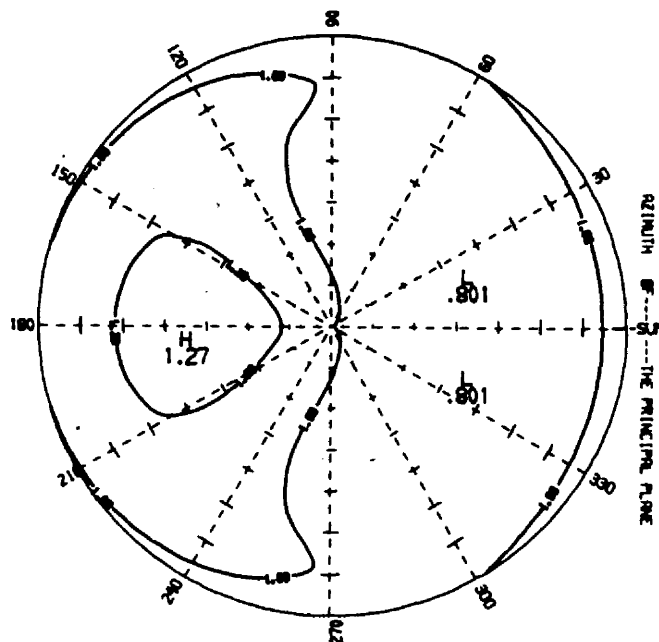


FIGURE AIV-4. REGRESSION COEFFICIENTS OF THE SPHERICAL HARMONIC APPROXIMATION TO THE DESERT CHIM-1 PATTERN FOR SOLAR ZENITH ANGLES FROM 30. TO 40. DEGREES AND THE CORRESPONDING PLOT OF THE PATTERN

I	C(I)	I	C(I)
1	0.37042235E+02	25	0.15363553E+02
2	-0.11342510E+03	26	0.00000000E+00
3	0.00000000E+00	27	0.00000000E+00
4	0.00000000E+00	28	0.12644040E+00
5	0.89514379E+02	29	0.00000000E+00
6	0.00000000E+00	30	0.00000000E+00
7	0.00000000E+00	31	0.00000000E+00
8	-0.16062025E+00	32	0.00000000E+00
9	0.00000000E+00	33	0.00000000E+00
10	0.00000000E+00	34	0.00000000E+00
11	0.00000000E+00	35	0.00000000E+00
12	0.35185013E+00	36	-0.27331163E+01
13	0.00000000E+00	37	0.00000000E+00
14	0.00000000E+00	38	0.00000000E+00
15	0.00000000E+00	39	0.00000000E+00
16	-0.47315669E+02	40	0.00000000E+00
17	-0.10176447E+00	41	0.00000000E+00
18	0.00000000E+00	42	0.00000000E+00
19	0.00000000E+00	43	0.00000000E+00
20	0.00000000E+00	44	0.00000000E+00
21	-0.76705975E-01	45	0.00000000E+00
22	0.00000000E+00	46	0.00000000E+00
23	0.00000000E+00	47	0.00000000E+00
24	0.00000000E+00	48	0.00000000E+00
25	0.16363553E+02	49	0.00000000E+00

NUMBER WEIGHTED RMS ERROR OF THE FIT EQUALS 4.0 PERCENT

DESERT CHIM-1 FOR SOLAR ZENITH FROM 40.00 TO 50.00 DEG

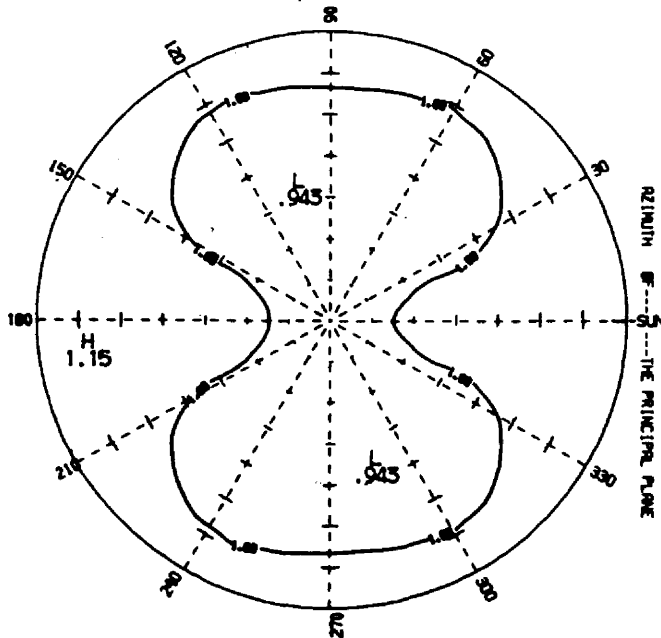


FIGURE AIV- 5. REGRESSION COEFFICIENTS OF THE SPHERICAL HARMONIC APPROXIMATION TO THE DESERT CHIM-1 PATTERN FOR SOLAR ZENITH ANGLES FROM 40. TO 50. DEGREES AND THE CORRESPONDING PLOT OF THE PATTERN

I	C(I)	I	C(I)
1	0.21295735E+02	25	0.22254195E+01
2	-0.23241441E+02	26	0.00000000E+00
3	0.45296185E+00	27	0.00000000E+00
4	0.00000000E+00	28	0.00000000E+00
5	0.16750721E+02	29	0.00000000E+00
6	-0.58446670E+00	30	0.00000000E+00
7	0.00000000E+00	31	0.00000000E+00
8	0.00000000E+00	32	0.00000000E+00
9	0.00000000E+00	33	0.00000000E+00
10	0.00000000E+00	34	0.00000000E+00
11	0.00000000E+00	35	0.00000000E+00
12	0.00000000E+00	36	-0.21239292E+00
13	0.00000000E+00	37	0.00000000E+00
14	0.12243796E+00	38	0.00000000E+00
15	0.00000000E+00	39	0.00000000E+00
16	-0.80217779E+01	40	0.00000000E+00
17	-0.41430332E+00	41	0.00000000E+00
18	0.00000000E+00	42	0.00000000E+00
19	0.00000000E+00	43	0.00000000E+00
20	0.00000000E+00	44	0.00000000E+00
21	0.00000000E+00	45	0.00000000E+00
22	0.00000000E+00	46	0.00000000E+00
23	0.00000000E+00	47	0.00000000E+00
24	0.00000000E+00	48	0.00000000E+00
25	0.22254195E+01	49	0.00000000E+00

NUMBER WEIGHTED RMS ERROR OF THE FIT EQUALS 11.3 PERCENT

DESERT CHIM--1 FOR SOLAR ZENITH FROM 50.00 TO 60.00 DEG

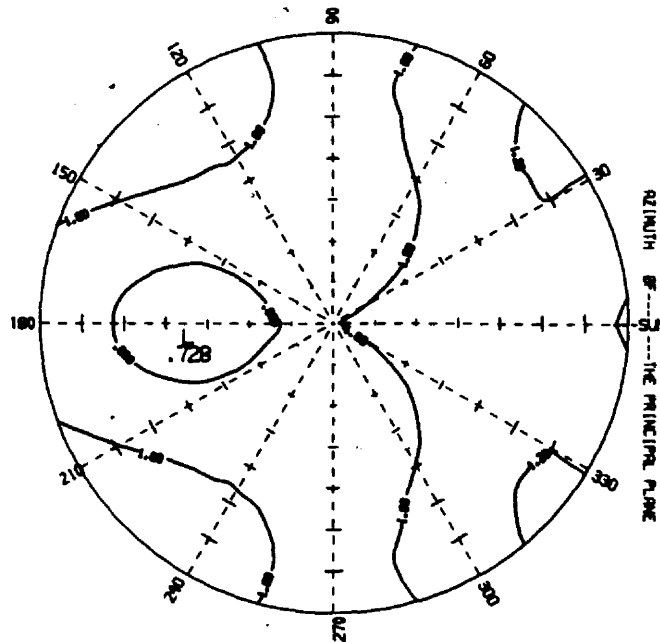


FIGURE AIV- 5. REGRESSION COEFFICIENTS OF THE SPHERICAL HARMONIC APPROXIMATION TO THE DESERT CHIM--1 PATTERN FOR SOLAR ZENITH ANGLES FROM 50. TO 60. DEGREES AND THE CORRESPONDING PLOT OF THE PATTERN

I	C(I)	I	C(I)
1	0.23243704E+03	25	0.43292215E+02
2	-0.31099940E+03	26	0.00000000E+00
3	-0.24716367E+01	27	0.00000000E+00
4	0.00000000E+00	28	0.11049346E+00
5	0.24261587E+03	29	0.00000000E+00
6	0.17995952E+01	30	-0.54721380E-01
7	0.00000000E+00	31	0.00000000E+00
8	-0.19691736E+01	32	0.54075330E-01
9	0.00000000E+00	33	0.00000000E+00
10	0.38708172E+00	34	0.33457609E-01
11	0.00000000E+00	35	0.00000000E+00
12	0.26350701E+01	36	-0.72870736E+01
13	0.00000000E+00	37	0.00000000E+00
14	0.00000000E+00	38	0.00000000E+00
15	0.00000000E+00	39	0.00000000E+00
16	-0.12833022E+03	40	0.00000000E+00
17	0.00000000E+00	41	0.00000000E+00
18	0.00000000E+00	42	0.00000000E+00
19	-0.31147150E+00	43	0.00000000E+00
20	0.00000000E+00	44	0.00000000E+00
21	-0.12516547E+01	45	0.00000000E+00
22	0.00000000E+00	46	0.00000000E+00
23	-0.51852209E+00	47	0.00000000E+00
24	0.00000000E+00	48	0.00000000E+00
25	0.43292215E+02	49	0.00000000E+00

NUMBER WEIGHTED RMS ERROR OF THE FIT EQUALS 5.1 PERCENT

DESERT CHI**2 FOR SOLAR ZENITH FROM 60.00 TO 70.00 DEG

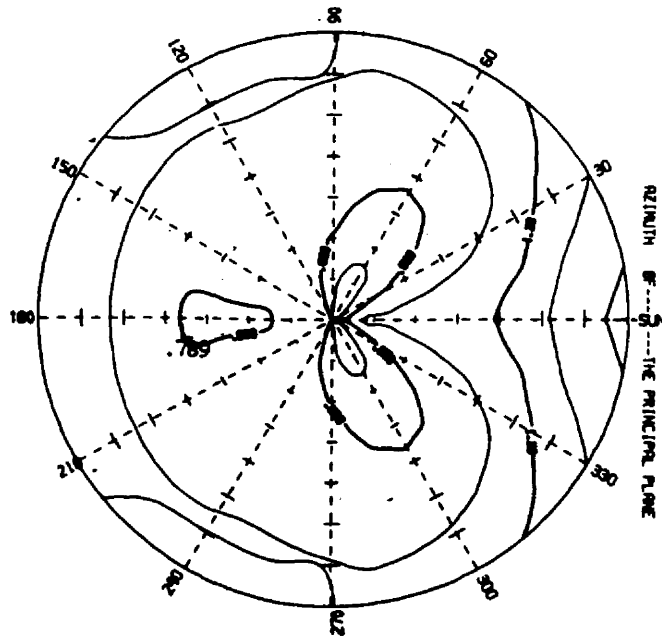


FIGURE AIV- 7. REGRESSION COEFFICIENTS OF THE SPHERICAL HARMONIC APPROXIMATION TO THE DESERT CHI**2 PATTERN FOR SOLAR ZENITH ANGLES FROM 60. TO 70. DEGREES AND THE CORRESPONDING PLOT OF THE PATTERN

I	C(I)	I	C(I)
1	0.11239084E+04	25	0.36163957E+03
2	-0.16255244E+04	26	0.41235179E+03
3	0.55310542E+01	27	0.00000000E+00
4	0.00000000E+00	28	-0.11410982E+01
5	0.13721909E+04	29	0.00000000E+00
6	-0.70389321E+01	30	0.00000000E+00
7	0.00000000E+00	31	0.00000000E+00
8	0.29965315E+01	32	0.00000000E+00
9	0.00000000E+00	33	0.00000000E+00
10	0.95630936E+00	34	0.44365720E-01
11	0.00000000E+00	35	0.00000000E+00
12	-0.21303846E+01	36	-0.10328104E+03
13	0.00000000E+00	37	0.00000000E+00
14	0.54910382E+00	38	0.00000000E+00
15	0.00000000E+00	39	0.00000000E+00
16	-0.83316300E+03	40	0.00000000E+00
17	0.12101903E+01	41	0.43522552E+03
18	0.00000000E+00	42	0.00000000E+00
19	-0.61199725E+00	43	-0.52822242E+00
20	0.00000000E+00	44	0.00000000E+00
21	0.66194092E+00	45	0.00000000E+00
22	0.00000000E+00	46	0.00000000E+00
23	0.31188052E+01	47	0.16737235E+03
24	0.00000000E+00	48	0.00000000E+00
25	0.36163957E+03	49	0.15038401E+02

NUMBER WEIGHTED RMS ERROR OF THE FIT EQUALS 5.9 PERCENT

DESERT CHIM-1 FOR SOLAR ZENITH FROM 70.00 TO 80.00 DEG

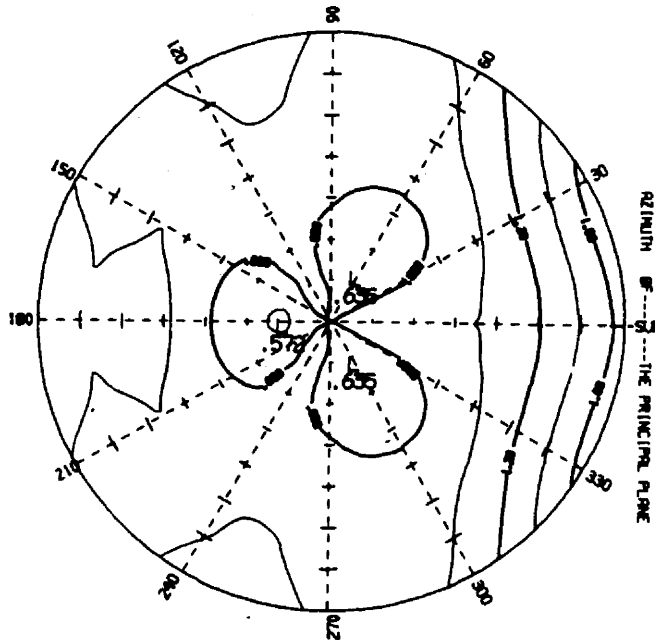


FIGURE AIV- 3. REGRESSION COEFFICIENTS OF THE SPHERICAL HARMONIC APPROXIMATION TO THE DESERT CHIM-1 PATTERN FOR SOLAR ZENITH ANGLES FROM 70. TO 80. DEGREES AND THE CORRESPONDING PART OF THE PATTERN

AIV-1Z

L	C(L)	L	C(L)
1	0.79655782E+03	25	0.25142935E+03
2	-0.11473741E+04	26	0.00000000E+00
3	-0.72564352E+00	27	0.00000000E+00
4	0.00000000E+00	28	-0.10849542E+01
5	0.96666217E+03	29	0.00000000E+00
6	0.61672278E+00	30	-0.40227592E-01
7	0.00000000E+00	31	0.00000000E+00
8	-0.11093550E+01	32	0.00000000E+00
9	0.00000000E+00	33	0.00000000E+00
10	0.56368900E+00	34	0.00000000E+00
11	0.00000000E+00	35	0.00000000E+00
12	0.14834376E+01	36	-0.70692626E+02
13	0.00000000E+00	37	0.00000000E+00
14	-0.14779279E+01	38	0.00000000E+00
15	0.00000000E+00	39	-0.71172926E-01
16	-0.58396219E+03	40	0.00000000E+00
17	0.10541797E+01	41	0.97321824E+00
18	0.00000000E+00	42	0.00000000E+00
19	-0.96279819E+00	43	0.12713375E+01
20	0.00000000E+00	44	0.00000000E+00
21	-0.80551384E+00	45	0.00000000E+00
22	0.00000000E+00	46	-0.22937022E+00
23	-0.71971606E+00	47	0.00000000E+00
24	0.00000000E+00	48	0.00000000E+00
25	0.25142935E+03	49	0.99113909E+01

NUMBER WEIGHTED RMS ERROR OF THE FIT EQUALS 12.9 PERCENT

HIMALAYA CHI**=1 FOR SOLAR ZENITH FROM 10.00 TO 20.00 DEG

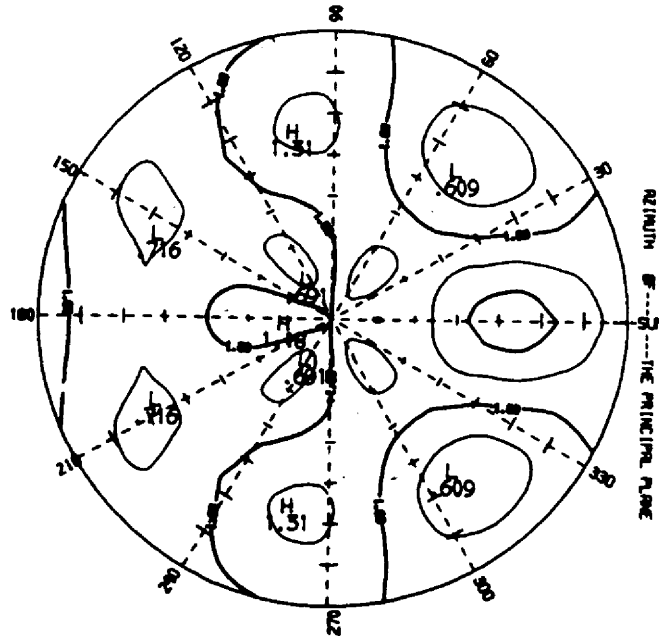


FIGURE AIV- 9. REGRESSION COEFFICIENTS OF THE SPHERICAL HARMONIC APPROXIMATION TO THE HIMALAYA CHI**=1 PATTERN FOR SOLAR ZENITH ANGLES FROM 10. TO 20. DEGREES AND THE CORRESPONDING PLOT OF THE PATTERN

I	C(I)	I	C(I)
1	0.16730077E+00	25	0.00000000E+00
2	0.33730415E+01	26	0.00000000E+00
3	0.00000000E+00	27	0.00000000E+00
4	0.00000000E+00	28	0.00000000E+00
5	-0.92518670E+00	29	0.00000000E+00
6	0.00000000E+00	30	0.00000000E+00
7	0.00000000E+00	31	0.00000000E+00
8	0.00000000E+00	32	0.00000000E+00
9	0.00000000E+00	33	0.00000000E+00
10	0.16365636E+00	34	0.00000000E+00
11	0.00000000E+00	35	0.00000000E+00
12	0.00000000E+00	36	0.00000000E+00
13	0.00000000E+00	37	0.00000000E+00
14	0.00000000E+00	38	0.00000000E+00
15	0.00000000E+00	39	0.00000000E+00
16	0.00000000E+00	40	0.00000000E+00
17	0.00000000E+00	41	0.00000000E+00
18	0.00000000E+00	42	0.00000000E+00
19	0.00000000E+00	43	0.00000000E+00
20	0.00000000E+00	44	0.00000000E+00
21	0.00000000E+00	45	0.00000000E+00
22	0.00000000E+00	46	0.00000000E+00
23	0.00000000E+00	47	0.00000000E+00
24	0.00000000E+00	48	0.00000000E+00
25	0.00000000E+00	49	0.00000000E+00

NUMBER WEIGHTED RMS ERROR OF THE FIT EQUALS 17.4 PERCENT

HIMALA CHIM-1 FOR SOLAR ZENITH FROM 20.00 TO 50.00 DEG

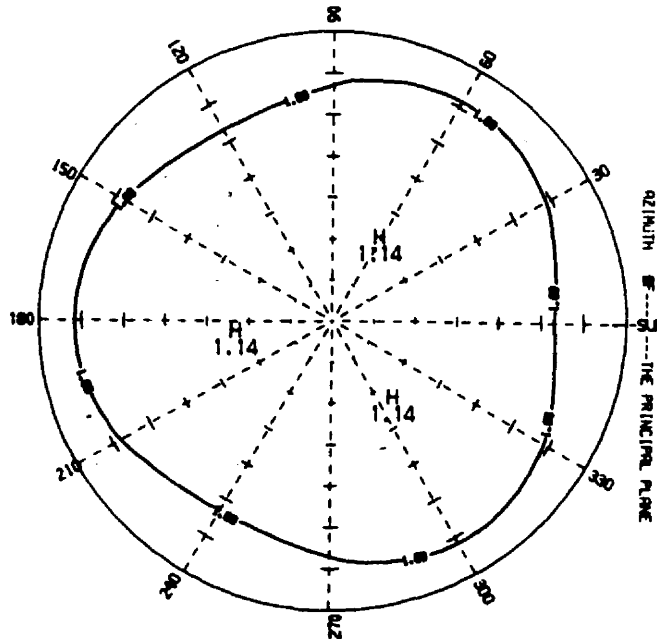


FIGURE AIV-10. REGRESSION COEFFICIENTS OF THE SPHERICAL HARMONIC APPROXIMATION TO THE HIMALAYA CHIM-1 PATTERN FOR SOLAR ZENITH ANGLES FROM 20. TO 50. DEGREES AND THE CORRESPONDING PLOT OF THE PATTERN

I	C(I)	I	C(I)
1	-0.14572218E+04	25	-0.28308176E+03
2	0.20013637E+04	26	0.00000000E+00
3	-0.12886657E+01	27	0.00000000E+00
4	0.00000000E+00	28	0.29529130E+00
5	-0.15562625E+04	29	0.00000000E+00
6	0.13121840E+01	30	0.00000000E+00
7	0.00000000E+00	31	0.00000000E+00
8	0.23608131E+01	32	0.00000000E+00
9	0.00000000E+00	33	0.00000000E+00
10	0.00000000E+00	34	0.00000000E+00
11	0.00000000E+00	35	0.00000000E+00
12	-0.22264669E+01	36	0.49244446E+02
13	0.00000000E+00	37	0.00000000E+00
14	0.00000000E+00	38	0.00000000E+00
15	0.00000000E+00	39	0.00000000E+00
16	0.33018095E+03	40	0.00000000E+00
17	0.00000000E+00	41	0.00000000E+00
18	0.00000000E+00	42	0.00000000E+00
19	0.00000000E+00	43	0.00000000E+00
20	0.00000000E+00	44	0.00000000E+00
21	0.95501962E+00	45	0.00000000E+00
22	0.00000000E+00	46	0.00000000E+00
23	-0.90313147E+00	47	0.00000000E+00
24	0.00000000E+00	48	0.00000000E+00
25	-0.28308176E+03	49	0.00000000E+00

NUMBER WEIGHTED RMS ERROR OF THE FIT EQUALS 11.6 PERCENT

OCEAN CHI**=1 FOR SOLAR ZENITH FROM 0.00 TO 10.00 DEG

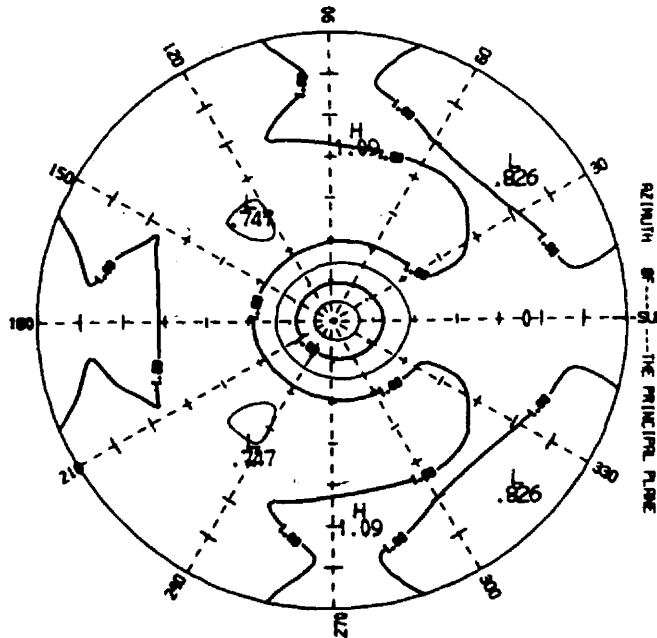


FIGURE AIV-11. REGRESSION COEFFICIENTS OF THE SPHERICAL HARMONIC APPROXIMATION TO THE OCEAN CHI**=1 PATTERN FOR SOLAR ZENITH ANGLES FROM 0. TO 10. DEGREES AND THE CORRESPONDING PLOT OF THE PATTERN

I	C(I)	I	C(I)
1	-0.62549406E+03	25	-0.16698879E+03
2	-0.88870237E+03	26	0.00000000E+00
3	-0.10406269E+02	27	0.00000000E+00
4	0.00000000E+00	28	0.00000000E+00
5	-0.73574254E+03	29	0.00000000E+00
6	0.10518317E+02	30	0.00000000E+00
7	0.00000000E+00	31	0.00000000E+00
8	0.17589374E+01	32	-0.32024273E-01
9	0.00000000E+00	33	0.00000000E+00
10	-0.74859867E+00	34	0.00000000E+00
11	0.00000000E+00	35	0.00000000E+00
12	-0.12198669E+01	36	0.38246289E+02
13	0.00000000E+00	37	0.00000000E+00
14	-0.32116268E+00	38	0.00000000E+00
15	0.00000000E+00	39	0.00000000E+00
16	0.42611873E+03	40	0.00000000E+00
17	-0.46211861E+00	41	-0.15813063E+00
18	0.00000000E+00	42	0.00000000E+00
19	0.49936552E+00	43	0.30499889E+00
20	0.00000000E+00	44	0.00000000E+00
21	0.44294329E+00	45	0.00000000E+00
22	0.00000000E+00	46	-0.38226358E+00
23	-0.50883211E+01	47	0.00000000E+00
24	0.00000000E+00	48	0.00000000E+00
25	-0.16698879E+03	49	-0.29073208E+01

NUMBER WEIGHTED RMS ERROR OF THE FIT EQUALS 18.8 PERCENT

OCEAN CH1**1 FOR SOLAR ZENITH FROM 10.00 TO 20.00 DEG

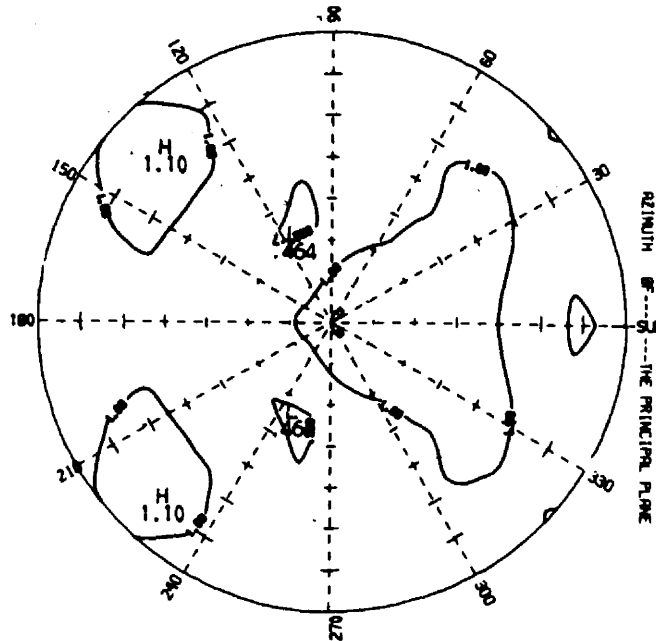


FIGURE AIV-12. REGRESSION COEFFICIENTS OF THE SPHERICAL HARMONIC APPROXIMATION TO THE OCEAN CH1**1 PATTERN FOR SOLAR ZENITH ANGLES FROM 10. TO 20. DEGREES AND THE CORRESPONDING PLOT OF THE PATTERN

I	C(I)	I	C(I)
1	0.75611140E+03	25	0.12888557E+03
2	-0.10245403E+04	26	-0.13886912E+00
3	-0.10787253E+02	27	0.00000000E+00
4	0.00000000E+00	28	0.12014595E+01
5	0.78095580E+03	29	0.00000000E+00
6	0.10553705E+02	30	0.00000000E+00
7	0.00000000E+00	31	0.00000000E+00
8	0.10264940E+02	32	0.57229498E-01
9	0.00000000E+00	33	0.00000000E+00
10	-0.39423902E+00	34	0.00000000E+00
11	0.00000000E+00	35	0.00000000E+00
12	-0.95552764E+01	36	-0.20526497E+02
13	0.00000000E+00	37	0.00000000E+00
14	0.43307064E+00	38	0.00000000E+00
15	0.00000000E+00	39	0.00000000E+00
16	-0.39807902E+03	40	0.00000000E+00
17	-0.17849098E+01	41	0.00000000E+00
18	0.00000000E+00	42	0.00000000E+00
19	0.74152239E+00	43	0.00000000E+00
20	0.00000000E+00	44	0.00000000E+00
21	0.36677238E+01	45	0.00000000E+00
22	0.00000000E+00	46	0.00000000E+00
23	-0.52833380E+01	47	0.00000000E+00
24	0.00000000E+00	48	0.00000000E+00
25	0.12888557E+03	49	0.00000000E+00

NUMBER WEIGHTED RMS ERROR OF THE FIT EQUALS 16.7 PERCENT

OCEAN CHI**1 FOR SOLAR ZENITH FROM 20.00 TO 30.00 DEG

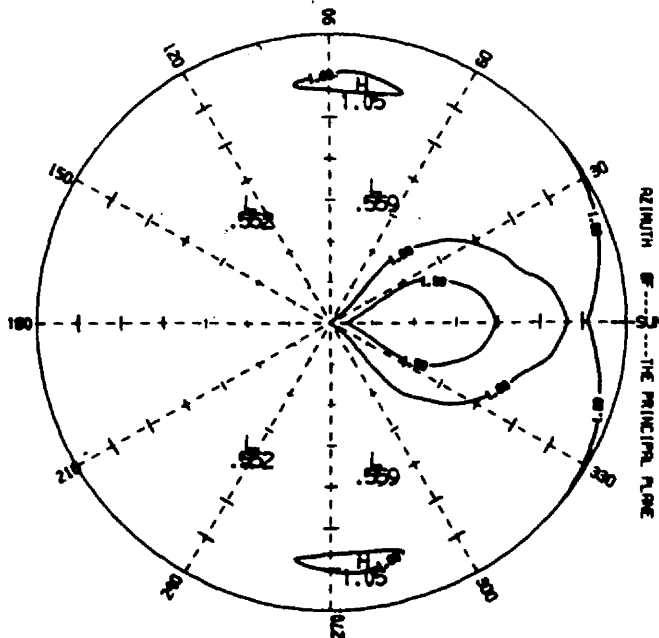


FIGURE AIV-13. REGRESSION COEFFICIENTS OF THE SPHERICAL HARMONIC APPROXIMATION TO THE OCEAN CHI**1 PATTERN FOR SOLAR ZENITH ANGLES FROM 20. TO 30. DEGREES AND THE CORRESPONDING PLOT OF THE PATTERN

I	C(I)	I	C(I)
1	0.56256406E+02	25	0.28857299E+01
2	-0.54908492E+02	26	0.00000000E+00
3	-0.71214027E+01	27	0.00000000E+00
4	0.00000000E+00	28	0.00000000E+00
5	0.40425897E+02	29	0.00000000E+00
6	0.47682910E+01	30	0.00000000E+00
7	0.00000000E+00	31	0.00000000E+00
8	0.12515581E+02	32	0.00000000E+00
9	0.00000000E+00	33	0.00000000E+00
10	-0.11063836E+01	34	0.00000000E+00
11	0.00000000E+00	35	0.00000000E+00
12	-0.10111941E+02	36	0.00000000E+00
13	0.00000000E+00	37	0.00000000E+00
14	0.54467552E-01	38	0.00000000E+00
15	0.00000000E+00	39	0.00000000E+00
16	-0.15363034E+02	40	0.00000000E+00
17	0.94603841E+00	41	0.00000000E+00
18	0.00000000E+00	42	0.00000000E+00
19	-0.22271064E+00	43	0.00000000E+00
20	0.00000000E+00	44	0.00000000E+00
21	0.35138559E+01	45	0.00000000E+00
22	0.00000000E+00	46	0.00000000E+00
23	-0.17244288E+01	47	0.00000000E+00
24	0.00000000E+00	48	0.00000000E+00
25	0.28857299E+01	49	0.00000000E+00

NUMBER WEIGHTED RMS ERROR OF THE FIT EQUALS 14.4 PERCENT

OCEAN CHI**1 FOR SOLAR ZENITH FROM 40.00 TO 50.00 DEG

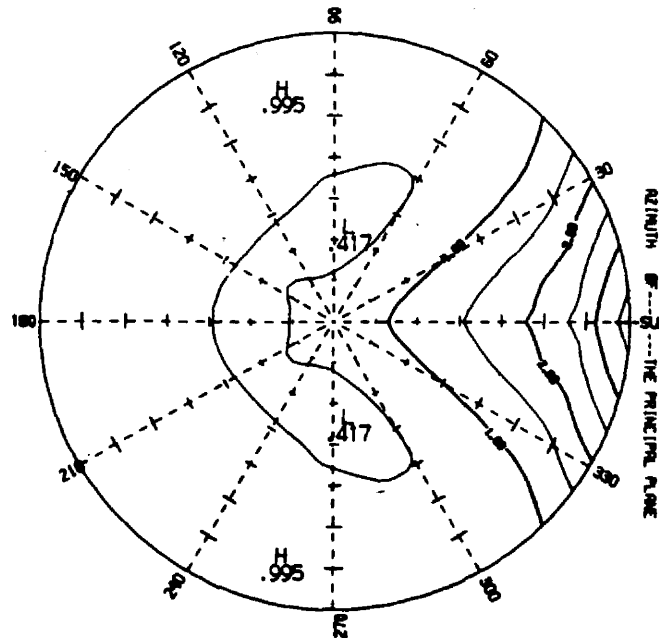


FIGURE AIV-15. REGRESSION COEFFICIENTS OF THE SPHERICAL HARMONIC APPROXIMATION TO THE OCEAN CHI**1 PATTERN FOR SOLAR ZENITH ANGLES FROM 40. TO 50. DEGREES AND THE CORRESPONDING PLOT OF THE PATTERN

I	C(I)	I	C(I)
1	0.27525898E+04	25	0.57985319E+03
2	-0.38445068E+04	26	-0.33425362E+00
3	-0.39464542E+01	27	0.00000000E+00
4	0.00000000E+00	28	-0.15606466E+01
5	0.30929106E+04	29	0.00000000E+00
6	0.24715224E+01	30	-0.36193784E-01
7	0.00000000E+00	31	0.00000000E+00
8	-0.22038003E+01	32	0.00000000E+00
9	0.00000000E+00	33	0.00000000E+00
10	0.18589969E+01	34	0.00000000E+00
11	0.00000000E+00	35	0.00000000E+00
12	0.37592717E+01	36	-0.16771965E+03
13	0.00000000E+00	37	0.00000000E+00
14	0.38908847E-01	38	0.00000000E+00
15	0.00000000E+00	39	0.18805943E+00
16	-0.17418813E+04	40	0.00000000E+00
17	0.20723451E+01	41	0.92425107E+00
18	0.00000000E+00	42	0.00000000E+00
19	-0.17303183E+01	43	-0.49773899E+00
20	0.00000000E+00	44	0.00000000E+00
21	-0.14447611E+01	45	0.00000000E+00
22	0.00000000E+00	46	-0.56293856E-01
23	-0.57241061E+00	47	-0.94761714E-01
24	0.00000000E+00	48	0.00000000E+00
25	0.67985319E+03	49	0.19979951E+02

NUMBER WEIGHTED RMS ERROR OF THE FIT EQUALS 15.1 PERCENT

OCEAN CHIM*-1 FOR SOLAR ZENITH FROM 50.00 TO 60.00 DEG

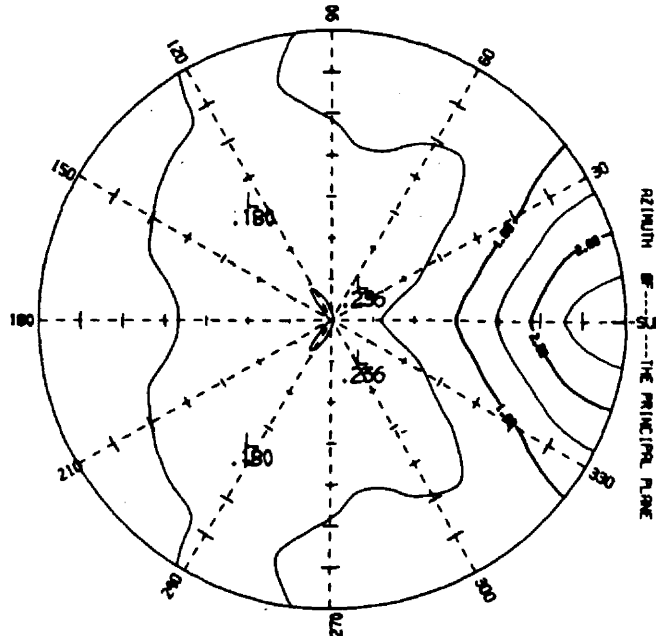


FIGURE AIV-16. REGRESSION COEFFICIENTS OF THE SPHERICAL HARMONIC APPROXIMATION TO THE OCEAN CHIM*-1 PATTERN FOR SOLAR ZENITH ANGLES FROM 50. TO 60. DEGREES AND THE CORRESPONDING PLOT OF THE PATTERN

I	C(I)	I	C(I)
1	0.54887475E+01	25	0.36384400E+00
2	-0.23948032E+01	26	0.00000000E+00
3	0.24645216E+00	27	0.00000000E+00
4	0.00000000E+00	28	0.00000000E+00
5	0.15507438E+01	29	0.00000000E+00
6	0.00000000E+00	30	0.00000000E+00
7	0.00000000E+00	31	0.00000000E+00
8	0.00000000E+00	32	0.00000000E+00
9	0.00000000E+00	33	0.00000000E+00
10	-0.14397941E+00	34	0.00000000E+00
11	0.00000000E+00	35	0.00000000E+00
12	0.00000000E+00	36	0.00000000E+00
13	0.00000000E+00	37	0.00000000E+00
14	0.00000000E+00	38	0.00000000E+00
15	0.00000000E+00	39	0.00000000E+00
16	0.00000000E+00	40	0.00000000E+00
17	0.00000000E+00	41	0.00000000E+00
18	0.00000000E+00	42	0.00000000E+00
19	0.00000000E+00	43	0.00000000E+00
20	0.00000000E+00	44	0.00000000E+00
21	0.00000000E+00	45	0.00000000E+00
22	0.00000000E+00	46	0.00000000E+00
23	0.00000000E+00	47	0.00000000E+00
24	0.00000000E+00	48	0.00000000E+00
25	0.36384400E+00	49	0.00000000E+00

NUMBER WEIGHTED RMS ERROR OF THE FIT EQUALS 9.1 PERCENT

INDIAN CHI**1 FOR SOLAR ZENITH FROM 0.00 TO 10.00 DEG

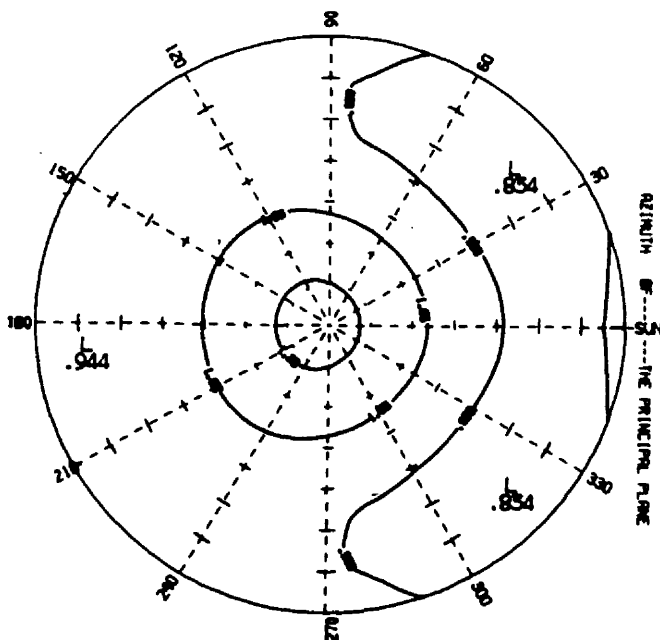


FIGURE AIV-17. REGRESSION COEFFICIENTS OF THE SPHERICAL HARMONIC APPROXIMATION TO THE INDIAN CHI**1 PATTERN FOR SOLAR ZENITH ANGLES FROM 0. TO 10. DEGREES AND THE CORRESPONDING PLOT OF THE PATTERN

I	C(I)	I	C(I)
1	-0.30755023E+02	25	-0.13404000E+01
2	0.42756150E+02	26	0.00000000E+00
3	0.40208881E+01	27	0.00000000E+00
4	0.00000000E+00	28	0.00000000E+00
5	-0.27257787E+02	29	0.00000000E+00
6	-0.37319699E+01	30	0.00000000E+00
7	0.00000000E+00	31	0.00000000E+00
8	-0.62766674E+01	32	0.00000000E+00
9	0.00000000E+00	33	0.00000000E+00
10	0.15643516E+01	34	0.00000000E+00
11	0.00000000E+00	35	0.00000000E+00
12	0.58871137E+01	36	0.00000000E+00
13	0.00000000E+00	37	0.00000000E+00
14	0.00000000E+00	38	0.00000000E+00
15	0.00000000E+00	39	0.00000000E+00
16	0.98727411E+01	40	0.00000000E+00
17	0.36316292E+00	41	0.00000000E+00
18	0.00000000E+00	42	0.00000000E+00
19	-0.11038815E+01	43	0.00000000E+00
20	0.00000000E+00	44	0.00000000E+00
21	-0.20368578E+01	45	0.00000000E+00
22	0.00000000E+00	46	0.00000000E+00
23	0.15063430E+01	47	0.00000000E+00
24	0.00000000E+00	48	0.00000000E+00
25	-0.13404000E+01	49	0.00000000E+00

NUMBER WEIGHTED RMS ERROR OF THE FIT EQUALS 14.2 PERCENT

INDIAN CHIM*-1 FOR SOLAR ZENITH FROM 10.00 TO 20.00 DEG

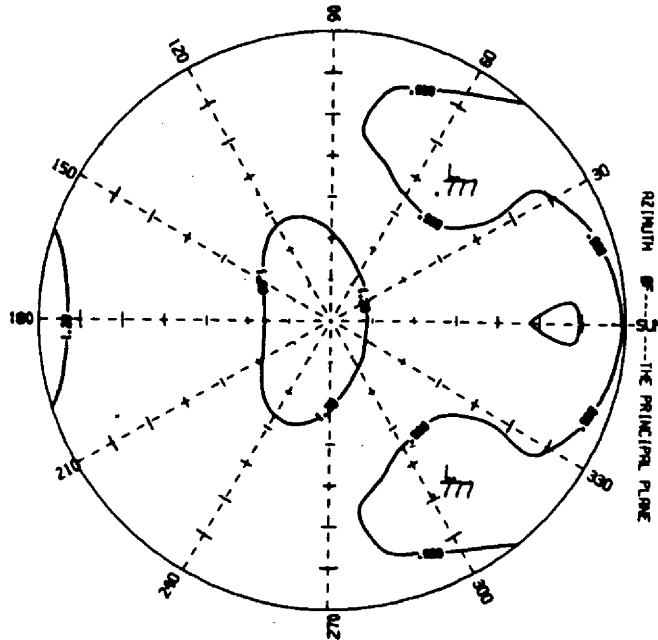


FIGURE AIV-14. REGRESSION COEFFICIENTS OF THE SPHERICAL HARMONIC APPROXIMATION TO THE INDIAN CHIM*-1 PATTERN FOR SOLAR ZENITH ANGLES FROM 10. TO 20. DEGREES AND THE CORRESPONDING PLOT OF THE PATTERN

I	C(I)	I	C(I)
1	0.70050609E+01	25	0.23547293E+00
2	-0.45240934E+01	26	0.00000000E+00
3	-0.11526312E+01	27	0.00000000E+00
4	0.00000000E+00	28	0.00000000E+00
5	0.34143195E+01	29	0.00000000E+00
6	0.11585230E+01	30	0.00000000E+00
7	0.00000000E+00	31	0.00000000E+00
8	-0.83096912E+00	32	0.00000000E+00
9	0.00000000E+00	33	0.00000000E+00
10	-0.49912287E+00	34	0.00000000E+00
11	0.00000000E+00	35	0.00000000E+00
12	0.57035129E+00	36	0.00000000E+00
13	0.00000000E+00	37	0.00000000E+00
14	0.87840209E-01	38	0.00000000E+00
15	0.00000000E+00	39	0.00000000E+00
16	-0.13768365E+01	40	0.00000000E+00
17	0.22201240E+00	41	0.00000000E+00
18	0.00000000E+00	42	0.00000000E+00
19	0.00000000E+00	43	0.00000000E+00
20	0.00000000E+00	44	0.00000000E+00
21	0.00000000E+00	45	0.00000000E+00
22	0.00000000E+00	46	0.00000000E+00
23	-0.19861207E+00	47	0.00000000E+00
24	0.00000000E+00	48	0.00000000E+00
25	0.23547293E+00	49	0.00000000E+00

NUMBER WEIGHTED RMS ERROR OF THE FIT EQUALS 9.4 PERCENT

INDIAN CHI**2 FOR SOLAR ZENITH FROM 20.00 TO 30.00 DEG

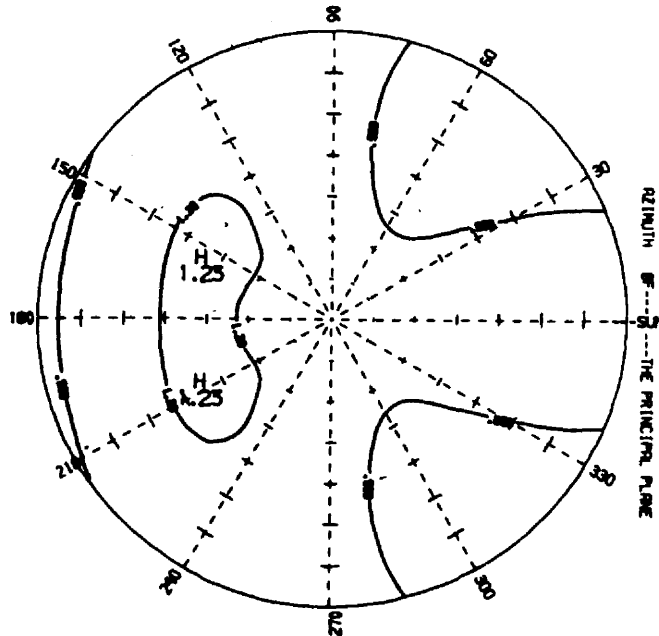


FIGURE AIV-19. REGRESSION COEFFICIENTS OF THE SPHERICAL HARMONIC APPROXIMATION TO THE INDIAN CHI**2 PATTERN FOR SOLAR ZENITH ANGLES FROM 20. TO 30. DEGREES AND THE CORRESPONDING PLOT OF THE PATTERN

I	C(I)	I	C(I)
1	0.40839868E+01	25	0.00000000E+00
2	-0.55195686E+01	26	0.00000000E+00
3	0.38411539E+00	27	0.00000000E+00
4	0.00000000E+00	28	0.00000000E+00
5	0.33032172E+01	29	0.00000000E+00
6	-0.20642818E+00	30	0.00000000E+00
7	0.00000000E+00	31	0.00000000E+00
8	0.00000000E+00	32	0.00000000E+00
9	0.00000000E+00	33	0.00000000E+00
10	-0.17243806E+00	34	0.00000000E+00
11	0.00000000E+00	35	0.00000000E+00
12	0.00000000E+00	36	0.00000000E+00
13	0.00000000E+00	37	0.00000000E+00
14	0.00000000E+00	38	0.00000000E+00
15	0.00000000E+00	39	0.00000000E+00
16	-0.11045876E+01	40	0.00000000E+00
17	0.00000000E+00	41	0.00000000E+00
18	0.00000000E+00	42	0.00000000E+00
19	0.00000000E+00	43	0.00000000E+00
20	0.00000000E+00	44	0.00000000E+00
21	0.16376183E+00	45	0.00000000E+00
22	0.00000000E+00	46	0.00000000E+00
23	0.39093444E+00	47	0.00000000E+00
24	0.00000000E+00	48	0.00000000E+00
25	0.00000000E+00	49	0.00000000E+00

NUMBER WEIGHTED RMS ERROR OF THE FIT EQUALS 5.7 PERCENT

INDIAN CHI**2 FOR SOLAR ZENITH FROM 30.00 TO 40.00 DEG

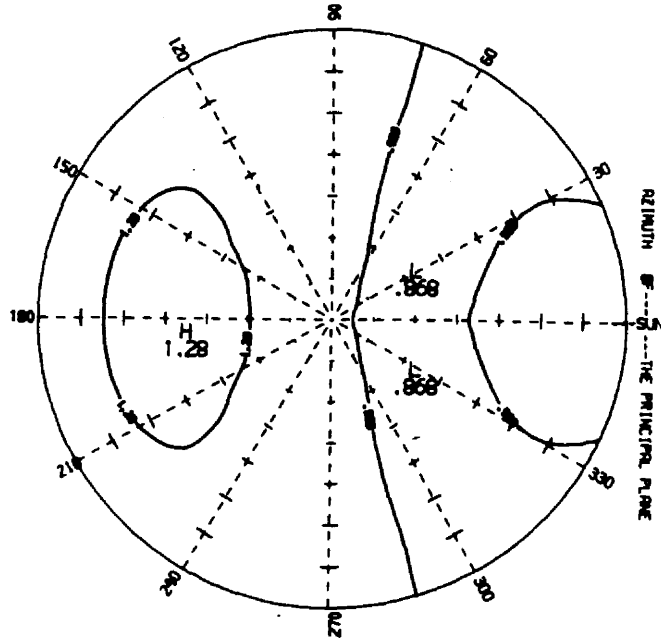


FIGURE AIV-20. REGRESSION COEFFICIENTS OF THE SPHERICAL HARMONIC APPROXIMATION TO THE INDIAN CHI**2 PATTERN FOR SOLAR ZENITH ANGLES FROM 30. TO 40. DEGREES AND THE CORRESPONDING PLOT OF THE PATTERN

I	C(I)	I	C(I)
1	0.51211439E+01	25	0.00000000E+00
2	-0.27530626E+01	26	0.00000000E+00
3	0.16484158E+01	27	0.00000000E+00
4	0.00000000E+00	28	0.00000000E+00
5	0.10781258E+01	29	0.00000000E+00
6	-0.10001635E+01	30	0.00000000E+00
7	0.00000000E+00	31	0.00000000E+00
8	0.12458647E+01	32	0.00000000E+00
9	0.00000000E+00	33	0.00000000E+00
10	0.34440842E+00	34	0.00000000E+00
11	0.00000000E+00	35	0.00000000E+00
12	0.00000000E+00	36	0.00000000E+00
13	0.00000000E+00	37	0.00000000E+00
14	0.00000000E+00	38	0.00000000E+00
15	0.00000000E+00	39	0.00000000E+00
16	0.00000000E+00	40	0.00000000E+00
17	0.00000000E+00	41	0.00000000E+00
18	0.00000000E+00	42	0.00000000E+00
19	0.00000000E+00	43	0.00000000E+00
20	0.00000000E+00	44	0.00000000E+00
21	0.00000000E+00	45	0.00000000E+00
22	0.00000000E+00	46	0.00000000E+00
23	0.00000000E+00	47	0.00000000E+00
24	0.00000000E+00	48	0.00000000E+00
25	0.00000000E+00	49	0.00000000E+00

NUMBER WEIGHTED RMS ERROR OF THE FIT EQUALS 16.7 PERCENT

CLOUD1 CHI**2 FOR SOLAR ZENITH FROM 0.00 TO 10.00 DEG

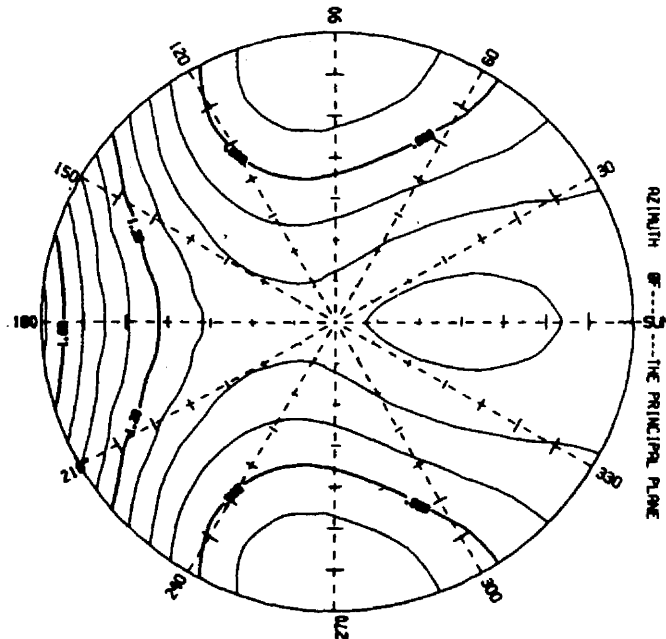


FIGURE AIV-21. REGRESSION COEFFICIENTS OF THE SPHERICAL HARMONIC APPROXIMATION TO THE CLOUD1 CHI**2 PATTERN FOR SOLAR ZENITH ANGLES FROM 0. TO 10. DEGREES AND THE CORRESPONDING PLOT OF THE PATTERN

I	C(I)	I	C(I)
1	0.39761121E+03	25	0.13174793E+03
2	-0.57447999E+03	26	0.00000000E+00
3	0.46583297E+00	27	0.00000000E+00
4	0.00000000E+00	28	0.24760522E+00
5	0.48824665E+03	29	0.00000000E+00
6	-0.12056741E+00	30	-0.71080145E-01
7	0.00000000E+00	31	0.00000000E+00
8	0.18943131E+00	32	0.00000000E+00
9	0.00000000E+00	33	0.00000000E+00
10	0.49195675E+00	34	0.00000000E+00
11	0.00000000E+00	35	0.00000000E+00
12	0.00000000E+00	35	-0.38172471E+02
13	0.00000000E+00	37	0.00000000E+00
14	-0.69522092E+00	38	0.00000000E+00
15	0.00000000E+00	39	0.00000000E+00
16	-0.29939200E+03	40	0.00000000E+00
17	-0.18343688E+00	41	-0.16897972E+00
18	0.00000000E+00	42	0.00000000E+00
19	-0.28590023E+00	43	0.24287230E+00
20	0.00000000E+00	44	0.00000000E+00
21	0.00000000E+00	45	0.00000000E+00
22	0.00000000E+00	46	0.00000000E+00
23	0.00000000E+00	47	-0.16814348E-01
24	0.00000000E+00	48	0.00000000E+00
25	0.13174793E+03	49	0.55453821E+01

NUMBER WEIGHTED RMS ERROR OF THE FIT EQUALS 10.1 PERCENT

CLOUD1 CHI**2-1 FOR SOLAR ZENITH FROM 10.00 TO 20.00 DEG

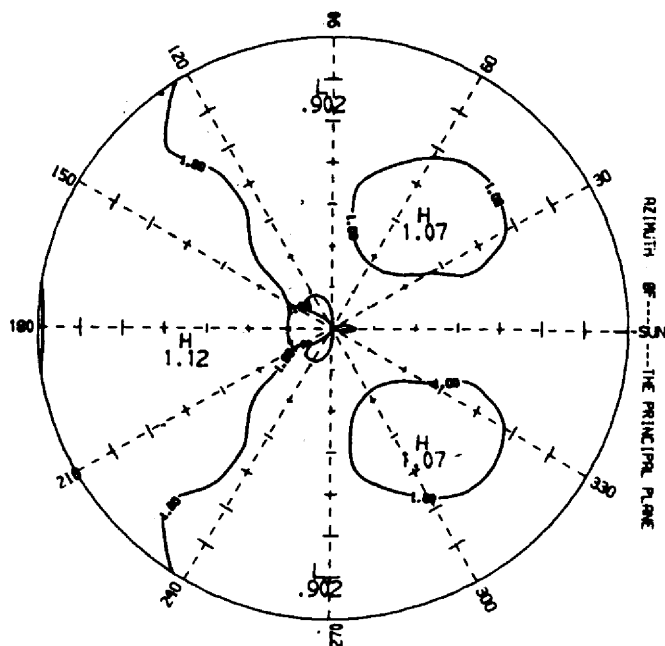


FIGURE AIV-22. REGRESSION COEFFICIENTS OF THE SPHERICAL HARMONIC APPROXIMATION TO THE CLOUD1 CHI**2-1 PATTERN FOR SOLAR ZENITH ANGLES FROM 10. TO 20. DEGREES AND THE CORRESPONDING PLOT OF THE PATTERN

I	C(I)	I	C(I)
1	0.30874370E+02	25	-0.29244909E+01
2	-0.30872877E+02	26	0.00000000E+00
3	-0.20246629E+00	27	0.00000000E+00
4	0.00000000E+00	28	0.10445468E+00
5	0.18904635E+02	29	0.00000000E+00
6	0.48133207E+00	30	0.00000000E+00
7	0.00000000E+00	31	0.00000000E+00
8	0.11690403E+01	32	-0.52625874E-01
9	0.00000000E+00	33	0.00000000E+00
10	0.56700254E+00	34	-0.98358794E-01
11	0.00000000E+00	35	0.00000000E+00
12	-0.13962537E+01	36	0.32304430E+01
13	0.00000000E+00	37	0.00000000E+00
14	-0.94856559E+00	38	0.00000000E+00
15	0.00000000E+00	39	0.00000000E+00
16	-0.44065620E+01	40	0.00000000E+00
17	-0.35631398E+00	41	-0.13923241E+00
18	0.00000000E+00	42	0.00000000E+00
19	-0.73448583E+00	43	0.75615812E+00
20	0.00000000E+00	44	0.00000000E+00
21	0.99451879E+00	45	0.00000000E+00
22	0.00000000E+00	46	0.00000000E+00
23	0.00000000E+00	47	-0.53848285E-01
24	0.00000000E+00	48	0.00000000E+00
25	-0.29244909E+01	49	-0.11319241E+01

NUMBER WEIGHTED RMS ERROR OF THE FIT EQUALS 10.7 PERCENT

CLOUD1 CHI**2-1 FOR SOLAR ZENITH FROM 20.00 TO 30.00 DEG

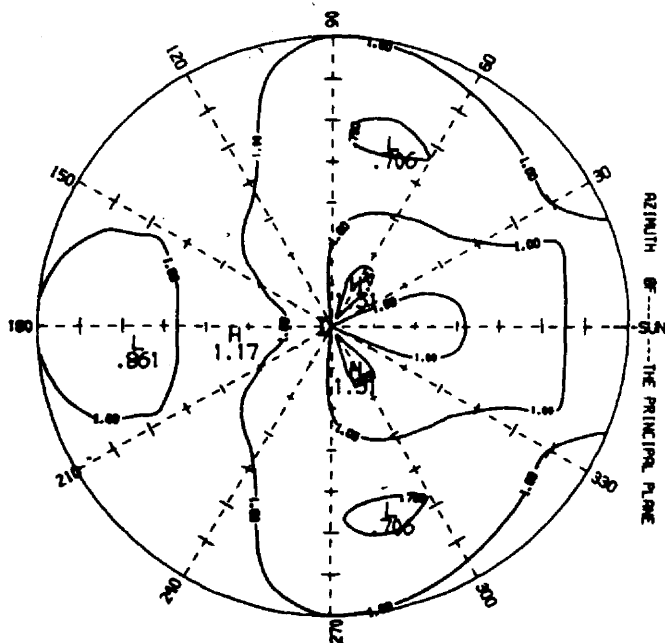


FIGURE AIV-23. REGRESSION COEFFICIENTS OF THE SPHERICAL HARMONIC APPROXIMATION TO THE CLOUD1 CHI**2-1 PATTERN FOR SOLAR ZENITH ANGLES FROM 20. TO 30. DEGREES AND THE CORRESPONDING PLOT OF THE PATTERN

I	C(I)	I	C(I)
1	0.11458851E+02	25	0.00000000E+00
2	-0.85784865E+01	26	0.00000000E+00
3	-0.76928055E+01	27	0.00000000E+00
4	0.00000000E+00	28	0.00000000E+00
5	0.35770745E+01	29	0.00000000E+00
6	0.55375024E+01	30	0.00000000E+00
7	0.00000000E+00	31	0.00000000E+00
8	0.40960294E+01	32	0.00000000E+00
9	0.00000000E+00	33	0.00000000E+00
10	-0.11617352E+01	34	0.00000000E+00
11	0.00000000E+00	35	0.00000000E+00
12	-0.35140000E+01	36	0.00000000E+00
13	0.00000000E+00	37	0.00000000E+00
14	0.16783070E+00	38	0.00000000E+00
15	0.00000000E+00	39	0.00000000E+00
16	-0.88874830E+00	40	0.00000000E+00
17	0.00000000E+00	41	0.00000000E+00
18	0.00000000E+00	42	0.00000000E+00
19	0.74432920E+00	43	0.00000000E+00
20	0.00000000E+00	44	0.00000000E+00
21	0.10476179E+01	45	0.00000000E+00
22	0.00000000E+00	46	0.00000000E+00
23	-0.21771554E+01	47	0.00000000E+00
24	0.00000000E+00	48	0.00000000E+00
25	0.00000000E+00	49	0.00000000E+00

NUMBER WEIGHTED RMS ERROR OF THE FIT EQUALS 15.4 PERCENT

CLOUD1 CHI**2-1 FOR SOLAR ZENITH FROM 30.00 TO 40.00 DEG

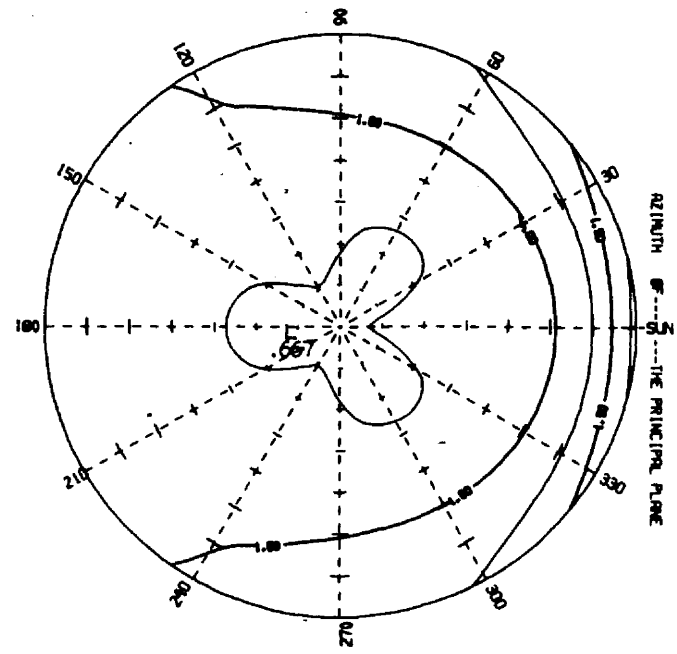


FIGURE AIV-24. REGRESSION COEFFICIENTS OF THE SPHERICAL HARMONIC APPROXIMATION TO THE CLOUD1 CHI**2-1 PATTERN FOR SOLAR ZENITH ANGLES FROM 30. TO 40. DEGREES AND THE CORRESPONDING PLOT OF THE PATTERN

I	C(I)	I	C(I)
1	0.77084321E+01	25	0.48040193E+00
2	-0.51348938E+01	26	0.00000000E+00
3	0.00000000E+00	27	0.00000000E+00
4	0.00000000E+00	28	0.00000000E+00
5	0.32659530E+01	29	0.00000000E+00
6	0.00000000E+00	30	0.00000000E+00
7	0.00000000E+00	31	0.00000000E+00
8	0.53498185E+00	32	0.00000000E+00
9	0.00000000E+00	33	0.00000000E+00
10	-0.17749533E+00	34	0.00000000E+00
11	0.00000000E+00	35	0.00000000E+00
12	-0.42952509E+00	36	0.00000000E+00
13	0.00000000E+00	37	0.00000000E+00
14	0.00000000E+00	38	0.00000000E+00
15	0.00000000E+00	39	0.00000000E+00
16	-0.15515412E+01	40	0.00000000E+00
17	0.24846867E+00	41	0.00000000E+00
18	0.00000000E+00	42	0.00000000E+00
19	0.11911590E+00	43	0.00000000E+00
20	0.00000000E+00	44	0.00000000E+00
21	0.00000000E+00	45	0.00000000E+00
22	0.00000000E+00	46	0.00000000E+00
23	0.16904268E+00	47	0.00000000E+00
24	0.00000000E+00	48	0.00000000E+00
25	0.48040193E+00	49	0.00000000E+00

NUMBER WEIGHTED RMS ERROR OF THE FIT EQUALS 15.2 PERCENT

CLOUD1 CHI**2 FOR SOLAR ZENITH FROM 40.00 TO 50.00 DEG

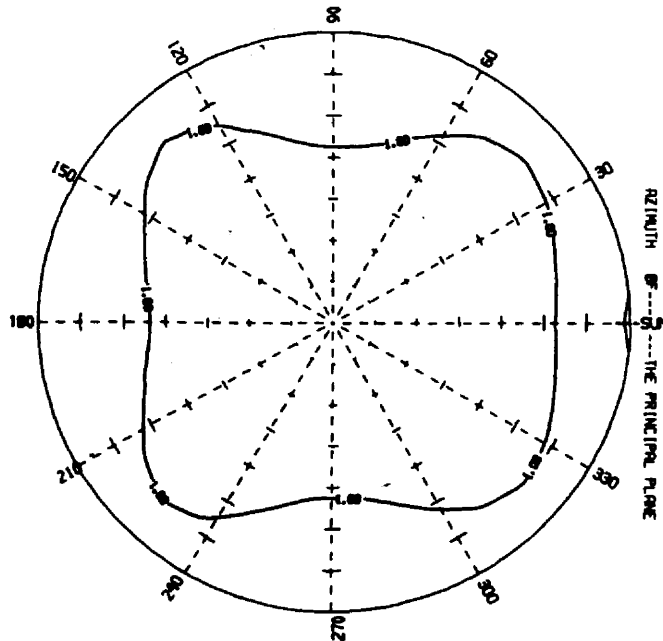


FIGURE AIV-25. REGRESSION COEFFICIENTS OF THE SPHERICAL HARMONIC APPROXIMATION TO THE CLOUD1 CHI**2 PATTERN FOR SOLAR ZENITH ANGLES FROM 40. TO 50. DEGREES AND THE CORRESPONDING PLOT OF THE PATTERN

I	C(I)	I	C(I)
1	0.36376987E+01	25	0.00000000E+00
2	0.43522770E+00	26	0.00000000E+00
3	0.78252878E+00	27	0.00000000E+00
4	0.00000000E+00	28	0.00000000E+00
5	-0.10649756E+01	29	0.00000000E+00
6	-0.68386661E+00	30	0.00000000E+00
7	0.00000000E+00	31	0.00000000E+00
8	0.71915932E+00	32	0.00000000E+00
9	0.00000000E+00	33	0.00000000E+00
10	0.00000000E+00	34	0.00000000E+00
11	0.00000000E+00	35	0.00000000E+00
12	-0.28237362E+00	36	0.00000000E+00
13	0.00000000E+00	37	0.00000000E+00
14	0.00000000E+00	38	0.00000000E+00
15	0.00000000E+00	39	0.00000000E+00
16	0.42252177E+00	40	0.00000000E+00
17	0.00000000E+00	41	0.00000000E+00
18	0.00000000E+00	42	0.00000000E+00
19	0.00000000E+00	43	0.00000000E+00
20	0.00000000E+00	44	0.00000000E+00
21	0.00000000E+00	45	0.00000000E+00
22	0.00000000E+00	46	0.00000000E+00
23	0.00000000E+00	47	0.00000000E+00
24	0.00000000E+00	48	0.00000000E+00
25	0.00000000E+00	49	0.00000000E+00

NUMBER WEIGHTED RMS ERROR OF THE FIT EQUALS 20.8 PERCENT

CLOUD2 CHI**2 FOR SOLAR ZENITH FROM 20.00 TO 30.00 DEG

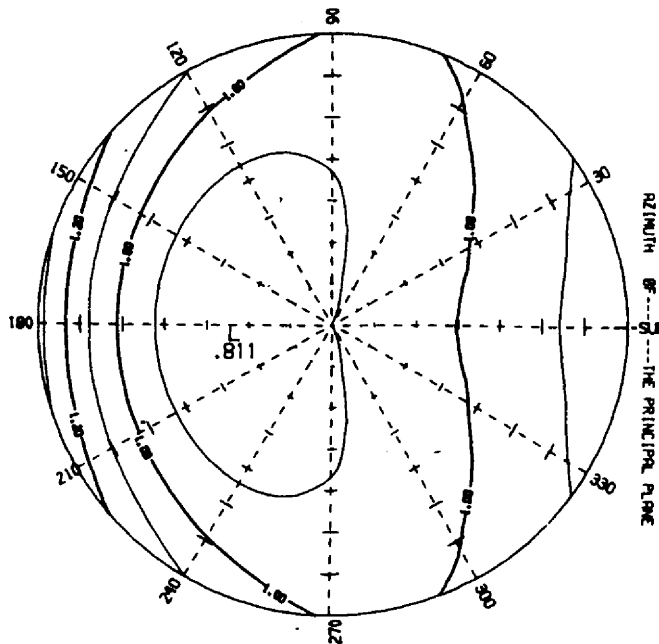


FIGURE AIV-26. REGRESSION COEFFICIENTS OF THE SPHERICAL HARMONIC APPROXIMATION TO THE CLOUD2 CHI**2 PATTERN FOR SOLAR ZENITH ANGLES FROM 20. TO 30. DEGREES AND THE CORRESPONDING PLOT OF THE PATTERN

I	C(I)	I	C(I)
1	0.34549014E+01	25	0.00000000E+00
2	0.14430336E+00	26	0.00000000E+00
3	-0.10903654E+01	27	0.00000000E+00
4	0.00000000E+00	28	0.00000000E+00
5	-0.13705449E+00	29	0.00000000E+00
6	0.77231121E+00	30	0.00000000E+00
7	0.00000000E+00	31	0.00000000E+00
8	0.00000000E+00	32	0.00000000E+00
9	0.00000000E+00	33	0.00000000E+00
10	-0.39285800E+00	34	0.00000000E+00
11	0.00000000E+00	35	0.00000000E+00
12	0.35153230E+00	36	0.00000000E+00
13	0.00000000E+00	37	0.00000000E+00
14	0.00000000E+00	38	0.00000000E+00
15	0.00000000E+00	39	0.00000000E+00
16	-0.14076610E+00	40	0.00000000E+00
17	0.00000000E+00	41	0.00000000E+00
18	0.00000000E+00	42	0.00000000E+00
19	0.00000000E+00	43	0.00000000E+00
20	0.00000000E+00	44	0.00000000E+00
21	0.00000000E+00	45	0.00000000E+00
22	0.00000000E+00	46	0.00000000E+00
23	0.00000000E+00	47	0.00000000E+00
24	0.00000000E+00	48	0.00000000E+00
25	0.00000000E+00	49	0.00000000E+00

NUMBER WEIGHTED RMS ERROR OF THE FIT EQUALS 10.4 PERCENT

CLOUD2 CHI**2 FOR SOLAR ZENITH FROM 40.00 TO 50.00 DEG

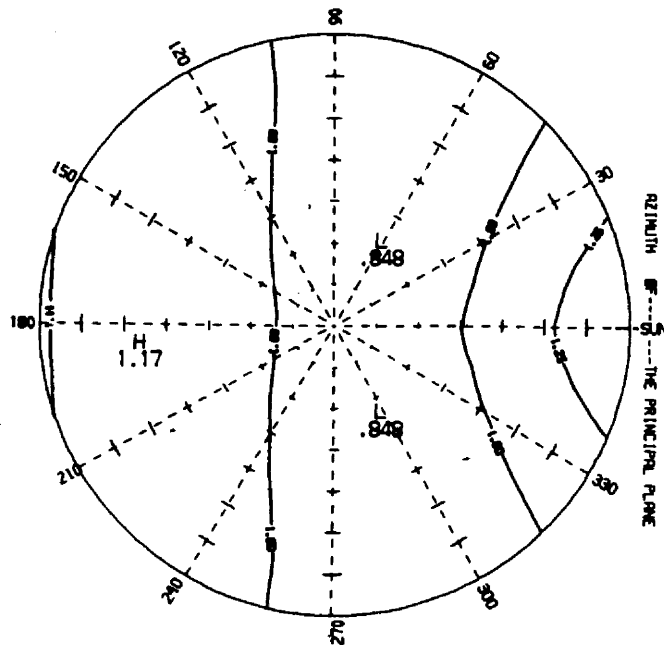


FIGURE AIV-28. REGRESSION COEFFICIENTS OF THE SPHERICAL HARMONIC APPROXIMATION TO THE CLOUD2 CHI**2 PATTERN FOR SOLAR ZENITH ANGLES FROM 40. TO 50. DEGREES AND THE CORRESPONDING PLOT OF THE PATTERN

I	C(I)	I	C(I)
1	0.41924001E+01	25	0.00000000E+00
2	-0.55074920E+00	26	0.00000000E+00
3	-0.18258786E+00	27	0.00000000E+00
4	0.00000000E+00	28	0.00000000E+00
5	0.00000000E+00	29	0.00000000E+00
6	0.00000000E+00	30	0.00000000E+00
7	0.00000000E+00	31	0.00000000E+00
8	0.00000000E+00	32	0.00000000E+00
9	0.00000000E+00	33	0.00000000E+00
10	0.00000000E+00	34	0.00000000E+00
11	0.00000000E+00	35	0.00000000E+00
12	0.00000000E+00	36	0.00000000E+00
13	0.00000000E+00	37	0.00000000E+00
14	0.00000000E+00	38	0.00000000E+00
15	0.00000000E+00	39	0.00000000E+00
16	0.00000000E+00	40	0.00000000E+00
17	0.00000000E+00	41	0.00000000E+00
18	0.00000000E+00	42	0.00000000E+00
19	0.00000000E+00	43	0.00000000E+00
20	0.00000000E+00	44	0.00000000E+00
21	0.00000000E+00	45	0.00000000E+00
22	0.00000000E+00	46	0.00000000E+00
23	0.00000000E+00	47	0.00000000E+00
24	0.00000000E+00	48	0.00000000E+00
25	0.00000000E+00	49	0.00000000E+00

NUMBER WEIGHTED RMS ERROR OF THE FIT EQUALS 16.5 PERCENT

ICE CHI**2 FOR SOLAR ZENITH FROM 40.00 TO 50.00 DEG

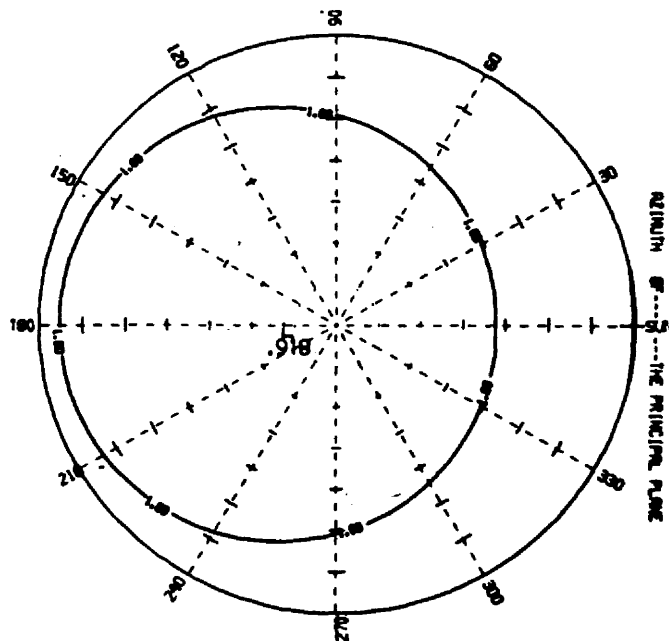


FIGURE AIV-29. REGRESSION COEFFICIENTS OF THE SPHERICAL HARMONIC APPROXIMATION TO THE ICE CHI**2 PATTERN FOR SOLAR ZENITH ANGLES FROM 40. TO 50. DEGREES AND THE CORRESPONDING PLOT OF THE PATTERN

I	C(I)	I	C(I)
1	0.82451030E+01	25	0.00000000E+00
2	-0.46522993E+01	26	0.00000000E+00
3	-0.27509140E+01	27	0.00000000E+00
4	0.00000000E+00	28	0.00000000E+00
5	0.12016706E+01	29	0.00000000E+00
6	0.19316564E+01	30	0.00000000E+00
7	0.00000000E+00	31	0.00000000E+00
8	0.23982155E+00	32	0.00000000E+00
9	0.00000000E+00	33	0.00000000E+00
10	-0.58090551E-01	34	0.00000000E+00
11	0.00000000E+00	35	0.00000000E+00
12	0.00000000E+00	36	0.00000000E+00
13	0.00000000E+00	37	0.00000000E+00
14	0.00000000E+00	38	0.00000000E+00
15	0.00000000E+00	39	0.00000000E+00
16	0.00000000E+00	40	0.00000000E+00
17	0.00000000E+00	41	0.00000000E+00
18	0.00000000E+00	42	0.00000000E+00
19	0.00000000E+00	43	0.00000000E+00
20	0.00000000E+00	44	0.00000000E+00
21	0.00000000E+00	45	0.00000000E+00
22	0.00000000E+00	46	0.00000000E+00
23	0.00000000E+00	47	0.00000000E+00
24	0.00000000E+00	48	0.00000000E+00
25	0.00000000E+00	49	0.00000000E+00

NUMBER WEIGHTED RMS ERROR OF THE FIT EQUALS 13.4 PERCENT

ICE CHIM-1 FOR SOLAR ZENITH FROM 50.00 TO 60.00 DEG

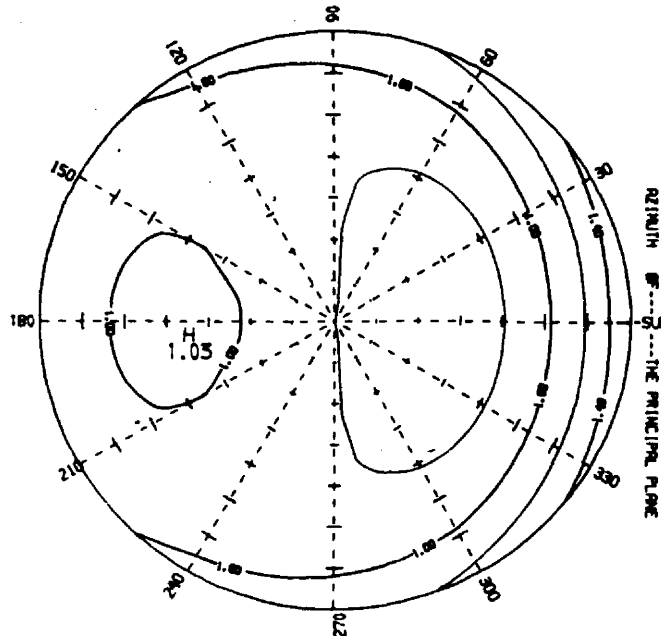


FIGURE AIV-30. REGRESSION COEFFICIENTS OF THE SPHERICAL HARMONIC APPROXIMATION TO THE ICE CHIM-1 PATTERN FOR SOLAR ZENITH ANGLES FROM 50. TO 60. DEGREES AND THE CORRESPONDING PLOT OF THE PATTERN